DEVELOPMENT OF A THICK CONTINUUM-BASED SHELL FINITE ELEMENT FOR SOFT TISSUE DYNAMICS

by

Bahareh Momenan

Thesis Submitted to the

Faculty of Graduate and Postdoctoral Studies

in Partial Fulfillment of the Requirements for the Degree of

DOCTORATE IN PHILOSOPHY

in Mechanical Engineering

Ottawa-Carleton Institute for Mechanical and Aerospace Engineering

Faculty of Engineering

University of Ottawa

Acknowledgement

I would like to begin this document with the name of God, the most compassionate and the most merciful, who has blessed me with health and intelligence, and surrounded me with the best of his creations.

I would like to express my genuine appreciation to my parents, Masoumeh Rezaei Nazari and Mohammad Momenan, and my brother, Amirabbas Momenan, for their unconditional support and love throughout my life. Accomplishments would not be possible without them.

I would like to express my sincere gratitude to my supervisor Dr. Michel Labrosse for the continuous support of my Ph.D. study and related research. His motivation, perfectionism, guidance, and immense knowledge made research, practice, and failing a joyful learning journey with a thrilled ending called success! In addition, I owe my professional development to Dr. Labrosse, who believed in me and gave me golden opportunities such as teaching as a part-time professor, and co-supervising students. His patience and personality have played a significant role in my personal development as well.

Besides my supervisor, I would like to thank the rest of my thesis committee: Dr. Davide Spinello, and Dr. John Hayes for their insightful comments and questions, which assured that the research is proceeding on the right track from various perspectives.

Last but not the least, I would like to thank my friends for supporting me spiritually and for all the fun we have had.

Abstract

Momenan, Bahareh. Ph.D., University of Ottawa, October 2016. *Development of a Thick Continuum-based Shell Finite Element for Soft Tissue Dynamics.* Supervised by Dr. Michel Labrosse.

The goal of the present doctoral research is to create a theoretical framework and develop a numerical implementation for a shell finite element that can potentially achieve higher performance (i.e. combination of speed and accuracy) than current Continuum-based (CB) shell finite elements (FE), in particular in applications related to soft biological tissue dynamics. Specifically, this means complex and irregular geometries, large distortions and large bending deformations, and anisotropic incompressible hyperelastic material properties.

The critical review of the underlying theories, formulations, and capabilities of the existing CB shell FE revealed that a general nonlinear CB shell FE with the abovementioned capabilities needs to be developed. Herein, we propose the theoretical framework of a new such CB shell FE for dynamic analysis using the total and the incremental updated Lagrangian (UL) formulations and explicit time integration. Specifically, we introduce the geometry and the kinematics of the proposed CB shell FE, as well as the matrices and constitutive relations which need to be evaluated for the total and the incremental UL formulations of the dynamic equilibrium equation. To verify the accuracy and efficiency of the proposed CB shell element, its large bending and distortion capabilities, as well as the accuracy of three different techniques presented for large strain analysis, we implemented the element in Matlab and tested its application in various geometries, with different material properties and loading conditions. The new high performance and accuracy element is shown to be insensitive to shear and membrane locking, and to initially irregular elements.

Contents

Acknowledgement ii

Abstract iii

List of Figures ix

List of Tables xiii

1 CHAPTER 1: INTRODUCTION 1

1.1 Proposal statement 3

1.2 Contributions 3

1.3 Thesis outline 4

2 CHAPTER 2: CONTEXT OF THE STUDY AND LITERATURE REVIEW 6

2.1 Soft tissues 7

2.2 Finite element formulations 7

2.2.1 Classical vs. Continuum-based shell elements 8

2.2.2 Interpolation (shape) functions 9

2.2.3 Principle of virtual work 11

2.2.4 Nonlinear finite element theory in dynamics 23

2.2.5 Comparison between the total and the updated Lagrangian formulations 26

2.2.6 Time integration 27

2.2.6.1 Explicit time integration in dynamics 28

2.3 Software packages 30

2.3.1 Commercial software packages 30

2.3.1.1 LS-DYNA 30

2.3.1.2 NEi Explicit 30

2.3.1.3 ABAQUS 31

2.3.1.4 SEPRAN 32

2.3.2 Open source software packages 33

2.3.2.1 Finite Element Analysis Program (FEAP) 33

2.3.2.2 Continuity 34

2.3.3 Summary of the software packages 35

2.4 Review of existing shell theories 36

2.4.1 First order shear deformation theory: Kirchhoff-Love shell theory 37

2.4.2 Second order shear deformation theory: Modified Mindlin-Reissner shell theory 38

2.4.3 Higher order shear deformation theories 39

2.5 Review of existing continuum-based (CB) shell elements 40

2.5.1 Hughes and Liu's CB shell element 42

2.5.1.1 Geometric and kinematic descriptions 43

2.5.1.1.1 Geometric description 43

2.5.1.1.2 Kinematic description 47

2.5.1.2 Coordinate systems 50

2.5.1.2.1 Global coordinate system 51

2.5.1.2.2 Lamina coordinate system 51

2.5.1.2.3 Fiber coordinate system 54

2.5.1.3 Derivation of the trial value for the displacement of a director 57

2.5.1.4 Number of degrees of freedom per node 58

2.5.1.5 Constitutive equations 59

2.5.2 Bathe and Bolourchi's CB shell element 60

2.5.2.1 Geometric and kinematic descriptions 61

2.5.2.2 Strain-displacement transformation matrix 61

2.5.3 Summary of the pros and cons of the existing CB shell elements 68

2.6 Measures of deformation in the global coordinate system 69

2.6.1 Deformation gradient 69

2.6.2 Right and left Cauchy-Green tensor 69

2.6.3 Green-Lagrange and Almansi strain tensors 70

2.7 Anisotropic nonlinear hyperplastic constitutive relations, incompressibility, and application of zero normal stress condition 70

2.8 Shear and membrane locking 74

2.8.1 Shear locking 74

2.8.2 Membrane locking 75

2.8.3 Summary of shear and membrane locking 75

2.9 Summary 76

3 CHAPTER 3: DEVELOPMENT OF A NEW THICK CONTINUUM-BASED SHELL FINITE ELEMENT WITH SPECIAL MANAGEMENT OF CONSTITUTIVE RELATIONS 77

3.1 Total and incremental updated Lagrangian formulation using explicit time integration 79

3.2 Geometric and kinematic descriptions 80

3.3 Coordinate systems 83

3.3.1 Limitation of the fiber coordinate system presented in Section 2.5.1.2.3 84

3.3.2 A new algorithm for fiber coordinate system 84

3.4 Nodal degrees of freedom 85

3.5 Transformation matrices 86

3.6 Jacobians 86

3.7 Measures of deformation in the lamina coordinate system 87

3.7.1 Deformation gradient 87

3.7.2 Right and left Cauchy-Green tensor 87

3.7.3 Green-Lagrange and Almansi strain tensors 88

3.8 Linear strain-displacement transformation matrix in the lamina coordinate system 88

3.9 Plane stress constitutive relations for small strain analysis 94

3.9.1 Application of zero normal stress condition 95
3.10 Constitutive relations for large strain analysis 96
3.10.1 Technique 1 96
3.10.2 Technique 2 99
3.10.3 Technique 3 100
3.11 Fiber length update algorithm for large membrane strains 100
3.12 Force vectors 102
3.12.1 External forces 102
3.12.2 Internal forces 104
3.13 Stiffness matrix 104
3.14 Mass matrices 105
3.14.1 M1: Hughes' lumped mass matrix 105
3.14.2 M2: Lumping the consistent mass matrix through row summing technique 107
3.15 Numerical integration for shell elements 108
3.16 Critical time step 111
3.17 Operation count 113
3.18 Numerical implementation of the present CB shell FE 114
4 CHAPTER 4: RESULTS AND DISCUSSION OF NUMERICAL TESTS 116
4.1 Small strain analysis of linear elastic materials: insensitivity to initially irregular elements and/or geometries, large deformations and rotations, shear and membrane locking 117
4.1.1 Test 1: Linear elastic, small bending deformation and rotations, small strains 117
4.1.2 Test 2: Elastic, moderate bending deformations and rotations, small strains 121
4.1.3 Test 3: Elastic, moderate pure bending deformations and rotations, small strains 123
4.1.4 Test 4: Elastic, large pure bending deformations and rotations, small strains 127
4.1.5 Test 5: Scordelis-Lo roof, initially singly-curved, membrane and bending deformation 131

4.1.6 Test 6: Large pre-twist, bending deformation in both planes 133

4.1.7 Test 7: Thick-walled cylinder, linear elastic, small in-plane strains..................... 135

4.2 Large strain analysis of linear elastic materials: insensitivity to initially irregular elements and/or geometries, large distortion, verifications of Techniques 1, 2, 3 and the fiber length update algorithm... 138

4.2.1 Test 8: Nonlinear isotropic elastic, large distortions, large strains 139

4.3 Large strain analysis of anisotropic nonlinear hyperelastic incompressible materials: insensitivity to initially curved geometry and large 3D deformations; verification of Technique 1 and of the fiber length update algorithm 144

4.3.1 Test 9: Nonlinear anisotropic incompressible hyperelastic: human thoracic aorta 145

4.3.2 Test 10: Nonlinear anisotropic incompressible hyperelastic: dog carotid artery.. 149

5 CHAPTER 5: CONCLUSION 155

5.1 Summary of findings.. 156

5.2 Specific contributions of the present CB shell FE and the UL constitutive relations.. 158

5.3 Limitations and recommendation for future work 159

5.4 Final remarks.. 159

Bibliography 161

List of Figures

Figure 2.1: 9-noded CB shell element based on an 18-node continuum element.......................... 9

Figure 2.2: 4 to 9 variable-number-node 2D element. $\boldsymbol{r}$ and $\boldsymbol{s}$ are the parent (also called natural and/or curvilinear) coordinate system (adapted from Bathe, 1996). 10

Figure 2.3: Configurations considered in nonlinear analyses (adapted from Bathe (1996), page 499). 14

Figure 2.4: Top: front view of a shell in an undeformed configuration. Bottom left: motion of the fiber in the Kirchhoff-Love shell theory. Bottom right: motion of the fiber in the Mindlin-Reissner shell theory. 38

Figure 2.5: Curvilinear coordinate system of a 9-noded CB shell element. 44

Figure 2.6: Left: mapping of a general cube into the physical shell element. Right: illustration of Equations 2.35 to 2.41. The script 0 denoting the undeformed configurations is dropped for convenience.. 46

Figure 2.7: A general representation of the displacement of the reference surface with time. 48

Figure 2.8: Nodal fiber inextensibility condition maintained by radial return normalization. 50

Figure 2.9: Lamina coordinate system shown on a typical lamina. 51

Figure 2.10: Lamina coordinate system along a fiber... 52

Figure 2.11: Illustration of the lamina coordinate system with respect to the parent coordinate system. 53

Figure 2.12: Nodal fiber coordinate system. $\Delta\boldsymbol{\theta 1}$ and $\Delta\boldsymbol{\theta 2}$ denote rotation increments about the basis $\boldsymbol{e1f}$ and $\boldsymbol{e2f}$, respectively. 55

Figure 2.13: relationship between the three orthogonal transformation matrices. 57

Figure 3.1: Kinematics. Right subscripts $\boldsymbol{a}$ denoting the node number are dropped for convenience.. 83

Figure 3.2: Left: physically expected rotation of the fiber coordinate system as the element deflects. Right: Fiber coordinate system at the 90° deflection of the element obtained from the algorithm presented in Section 2.5.1.2.3, changes orientation from that of the initial configuration. 84

Figure 3.3: Main routine and operation count. 114

Figure 3.4: Flowchart of the numerical implementation of the present CB shell FE. 115

Figure 4.1: Geometry, loading condition, and analytical linear static solution. 118

Figure 4.2: Dynamic response of the simply supported plate due to step pressure. 118
Figure 4.3: Vertical displacements at the maximum deflection obtained from the 4 shells per quarter mesh. Units are in meters. 119
Figure 4.4: Geometry, loading condition, and analytical nonlinear static solution. 121
Figure 4.5: Vertical displacements at the maximum deflection obtained from 3-element mesh. Units are in meters. 122
Figure 4.6: Geometry, loading condition, and material properties. 124
Figure 4.7: Schematic of the four meshes considered. 124
Figure 4.8: Deformation of the cantilever beam at the maximum load configuration, using the irregular 4-element mesh. Units are in meters. 125
Figure 4.9: Pure bending of a cantilever beam. Left: 3-element mesh; Right: 4-element mesh. 126
Figure 4.10: Geometry, loading condition, and material properties. 128
Figure 4.11: Failure in the deformation of the cantilever beam subjected to a pure tip bending moment due the limitation of the former fiber coordinate system, as discussed in Section 3.3.1 . Units are in meters. 129
Figure 4.12: Comparison between the end displacements, in large pure bending of a cantilever beam, obtained from M1 (mass matrix presented in Section 3.14.1) and M2 (mass matrix presented in Section 3.14.2). In both cases, the new fiber coordinate system (Section 3.3.2) is employed. 130
Figure 4.13: Deformation of the cantilever beam at the maximum load configuration obtained from the new fiber coordinate system (Section 3.3.2) and M1 (mass matrix of Section 3.14.1). Units are in meters. 130
Figure 4.14: Geometry, material properties, boundary conditions, and loading condition for a Scordelis-Lo roof. 131
Figure 4.15: Convergence of Test 5 to the analytical solution. 132
Figure 4.16: Vertical displacement in region 1 of the Scordelis-Lo roof with a 6×6 mesh. Units are in meters. 132
Figure 4.17: Geometry, material properties, and loading condition of a cantilevered beam with an overall pre-twist of 90°. 133
Figure 4.18: Convergence of the normalized (numerical/theoretical) displacements in the X- and Y-directions due to mesh refinement. 134

Figure 4.19: displacement in X-direction using 8 elements along the pre-twisted cantilevered beam. Units are in inches. 134

Figure 4.20: Geometry, material properties, and loading condition. $\boldsymbol{m}$ and $\boldsymbol{n}$ represent the number of elements in the circumferential and radial directions, respectively. 136

Figure 4.21: Comparison between the analytical and finite element stress results in the circumferential (left) and radial (right) directions. Readings are taken at the integration points closest to the inner, middle, and outer radii, under an internal pressure of 1 MPa, with v=0.49. 136

Figure 4.22: Circumferential (left) and radial (right) stress distribution across the pipe wall for the 2×3 mesh. Units for stress and radius are MPa and mm, respectively. 137

Figure 4.23: Left: Geometry and material properties; Middle: Mesh employed in (Bathe et al., 1975); Right: Mesh employed herein; Bottom: Loading rates. Δt is the average time step for Techniques 1, 2 and 3. 140

Figure 4.24: Load vs. displacement curves obtained from Technique 1 at locations A, B and C. Left: 60 increments to final load. Right: 400 increments to final load. 141

Figure 4.25: Load vs. displacement curves obtained from Technique 2 at locations A, B and C. Left: 60 increments to final load. Right: 400 increments to final load. 141

Figure 4.26: Load vs. displacement curves obtained from Technique 3 at locations A, B and C. Left: 60 increments to final load. Right: 400 increments to final load. 142

Figure 4.27: Illustration of the initial configuration, maximum load (deformed) configuration and the distribution of the Green-Lagrange strains at the max load configuration, obtained from Technique 3 with 60 increments to final load. 142

Figure 4.28: Left: Human thoracic aorta geometry and material properties; Right: Loading rates. 146

Figure 4.29: Comparison between the experimental, analytical and finite element data for human thoracic aorta under pressurization with closed-end and free extension conditions: inner radius vs. pressure (top) and longitudinal stretch ratio vs. pressure (middle). Comparison between the analytical and finite element stress results across the aorta wall in the circumferential (bottom-left), longitudinal (bottom-middle), and radial (bottom-right) directions, measured at 13.33 kPa and close to the open end of the aorta. In the legend, M1 and M2 refer to the mass matrices of

Sections 3.14.1 and 3.14.2, respectively. Measurements are taken in the middle to prevent influence of the boundary conditions. 147
Figure 4.30: Deformation and distribution of pressure band (Equation 4.3) due to pressurization under closed-end and free extension conditions at the maximum load configuration obtained with M1 (mass matrix of Section 3.14.1) and the faster loading rate. 148
Figure 4.31: Deformation and distribution of pressure band (Equation 4.3) due to pressurization under closed-end and free extension conditions at the maximum load configuration obtained with M2 (mass matrix of Section 3.14.2) and the faster loading rate. 148
Figure 4.32: Left: Dog carotid artery geometry and material properties; Right: Loading rates. 149
Figure 4.33: Comparison between the experimental, analytical and finite element data for dog carotid artery under pressurization with closed-end and free extension conditions: inner radius vs. pressure (top) and longitudinal stretch ratio vs. pressure (middle). Comparison between the analytical and finite element stress results across the aortic wall in the circumferential (bottom-left), longitudinal (bottom-middle), and radial (bottom-right) directions, measured at 13.33 kPa and close to the open end of the artery. In the legends, M1 and M2 refer to the mass matrices of Sections 3.14.1 and 3.14.2, respectively. Measurements are taken in the middle to prevent influence of the boundary conditions. 150
Figure 4.34: Deformation and distribution of pressure band due to pressurization under closed-end and free extension conditions at the maximum load configuration obtained with M2 (mass matrix of Section 3.14.2) and the faster loading rate. 151
Figure 4.35: Deformation and distribution of pressure band due to pressurization under closed-end and free extension conditions at the maximum load configuration obtained with M2 (mass matrix of Section 3.14.2) and the slower loading rate. 151

List of Tables

Table 2.1: Interpolation functions (Bathe, 1996).. 11

Table 2.2: Capabilities of commercial software packages.. 35

Table 2.3: Analogy of locking phenomena (Belytschko et al., 2000). 76

Table 3.1: Normal and reduced Gaussian rules for Lagrange elements (Hughes and Liu, 1980). 109

Table 4.1: Results of Test 1. 120

Table 4.2: Results of Test 2. 122

Table 4.3: Results of Test 3. 125

Table 4.4: present errors obtained from Equation 4.1, and computation costs for different mesh sizes and Poison’s ratios. $\boldsymbol{ri}$ and $\boldsymbol{ro}$, respectively, represent the radii of the innermost and the outermost integration points across the pipe wall for each mesh. 137

Table 4.5: Results of Test 8. 140

CHAPTER 1: INTRODUCTION

Researchers have shown that the development of many diseases (such as atherosclerosis, asthma, and heart failure) may be associated with changes in cell mechanics, extracellular matrix structure, or mechanotransduction (i.e., the mechanisms by which cells sense and respond to mechanical signals) (Ingber, 2003). Therefore, it is important to be able to properly understand and simulate the mechanical behaviour of living tissues. Furthermore, accurate tissue deformation information and force feedback are also needed for the simulation of surgical procedures.

While hard tissues (e.g. bone) benefit from similarities with classical engineering materials, soft tissues (e.g. brain, blood vessels, and liver) require the use of advanced tools for their modeling and simulation. Specifically, given the complexity of the shapes and material properties involved, numerical solution schemes are required, such as those based on finite element (FE) methods.

There are many potential constitutive models for different types of soft tissues. Most constitutive models rely on the definition of a strain energy function (hyperelasticity). Selection of the mathematical form of the strain energy function must obey multiple principles of continuum mechanics. In addition, the material constants associated with a specific strain energy function must be obtained from an adequate set of experiments.

Assuming that a strain energy function and material constants are properly determined, they may or may not be available in general purpose FE software. Some commercial programmes allow implementation of user-defined strain energy functions (Famaey, 2008). However, user-defined strain energy functions are most often implemented using volume finite elements such as bricks (ABAQUS, 2005; LS-DYNA, 2011; Segal, 2010). In the case of structures with thin walls that experience bending, this undermines the performance and the accuracy of the computational models compared to what specialized shell elements might achieve. In the case of heart valves, where the leaflet thickness can be as small as 0.2 mm, the requirement of several brick elements through the thickness to properly capture bending leads to small critical time steps (proportional to dimensions of the smallest element, according to Courant's condition), which in turn give rise to large calculation times. For instance, in the case of a simulation tool for studying different types of aortic valve repair based on the explicit time-integration FE solver in commercial software LS-Dyna 971, about 8,5000 brick elements are needed in a typical model, making the computation too lengthy (4 to 9 hours) for real time simulations (Labrosse et al., 2011). In contrast, shell elements could potentially capture the bending behaviour of the whole tissue thickness at once, and feature larger critical time steps, both factors theoretically making shorter computational times possible for explicit time-integration simulations.

Although many shell elements already exist in the literature, and some shell elements have been proposed for the analysis of soft biological tissues, it will be detailed in Section 2.5 how they are affected by limited capabilities in modelling complex geometries, large bending deformations and large distortions.

1.1 Proposal statement

The goal of the present research is to develop and implement a shell finite element that can potentially achieve higher performance (i.e. combination of speed and accuracy) than current shell elements, in particular in applications related to soft biological tissue dynamics. Specifically, this means complex and irregular geometries, large distortions and large bending deformations, and anisotropic nonlinear incompressible hyperelastic material properties.

1.2 Contributions

To develop the present CB shell FE, a thorough understanding of the derivation of the detailed kinematics for the existing CB shell elements, as well as of the implementation of incompressible hyperelastic constitutive relations, was needed. In this dissertation, fundamental background that is not spelled out in the literature is presented. This makes it possible to expose some theoretical inaccuracies or mistakes that have been made by some authors over the years. We endeavoured to identify and correct them wherever possible.

The most important contributions of the new proposed CB shell FE compared to existing similar elements lie in its accuracy and efficiency in analyzing large bending deformations and its insensitivity to initially irregular elements and geometries as well as large distortions. Improvement in accuracy was achieved by employing a 9-noded quadrilateral element, two independent coordinate systems to implement the kinematic and kinetic assumptions of the modified Mindlin-Reissner shell theory, and proper selection of the number of integration points. Insensitivity of the present CB shell FE to large deformations, and initially irregular elements and geometries made it possible to use fewer, larger elements, which, combined with formulation of Section 3.16, allowed for larger time step (Δt). Overall efficiency was achieved by circumvention of the equilibrium iterations, reduction of the number of elements, and increased Δt. These claims were tested and verified.

In addition, three techniques presented in Section 3.10, and a fiber length update algorithm presented in Section 3.11 were developed to enable accurate modelling of large in-plane and out of plane (3D) distortions, and large 3D strains. Technique 1 details the appropriate derivation of the constitutive relations from the hyperelastic strain energy function, their transformation to the current configuration within the lamina coordinate system, and the direct application of the zero normal stress condition through volume evolution constraints. Techniques 2 and 3, which allow for the accurate modelling of large strains using a constant constitutive tensor in the total and incremental UL formulations, bypass the need of determining the material constants used in Technique 1 for hyperelastic strain energy functions. The accuracy of these techniques was verified (in Chapter 4).

1.3 Thesis outline

The current Chapter 1 presents a brief introduction to the importance of understanding and simulating biological soft tissues; the overall objectives, motivation and contribution of the research are provided.

Chapter 2 begins with a brief introduction to the properties of biological soft tissues. Then, the application of finite element formulation for the modeling of soft tissues, and the relevant capabilities of existing commercial and open source software packages are reviewed. Next, the capabilities of existing shell theories and CB shell elements are investigated. Finally, derivation of the constitutive relations, methods for enforcing incompressibility, and application of the zero normal stress condition are presented. This chapter is concluded by a summary of the pros and cons of the CB shell elements that are most applicable to the present work.

Having the background knowledge (state of art) discussed in Chapter 2, all our modifications and new developments are presented in Chapter 3. This chapter details the kinematics and kinetics development of our hyperelastic anisotropic incompressible nonlinear dynamic CB thick shell element using the total and the incremental updated Lagrangian formulation.

We implemented our CB shell element in Matlab. In Chapter 4, quantitative results obtained from multiple tests concerning different geometries, material properties, loading conditions, and modes of deformation are presented, and the accuracy of the results is discussed against existing solutions from the literature.

Chapter 5 discusses and concludes the contributions and limitations of the present CB shell finite element, based on the accuracy and reliability of the results obtained.

CHAPTER 2: CONTEXT OF THE STUDY AND LITERATURE REVIEW

2.1 Soft tissues

Soft tissues are composed of living cells embedded in extracellular matrix. Cells are the fundamental functional unit of tissues and organs. There are about 200 different types of cells in the human body which serve different functions. The extracellular matrix consists of collagen, elastin and ground substance.

The main characteristic of soft tissues is their capability to sustain large (i.e. non-infinitesimal) deformations under physiological or abnormal conditions. Researchers have shown that the aligned fibrous structure of biological soft tissues gives rise to anisotropic hyperelasticity in the physiological ranges of strain rates (Fung, 1967). Additionally, the observation that a significant portion of the tissue volume is composed of water that appears to be tightly bound to the solid matrix justifies the assumption that soft tissues are largely incompressible.

Because of their complex mechanical properties associated with finite deformations, it is important to study soft tissues using the proper theoretical framework.

2.2 Finite element formulations

Finite element analysis is being applied with ever increasing frequency to examine problems in the biological and clinical realms. Quite often, this requires that nonlinear soft tissues be represented in the models. While linear elasticity may be useful to model bone tissue, it is not suited for soft tissue mechanics. The reasons are that:

1. most soft tissues undergo strains that qualify as large deformations (geometric nonlinearity),
2. the relationship between stress and strain for soft tissues is generally nonlinear (material nonlinearity).

Therefore, the stiffness of a soft tissue will change with deformation, unlike a linear elastic material where the stiffness is constant as long as the material is in the elastic range. In general, soft tissues are hyperelastic (they may be able to sustain strains of up to 800% without any permanent deformations), nearly-incompressible, and anisotropic (due to their aligned fibrous structure).

2.2.1 Classical vs. Continuum-based shell elements

As described in (Belytschko et al., 2000), shell finite elements can be developed in two ways:

1. by using a weak form of the classical shell equations for momentum balance (or equilibrium),
2. by developing the element directly from a continuum element by imposing special structural assumptions. This is called the continuum-based (CB) approach.

Since the governing equations for nonlinear shells are usually formulated in terms of curvilinear components of tensors, features such as variations in thickness are generally difficult to incorporate. Therefore, the first approach is not efficient for the purpose of this project.

On the other hand, the CB approach is simpler and provides a more appealing framework for developing shell elements. Basically, a CB shell element (Figure 2.1) is developed by imposing the kinematic or kinetic assumptions of the shell theory of interest on the discrete equations of the continuum finite element (i.e. equations of motion), such that it is modified to behave like the shell of pre-specified properties. This approach is also called the degenerated continuum approach. The shell element produced is called a continuum-based (CB) shell element. Bathe and Bolourchi (1979) praised CB shell elements for their:

- generality in the analysis of two and three dimensional continuum problems,
- independence to any specific classical plate or shell theory,
- ability for direct discretization and interpolation of the geometry and the displacement field of the structure as the analysis of continuum problems,
- efficiency in the analysis of general structural configurations by using variable-number-nodes.

The CB approach is widely used in commercial software and research. Therefore, the present research is concentrated on the CB methodology.

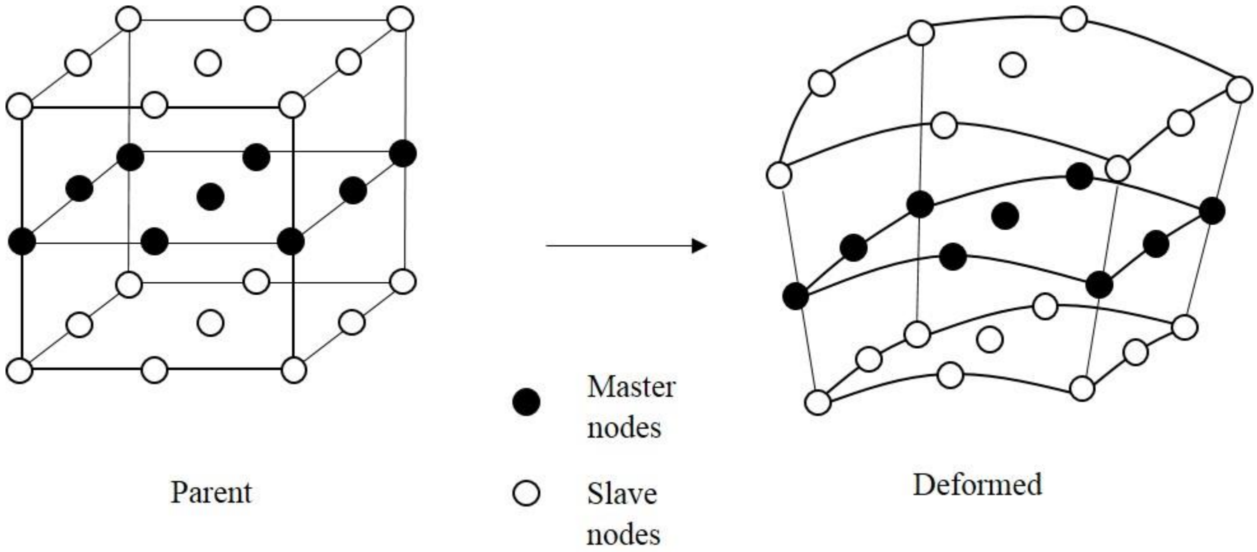

Figure 2.1: 9-noded CB shell element based on an 18-node continuum element.

However, two possible shortcomings of CB shell elements are shear and membrane lockings. A detailed study of these locking types will be presented in Section 2.8, and their prevention will be addressed in the development of our CB shell element.

2.2.2 Interpolation (shape) functions

In finite element methods, continuous models are approximated using information at a finite number of discrete locations. Dividing the structure into discrete elements is called discretization. Interpolation of the solution between the discrete values obtained at nodes is achieved through interpolations (also called shape) functions within the elements. Basically, considering Figure 2.2, knowing the value of any variable of interest at the nodes ($\emptyset_i$), its value at any location inside the element is evaluated by substituting the corresponding parent coordinates (r and s) inside the shape functions, and multiplying them by the value of the variable of interest at the nodes. That is:

$$\emptyset(r,s) = \begin{bmatrix} N_1(r,s) & N_2(r,s) & \cdots & N_{n_{en}}(r,s) \end{bmatrix} \begin{Bmatrix} \emptyset_1 \\ \emptyset_2 \\ \vdots \\ \emptyset_{n_{en}} \end{Bmatrix} \qquad \forall\, r,s \in [-1,1],$$

where $[N] = [N_1(r,s) \quad N_2(r,s) \quad \cdots \quad N_{n_{en}}(r,s)]$ is called interpolation matrix, and n_{en} represents the number of element nodes.

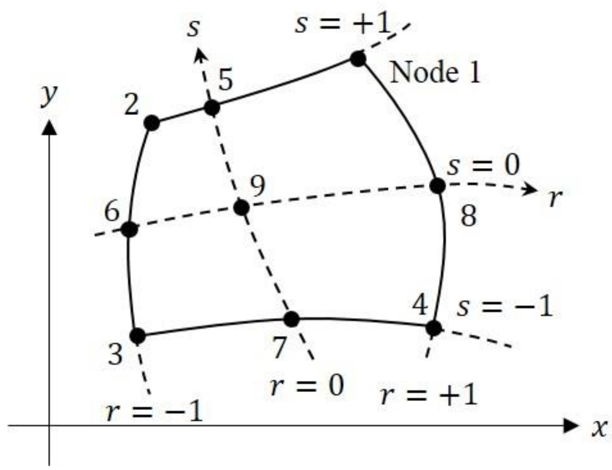

Figure 2.2: 4 to 9 variable-number-node 2D element. r and s are the parent (also called natural and/or curvilinear) coordinate system (adapted from Bathe, 1996).

The interpolation functions of a biunit square element having 4 to 9 variable-number-nodes are given in Table 2.1.

Three rules are associated with shape functions:

1. $N_i = 1$ at node i, and 0 at other nodes, for $i = 1$ to n_{en},
2. at Node i, only $N_i = 1$, the others are 0,
3. $\sum_{i=1}^{n_{en}} N_i(r,s) = 1 \quad \forall\, r,s \in [-1,1]$.

Shells are essentially curved plates and thus, more than two nodes per edge are required to represent the curved geometry. Inclusion of internal nodes enhances the accuracy of an element by achieving higher degrees of polynomial completeness (Hughes, 2000). Thus, we adopted a quadrilateral shell element formulation with three nodes per side, and one central node, for nine nodes in total. The literature refers to such elements that include interior nodes as *Lagrangian elements*.

Table 2.1: Interpolation functions (Bathe, 1996).

		Include only if node $\boldsymbol{i}$ is defined				
		$i = 5$	$i = 6$	$i = 7$	$i = 8$	$i = 9$
$\boldsymbol{N_1} =$	$\frac{1}{4}(1+r)(1+s)$	$-\frac{1}{2}N_5$			$-\frac{1}{2}N_8$	$-\frac{1}{4}N_9$
$\boldsymbol{N_2} =$	$\frac{1}{4}(1-r)(1+s)$	$-\frac{1}{2}N_5$	$-\frac{1}{2}N_6$			$-\frac{1}{4}N_9$
$\boldsymbol{N_3} =$	$\frac{1}{4}(1-r)(1-s)$		$-\frac{1}{2}N_6$	$-\frac{1}{2}N_7$		$-\frac{1}{4}N_9$
$\boldsymbol{N_4} =$	$\frac{1}{4}(1+r)(1-s)$			$-\frac{1}{2}N_7$	$-\frac{1}{2}N_8$	$-\frac{1}{4}N_9$
$\boldsymbol{N_5} =$	$\frac{1}{2}(1-r^2)(1+s)$					$-\frac{1}{2}N_9$
$\boldsymbol{N_6} =$	$\frac{1}{2}(1-s^2)(1-r)$					$-\frac{1}{2}N_9$
$\boldsymbol{N_7} =$	$\frac{1}{2}(1-r^2)(1-s)$					$-\frac{1}{2}N_9$
$\boldsymbol{N_8} =$	$\frac{1}{2}(1-s^2)(1+r)$					$-\frac{1}{2}N_9$
$\boldsymbol{N_9} =$	$(1-r^2)(1-s^2)$					

2.2.3 Principle of virtual work

The principle of virtual work (PVW, also called the principle of virtual displacement) forms the basis of the displacement-based finite element solution. The material covered in this section is taken from Bathe (1996) and Bathe et al. (1975), unless otherwise specified.

The PVW, in statics, states that if the work done by the external forces on the structure is equal to the increase in strain energy for any set of admissible virtual displacements (i.e. satisfying the prescribed displacements), then the system is in equilibrium. Thus:

Equation 2.1

$$\sum_{m=1}^{k} \int_{V^{(m)}} \{\delta\varepsilon^{(m)}\}^T \{\sigma^{(m)}\} dV^{(m)} = \sum_{m=1}^{k} \{\delta u^{(m)}\}^T \left\{R_{external}^{(m)}\right\} \qquad \forall \{\delta u^{(m)}\}, \{\delta\varepsilon^{(m)}\},$$

where

$\{\delta u^{(m)}\}$: virtual displacement vector (independent of actual displacements),

$\{\delta\varepsilon^{(m)}\}$: virtual strain vector (corresponding to virtual displacements),

$\{\sigma^{(m)}\}$: stress vector corresponding to the equilibrium under $\left\{R_{external}^{(m)}\right\}$,

$\left\{R_{external}^{(m)}\right\}$: the externally applied loads,

(m): element number,

$\sum_{m=1}^{k}$: finite element assemblage.

Note that the adjective "virtual" denotes that the displacements and the corresponding strains are not "real". In other words, the body does not actually undergo such displacements and strains as a result of the loading on the body. Instead, the virtual displacements are totally independent from the actual displacements.

In geometric and material linear analyses $\{\sigma^{(m)}\} = [C]\{\varepsilon^{(m)}\}$ and $\{\varepsilon^{(m)}\} = [B]\{U^{(m)}\}$,

where

$[C]$: material tangent modulus (also called elasticity tensor),

$\{\varepsilon^{(m)}\}$: strain vector,

$[B]$: linear strain-displacement transformation matrix, obtained from taking the first derivative of interpolation matrix $[N]$ with respect to the parent coordinates,

$\{U^{(m)}\}$: nodal displacements.

Therefore $\{\sigma^{(m)}\} = [C][B]\{U^{(m)}\}$. In addition, the vector of virtual displacements and virtual strains are obtained from the nodal point virtual displacements by $\{\delta u\} = \sum_{m=1}^{k}[N]\{\delta U^{(m)}\}$ and $\{\delta\varepsilon\} = \sum_{m=1}^{k}[B]\{\delta U^{(m)}\}$. Substituting these into Equation 2.1 yields:

$$\sum_{m=1}^{k}\int_{V^{(m)}}\{\delta U^{(m)}\}^T[B]^T[C][B]\{U^{(m)}\}dV^{(m)} = \sum_{m=1}^{k}\{\delta U^{(m)}\}^T[N]^T\{R_{external}^{(m)}\} \qquad \forall\,\{\delta U^{(m)}\}.$$

Knowing that the nodal displacements ($\{U^{(m)}\}$) and nodal virtual displacements ($\{\delta U^{(m)}\}$) are independent of the volume of the body, they can be taken out of the integral. Doing so, and cancelling out the nodal virtual displacements present on both sides of the equality, the PVW for geometric and material linear analysis reduces to:

Equation 2.2

$$\sum_{m=1}^{k}\int_{V^{(m)}}[B]^T[C][B]dV^{(m)}\,\{U^{(m)}\} = \sum_{m=1}^{k}[N]^T\{R_{external}^{(m)}\}.$$

However, in the nonlinear analysis, due to the nonlinearity in the geometry and material properties, an incremental approach is needed. Taking one step back, dropping the summation sign, and writing Equation 2.1 in indicial notation for convenience, gives:

Equation 2.3

$$\int_{{}^{\beta}V} {}^{\tau+\Delta\tau}_{\beta}\sigma_{ij}\;\delta\,{}^{\tau+\Delta\tau}_{\beta}\varepsilon_{ij}\,d\,{}^{\beta}V = \delta u_i\;{}^{\tau+\Delta\tau}R_i^{external} \qquad \forall\,\delta u_i, \delta\,{}^{\tau+\Delta\tau}_{\beta}\varepsilon_{ij}\,,$$

where the left superscript $(\tau + \Delta\tau)$ represents the time configuration under study, the left subscript (β) represent the reference configuration, the right subscripts are the indices, δu_i represents the virtual displacement increment, and Einstein summation applies on the repeated indices. Depending on the type of formulation, either the current (τ) or the initial (0) configurations can be taken as the reference configuration (β). Configurations considered in nonlinear analyses are illustrated in Figure 2.3.

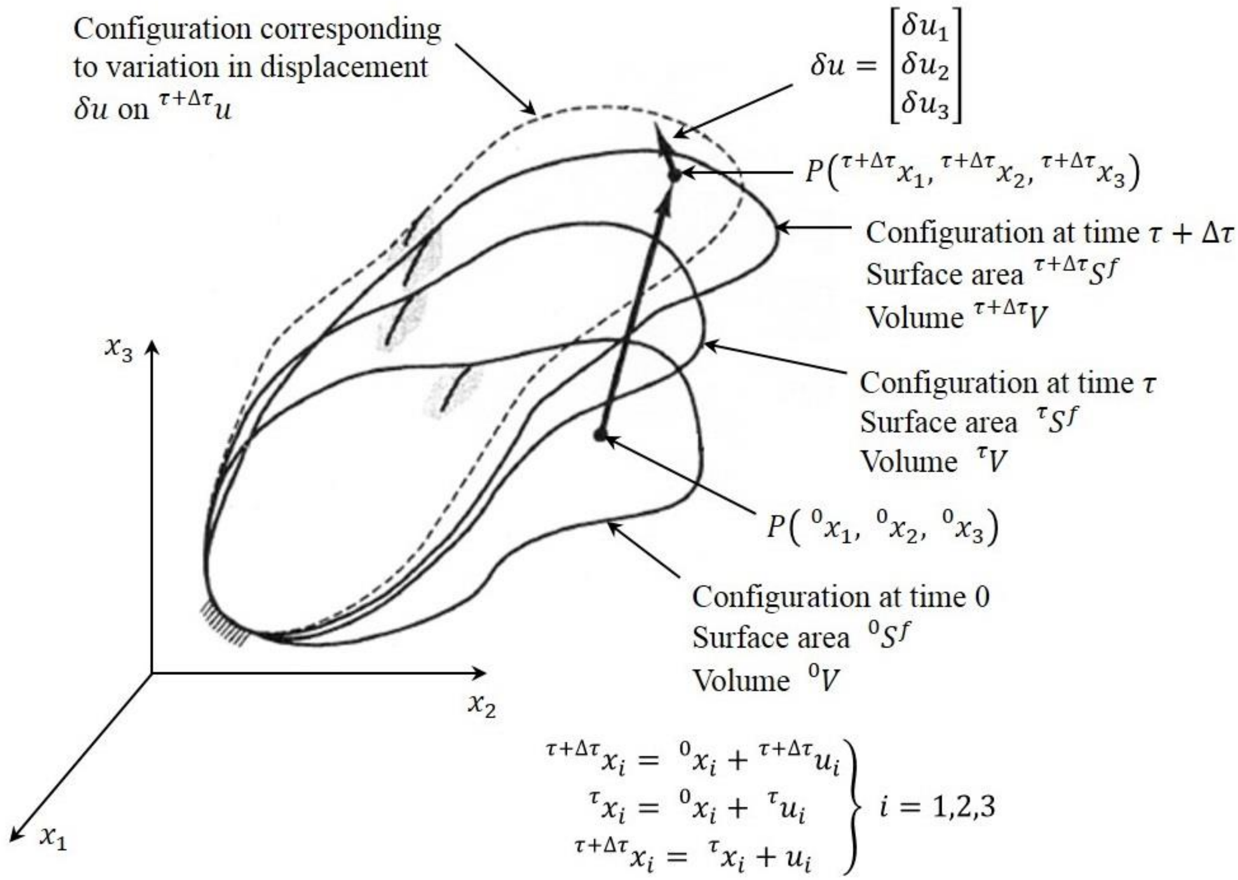

Figure 2.3: Configurations considered in nonlinear analyses (adapted from Bathe (1996), page 499).

The incremental decomposition suggests that:

Equation 2.4

$$ {}^{\tau+\Delta\tau}_{\beta}\sigma_{ij} = {}^{\tau}_{\beta}\sigma_{ij} + {}_{\beta}\sigma_{ij}, $$

Equation 2.5

$$ {}^{\tau+\Delta\tau}_{\beta}\varepsilon_{ij} = {}^{\tau}_{\beta}\varepsilon_{ij} + {}_{\beta}\varepsilon_{ij}. $$

In the above formulation ${}_{\beta}\sigma_{ij}$ and ${}_{\beta}\varepsilon_{ij}$ represent the increment in stresses and strains from time step τ to time step $\tau + \Delta\tau$, respectively. Furthermore, the strain increment is decomposed into:

Equation 2.6

$$ {}_{\beta}\varepsilon_{ij} = {}_{\beta}e_{ij} + {}_{\beta}\eta_{ij}, $$

where ${}_{\beta}e_{ij}$ is linear in displacement increment from time τ to $\tau + \Delta\tau$ (denoted by u_i) such that

Equation 2.7

$$ {}_{\beta}e_{ij} = \frac{1}{2}\left({}_{\beta}u_{i,j} + {}_{\beta}u_{j,i} + \text{initial displacement effects}\right), $$

where

$$ \text{initial displacement effects} = \begin{cases} 0 & \text{if} \quad \beta = \tau \\ {}^{\tau}_{0}u_{k,i} \; {}_{0}u_{k,j} + {}_{0}u_{k,i} \; {}^{\tau}_{0}u_{k,j} & \text{if} \quad \beta = 0 \end{cases}, $$

and

Equation 2.8

$$ {}_{\beta}\eta_{ij} = \frac{1}{2} \, {}_{\beta}u_{k,i} \, {}_{\beta}u_{k,j}, $$

where ${}_{\beta}\eta_{ij}$ is nonlinear in displacement increment from time τ to $\tau + \Delta\tau$ (denoted by u_i). In the above expressions and in what follows, comma between the indices represent partial derivatives, thus:

Equation 2.9

$$ {}_{\beta}u_{i,j} = \frac{\partial u_i}{\partial \, {}^{\beta}x_j}, $$

where ${}_{\beta}x_j$ is the indicial representation of the position vector with respect to the reference configuration (β).

Considering Equation 2.5, ${}^{\tau}_{\beta}\varepsilon_{ij}$ represents the straining of the body from the reference to the current configuration (the strains that the body has actually undergone, thus, real and/or known strains), and ${}_{\beta}\varepsilon_{ij}$ represents the strain increment between time step τ and future time step $\tau + \Delta\tau$ (i.e. the body has not undergone this straining yet). Also, knowing that the virtual strains associated with a real (known) strain is zero (i.e. $\delta \, {}^{\tau}_{\beta}\varepsilon_{ij} = 0$), the virtual strains from the reference configuration to the future configuration ($\delta \, {}^{\tau+\Delta\tau}_{\beta}\varepsilon_{ij}$) can only include the virtual incremental strains. Thus:

Equation 2.10

$$ \delta \, {}^{\tau+\Delta\tau}_{\beta}\varepsilon_{ij} = \delta \, {}_{\beta}\varepsilon_{ij}, $$

where the virtual incremental strains, adapted from Equation 2.6, are

Equation 2.11

$$\delta\ {}_{\beta}\varepsilon_{ij} = \delta\ {}_{\beta}e_{ij} + \delta\ {}_{\beta}\eta_{ij}.$$

Knowing that the virtual strains associated with a real (known) strain is zero, using Equation 2.7 and Equation 2.8, $\delta\ {}_{\beta}e_{ij}$ and $\delta\ {}_{\beta}\eta_{ij}$ are obtained from:

Equation 2.12

$$\delta\ {}_{\beta}e_{ij} = \frac{1}{2}\Big(\delta\ {}_{\beta}u_{i,j} + \delta\ {}_{\beta}u_{j,i} + \delta(\text{initial displacement effects})\Big),$$

where $\delta(\text{initial displacement effects}) = \begin{cases} 0 & \text{if} \quad \beta = \tau \\ {}_{0}^{\tau}u_{k,i}\ \delta\ {}_{0}u_{k,j} + \delta\ {}_{0}u_{k,i}\ {}_{0}^{\tau}u_{k,j} & \text{if} \quad \beta = 0 \end{cases},$

and

Equation 2.13

$$\delta\ {}_{\beta}\eta_{ij} = \frac{1}{2}\ (\delta\ {}_{\beta}u_{k,i}\ \ {}_{\beta}u_{k,j} + \ {}_{\beta}u_{k,i}\ \delta\ {}_{\beta}u_{k,j}),$$

Similar to Equation 2.9:

$$\delta\ {}_{\beta}u_{i,j} = \frac{\partial(\delta u_i)}{\partial\ {}^{\beta}x_j},$$

where δu_i is the virtual displacement increment.

As identified by Equation 2.12, $\delta\ {}_{\beta}e_{ij}$ is linear in virtual displacement increment, but does not contain any displacement increment. Furthermore, according to Equation 2.13, $\delta\ {}_{\beta}\eta_{ij}$ is linear in both displacement increment and virtual displacement increment.

Substituting Equation 2.4 and Equation 2.10 in Equation 2.3 gives:

$$\int_{{}^{\beta}V} ({}_{\beta}^{\tau}\sigma_{ij} + \ {}_{\beta}\sigma_{ij})\ \delta\ {}_{\beta}\varepsilon_{ij}\ d\ {}^{\beta}V = \delta u_i\ {}^{\tau+\Delta\tau}R_i^{external} \qquad \forall\ \delta u_i, \delta\ {}_{\beta}\varepsilon_{ij},$$

which is expanded to:

Equation 2.14

$$\int_{{}^{\beta}V} {}_{\beta}^{\tau}\sigma_{ij}\ \delta\ {}_{\beta}\varepsilon_{ij}\ d\ {}^{\beta}V + \int_{{}^{\beta}V} {}_{\beta}\sigma_{ij}\ \delta\ {}_{\beta}\varepsilon_{ij}\ d\ {}^{\beta}V = \delta u_i\ {}^{\tau+\Delta\tau}R_i^{external} \qquad \forall\ \delta u_i, \delta\ {}_{\beta}\varepsilon_{ij}.$$

Inserting Equation 2.11 in the first integral of Equation 2.14 and expanding, gives:

Equation 2.15

$$\int_{{}^{\beta}V} {}^{\tau}_{\beta}\sigma_{ij}\,\delta\,{}_{\beta}e_{ij}\,d\,{}^{\beta}V + \int_{{}^{\beta}V} {}^{\tau}_{\beta}\sigma_{ij}\,\delta\,{}_{\beta}\eta_{ij}\,d\,{}^{\beta}V + \int_{{}^{\beta}V} {}_{\beta}\sigma_{ij}\,\delta\,{}_{\beta}\varepsilon_{ij}\,d\,{}^{\beta}V$$
$$= \delta u_i\,{}^{\tau+\Delta\tau}R_i^{external} \qquad \forall\,\delta u_i, \delta\,{}_{\beta}e_{ij}, \delta\,{}_{\beta}\eta_{ij}, \delta\,{}_{\beta}\varepsilon_{ij}.$$

Considering that ${}^{\tau}_{\beta}\sigma_{ij}$ and $\delta\,{}_{\beta}e_{ij}$ (Equation 2.12) do not contain displacement increment, and that $\delta\,{}_{\beta}\eta_{ij}$ is linear in displacement increment (Equation 2.13), the first two integrals of Equation 2.15 are linear in displacement increment (u_i). Considering the third integral, the stress increment ${}_{\beta}\sigma_{ij}$, contains strain increment ${}_{\beta}\varepsilon_{ij}$, which according to Equations 2.6 to 2.8, are nonlinear in displacement increment u_i. In addition, according to Equations 2.11 to 2.13, $\delta\,{}_{\beta}\varepsilon_{ij}$ contains terms that are linear in displacement increment. Thus, the third integral is highly nonlinear in displacement increment, and needs to be linearized using a Taylor series expansion. In a simple 1D case, a Taylor series expansion operates as follows:

$$f(x+h) - f(x) = \frac{\partial f}{\partial x}\bigg|_{x}\; h + \text{higher order terms.}$$

Knowing that ${}_{\beta}\sigma_{ij} = {}^{\tau+\Delta\tau}_{\beta}\sigma_{ij} - {}^{\tau}_{\beta}\sigma_{ij}$, a Taylor series expansion applied to the stress increment results in:

$${}_{\beta}\sigma_{ij} = \frac{\partial\,{}^{\tau}_{\beta}\sigma_{ij}}{\partial\,{}^{\tau}_{\beta}\varepsilon_{rs}}\bigg|_{\tau}\;\; {}_{\beta}\varepsilon_{rs} + \text{higher order terms.}$$

Noting that $\frac{\partial\,{}^{\tau}_{\beta}\sigma_{ij}}{\partial\,{}^{\tau}_{\beta}\varepsilon_{ij}} = {}_{\beta}C_{ijrs}$, and substituting Equation 2.6 in the above, gives:

Equation 2.16

$${}_{\beta}\sigma_{ij} = {}_{\beta}C_{ijrs}\left({}_{\beta}e_{rs} + {}_{\beta}\eta_{rs}\right) + \text{higher order terms.}$$

Substituting Equation 2.11, and Equation 2.16 in the third integral of Equation 2.15, gives

$$\int_{{}^{\beta}V} {}_{\beta}\sigma_{ij}\,\delta\,{}_{\beta}\varepsilon_{ij}\,d\,{}^{\beta}V =$$

$$\int_{^\beta V}\left({}_{\beta}C_{ijrs}\left({}_{\beta}e_{rs}+{}_{\beta}\eta_{rs}\right)+\text{higher order terms}\right)\left(\delta\,{}_{\beta}e_{ij}+\delta\,{}_{\beta}\eta_{ij}\right)d\,{}^{\beta}V.$$

Next, neglecting the higher order and nonlinear terms, the third integral of Equation 2.15 is linearized to:

$$\int_{^\beta V}{}_{\beta}\sigma_{ij}\,\delta\,{}_{\beta}\varepsilon_{ij}\,d\,{}^{\beta}V=\int_{^\beta V}{}_{\beta}C_{ijrs}\,{}_{\beta}e_{rs}\,\delta\,{}_{\beta}e_{ij}\,d\,{}^{\beta}V.$$

Finally, the linearized (in displacement increment) PVW in geometric and material nonlinear analyses (to first order) becomes:

Equation 2.17

$$\int_{^\beta V}{}_{\beta}^{\tau}\sigma_{ij}\,\delta\,{}_{\beta}e_{ij}\,d\,{}^{\beta}V+\int_{^\beta V}{}_{\beta}^{\tau}\sigma_{ij}\,\delta\,{}_{\beta}\eta_{ij}\,d\,{}^{\beta}V+\int_{^\beta V}{}_{\beta}C_{ijrs}\,{}_{\beta}e_{rs}\,\delta\,{}_{\beta}e_{ij}\,d\,{}^{\beta}V$$
$$=\delta u_i\,{}^{\tau+\Delta\tau}R_i^{external}\qquad\forall\,\delta u_i,\delta\,{}_{\beta}e_{ij},\delta\,{}_{\beta}\eta_{ij}.$$

Converting Equation 2.17 to matrix form, and using relations $\{\delta u\}=\sum_{m=1}^{k}[N]\{\delta U^{(m)}\}$ and $\{\delta\varepsilon\}=\sum_{m=1}^{k}[B]\{\delta U^{(m)}\}$, the linearized PVW in geometric and material nonlinear analyses becomes:

Equation 2.18

$$\sum_{m=1}^{k}\int_{^\beta V^{(m)}}\{\delta U^{(m)}\}^T\left[{}_{\beta}^{\tau}B_L\right]^T\{{}_{\beta}^{\tau}\sigma^{(m)}\}d\,{}^{\beta}V^{(m)}$$
$$+\sum_{m=1}^{k}\int_{^\beta V^{(m)}}\{\delta U^{(m)}\}^T\left[{}_{\beta}^{\tau}B_{NL}\right]^T\left[{}_{\beta}^{\tau}\sigma^{(m)}\right]\left[{}_{\beta}^{\tau}B_{NL}\right]\{U^{(m)}\}d\,{}^{\beta}V^{(m)}$$
$$+\sum_{m=1}^{k}\int_{^\beta V^{(m)}}\{\delta U^{(m)}\}^T\left[{}_{\beta}^{\tau}B_L\right]^T\left[{}_{\beta}C\right]\left[{}_{\beta}^{\tau}B_L\right]\{U^{(m)}\}d\,{}^{\beta}V^{(m)}$$
$$=\sum_{m=1}^{k}\{\delta U^{(m)}\}^T\left\{{}^{\tau+\Delta\tau}R_{external}^{(m)}\right\}\qquad\forall\,\{\delta U^{(m)}\},$$

where

$$\left[{}_{\beta}^{\tau}B_L\right]\{\delta U^{(m)}\}=\{\delta\,{}_{\beta}e\},$$

$\left[{}^{\tau}_{\beta}B_{NL}\right]\left\{\delta U^{(m)}\right\} = \left\{\delta\ {}_{\beta}\eta\right\}$,

$\left[{}^{\tau}_{\beta}B_{L}\right], \left[{}^{\tau}_{\beta}B_{NL}\right]$: linear and nonlinear strain-displacement transformation matrices, respectively,

$\{\delta\varepsilon\}$: virtual strain vector corresponding to $\{\delta u\}$,

$\left\{{}^{\tau}_{\beta}\sigma^{(m)}\right\}$: stress vector (in Voigt notation),

$\left[{}^{\tau}_{\beta}\sigma^{(m)}\right]$: stress matrix.

The most common forms of the external forces are the body forces $\{f_B\ \}$, surface forces $\left\{f_{S_f}\right\}$, and point loads $\{f_C\ \}$. Thus:

Equation 2.19

$$\left\{{}^{\tau+\Delta\tau}R_{external}\right\} = \int_{{}^{\beta}V}\left\{{}^{\tau+\Delta\tau}f_B\ \right\}d\,{}^{\beta}V \quad + \int_{{}^{\beta}Sf}\left\{{}^{\tau+\Delta\tau}f_{S_f}\right\}d\,{}^{\beta}S^{f} \quad + \left\{{}^{\tau+\Delta\tau}f_C\ \right\}.$$

If the applied forces vary with time, then the displacements must also vary with time. Note that Equation 2.18 is a statement of equilibrium for any specific point in time. However, if loads are applied rapidly, with respect to the natural frequencies of the system, inertial forces need to be considered (i.e. a dynamic solution is required). In addition, in actually measured dynamic responses of structures, it is observed that energy is dissipated through vibrations. This, in vibration analysis, is usually taken into account by introducing velocity-dependent damping forces. Therefore, the results of static finite element analysis can be expanded to the dynamics analysis using the d'Alembert's principle. In this principle, the elemental inertial and damping forces $\left\{{}^{\tau+\Delta}df_I{}^{(m)}\right\}$ and $\left\{{}^{\tau+\Delta}df_D{}^{(m)}\right\}$ are given by Equation 2.20 and Equation 2.21:

Equation 2.20

$$\left\{{}^{\tau+\Delta}df_I{}^{(m)}\right\} = -\rho\left\{{}^{\tau+\Delta\tau}\ddot{u}^{(m)}\right\}dV$$

Equation 2.21

$$\left\{{}^{\tau+\Delta}df_D{}^{(m)}\right\} = -[\mu]\left\{{}^{\tau+\Delta\tau}\dot{u}^{(m)}\right\}dV,$$

where

ρ: mass density,

$[\mu]$: viscous matrix,

$\left\{{}^{\tau+\Delta\tau}\ddot{u}^{(m)}\right\}$: acceleration vector,

$\left\{{}^{\tau+\Delta\tau}\dot{u}^{(m)}\right\}$: velocity vector.

In Equation 2.20 and Equation 2.21, the minus sign describes that these are resistive forces.

Using d'Alembert's principle, the inertial forces can be included as part of the body forces in the dynamic principle of virtual work. Rewriting Equation 2.20 and Equation 2.21 in matrix form and substituting them, along with Equation 2.19 in Equation 2.18, gives:

Equation 2.22

$$\sum_{m=1}^{k}\int_{{}^{\beta}V^{(m)}}\left\{\delta U^{(m)}\right\}^{T}\left[{}_{\beta}^{\tau}B_{L}\right]^{T}\left\{{}_{\beta}^{\tau}\sigma^{(m)}\right\}d\,{}^{\beta}V^{(m)}$$
$$+\sum_{m=1}^{k}\int_{{}^{\beta}V^{(m)}}\left\{\delta U^{(m)}\right\}^{T}\left[{}_{\beta}^{\tau}B_{NL}\right]^{T}\left[{}_{\beta}^{\tau}\sigma^{(m)}\right]\left[{}_{\beta}^{\tau}B_{NL}\right]\left\{U^{(m)}\right\}d\,{}^{\beta}V^{(m)}$$
$$+\sum_{m=1}^{k}\int_{{}^{\beta}V^{(m)}}\left\{\delta U^{(m)}\right\}^{T}\left[{}_{\beta}^{\tau}B_{L}\right]^{T}\left[{}_{\beta}C\right]\left[{}_{\beta}^{\tau}B_{L}\right]\left\{U^{(m)}\right\}d\,{}^{\beta}V^{(m)}$$
$$=-\sum_{m=1}^{k}\int_{{}^{\beta}V^{(m)}}\left\{\delta U^{(m)}\right\}^{T}[N]^{T}\rho[N]\left\{{}^{\tau+\Delta\tau}\ddot{U}^{(m)}\right\}d\,{}^{\beta}V^{(m)}$$
$$-\sum_{m=1}^{k}\int_{{}^{\beta}V^{(m)}}\left\{\delta U^{(m)}\right\}^{T}[N]^{T}[\mu][N]\left\{{}^{\tau+\Delta\tau}\dot{U}^{(m)}\right\}d\,{}^{\beta}V^{(m)}$$
$$+\sum_{m=1}^{k}\int_{{}^{\beta}V^{(m)}}\left\{\delta U^{(m)}\right\}^{T}[N]^{T}\left\{{}^{\tau+\Delta\tau}f_{B}^{(m)}\right\}d\,{}^{\beta}V^{(m)}$$
$$+\sum_{m=1}^{k}\int_{{}^{\beta}S^{f(m)}}\left\{\delta U^{(m)}\right\}^{T}[N]^{T}\left\{{}^{\tau+\Delta\tau}f_{S_f}^{(m)}\right\}d\,{}^{\beta}S^{f(m)}$$
$$+\sum_{m=1}^{k}\left\{\delta U^{(m)}\right\}^{T}\left\{{}^{\tau+\Delta\tau}f_{C}^{(m)}\right\}\qquad\forall\left\{\delta U^{(m)}\right\}.$$

In Equation 2.22, $\left\{\delta U^{(m)}\right\}, \left\{{}^{\tau+\Delta\tau}\ddot{U}^{(m)}\right\}, \left\{{}^{\tau+\Delta\tau}\dot{U}^{(m)}\right\}$ and $\left\{U^{(m)}\right\}$ are independent of the volume and surface area and thus can be taken out of the integrations giving Equation 2.23. Noting that the virtual displacements $\left\{\delta U^{(m)}\right\}$ are on both sides of the equality, they vanish. Thus, after simplifying and rearranging, the PVW for the nonlinear dynamic analysis yields Equation 2.24.

Equation 2.23

$$\sum_{m=1}^{k}\left\{\delta U^{(m)}\right\}^{T}\int_{^{\beta}V^{(m)}}\left[{}_{\beta}^{\tau}B_{L}\right]^{T}\left\{{}_{\beta}^{\tau}\sigma^{(m)}\right\}d\,{}^{\beta}V^{(m)}$$
$$+\sum_{m=1}^{k}\left\{\delta U^{(m)}\right\}^{T}\int_{^{\beta}V^{(m)}}\left[{}_{\beta}^{\tau}B_{NL}\right]^{T}\left[{}_{\beta}^{\tau}\sigma^{(m)}\right]\left[{}_{\beta}^{\tau}B_{NL}\right]d\,{}^{\beta}V^{(m)}\left\{U^{(m)}\right\}$$
$$+\sum_{m=1}^{k}\left\{\delta U^{(m)}\right\}^{T}\int_{^{\beta}V^{(m)}}\left[{}_{\beta}^{\tau}B_{L}\right]^{T}\left[{}_{\beta}C\right]\left[{}_{\beta}^{\tau}B_{L}\right]d\,{}^{\beta}V^{(m)}\left\{U^{(m)}\right\}$$
$$=-\sum_{m=1}^{k}\left\{\delta U^{(m)}\right\}^{T}\int_{^{\beta}V^{(m)}}[N]^{T}\rho[N]d\,{}^{\beta}V^{(m)}\left\{{}^{\tau+\Delta\tau}\ddot{U}^{(m)}\right\}$$
$$-\sum_{m=1}^{k}\left\{\delta U^{(m)}\right\}^{T}\int_{^{\beta}V^{(m)}}[N]^{T}[\mu][N]d\,{}^{\beta}V^{(m)}\left\{{}^{\tau+\Delta\tau}\dot{U}^{(m)}\right\}$$
$$+\sum_{m=1}^{k}\left\{\delta U^{(m)}\right\}^{T}\int_{^{\beta}V^{(m)}}[N]^{T}\left\{{}^{\tau+\Delta\tau}f_{B}^{(m)}\right\}d\,{}^{\beta}V^{(m)}$$
$$+\sum_{m=1}^{k}\left\{\delta U^{(m)}\right\}^{T}\int_{^{\beta}S^{f(m)}}[N]^{T}\left\{{}^{\tau+\Delta\tau}f_{S_f}^{(m)}\right\}d\,{}^{\beta}S^{f(m)}$$
$$+\sum_{m=1}^{k}\left\{\delta U^{(m)}\right\}^{T}\left\{{}^{\tau+\Delta\tau}f_{C}^{(m)}\right\}\qquad\forall\left\{\delta U^{(m)}\right\}.$$

Equation 2.24

$$\sum_{m=1}^{k}\int_{^{\beta}V^{(m)}}[N]^{T}\rho[N]d\,{}^{\beta}V^{(m)}\left\{{}^{\tau+\Delta\tau}\ddot{U}^{(m)}\right\}+\sum_{m=1}^{k}\int_{^{\beta}V^{(m)}}[N]^{T}[\mu][N]d\,{}^{\beta}V^{(m)}\left\{{}^{\tau+\Delta\tau}\dot{U}^{(m)}\right\}$$
$$+\sum_{m=1}^{k}\int_{^{\beta}V^{(m)}}\left[{}_{\beta}^{\tau}B_{L}\right]^{T}\left[{}_{\beta}C\right]\left[{}_{\beta}^{\tau}B_{L}\right]d\,{}^{\beta}V^{(m)}\left\{U^{(m)}\right\}$$
$$+\sum_{m=1}^{k}\int_{^{\beta}V^{(m)}}\left[{}_{\beta}^{\tau}B_{NL}\right]^{T}\left[{}_{\beta}^{\tau}\sigma^{(m)}\right]\left[{}_{\beta}^{\tau}B_{NL}\right]d\,{}^{\beta}V^{(m)}\left\{U^{(m)}\right\}$$
$$=\sum_{m=1}^{k}\int_{^{\beta}V^{(m)}}[N]^{T}\left\{{}^{\tau+\Delta\tau}f_{B}^{(m)}\right\}d\,{}^{\beta}V^{(m)}+\sum_{m=1}^{k}\int_{^{\beta}S^{f(m)}}[N]^{T}\left\{{}^{\tau+\Delta\tau}f_{S_f}^{(m)}\right\}d\,{}^{\beta}S^{f(m)}$$
$$+\sum_{m=1}^{k}\left\{{}^{\tau+\Delta\tau}f_{C}^{(m)}\right\}-\sum_{m=1}^{k}\int_{^{\beta}V^{(m)}}\left[{}_{\beta}^{\tau}B_{L}\right]^{T}\left\{{}_{\beta}^{\tau}\sigma^{(m)}\right\}d\,{}^{\beta}V^{(m)}.$$

For simplicity, Equation 2.24 can be rewritten as:

Equation 2.25

$$[M]\{{}^{\tau+\Delta\tau}\ddot{U}\} + [D]\{{}^{\tau+\Delta\tau}\dot{U}^{(m)}\} + \left([{}_{\beta}^{\tau}K_L] + [{}_{\beta}^{\tau}K_{NL}]\right)\{U\} = \{{}^{\tau+\Delta\tau}R\} - \{{}_{\beta}^{\tau}F\},$$

where

$$[M] = \sum_{m=1}^{k} \int_{{}^{\beta}V^{(m)}} [N]^T \rho [N] d\,{}^{\beta}V^{(m)},$$

$$[D] = \sum_{m=1}^{k} \int_{{}^{\beta}V^{(m)}} [N]^T [\mu][N] d\,{}^{\beta}V^{(m)},$$

$$[{}_{\beta}^{\tau}K_L] = \sum_{m=1}^{k} \int_{{}^{\beta}V^{(m)}} [{}_{\beta}^{\tau}B_L]^T [{}_{\beta}C][{}_{\beta}^{\tau}B_L] d\,{}^{\beta}V^{(m)},$$

$$[{}_{\beta}^{\tau}K_{NL}] = \sum_{m=1}^{k} \int_{{}^{\beta}V^{(m)}} [{}_{\beta}^{\tau}B_{NL}]^T [{}_{\beta}^{\tau}\sigma^{(m)}][{}_{\beta}^{\tau}B_{NL}] d\,{}^{\beta}V^{(m)},$$

$$\{{}_{\beta}^{\tau+\Delta\tau}R\} = \sum_{m=1}^{k} \int_{{}^{\beta}V^{(m)}} [N]^T \left\{{}^{\tau+\Delta\tau}f_B^{(m)}\right\} d\,{}^{\beta}V^{(m)} + \sum_{m=1}^{k} \int_{{}^{\beta}S^{f(m)}} [N]^T \left\{{}^{\tau+\Delta\tau}f_{S_f}^{(m)}\right\} d\,{}^{\beta}S^{f(m)}$$
$$+ \sum_{m=1}^{k} \left\{{}^{\tau+\Delta\tau}f_C^{(m)}\right\},$$

$$\{{}_{\beta}^{\tau}F\} = \sum_{m=1}^{k} \int_{{}^{\beta}V^{(m)}} [{}_{\beta}^{\tau}B_L]^T \{{}_{\beta}^{\tau}\sigma^{(m)}\} d\,{}^{\beta}V^{(m)}.$$

2.2.4 Nonlinear finite element theory in dynamics

In the following finite element discretization, it is assumed that the damping effects (present in Equation 2.25) are negligible, or can be modeled in the nonlinear constitutive relationships (for example by use of a strain-rate-dependent material law).

Recall that the left subscript β represents the reference configurations, and that the reference configurations is taken as the initial (0) and the current (τ) configurations, respectively, in the total Lagrangian (TL) and the updated Lagrangian (UL) formulations. Thus, the dynamic nonlinear finite element equations of motion in these formulations are obtained by replacing left subscript β in Equation 2.25 with the corresponding time configuration (0 or τ). In addition, to obtain the FE solution at time $\tau + \Delta\tau$, the equilibrium condition can either be considered at time $\tau + \Delta\tau$ or at time τ. Due to the dependency of the solution on the equilibrium state in the former formulation (where equilibrium at time $\tau + \Delta\tau$ is considered to obtain the solution at time $\tau + \Delta\tau$), an implicit time integration is needed. On the other hand, if the equilibrium at time τ is considered, the solution at time $\tau + \Delta\tau$ can be explicitly solved for. The equilibrium equations for each of the aforementioned formulations are listed below:

<u>Total Lagrangian formulation (TL):</u>

Implicit time integration:

$$[M]\left\{{}^{\tau+\Delta\tau}\ddot{U}\right\} + ([{}^{\tau}_{0}K_L] + [{}^{\tau}_{0}K_{NL}])\{U\} = \left\{{}^{\tau+\Delta\tau}R\right\} - \{{}^{\tau}_{0}F\}.$$

Explicit time integration:

$$[M]\left\{{}^{\tau}\ddot{U}\right\} = \{{}^{\tau}R\} - \{{}^{\tau}_{0}F\}.$$

Similar to Equation 2.25, the above finite element matrices are evaluated as follows:

Equation 2.26

$$[{}^{\tau}_{0}K_L] = \int_{{}^{0}V} [{}^{\tau}_{0}B_L]^T \left[{}_{0}C\right][{}^{\tau}_{0}B_L]\, d^0V,$$

$$[{}^{\tau}_{0}K_{NL}] = \int_{{}^{0}V} [{}^{\tau}_{0}B_{NL}]^T [{}^{\tau}_{0}S][{}^{\tau}_{0}B_{NL}]\, d^0V,$$

$$\{{}^{\tau}_{0}F\} = \int_{{}^{0}V} [{}^{\tau}_{0}B_L]^T \{{}^{\tau}_{0}S\}\, d^0V.$$

Updated Lagrangian formulation (UL):

Implicit time integration:

$$[M]\left\{{}^{\tau+\Delta\tau}\ddot{U}\right\} + ([{}_{\tau}^{\tau}K_L] + [{}_{\tau}^{\tau}K_{NL}])\{U\} = \left\{{}^{\tau+\Delta\tau}R\right\} - \{{}_{\tau}^{\tau}F\}.$$

Explicit time integration:

Equation 2.27

$$[M]\left\{{}^{\tau}\ddot{U}\right\} = \{{}^{\tau}R\} - \{{}_{\tau}^{\tau}F\}.$$

The above finite element matrices are evaluated as follows,

Equation 2.28

$$[{}_{\tau}^{\tau}K_L] = \int_{{}^{\tau}V} [{}_{\tau}^{\tau}B_L]^T [{}_{\tau}C][{}_{\tau}^{\tau}B_L] d^{\tau}V,$$

$$[{}_{\tau}^{\tau}K_{NL}] = \int_{{}^{\tau}V} [{}_{\tau}^{\tau}B_{NL}]^T [{}^{\tau}\sigma][{}_{\tau}^{\tau}B_{NL}] d^{\tau}V,$$

$$\{{}_{\tau}^{\tau}F\} = \int_{{}^{\tau}V} [{}_{\tau}^{\tau}B_L]^T \{{}^{\tau}\sigma\} d^{\tau}V.$$

Both formulations (TL and UL):

$$\left\{{}^{\tau+\Delta\tau}R\right\} = \int_{{}^{0}V} [N]^T \left\{{}^{\tau+\Delta\tau}f^B\right\} d^0V + \int_{{}^{0}S^f} [N]^T \left\{{}^{\tau+\Delta\tau}f^{S_f}\right\} d^0S^f + \sum_{m=1}^{k} \left\{{}^{\tau+\Delta\tau}f_C^{(m)}\right\}.$$

The arrays present in both (TL and UL) formulations are termed as follows:

$[M]$: mass matrix,

$[{}_{0}^{\tau}K_L]$, $[{}_{\tau}^{\tau}K_L]$: linear incremental stiffness matrices,

$[{}_{0}^{\tau}K_{NL}]$, $[{}_{\tau}^{\tau}K_{NL}]$: nonlinear incremental stiffness matrices,

$\{{}^{\tau+\Delta\tau}R\}$, $\{{}^{\tau}R\}$: vectors of externally applied nodal point loads at time $\tau+\Delta\tau$ and τ respectively,

$\{{}^{\tau}F\}$, $\{{}^{\tau}_{0}F\}$, $\{{}^{\tau}_{\tau}F\}$: internal nodal point force vectors,

$\{U\}$: vector of incremental nodal point displacements,

$\{{}^{\tau+\Delta\tau}\ddot{U}\}$, $\{{}^{\tau}\ddot{U}\}$: vectors of nodal point accelerations at time $\tau+\Delta\tau$ and τ respectively.

$[N]$: displacement interpolation matrix,

$[{}^{\tau}_{o}B_{L}]$, $[{}^{\tau}_{\tau}B_{L}]$: linear displacement transformation matrices,

$[{}^{\tau}_{o}B_{NL}]$, $[{}^{\tau}_{\tau}B_{NL}]$: nonlinear displacement transformation matrices,

$[{}_{o}C]$, $[{}_{\tau}C]$: material tangent modulus matrices,

$[{}^{\tau}_{o}S]$: second Piola-Kirchoff stress tensor,

$\{{}^{\tau}_{o}S\}$: vector (in Voigt notation) of the second Piola-Kirchoff stresses,

$[{}^{\tau}\sigma]$: Cauchy stress tensor,

$\{{}^{\tau}\sigma\}$: vector of the Cauchy stresses (in Voigt notation).

2.2.5 Comparison between the total and the updated Lagrangian formulations

Selection between the total Lagrangian and the updated Lagrangian formulations depends on their relative numerical efficiency. According to Bathe (1996), all matrices of both formulations (including $[{}^{\tau}_{\tau}B_{L}]$) contain many zero elements, except $[{}^{\tau}_{0}B_{L}]$ which is a full matrix and contains no zero terms. The strain-displacement transformation matrix $[{}^{\tau}_{0}B_{L}]$ is full because of the initial displacement effect in the linear strain terms. Therefore, computation of the matrix product $[{}^{\tau}_{\tau}B_{L}]^{T}[{}_{\tau}C][{}^{\tau}_{\tau}B_{L}]$ (Equation 2.28) in the UL formulation is less expensive than that of $[{}^{\tau}_{0}B_{L}]^{T}[{}_{0}C][{}^{\tau}_{0}B_{L}]$ (Equation 2.26) in the TL formulation (Bathe et al., 1975).

From a different point of view, in the TL formulation, all derivatives of interpolation functions are with respect to the initial coordinate system, whereas in the UL formulation, all derivatives are with respect to the current coordinates at time τ. Therefore, in the TL formulation, the derivatives could be calculated only once in the first load step and stored in back-up storage for use in all subsequent load steps. In 1996, Bathe claimed that this storage is expensive and in a computer implementation the derivatives of the interpolation functions must be recalculated at each time step for better accuracy (Bathe, 1996). Later, in 2007, Miller et al. claimed that: *"The advantage of the UL approach is the simplicity of incremental strain description. The disadvantage is that all derivatives with respect to current configuration must be recomputed in each time step, because the reference configuration is changing. The reason for this choice is historical—at the time of solver development the memory was expensive and caused more problems than actual speed of computations"*. Although storage is not a problem nowadays, the displacement transformation matrices for the finite elements (such as shells) that have rotational degrees of freedom must be updated at each time step and thus, as mentioned by Bathe (1996), the derivatives must be recalculated for each time step for better accuracy.

In addition to the above arguments, the great majority of commercial finite element programs (example: Ansys, ABAQUS, LS-Dyna, etc.), as well as other authors such as Belytschko et al., (2000) and Bonet and Wood (2008) have only adopted the UL formulation to analyze the nonlinear dynamic problems. This indicates that the UL formulation is agreed to be an efficient formulation.

2.2.6 Time integration

The output of the finite element formulation in nonlinear dynamics is a set of nonlinear ordinary differential equations in time. To construct the solution to a nonlinear dynamics problem, and as mentioned in the previous section, implicit or explicit time integration schemes are used. For nonlinear problems using the implicit method:

- the solution is obtained using a series of linear approximations. Therefore many equilibrium iterations may be necessary for each time step;
- the solution requires inversion of the nonlinear dynamic equivalent stiffness matrix;
- small iterative time steps may be required to achieve convergence;
- convergence is not guaranteed for highly nonlinear problems.

On the other hand, in an explicit finite element formulation, the solution proceeds with many inexpensive time steps. For very large models with a large number of degrees of freedom, solution by explicit integration can represent significant savings in computational costs as opposed to implicit integration. Furthermore, convergence can be assured by respecting a maximum time step criterion ($\Delta\tau_{critical}$) (Bathe, 1996; Belytschko et al., 2000). Therefore the explicit method is proposed to be used for the nonlinear finite element theory explored below.

2.2.6.1 Explicit time integration in dynamics

The central difference operator is the most common explicit time integration operator used in nonlinear dynamic analysis (Bathe, 1996). The central difference method is based on the second order approximation of the differential equations of motion. The equilibrium of the finite element system (Equation 2.27) is considered at time τ and the displacement at time $\tau + \Delta\tau$ needs to be calculated.

Therefore, using the central difference method, the second time differential is approximated by:

Equation 2.29

$$\{\,{}^{\tau}\ddot{U}\} = \frac{\{{}^{\tau-\Delta\tau}U\} - 2\{\,{}^{\tau}U\} + \{{}^{\tau+\Delta\tau}U\}}{\Delta\tau^2}.$$

It is also known that

Equation 2.30

$$\{\,{}^{\tau}\dot{U}\} = \frac{-\{{}^{\tau-\Delta\tau}U\} + \{{}^{\tau+\Delta\tau}U\}}{2\,\Delta\tau}.$$

By rearranging Equation 2.27 one gets:

$$\{\,{}^{\tau}\ddot{U}\} = [M]^{-1}(\{\,{}^{\tau}R\} - \{\,{}^{\tau}F\}),$$

where, the dimension of the square mass matrix $[M]$ is equal to the total number of the degrees of freedom of the system, and thus computation of the inverse of the mass matrix is computationally expensive. However, if $[M]$ is diagonalized (also referred to as mass-lumping), the inversion process is circumvented and the above equation becomes:

Equation 2.31

$$\{\,{}^{\tau}\ddot{U}\} = \frac{1}{[M_{ii}]}(\{\,{}^{\tau}R\} - \{\,{}^{\tau}F\}),$$

where $[M_{ii}]$ is the diagonalized (lumped) mass matrix. Thus, substituting Equation 2.29 into Equation 2.31 gives:

$$\frac{\left\{{}^{\tau-\Delta\tau}U\right\} - 2\{\,{}^{\tau}U\} + \left\{{}^{\tau+\Delta\tau}U\right\}}{\Delta\tau^2} = \frac{1}{[M_{ii}]}(\{\,{}^{\tau}R\} - \{\,{}^{\tau}F\}),$$

and

Equation 2.32

$$\left\{{}^{\tau+\Delta\tau}U\right\} = \frac{\Delta\tau^2}{[M_{ii}]}(\{\,{}^{\tau}R\} - \{\,{}^{\tau}F\}) + 2\{\,{}^{\tau}U\} - \left\{{}^{\tau-\Delta\tau}U\right\}.$$

Equation 2.32 confirms the explicit form of the central difference approximation: to compute displacement $\left\{{}^{\tau+\Delta\tau}U\right\}$, only the displacements in the two previous time steps are needed.

In summary for nonlinear problems with the explicit method:

- a diagonalized mass matrix is required for simple solution,
- the equations become uncoupled and can be solved for directly (explicitly),
- no inversion of the stiffness matrix is required,
- the linearity (elastic) or nonlinearity (hyperelastic) of the constitutive relations are embedded in the formulation of the internal force vector ($\{\,{}^{\tau}F\}$).
- the major computational expense is in calculating the internal forces,
- $\Delta\tau < \Delta\tau_{critical}$ are required to maintain stability.

As shown in Equation 2.32, the calculation of $\left\{{}^{\tau+\Delta\tau}U\right\}$ involves $\{\,{}^{\tau}U\}$ and $\left\{{}^{\tau-\Delta\tau}U\right\}$. Therefore, a special starting procedure must be used at $\tau = 0$ to calculate the solution at the previous time step, (i.e. at time $-\Delta\tau$). The procedure followed herein is adopted from Bathe (1996). Since $\{\,{}^{0}U\}$ and $\{\,{}^{0}\dot{U}\}$ are known and $\{\,{}^{0}\ddot{U}\}$ is calculated from Equation 2.31 at time $\tau = 0$, the relations in Equation 2.29 and Equation 2.30 can be used to obtain:

$$\left\{{}^{-\Delta\tau}U\right\} = \{\,{}^{0}U\} - \Delta\tau\,\{\,{}^{0}\dot{U}\} + \frac{\Delta\tau^2}{2}\{\,{}^{0}\ddot{U}\}.$$

2.3 Software packages

The solution procedure considered can only be solved with a computer program. To minimize programming work, the original intention was for us to determine which existing package could be used as a basis onto which a special shell finite element for soft tissues could be added. In this section, current commercial and open source finite element software packages are reviewed for their potential capabilities to model soft tissues.

2.3.1 Commercial software packages

2.3.1.1 LS-DYNA

The explicit method of solution used by LS-DYNA provides fast solutions for short-time, large deformation dynamics, quasi-static problems with large deformations and multiple nonlinearities, and complex contact/impact problems (ANSYS, 2008).

LS-DYNA has numerous applications which span many fields of engineering and physics. LS-DYNA's features can be combined to model a wide range of physical events. LS-DYNA finds applications in biomechanics and in modelling heart valves (LSTC Aplications, 2011).

LS-DYNA's element library includes shell elements (3, 4, 6, and 8-node including 3-D shells) and membranes (LS-DYNA, 2011). However, these shell elements are either limited to small rotational strains (Section 2.4.1), or are more applicable when combined with plastic as opposed to hyperelastic material properties (Section 2.5.1). In addition, no shell model can currently be combined with anisotropic hyperelastic material models. Therefore, our research group has been using brick elements for many years in all its models of heart valves and aortas.

2.3.1.2 NEi Explicit

NEi Explicit is an explicit solver integrated within the NEi Nastran environment. NEi Explicit can solve complex nonlinear material problems, large deformation contact problems, and very large static and quasi-static models. The NEi Explicit solver is well suited for large types of nonlinear problems providing fast and robust performance because there are no matrices formed, which means a small memory footprint for the model. The explicit architecture lends itself to scalable parallel performance, and large deformation contact solutions with highly nonlinear material behavior (NEI Explicit, 2011).

NEi Explicit can solve problems with shell elements. Furthermore, the Nastran library includes hyperelastic elements that are intended for fully nonlinear analysis including the effect of large strain and large rotation. In addition, the elements are especially designed to handle nonlinear elastic materials at the nearly incompressible limit (Nastran, 2005). Anisotropy can be specified for all types of shell elements. The hyperelastic elements can be defined on the same connection entries as the other shell and solid elements. The above information about NEi Explicit relies on the available documentation (NEI Explicit, 2011). From past experience, the real capabilities of the software can only be evaluated by direct trial, and unfortunately, NEi Explicit was not available to us.

2.3.1.3 ABAQUS

ABAQUS is a commercial software package for finite element analysis and has the ability to solve a wide variety of simulations. ABAQUS consists of three core products, namely: ABAQUS/Standard, ABAQUS/Explicit, and ABAQUS/CAE. ABAQUS/Explicit is focused on transient dynamics and quasi-static analyses using the explicit approach (ABAQUS, 2013).

ABAQUS's shell element library is divided into three categories consisting of thin (small rotational strains), thick (large rotational strains), and general-purpose 3D (applicable to both thin and thick) shell elements. However, ABAQUS/Explicit provides only general-purpose shell elements. These general-purpose shell elements are either axisymmetric, triangular, three-dimensional (not CB), or small-strain elements (ABAQUS, 2013). Thus, one of the major limitations of ABAQUS is that CB shell elements cannot be used with the hyperelastic material models. For instance, ABAQUS was used to model breast tissue as hyperelastic material undergoing finite deformations (Samani A., 2004). However, the authors noted that, due to the aforementioned limitation, conventional shell elements should ideally have been used instead to accommodate the large deformations.

Many of the constitutive models in ABAQUS require tensors to be stored to define the state at a material calculation point. Such “material state tensors” are stored as their components in a local, orthonormal, system at the material calculation point. The orientation of this system with respect to the global $\vec{e}_1, \vec{e}_2, \vec{e}_3$ spatial system is stored as a rotation from the global axis system. With isotropic materials, the material basis is always the same as the element basis, but for structural elements, the material basis changes with time. For anisotropic materials, the material basis must be defined by the user and rotates with the average rigid body spin of the material. In this case, the material basis and the element basis are not the same. When anisotropic material behavior is defined in continuum elements, a user-defined orientation is necessary for the anisotropic behavior to be associated with material directions, which adds complexity (SIMULIA, 2011).

Considering that we are interested in using an incompressible hyperelastic CB shell finite element for explicit time integrations, ABAQUS did not turn out to be an applicable software package.

2.3.1.4 SEPRAN

SEPRAN is commercially available finite element software. It includes preprocessor (SEPMESH), computational engine (SEPCOMP) and postprocessor (SEPPOST). An advantage of SEPRAN is that if the user does not want to use the standard program SEPCOMP, an alternative main program can be written. The main program written by the user may also contain pre-processing and post-processing. The programing language is standard FORTAN 77 (Segal, 2010). SEPRAN allows manipulation of stiffness matrices, stresses and displacements without access to the source code. A concrete and complete theoretical manual for SEPRAN is not available in the literature. SEPRAN was recently used (Speelman, et al., 2008) to calculate the local stresses and the corresponding deformations at the wall of abdominal aortic aneurysm in an incompressible isotropic non-linear hyperelastic material model. However, to our best knowledge, SEPRAN has a limited element library and its most applicable element to our work would be thick plate elements. In addition, SEPRAN is only capable of implicit time integration for solid elements.

2.3.2 Open source software packages

Moving away from commercial packages, the capabilities of relevant open source packages are investigated next.

2.3.2.1 Finite Element Analysis Program (FEAP)

FEAP is non-commercial software written in FORTRAN. The FEAP program includes options for defining one, two, and three dimensional meshes, defining a wide range of linear and nonlinear solution algorithms, graphics options for displaying meshes and contouring solution values, an element library for linear and nonlinear solids, thermal elements, two and three dimensional frame (rod/beam) elements, plate and shell elements, and multiple rigid body options with joint interactions. Constitutive models include linear and finite elasticity, viscoelasticity with damage, and elasto-plasticity. This is a code for people interested in performing finite element code development research and those with particularly unusual problems that cannot be handled by commercial codes (FEAP, 2012).

FEAP is capable of modeling nonlinear, incompressible and hyperelastic materials provided that the corresponding constitutive equations and finite element equations are used. The source code of the full program is available for compilation using standard operating systems. The system may also be used in conjunction with mesh generation programs that have an option to output nodal coordinates and element connection arrays. In this case, it may be necessary to write user functions to input the data generated from the mesh generation program. FEAP is the companion to the books: "The Finite Element Method, 6th edition, Volumes 1 and 2 (but not Vol 3)", authored by O.C. Zienkiewicz and R.L. Taylor and published by Elsevier, Oxford, 2005 (A Finite Element Analysis Program, 2011).

FEAP includes an integrated set of modules to perform:

1. input of data that describes a finite element model,
2. an element library for solids, structures and thermal analysis,
3. construction of solution algorithms to address a wide range of applications,
4. graphical and numerical output of the solution results.

Furthermore, a Matlab interface is a standard part of versions 8.1 and later. The Matlab program permits easy solutions using many different algorithms.

Despite all the advantages mentioned above, FEAP's capabilities for modeling isotropic/anisotropic material properties, and large rotational strains are not revealed.

2.3.2.2 Continuity

Continuity 6 is a problem-solving environment and is used for multi-scale modeling and solving problems in biomechanics, biotransport and physiology. It also has tools to facilitate symbolic model authoring and compilation, and mesh generation including simple image processing, mesh fitting, and mesh refinement.

Continuity 6 is based on Python, a high-level, object-oriented, open-source language for scripting and component integration. In addition to multi-scale modeling tools, Continuity 6 also has facilities for least-squares fitting of anatomic meshes and parametric models to experimental data including medical, morphological and histological images, physiological and biomechanical measurements. It is designed to facilitate interoperability with Microsoft Excel and Matlab. The distribution includes a suite of examples and data including anatomic, material and cellular models (McCulloch, 2011). Continuity contains the Mesh Module, Imaging Module, Fitting Module, Biomechanics Module, and Electrophysiology Module. The capabilities of the Biomechanics Module are discussed in what follows.

The Biomechanics Module is used for setting up, specifying and running biomechanical models. It enables modeling soft tissue deformations as a function of the boundary conditions, active stress, and nonlinear tissue properties. Furthermore, the numerical libraries available in Continuity are used for problem definition, assembly, fitting and solving nonlinear hyperelasticity and large displacement elastic problems. Biomechanics problem class definitions including material properties, equations and solution control, strain energy computation used for solving problems in finite deformation elasticity and biomechanics including active properties such as muscle contraction and growth.

The biomechanics module is a nonlinear solver and the following items can be treated as variables: steps, iterations, increment, initial time, final time, time step, and error tolerances.

Again, the above information about Continuity relies on the available documentation (McCulloch, 2011). From past experience, the real capabilities of the software can only be evaluated by direct trial. Finally, Continuity's material library does not include thick shell elements. Thus, it is limited to small rotational strains only.

2.3.3 Summary of the software packages

A summary of the capacities of the aforementioned commercial software packages is provided in Table 2.2.

Table 2.2: Capabilities of commercial software packages.

	Time integration	Non-linear elasticity	Maximum hyperelastic deformations	Anisotropic materials	Incompressible materials	CB shell element
LS-DYNA	Explicit	Yes	~50%	No	Yes	Yes
NEi Explicit	Explicit	Yes	~40%	Yes	Yes	Yes
ABAQUS	Explicit	Yes	~40%	User-defined	Yes	No
SEPRAN	Implicit	Yes	Yes	No	Yes	No

Commercial FE software packages were originally designed for mechanical engineering applications relying on linear elasticity, and their material libraries are mostly limited to engineering materials. The review of the capabilities of the commercial software packages suggests that most can handle incompressible isotropic hyperelastic shell elements. However, experience has shown that the hyperelasticity that literature is referring to, for these packages, is limited to "not-so-large" deformations. As an example, one specific material model in LS-DYNA is capable of modeling anisotropic hyperelastic material, but only in the range of tendon's deformation, which is about 50%. However, deformations of 100% or more are of interest in this project.

The study of the open source software packages suggests that:

1. FEAP is capable of modeling nonlinear, incompressible and hyperelastic materials, but its capabilities for modelling the isotropic/anisotropic material properties, and large rotational strains are not revealed,
2. Continuity is not capable of modeling large rotational strains.

From this section it is concluded that neither the commercial nor the open source software packages are close enough to featuring a nonlinear incompressible hyperelastic CB shell finite element for soft tissue dynamics using explicit time integration. It is well known that due to numerous "black boxes", commercial software packages cannot easily be modified. The decision of whether or not to use an open source software package depends on the theoretical framework required for the development of the shell element of interest. As will be discussed in Section 2.5.3, we require profound modifications to the formulation of the existing shell elements. Therefore, we decided to write our FE code from scratch.

2.4 Review of existing shell theories

Idealization is necessary to pass from the physical system to a mathematical model. The mathematical model must necessarily be an abstraction of the physical reality by "filtering out" the physical details that are not relevant to the design and analysis process. For example, a continuum material model filters out the aggregate, crystal, molecular and atomic levels of matter. Engineers are typically interested in a few integrated quantities, such as maximum deflection of a structure. Although to a physicist, this is the result of the interaction of billions of molecules, such details are weeded out by the modeling process. Consequently, picking a mathematical model is equivalent to choosing an information filter. Thus, for the development of a shell element with the properties of interest, a thorough understanding of the advantages, disadvantages, and the range of applicability of different shell theories (which are the mathematical models) is required.

There are two basic types of kinematic assumptions for shells (Belytschko et al., 2000):

1. those that admit transverse shear strains in the normal direction of the shell,
2. those that do not.

Before potentially developing a CB shell theory, the kinematic and kinetic assumptions of different shell theories are reviewed.

2.4.1 First order shear deformation theory: Kirchhoff-Love shell theory

In the Kirchhoff-Love shell theory, the fibers (i.e. the normals to the reference surface of the shell in the undeformed configuration- this has nothing to do with actual collagen fibers in soft tissues) are assumed to remain straight and normal after deformation (Figure 2.4, bottom left). Therefore, in this theory, constraining the motion of the fiber is equivalent to constraining the motion of the normal. During deformation, it is necessary for the fibers to remain closely aligned with the normals to the reference surface. This constraint limits the analysis to small rotational strains, and eventually results in zero transverse shear strains. It is well known that, in a beam, the transverse shear must be nonzero if the bending moment is not constant. Thus, the zero transverse shear strain assumption is inconsistent with general equilibrium. However, comparison with experiments proves that this is fairly accurate for thin shells. Therefore, this theory has application for thin shells, where the transverse shear energy will tend to zero (Belytschko et al., 2000). The Kirchhoff-Love shell theory numerically is implemented for instance in LS-Dyna under the name Belytschko-Lin-Tsay shell theory (LS-DYNA, 2011).

Note that the reference surface can be taken either at the top, middle, or bottom of the shell. However, everywhere in this document, the reference surface is arbitrarily taken as the mid-surface. As shown in Figure 2.4, the nodes that are located on the reference surface (mid-surface) are called *master nodes* and those located on the top and bottom surfaces of the shell are called *slave nodes*.

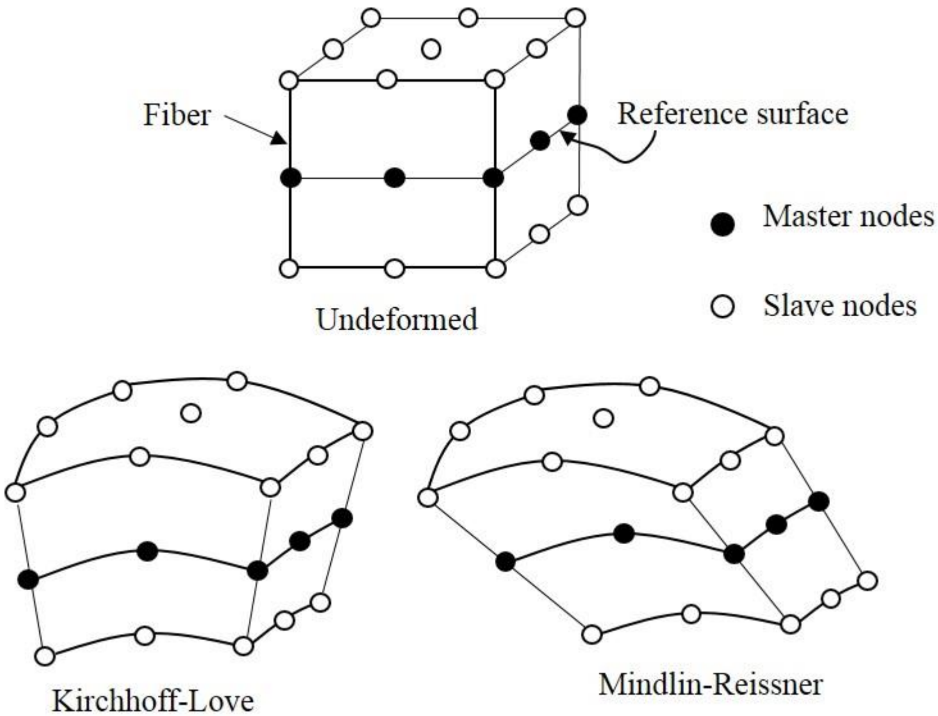

Figure 2.4: Top: front view of a shell in an undeformed configuration. Bottom left: motion of the fiber in the Kirchhoff-Love shell theory. Bottom right: motion of the fiber in the Mindlin-Reissner shell theory.

2.4.2 Second order shear deformation theory: Modified Mindlin-Reissner shell theory

In the modified Mindlin-Reissner shell theory, the following assumptions are made about the motion and stress state:

1) the fibers remain straight but not normal after the deformation (Figure 2.4, bottom right),
2) fibers are inextensible,
3) the stress normal to the reference surface of the shell is negligible, which is called the plane stress condition or zero normal stress condition.

The first assumption differs from the classical Mindlin-Reissner assumption which requires the normal to remain normal and straight. Therefore, in the modified Mindlin-Reissner theory, fibers are usually not normal to the reference surface, and constraining the motion of the fibers is not equivalent to constraining the motion of the normals.

According to the second assumption, no deformation occurs along the fibers and they rotate as rigid bodies. Therefore, this theory admits transverse shear strains. To overcome the artificial stiffening induced by the assumed inextensibility of the fibers, the normal stress component (with respect to the reference surface) is constrained to be zero. It should be noted that the fiber direction is independent of the normal direction. In addition, the normal strain (which is also independent from the inextensibility of the fiber) is obtained from the constitutive equation by requiring zero normal stress. The change in thickness is computed from the normal strain; in other words, the thickness is obtained from the conservation of matter. Next, the nodal internal forces are modified to reflect the thickness changes. Thus the inextensibility assumption applies only to the kinematics (Belytschko et al., 2000).

One might think that the zero normal stress assumption is not physical when a normal traction is applied to either surface of the shell. It is obvious that equilibrium enforces the normal stress to balance the applied normal tractions. However, normal stresses can be neglected in structural theories because they are much smaller than the in-plane stresses.

The modified Mindlin-Reissner shell theory admits constant transverse shear stress through the depth of the shell. However, unless a shear traction is applied to the top or bottom surfaces, the transverse shear must vanish at these surfaces because of the symmetry of the stress tensor. Therefore, a constant shear stress distribution overestimates the shear energy. In order to reduce the shear energy associated with the transverse shear, a shear correction factor is often used. Accurate estimates of this factor can be made for linear elastic shells, but are difficult to obtain for nonlinear materials.

2.4.3 Higher order shear deformation theories

Higher order shear deformation theories are progressively obtained by additionally discarding the first, and then the third assumption associated with the second order shear deformation theory (Modified Mindlin-Reissner shell theory), leading to a full 3D continuum theory with explicit modelling of all stress and strain components. Therefore, their implementation is not desirable in the context of a shell element.

2.5 Review of existing continuum-based (CB) shell elements

A CB shell finite element (FE) with independent translational and rotational degrees of freedom was first developed in (Ahmad et al., 1970) based on the Kirchhoff-Love theory (first order shear deformation theory) for the linear analysis of moderately thick and thin shells. As expected, the normal strain (due to large in-plane stretching) and the transverse shear strains (due to large bending/rotations) were not considered. Since then, other authors have applied the CB technique to develop shell elements with more capabilities (Bathe et al., 1975; Krakeland, 1977; Ramm, 1977; Bathe and Bolourchi, 1979; Kanoknukulchai, 1979; Hughes and Liu, 1980; Hughes et al., 1981; Hughes and Carnoy, 1982; Bathe et al., 1983; Dvorkin and Bathe, 1984; Bucalem and Bathe, 1993; Dvorkin, 1995; Einstein et al., 2003; Kiendl et al., 2015). Despite the advances made, the elements developed in (Bathe et al., 1975; Krakeland, 1977; Ramm, 1977; Bathe and Bolourchi, 1979; Kanoknukulchai, 1979; Bathe et al., 1983; Kiendl et al., 2015) are limited to small strains and small bending deformation/rotations, and are essentially the same as those described in (Ahmad et al., 1970). For example, the improvements brought in (Bathe and Bolourchi, 1979) made the formulation of the material matrices and the constitutive relations easier. Although large in-plane stretching is formulated in (Bathe et al., 1975) and (Ramm, 1977), the normal strains are not calculated, and nor is the thickness of the shell element updated, because of the fiber inextensibility assumption. Thus, volume evolution according to the constitutive relations is neglected. Such limitations arise from the use of only one coordinate system that is corotational with the fibers, as dictated by the Kirchhoff-Love theory, and in which the zero normal stress is enforced (Bathe et al., 1975; Krakeland, 1977; Ramm, 1977; Bathe and Bolourchi, 1979; Kanoknukulchai, 1979; Bathe et al., 1983; Kiendl et al., 2015). Therefore, in these formulations, the fibers are forced to remain normal to the reference surface of the shell, causing shear and membrane locking. As a remedy, the authors in (Dvorkin and Bathe, 1984; Bucalem and Bathe, 1993; Dvorkin, 1995) used the mixed interpolation of tensorial components (MITC), where the bending and membrane strain components were classically calculated from the displacement interpolations, while the transverse shear strain components were interpolated differently. More specifically, the element was formulated in a convected coordinate system and the covariant shear strain components were interpolated. Lagrange multipliers enforced the transformation of the transverse shear strains such that the kinematic relations were satisfied. Thus, the governing finite element equations consisted of the contravariant components of the stress tensor and the covariant components of the strain tensor. In this formulation, not only does the thickness of the element measured along the fiber remain constant during the deformation (hence only small strains are considered); but also, the accuracy with which transverse shear stresses are predicted depends to a great degree on the mesh used and the geometric distortions of the element (Dvorkin and Bathe, 1984; Dvorkin, 1995).

To facilitate the implementation of the modified Mindlin-Reissner theory (second order shear deformation theory) with large deformations of the fibers (both in-plane stretching and rotations) without creating artificial stiffening (thus preventing shear locking) and with the zero normal stress condition, the authors in (Hughes and Liu, 1980; Hughes et al., 1981; Hughes and Carnoy, 1982) assumed two independent coordinate systems to handle the kinematic and the kinetic constraints. Large in-plane stretching requires the adaptation of the thickness such that the volume evolution dictated by the constitutive relations is satisfied. The authors in (Hughes and Carnoy, 1982) addressed this issue in the context of hypoelasticity in which the dependency of the deformations on the loading rate/path is represented by rate-form constitutive relations. However, application of this formulation to hyperelastic materials (load independent nonlinear with large strains and large deformations) would require extensive time integrations that would only add to the complexity of the formulation. Inspired by Hughes and co-authors' formulation of large 3D straining, Einstein et al. (2003) implemented a membrane element with application to biological soft tissues. This membrane element, just like thin shell elements, lacks the transverse shear strains and stresses. However, the normal strain (in the thickness direction) is evaluated seperately and from the statement of incompressibility.

Higher order shear deformation theories are also discretized using finite elements in two approaches: 1) using 3D solid elements, 2) using 3D continuum shell elements (Sussman and Bathe, 2013). Note that neither one of these two approached produces a CB shell element. The 3D solid element produced from the first approach, contains 3 times as many nodes as the CB shell FE to represent the 3D solid element, and a single layer to allow for straining through the shell thickness. These models suffer from different locking types (i.e. the element appears stiffer, in specific loading conditions), hence very fine meshes are needed, making the computations more expensive. The 3D continuum shell element produced from the second approach, contains kinematics of the 3D solid elements (used in the first approach), but the geometry and the displacement behaviour are described with the variables on the reference surface. An example, is the three-dimensional MITC shell elements. These elements, were built upon the conventional MITC shell elements with five (or six) degrees of freedom at each node plus two (or three) additional degrees of freedom to represent the thickness straining and wrapping of the fibers (Kim and Bathe, 2008; Bathe, 2013; Sussman and Bathe, 2013). These elements, which are available in the ADINA commercial finite element program, include the important 3D effects and are capable of modelling very large deformations and large elastic or plastic strains. However, the mixed interpolation of tensorial components used in these formulations, and the additional degrees of freedom, add up to the computational expense, especially when a complex structure is considered.

Overall, two of the most applicable CB shell elements are namely: Hughes and Liu’s, and Bathe and Bolourchi’s. Following, the applicable or useful features of these two CB shell elements are presented.

2.5.1 Hughes and Liu’s CB shell element

Hughes and Liu presented a nonlinear finite element formulation for three dimensional shell elements accounting for large strain and large rotational effects, as well as the bending behavior. The Hughes and Liu shell element is based on the CB shell formulation. For the development of a general nonlinear shell analysis procedure, Hughes and Liu directly began with the fundamental equations of nonlinear continuum mechanics, and then applied the shell theory constraints to their equations of motion (as is done in the CB approach). Their methodology represents a generalization of the Mindlin hypotheses.

Assumptions:

- nonlinear, 3D, large strain and large rotation effects,
- exact stress updates for large rigid rotations of stress point neighbourhoods,
- zero normal stress condition in the rotating stress coordinate system,
- fiber inextensibility.

The second assumption ensures that, when large rotations are experienced, no fake stressing will develop. The third assumption constrains the stress component normal to the reference surface (through the stress point) to be continuously zero for the 3D constitutive equations. This overcomes the artificial stiffening induced by the assumed inextensibility of the fibers (i.e. they may rotate but cannot stretch or contract), and is consistent with the classical plate/shell theory assumptions (example: Mindlin-Reissner). This allows for the use of the general 3D nonlinear constitutive equations without the need of modification to the zero normal stress condition.

2.5.1.1 Geometric and kinematic descriptions

In the following subsections, Hughes' geometric and kinematic descriptions for shells are presented. However, to enable the application of Hughes' element to the total (Equation 3.1) and the incremental (Equation 3.2) UL formulation, the notations are vastly reworked and described herein.

2.5.1.1.1 Geometric description

Let us define the initial geometry of a typical quadrilateral shell. The curvilinear parent coordinates (r, s, t) of a 9-noded CB shell element are shown in Figure 2.5. Each surface of constant t is called a *lamina*. As mentioned previously, the reference surface (in this document) corresponds to $t = 0$. The reference surface is parameterized by two curvilinear coordinates. Lines parallel to the t axis are called *fibers*, and a unit vector along a fiber is called a *director*. Slave nodes are located at the intersections of the fibers, that are emanated from the master nodes (located on the reference surface), and the top and bottom surfaces of the shell.

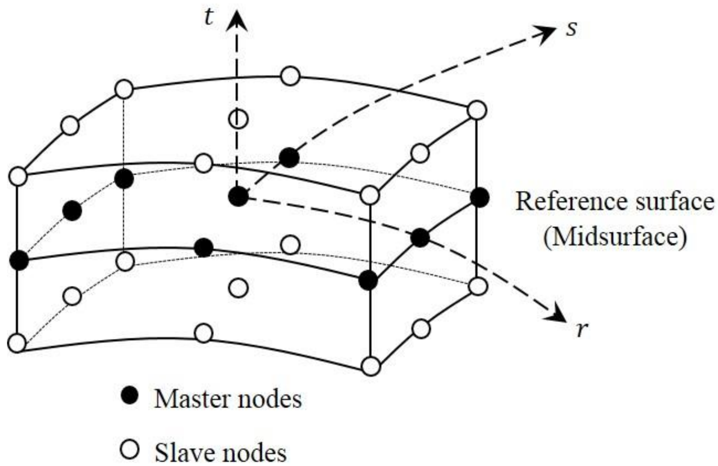

Figure 2.5: Curvilinear coordinate system of a 9-noded CB shell element.

The continuum representation of the geometry of a quadrilateral shell element is defined as follows:

Equation 2.33

$$^{0}y(r,s,t) = {}^{0}\bar{y}(r,s) + {}^{0}Y(r,s,t),$$

where the left script 0 denotes the initial (undeformed) configuration,

$\bar{\bigcirc}$: the accent bar represents the reference surface quantities,

$^{0}y(r,s,t)$: the position vector of a generic point of the shell in the undeformed configuration,

Equation 2.34

$$^{0}\bar{y}(r,s) = \sum_{a=1}^{n_{en}} N_a(r,s)\ {}^{0}\bar{y}_a,$$

Equation 2.35

$$^{0}\bar{y}_a = \frac{1}{2}(1-\bar{t}\,)y_a^{-} + \frac{1}{2}(1+\bar{t}\,)y_a^{+},$$

n_{en}: number of element nodes,

$^{0}\bar{y}(r,s)$: the position vector of a point in the reference surface,

$N_a(r,s)$: the 2D shape function associated with node a,

${}^0\bar{y}_a$: the position vector of a nodal point a,

y_a^+ and y_a^-: the position vector of the top and bottom surfaces (respectively) of the shell along each nodal fiber.

In addition, $\bar{t}$ defines the location of the reference surface. In general, $\bar{t} = -1, 0, 1$ corresponds to the reference surface taken to be the bottom, middle, and top respectively (Figure 2.6). However, as mentioned previously, in this document the reference surface is taken as the mid-surface. Thus, $\bar{t} = 0$.

Equation 2.36

$${}^0Y(r,s,t) = \sum_{a=1}^{n_{en}} N_a(r,s)\ {}^0Y_a(t),$$

${}^0Y_a(t)$: position vector based at a point in the reference surface which defines the fiber through the point,

${}^0\hat{Y}_a$: director emanating from node a,

Equation 2.37

$${}^0Y_a(t) = \frac{1}{2}(t-\bar{t})\|y_a^+ - y_a^-\|\ \ {}^0\hat{Y}_a \qquad \text{no sum,}$$

Equation 2.38

$${}^0\hat{Y}_a = \frac{(y_a^+ - y_a^-)}{\|y_a^+ - y_a^-\|},$$

Equation 2.39

$$z_a(t) = N_+(t)z_a^+ + N_-(t)z_a^-,$$

Equation 2.40

$$z_a^+ = \frac{1}{2}(1-\bar{t})\|y_a^+ - y_a^-\|,$$

Equation 2.41

$$z_a^- = -\frac{1}{2}(1+\bar{t})\|y_a^+ - y_a^-\|,$$

Equation 2.42

$$N_+(t) = \frac{1}{2}(1+t) \qquad N_-(t) = \frac{1}{2}(1-t),$$

$z_a(t)$: a "thickness function" associated with node $\boldsymbol{a}$, which is defined by the location of the midsurface (i.e. the total thickness of the shell at node a),

z_a^+ and z_a^-: the distance from the reference surface to the top and bottom surfaces (respectively) along the director.

‖ ‖ denotes the Euclidean norm, for example: $\|y\| = \sqrt{y_1^2 + y_2^2 + y_3^2}$.

Fixing t in Equation 2.33 defines the lamina (reference surface). Fixing r and s in Equation 2.33 defines a fiber. Fibers are not generally normal to the lamina.

Equations 2.33 to 2.41 represent the mapping of a general biunit cube into the physical shell domain (Figure 2.6).

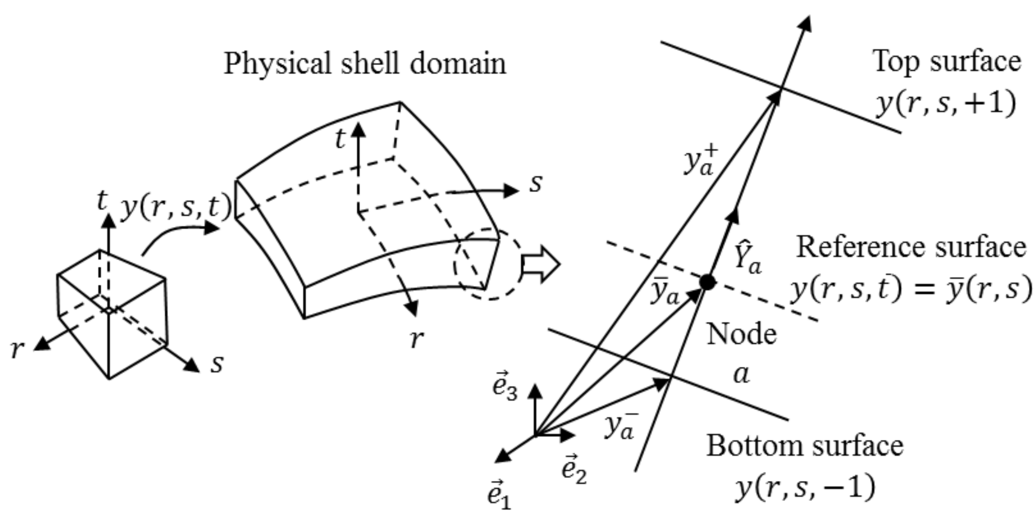

Figure 2.6: Left: mapping of a general cube into the physical shell element. Right: illustration of Equations 2.35 to 2.41. The script 0 denoting the undeformed configurations is dropped for convenience.

For application to large membrane strain situations, in which the thickness changes, it is convenient to introduce a nodal thickness parameter h_a which, in the undeformed configuration (at time $\tau = 0$), is defined to be:

Equation 2.43

$$h_a\big|_{\tau=0} = \|y_a^+ - y_a^-\|.$$

In general, it is more correct to think of h_a as the fiber length rather than the actual thickness of the shell, because fibers are not constrained to remain normal to the surface of the shell (Hughes and Carnoy, 1983).

2.5.1.1.2 Kinematic description

Displacement of the reference surface with time is represented in Figure 2.7. Since the shell element is assumed to be isoparametric (i.e. the same shape functions are used to represent both the geometry and displacements), the kinematic expressions can be easily obtained by replacing the displacement variables with the coordinate variables (Equations 2.44 to 2.53 are obtained from Equations 2.33 to 2.37, respectively). This gives:

Equation 2.44

$${}_0^\tau u(r,s,t) = {}_0^\tau \bar{u}(r,s) + {}_0^\tau U(r,s,t),$$

Equation 2.45

$${}_0^\tau \bar{u}(r,s) = \sum_{a=1}^{n_{en}} N_a(r,s)\, {}_0^\tau \bar{u}_a,$$

Equation 2.46

$${}_0^\tau U(r,s,t) = \sum_{a=1}^{n_{en}} N_a(r,s)\, {}_0^\tau U_a(t),$$

Equation 2.47

$${}_0^\tau U_a(t) = {}_0^\tau z_a(t)\, {}_0^\tau \hat{U}_a \qquad \text{no sum,}$$

$${}_0^\tau z_a(t) = \frac{1}{2}(t - \bar{t}\,)\, {}_0^\tau h_a,$$

where

$\overline{\bigcirc}$: the accent bar represents the reference surface quantities,

${}_{0}^{\tau}u(r,s,t)$: the displacement of a generic point of the shell,

${}_{0}^{\tau}\bar{u}(r,s)$: the displacement of a point in the reference surface,

${}_{0}^{\tau}\bar{u}_a$: the displacement of a node in the reference surface,

${}_{0}^{\tau}U(r,s,t)$: the fiber displacement,

${}_{0}^{\tau}\widehat{U}_a(t)$: the displacement of a director at a specific node,

and, ${}_{0}^{\tau}U_a(t)$ is used to account for the thickness changes.

Recall that the nodal fiber length (thickness) in the undeformed configuration is obtained by Equation 2.43. Updating the thickness as the element deforms is neglected in the majority of the references in the literature. However, this is an important aspect to address when the materials modelled are nearly or completely incompressible.

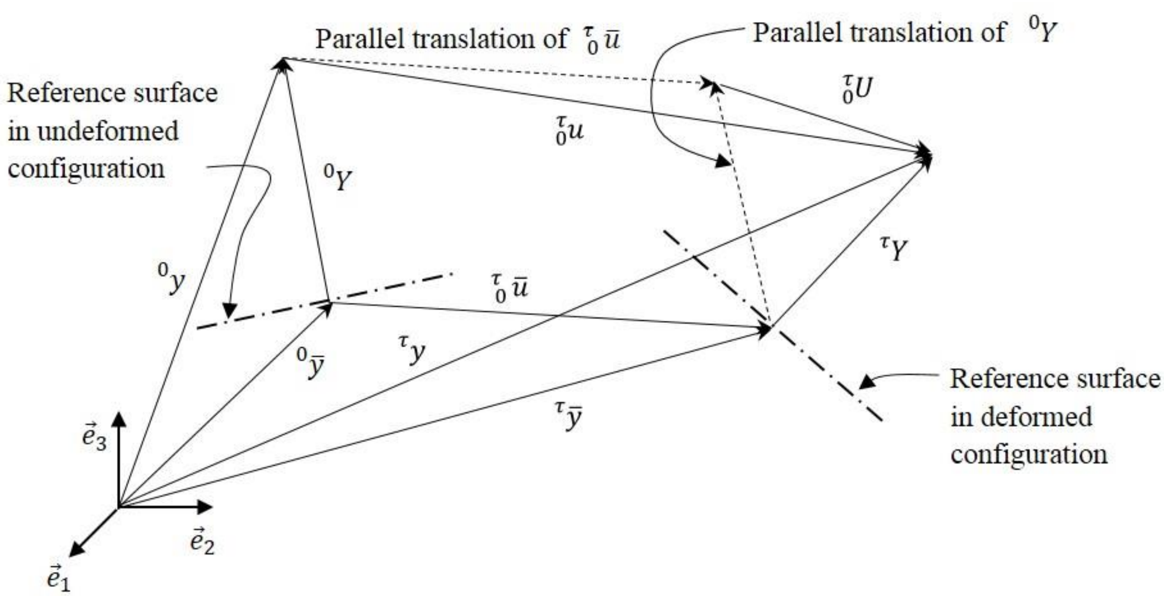

Figure 2.7: A general representation of the displacement of the reference surface with time.

As shown in Figure 2.7, the deformed geometry is defined by the following equations:

Equation 2.48

$$^{\tau}y(r,s,t) = {}^{\tau}\bar{y}(r,s) + {}^{\tau}Y(r,s,t),$$

Equation 2.49

$$^{\tau}\bar{y}(r,s) = {}^{0}\bar{y}(r,s) + {}_{0}^{\tau}\bar{u}(r,s),$$

Equation 2.50

$$^{\tau}\bar{y}_a = {}^{0}\bar{y}_a + {}_{0}^{\tau}\bar{u}_a,$$

where

$\bar{\bigcirc}$: the accent bar represent the reference surface quantities,

$^{\tau}y(r,s,t)$: the position vector of a generic point of the shell in the deformed configuration,

$^{\tau}\bar{y}(r,s)$: the position vector of a point in the reference surface in the deformed configuration,

$^{\tau}\bar{y}_a$: the position vector of a nodal point a in the deformed configuration,

$^{\tau}Y(r,s,t)$: position vector based at a point on the reference surface (in the deformed configuration) which defines the fiber direction through the point,

Equation 2.51

$$^{\tau}Y(r,s,t) = {}^{0}Y(r,s,t) + {}_{0}^{\tau}U(r,s,t),$$

Equation 2.52

$$^{\tau}Y_a(t) = {}^{0}Y_a(t) + {}_{0}^{\tau}U_a(t),$$

Equation 2.53

$$^{\tau}\hat{Y}_a = {}^{0}\hat{Y}_a + {}_{0}^{\tau}\hat{U}_a,$$

$^{\tau}\hat{Y}_a(t)$: director emanating from node a in the deformed configuration.

As previously stated, the fibers are assumed to be inextensible (in kinematics only), meaning that they can rotate but cannot stretch or contract. Therefore:

Equation 2.54

$$\left\| {}^{\tau}\hat{Y}_a \right\| = 1$$

Hughes and Liu suggested a trial value of $\hat{U}_a(t)$ (i.e $\hat{U}_a^{trial}$) to be calculated and then projected radially (Figure 2.8) to maintain Equation 2.54. The steps are as follows:

$$^{\tau}\hat{Y}_a = \frac{\left({}^{0}\hat{Y}_a + {}_{0}^{\tau}\hat{U}_a^{trial} \right)}{\left\| {}^{0}\hat{Y}_a + {}_{0}^{\tau}\hat{U}_a^{trial} \right\|}$$

$${}_{0}^{\tau}\hat{U}_a = {}^{\tau}\hat{Y}_a - {}^{0}\hat{Y}_a$$

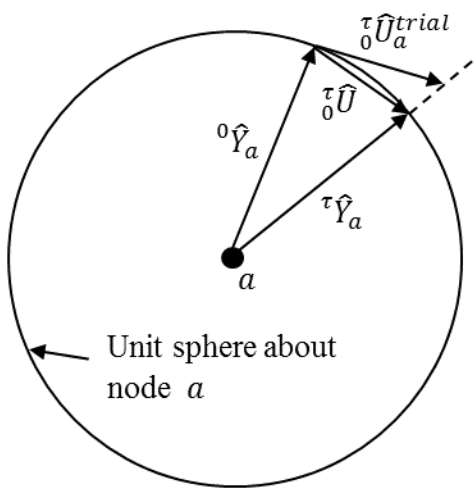

Figure 2.8: Nodal fiber inextensibility condition maintained by radial return normalization.

A complete discussion of the derivation of ${}_{0}^{\tau}\hat{U}_a^{trial}$ will be made in Section 2.5.1.3.

2.5.1.2 Coordinate systems

As mentioned earlier, multiple independent coordinate systems are required in order to apply both the fiber inextensibility and the zero normal stress assumptions.

2.5.1.2.1 Global coordinate system

As represented in Figure 2.6 and Figure 2.7, the vectors defining the position of any point within the shell in the undeformed and deformed configurations (i.e. x, $\bar{x}$, x_a^+, x_a^-, y and $\bar{y}$) are defined with respect to the orthonormal coordinate bases:

$$\vec{e}_1 = \begin{bmatrix} 1 \\ 0 \\ 0 \end{bmatrix}, \qquad \vec{e}_2 = \begin{bmatrix} 0 \\ 1 \\ 0 \end{bmatrix} \qquad \text{and} \qquad \vec{e}_3 = \begin{bmatrix} 0 \\ 0 \\ 1 \end{bmatrix},$$

that are global to the shell (or the entire structure) throughout the analysis.

2.5.1.2.2 Lamina coordinate system

The constitutive equations are written with respect to coordinate axes naturally defined by the geometry of the shell (Figure 2.9). This is the most convenient way of representing a general nonlinear shell formulation. The lamina coordinate systems, denoted by $\left((\vec{e}_1^{\,l})^a, (\vec{e}_2^{\,l})^a, (\vec{e}_3^{\,l})^a\right)$, are adopted at each stress storage point (node). Therefore, these coordinate systems vary from point to point within an element and undergo finite rotations (Hughes and Liu, 1980; Hughes, 2000; Belytschko et al., 2000).

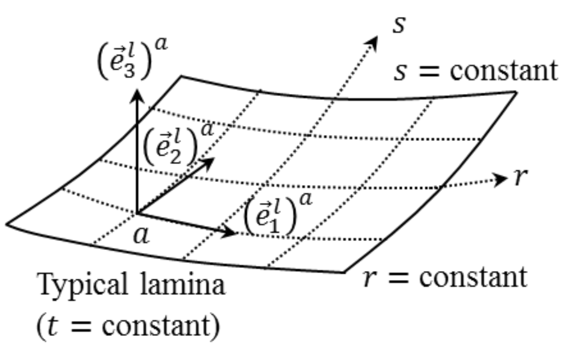

Figure 2.9: Lamina coordinate system shown on a typical lamina.

For simplicity, the superscript a defining the node number is excluded in what follows.

The lamina basis rotates rigidly as the element deforms. Note that $\vec{e}_1^{\,l}$ and $\vec{e}_2^{\,l}$ are tangent to the lamina and $\vec{e}_3^{\,l}$ is normal to the lamina. Furthermore, it may be observed that $\vec{e}_3^{\,l}$ is not generally tangent to the fiber direction at the point under study (Figure 2.10).

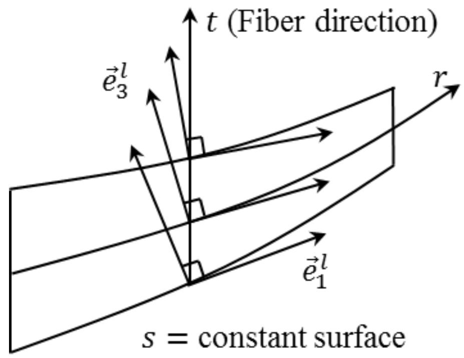

Figure 2.10: Lamina coordinate system along a fiber.

The bases of the lamina coordinate system in any configuration are obtained through the following procedure (Hughes, 2000):

Equation 2.55

$$\vec{e}_r = \frac{y_{,r}}{\|y_{,r}\|},$$

Equation 2.56

$$\vec{e}_s = \frac{y_{,s}}{\|y_{,s}\|},$$

where y denotes the current (deformed) nodal coordinates in the global coordinate system $(\vec{e}_1, \vec{e}_2, \vec{e}_3)$ and a comma is used to denote partial differentiation. Therefore, Equation 2.55 and Equation 2.56 become:

$$\vec{e}_r = \frac{\begin{bmatrix}\frac{\partial y_1}{\partial r} & \frac{\partial y_2}{\partial r} & \frac{\partial y_3}{\partial r}\end{bmatrix}^T}{\left\|\begin{bmatrix}\frac{\partial y_1}{\partial r} & \frac{\partial y_2}{\partial r} & \frac{\partial y_3}{\partial r}\end{bmatrix}\right\|} = \frac{\begin{bmatrix}\frac{\partial y_1}{\partial r} & \frac{\partial y_2}{\partial r} & \frac{\partial y_3}{\partial r}\end{bmatrix}^T}{\sqrt{\left(\frac{\partial y_1}{\partial r}\right)^2 + \left(\frac{\partial y_2}{\partial r}\right)^2 + \left(\frac{\partial y_3}{\partial r}\right)^2}},$$

$$\vec{e}_s = \frac{\begin{bmatrix}\frac{\partial y_1}{\partial s} & \frac{\partial y_2}{\partial s} & \frac{\partial y_3}{\partial s}\end{bmatrix}^T}{\left\|\begin{bmatrix}\frac{\partial y_1}{\partial s} & \frac{\partial y_2}{\partial s} & \frac{\partial y_3}{\partial s}\end{bmatrix}\right\|} = \frac{\begin{bmatrix}\frac{\partial y_1}{\partial s} & \frac{\partial y_2}{\partial s} & \frac{\partial y_3}{\partial s}\end{bmatrix}^T}{\sqrt{\left(\frac{\partial y_1}{\partial s}\right)^2 + \left(\frac{\partial y_2}{\partial s}\right)^2 + \left(\frac{\partial y_3}{\partial s}\right)^2}}.$$

Then,

Equation 2.57

$$\vec{e}_3^{\,l} = \frac{\vec{e}_r \times \vec{e}_s}{\|\vec{e}_r \times \vec{e}_s\|},$$

where × denotes the cross product.

Following (Hughes, 2000), the vectors tangent to the lamina are selected such that the angle between $\vec{e}_1^{\,l}$ and $\vec{e}_r$ (i.e. the vector tangent to r) is equal to the angle between $\vec{e}_s$ and $\vec{e}_2^{\,l}$. In addition, the $\vec{e}_1^{\,l}$ and $\vec{e}_2^{\,l}$ basis is as close as possible to the $\vec{e}_r$ and $\vec{e}_s$ basis (Figure 2.11).

$$\vec{e}_1^{\,l} = \frac{\sqrt{2}}{2}(\vec{e}_\alpha - \vec{e}_\beta),$$

$$\vec{e}_2^{\,l} = \frac{\sqrt{2}}{2}(\vec{e}_\alpha + \vec{e}_\beta),$$

where

$$\vec{e}_\alpha = \frac{0.5 \times (\vec{e}_r + \vec{e}_s)}{\|0.5 \times (\vec{e}_r + \vec{e}_s)\|},$$

and

$$\vec{e}_\beta = \frac{\vec{e}_3^{\,l} \times \vec{e}_\alpha}{\|\vec{e}_3^{\,l} \times \vec{e}_\alpha\|}.$$

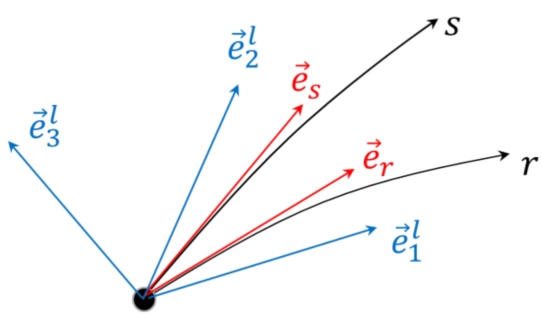

Figure 2.11: Illustration of the lamina coordinate system with respect to the parent coordinate system.

It will be necessary, in what follows, to transform quantities from the global coordinate system to the lamina system. This is facilitated by the following matrix:

$$[q]\text{: global} \rightarrow \text{lamina},$$

$$[q] = [\vec{e}_1^{\,l} \quad \vec{e}_2^{\,l} \quad \vec{e}_3^{\,l}]^T,$$

where, the superscript T stands for transpose. Therefore,

Equation 2.58

$$[q] = \begin{bmatrix} \left(\vec{e}_1^{\,l}\right)_1 & \left(\vec{e}_1^{\,l}\right)_2 & \left(\vec{e}_1^{\,l}\right)_3 \\ \left(\vec{e}_2^{\,l}\right)_1 & \left(\vec{e}_2^{\,l}\right)_2 & \left(\vec{e}_2^{\,l}\right)_3 \\ \left(\vec{e}_3^{\,l}\right)_1 & \left(\vec{e}_3^{\,l}\right)_2 & \left(\vec{e}_3^{\,l}\right)_3 \end{bmatrix}.$$

Note that since the nodal spatial coordinates in the global system change with time, the transformation matrix $[q]$ needs to be updated at every time step.

2.5.1.2.3 Fiber coordinate system

The fiber coordinate system, which is a unique local Cartesian coordinate system, is constructed at each master node. One of the bases of this coordinate system, the director, must coincide with the fiber direction (Figure 2.12). The rotation of a node is specified about the director. The incremental components of the displacement of this vector may be identified with classical rotation increments.

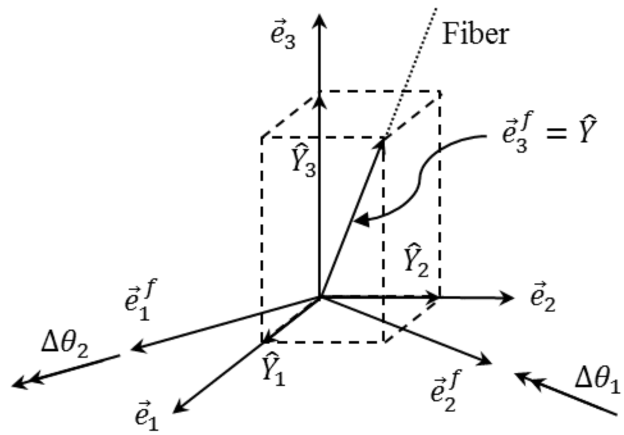

Figure 2.12: Nodal fiber coordinate system. $\Delta\theta_1$ and $\Delta\theta_2$ denote rotation increments about the basis $\vec{e}_1^{\,f}$ and $\vec{e}_2^{\,f}$, respectively.

$\hat{Y}$ denotes the unit basis vector in the fiber direction (director) in the deformed configuration. Therefore $\vec{e}_1^{\,f}, \vec{e}_2^{\,f}, \vec{e}_3^{\,f}$ represent the fiber coordinate system at any node and in the deformed configuration. As shown in Figure 2.12, $\hat{Y}_i$ (where $i = 1, 2, 3$) denotes the projections of the director $(\hat{Y})$ on the global Cartesian coordinate basis. Therefore:

$$\hat{Y} = |\hat{Y}_1|\vec{e}_1 + |\hat{Y}_2|\vec{e}_2 + |\hat{Y}_3|\vec{e}_3.$$

So far, the direction of one of the fiber coordinate system axes $(\vec{e}_3^{\,f} = \hat{Y})$ has been determined to be coincident with the fiber direction. In order to determine the direction of the other two axes, Hughes (2000) suggested the following algorithm:

Step 1: let $b_i = |\hat{Y}_i|,\ i = 1, 2, 3,$

Step 2: $j = 1,$

Step 3: If $b_1 > b_3$, then $b_3 = b_1$ and $j = 2,$

Step 4: If $b_2 > b_3$, then $j = 3,$

Step 5: $\vec{e}_3^{\,f} = \hat{Y},$

Step 6: $\vec{e}_2^{\,f} = (\hat{Y} \times \vec{e}_j)/\|\hat{Y} \times \vec{e}_j\|$,

Step 7: $\vec{e}_1^{\,f} = (\vec{e}_2^{\,f} \times \hat{Y})$.

The above algorithm ensures that the obtained orthonormal fiber basis $(\vec{e}_1^{\,f}, \vec{e}_2^{\,f}, \vec{e}_3^{\,f})$ satisfies the condition that if $\hat{Y}$ is close to $\vec{e}_3$, then $\vec{e}_1^{\,f}, \vec{e}_2^{\,f}, \vec{e}_3^{\,f}$ will be close to $\vec{e}_1, \vec{e}_2, \vec{e}_3$, respectively. Note that the fiber basis rotates rigidly with the nodal fiber.

It is often necessary to transform the quantities from the nodal fiber system to the global or the lamina system. Transformation between the global and the nodal fiber coordinate system is done using the orthogonal transformation matrix $[s]$ as follows:

$$[s]\text{: fiber} \rightarrow \text{global},$$

Equation 2.59

$$[s] = \begin{bmatrix} \vec{e}_1^{\,f} & \vec{e}_2^{\,f} & \vec{e}_3^{\,f} \end{bmatrix}.$$

In order to denote the particular nodal fiber coordinate system to which $[s]$ is associated, a nodal subscript can be used (e.g. $[s_a]$).

In addition, transformation from the nodal fiber system to the lamina system can be done using the orthogonal matrix $[r]$ defined as follows:

$$[r]\text{: fiber} \rightarrow \text{lamina},$$

Equation 2.60

$$[r] = [r_{ij}]; \qquad r_{ij} = \vec{e}_i^{\,l} \cdot \vec{e}_j^{\,f},$$

where, $\vec{e}_1^{\,f}, \vec{e}_2^{\,f}, \vec{e}_3^{\,f}$ are defined by Hughes and Liu's algorithm mentioned earlier. In addition, the dot $'\cdot'$ denotes the dot product. Note that since both the lamina and the fiber coordinate systems are defined with respect to the global coordinate system, the dot product in Equation 2.60 is between the components of the global coordinate system. To keep track of the particular node to which $[r]$ is associates, a subscript can be added representing the node number (e.g. r_a).

The relationship between the three orthogonal transformation matrices is summarized in Figure 2.13.

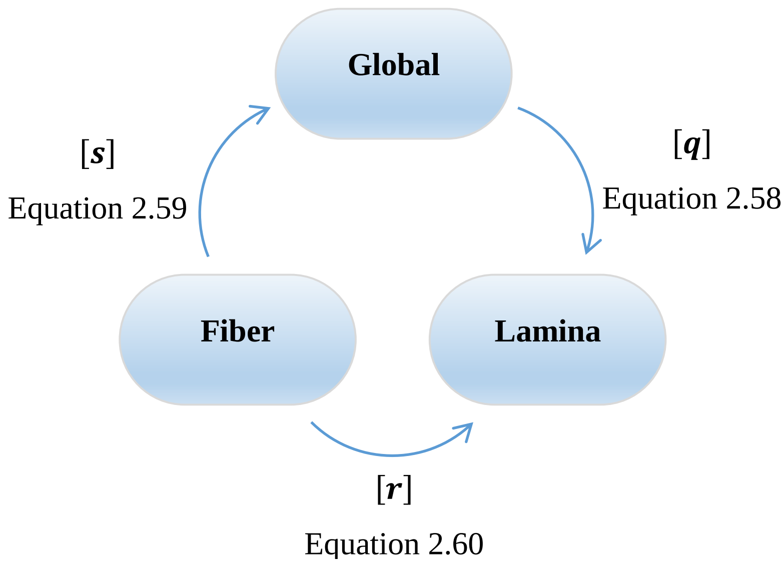

Figure 2.13: relationship between the three orthogonal transformation matrices.

Therefore it is concluded that: $[q] = [r][s]^T$.

2.5.1.3 Derivation of the trial value for the displacement of a director

In this section, the derivation of $\widehat{U}_a^{trial}$ (the trial value of the displacement of the director at node a) is detailed (Hughes and Liu, 1980; Hughes, 2000). The superscript a referring to a specific node is dropped for convenience.

Letting $\Delta\theta_1$ and $\Delta\theta_2$ respectively denote rotation increments about the basis vectors $\vec{e}_2^{\,f}$ and $\vec{e}_1^{\,f}$, and following the sign convention used in Figure 2.12, the linearized relationship between the components of $\widehat{U}$ (the displacement of the director) in the fiber system $\left(\text{namely: } \widehat{U}_1^f,\ \widehat{U}_2^f,\ \widehat{U}_3^f\right)$ and the incremental rotations becomes:

Equation 2.61

$$\begin{Bmatrix} {}^{\tau}_{0}\widehat{U}^{f}_{1} \\ {}^{\tau}_{0}\widehat{U}^{f}_{2} \\ {}^{\tau}_{0}\widehat{U}^{f}_{3} \end{Bmatrix} = \begin{bmatrix} -1 & 0 \\ 0 & -1 \\ 0 & 0 \end{bmatrix} \begin{Bmatrix} \Delta\theta_1 \\ \Delta\theta_2 \end{Bmatrix}.$$

Equation 2.61 enables the reduction of the nodal degrees of freedom from 6 to 5 (Hughes and Liu, 1980). As will be explained in the next section, this reduction in the number of DOFs eliminates the need to develop artificial in-plane torsional stiffness to numerically stabilize rotations about the fiber direction.

It can be concluded from Equation 2.61 that the components of $\widehat{U}$ in an arbitrary coordinate system can be identified with the incremental rotations in that system. Thus, to find the trial value of the fiber displacements in the global coordinate system, we can premultiply Equation 2.61 with $[s]$ to get:

Equation 2.62

$$\begin{Bmatrix} {}^{\tau}_{0}\widehat{U}^{trial}_{1} \\ {}^{\tau}_{0}\widehat{U}^{trial}_{2} \\ {}^{\tau}_{0}\widehat{U}^{trial}_{3} \end{Bmatrix} = {}^{\tau}[s] \begin{Bmatrix} {}^{\tau}_{0}\widehat{U}^{f}_{1} \\ {}^{\tau}_{0}\widehat{U}^{f}_{2} \\ {}^{\tau}_{0}\widehat{U}^{f}_{3} \end{Bmatrix} = \begin{bmatrix} \left(\vec{e}^{f}_{1}\right)_1 & \left(\vec{e}^{f}_{2}\right)_1 & \left(\vec{e}^{f}_{3}\right)_1 \\ \left(\vec{e}^{f}_{1}\right)_2 & \left(\vec{e}^{f}_{2}\right)_2 & \left(\vec{e}^{f}_{3}\right)_2 \\ \left(\vec{e}^{f}_{1}\right)_3 & \left(\vec{e}^{f}_{2}\right)_3 & \left(\vec{e}^{f}_{3}\right)_3 \end{bmatrix} \begin{bmatrix} -1 & 0 \\ 0 & -1 \\ 0 & 0 \end{bmatrix} \begin{Bmatrix} \Delta\theta_1 \\ \Delta\theta_2 \end{Bmatrix},$$

$$\therefore \quad \begin{Bmatrix} {}^{\tau}_{0}\widehat{U}^{trial}_{1} \\ {}^{\tau}_{0}\widehat{U}^{trial}_{2} \\ {}^{\tau}_{0}\widehat{U}^{trial}_{3} \end{Bmatrix} = \begin{bmatrix} -\left(\vec{e}^{f}_{1}\right)_1 & -\left(\vec{e}^{f}_{2}\right)_1 \\ -\left(\vec{e}^{f}_{1}\right)_2 & -\left(\vec{e}^{f}_{2}\right)_2 \\ -\left(\vec{e}^{f}_{1}\right)_3 & -\left(\vec{e}^{f}_{2}\right)_3 \end{bmatrix} \begin{Bmatrix} \Delta\theta_1 \\ \Delta\theta_2 \end{Bmatrix}.$$

2.5.1.4 Number of degrees of freedom per node

Displacement of a slave node in a shell element consists of the sum of the translational displacements in the reference surface, the bending displacements, and the displacement due to the change in thickness. The bending displacement depends on the rotational displacements of the director. The component of the rotational displacement parallel to the director (i.e. rotation about the director) is irrelevant since it causes no change in the position of the director. This component is called the *drilling component*. The effect of the drilling component adds to the in-plane torsion due to the translational displacement of the nodal points in the reference surface

(Kanoknukulchai, 1979; Belytscho et al., 2000). In-plane torsion naturally takes place when the drilling effect is introduced. To eliminate the need to include artificial in-plane torsional stiffness to numerically stabilize rotations about the fiber direction, the drilling component is excluded from the analysis (as is done in Equation 2.62). The displacement due to the change in thickness is not retained in the equations of motion, since it represents an insignificant inertia. But it is used in updating the geometry, so it does affect the internal nodal forces, which depend on the current geometry. The displacement due to the change in thickness is obtained from the constitutive equation or conservation of matter.

Therefore, as was presented in Section 2.5.1.1.2, the motion of a shell in the absence of kinks and junctions can be treated with 5 degrees of freedom per node (Belytscho et al., 2000), with the following nodal displacements at a master node:

$$\{u_a\} = [u_1^a \quad u_2^a \quad u_3^a \quad \Delta\theta_1^a \quad \Delta\theta_2^a]^T,$$

where u_i^a are the Cartesian components of the translational displacement of master node a with respect to the global coordinate system, and $\Delta\theta_1^a$ and $\Delta\theta_2^a$ are the rotational displacements of the director at node a.

2.5.1.5 Constitutive equations

Hughes and Liu (1980) employed rate-form constitutive equations. This type of equations have applications in many theories related to elasto-plasticity, viscoelasticity, and viscoplasticity. In addition, nonlinear elasticity can be treated with rate equations by time differentiating the more usual forms. Rate-form constitutive equations facilitate maintaining the zero normal stress condition incrementally (Hughes and Liu, 1980; Belytschko et al., 2000). However, the following two aspects must be considered in the integration of the rate-form constitutive equations:

1. the stress components are referred to the lamina (rotating) basis,
2. the zero normal stress constraint (which is imposed in the lamina coordinate system) needs to be enforced with respect to the 3-directions of the lamina basis.

On the other hand, the energy stored in hyperelastic material depends only on the initial and final states of deformation and is independent of the deformation or load path (Belytschko et. al., 2000). Therefore the rate-form is not an efficient tool to be employed for the hyperelastic materials to represent soft tissues. This is a significant departure point from Hughes and Liu's shell theory.

2.5.2 Bathe and Bolourchi's CB shell element

Bathe and Bolourchi (1979) had the objective to present a formulation, interpolation and application of a general variable-number-node rotation/displacement isoparametric element for linear as well as geometric and material nonlinear analyses of plates and shells. In essence, their goal was to develop a shell element that accommodates very large displacements and rotations. These authors presented the large displacement formulations of their shell element starting from the principle of virtual work, and then adapted the updated Lagrangian (UL) and the total Lagrangian (TL) formulations to allow for large deformations and material nonlinearity. These formulations were used to express the equilibrium of the body at time $\tau + \Delta\tau$. Both formulations included all nonlinear effects due to large displacements, large strains and material nonlinearities.

However, we are interested in adopting the UL formulation, and thus, the focus of this section is on Bathe's UL formulation only. Bathe and Bolourchi (1979) have similar geometric and kinematic descriptions/assumptions as Hughes and Liu. The only difference is that the formulation presented by Bathe and Bolourchi assumes that the lamina coordinate system is always coincident with the fiber coordinate system (i.e. both coordinate systems are co-rotational). Therefore, the fibers are forced to remain straight and normal to the reference surface. Consequently, the element cannot handle large rotational strains. The authors hinted that for a general nonlinear shell, the constitutive relations must be applied in the coordinate system naturally defined by the geometry of the shell (i.e. the lamina coordinate system) and then transformed to the global coordinate system. No additional information or demonstration was provided. Therefore, the goal of the following sections is to develop a general understanding of the derivation of the matrices required in the explicit UL formulation. Note that these matrices are developed for the corotational lamina and fiber coordinate systems.

2.5.2.1 Geometric and kinematic descriptions

As mentioned, Bathe and Bolourchi defined the geometry and the kinematics of their shell element similar to what is done by Hughes and Liu (Section 2.5.1.1), and thus, their definitions are not repeated here. However, to enable derivations of the kinetics, the displacements equation (Equation 2.44) is written in matrix form as follows:

Equation 2.63

$$\begin{Bmatrix} {}_0^\tau u_1 \\ {}_0^\tau u_2 \\ {}_0^\tau u_3 \end{Bmatrix} = \begin{bmatrix} \dots & N_a & 0 & 0 & -\frac{(t-\bar{t})}{2} h_a N_a \left(\vec{e}_1^{\,f}\right)_1^a & -\frac{(t-\bar{t})}{2} h_a N_a \left(\vec{e}_2^{\,f}\right)_1^a & \dots \\ \dots & 0 & N_a & 0 & -\frac{(t-\bar{t})}{2} h_a N_a \left(\vec{e}_1^{\,f}\right)_2^a & -\frac{(t-\bar{t})}{2} h_a N_a \left(\vec{e}_2^{\,f}\right)_2^a & \dots \\ \dots & 0 & 0 & N_a & -\frac{(t-\bar{t})}{2} h_a N_a \left(\vec{e}_1^{\,f}\right)_3^a & -\frac{(t-\bar{t})}{2} h_a N_a \left(\vec{e}_2^{\,f}\right)_3^a & \dots \end{bmatrix} \begin{Bmatrix} \vdots \\ {}_0^\tau u_1^a \\ {}_0^\tau u_2^a \\ {}_0^\tau u_3^a \\ \Delta\theta_1^a \\ \Delta\theta_2^a \\ \vdots \end{Bmatrix}.$$

Recall that, in this document, the reference surface taken as the mid-surface, thus, $\bar{t} = 0$.

2.5.2.2 Strain-displacement transformation matrix

In the updated Lagrangian formulation, the linear strain-displacement transformation matrix $[B_L]$ is obtained by taking the partial derivatives of Equation 2.63 with respect to the Cartesian coordinates of the position vector in the current configuration. Considering that the displacement and the position vectors are both functions of the parent coordinate system, the derivation process is not direct and several steps are required. In what follows, the left super- and subscripts (τ and 0) are dropped for convenience.

As a starting point, take the partial derivatives of Equation 2.63 with respect to the parent coordinates (r, s, t) :

Equation 2.64

$$
\begin{Bmatrix} \frac{\partial u_1}{\partial r} \\ \frac{\partial u_1}{\partial s} \\ \frac{\partial u_1}{\partial t} \\ \frac{\partial u_2}{\partial r} \\ \frac{\partial u_2}{\partial s} \\ \frac{\partial u_2}{\partial t} \\ \frac{\partial u_3}{\partial r} \\ \frac{\partial u_3}{\partial s} \\ \frac{\partial u_3}{\partial t} \end{Bmatrix} = \begin{bmatrix}
\cdots & \frac{\partial N_a}{\partial r} & 0 & 0 & \frac{\partial}{\partial r}\left(-\frac{(t-\bar{t}\,)}{2}h_a\left(\vec{e}_1^{\,f}\right)_1^a N_a\right) & \frac{\partial}{\partial r}\left(-\frac{(t-\bar{t}\,)}{2}h_a\left(\vec{e}_2^{\,f}\right)_1^a N_a\right) & \cdots \\
\cdots & \frac{\partial N_a}{\partial s} & 0 & 0 & \frac{\partial}{\partial s}\left(-\frac{(t-\bar{t}\,)}{2}h_a\left(\vec{e}_1^{\,f}\right)_1^a N_a\right) & \frac{\partial}{\partial s}\left(-\frac{(t-\bar{t}\,)}{2}h_a\left(\vec{e}_2^{\,f}\right)_1^a N_a\right) & \cdots \\
\cdots & \frac{\partial N_a}{\partial t} & 0 & 0 & \frac{\partial}{\partial t}\left(-\frac{(t-\bar{t}\,)}{2}h_a\left(\vec{e}_1^{\,f}\right)_1^a N_a\right) & \frac{\partial}{\partial t}\left(-\frac{(t-\bar{t}\,)}{2}h_a\left(\vec{e}_2^{\,f}\right)_1^a N_a\right) & \cdots \\
\cdots & 0 & \frac{\partial N_a}{\partial r} & 0 & \frac{\partial}{\partial r}\left(-\frac{(t-\bar{t}\,)}{2}h_a\left(\vec{e}_1^{\,f}\right)_2^a N_a\right) & \frac{\partial}{\partial r}\left(-\frac{(t-\bar{t}\,)}{2}h_a\left(\vec{e}_2^{\,f}\right)_2^a N_a\right) & \cdots \\
\cdots & 0 & \frac{\partial N_a}{\partial s} & 0 & \frac{\partial}{\partial s}\left(-\frac{(t-\bar{t}\,)}{2}h_a\left(\vec{e}_1^{\,f}\right)_2^a N_a\right) & \frac{\partial}{\partial s}\left(-\frac{(t-\bar{t}\,)}{2}h_a\left(\vec{e}_2^{\,f}\right)_2^a N_a\right) & \cdots \\
\cdots & 0 & \frac{\partial N_a}{\partial t} & 0 & \frac{\partial}{\partial t}\left(-\frac{(t-\bar{t}\,)}{2}h_a\left(\vec{e}_1^{\,f}\right)_2^a N_a\right) & \frac{\partial}{\partial t}\left(-\frac{(t-\bar{t}\,)}{2}h_a\left(\vec{e}_2^{\,f}\right)_2^a N_a\right) & \cdots \\
\cdots & 0 & 0 & \frac{\partial N_a}{\partial r} & \frac{\partial}{\partial r}\left(-\frac{(t-\bar{t}\,)}{2}h_a\left(\vec{e}_1^{\,f}\right)_3^a N_a\right) & \frac{\partial}{\partial r}\left(-\frac{(t-\bar{t}\,)}{2}h_a\left(\vec{e}_2^{\,f}\right)_3^a N_a\right) & \cdots \\
\cdots & 0 & 0 & \frac{\partial N_a}{\partial s} & \frac{\partial}{\partial s}\left(-\frac{(t-\bar{t}\,)}{2}h_a\left(\vec{e}_1^{\,f}\right)_3^a N_a\right) & \frac{\partial}{\partial s}\left(-\frac{(t-\bar{t}\,)}{2}h_a\left(\vec{e}_2^{\,f}\right)_3^a N_a\right) & \cdots \\
\cdots & 0 & 0 & \frac{\partial N_a}{\partial t} & \frac{\partial}{\partial t}\left(-\frac{(t-\bar{t}\,)}{2}h_a\left(\vec{e}_1^{\,f}\right)_3^a N_a\right) & \frac{\partial}{\partial t}\left(-\frac{(t-\bar{t}\,)}{2}h_a\left(\vec{e}_2^{\,f}\right)_3^a N_a\right) & \cdots
\end{bmatrix} \begin{Bmatrix} \vdots \\ u_1^a \\ u_2^a \\ u_3^a \\ \Delta\theta_1^a \\ \Delta\theta_2^a \\ \vdots \end{Bmatrix}.
$$

Noting that:

1. h_a is the nodal thickness (i.e. constant) thus its derivatives are zero,
2. the shape functions are 2D (i.e. independent of t), thus $\frac{\partial N_a}{\partial t} = 0$,
3. $\bar{t}$ is a constant and its derivatives are zero,
4. $\frac{\partial t}{\partial t} = 1$ and $\frac{\partial t}{\partial r} = \frac{\partial t}{\partial s} = 0$,

and letting:

5. $\left.\begin{matrix} g_{1i}^a = -\frac{1}{2}h_a\left(\vec{e}_1^{\,f}\right)_i^a \\ g_{2i}^a = -\frac{1}{2}h_a\left(\vec{e}_2^{\,f}\right)_i^a \end{matrix}\right\}, \quad i = 1,2,3$
6. $(t - \bar{t}) = \tilde{t},$

Equation 2.64 simplifies into:

Equation 2.65

$$\begin{Bmatrix} \frac{\partial u_1}{\partial r} \\ \frac{\partial u_1}{\partial s} \\ \frac{\partial u_1}{\partial t} \\ \frac{\partial u_2}{\partial r} \\ \frac{\partial u_2}{\partial s} \\ \frac{\partial u_2}{\partial t} \\ \frac{\partial u_3}{\partial r} \\ \frac{\partial u_3}{\partial s} \\ \frac{\partial u_3}{\partial t} \end{Bmatrix} = \begin{bmatrix} \cdots & \frac{\partial N_a}{\partial r} & 0 & 0 & \tilde{t} g_{11}^a \frac{\partial N_a}{\partial r} & \tilde{t} g_{21}^a \frac{\partial N_a}{\partial r} & \cdots \\ \cdots & \frac{\partial N_a}{\partial s} & 0 & 0 & \tilde{t} g_{11}^a \frac{\partial N_a}{\partial s} & \tilde{t} g_{21}^a \frac{\partial N_a}{\partial s} & \cdots \\ \cdots & 0 & 0 & 0 & g_{11}^a N_a & g_{21}^a N_a & \cdots \\ \cdots & 0 & \frac{\partial N_a}{\partial r} & 0 & \tilde{t} g_{12}^a \frac{\partial N_a}{\partial r} & \tilde{t} g_{22}^a \frac{\partial N_a}{\partial r} & \cdots \\ \cdots & 0 & \frac{\partial N_a}{\partial s} & 0 & \tilde{t} g_{12}^a \frac{\partial N_a}{\partial s} & \tilde{t} g_{22}^a \frac{\partial N_a}{\partial s} & \cdots \\ \cdots & 0 & 0 & 0 & g_{12}^a N_a & g_{22}^a N_a & \cdots \\ \cdots & 0 & 0 & \frac{\partial N_a}{\partial r} & \tilde{t} g_{13}^a \frac{\partial N_a}{\partial r} & \tilde{t} g_{23}^a \frac{\partial N_a}{\partial r} & \cdots \\ \cdots & 0 & 0 & \frac{\partial N_a}{\partial s} & \tilde{t} g_{13}^a \frac{\partial N_a}{\partial s} & \tilde{t} g_{23}^a \frac{\partial N_a}{\partial s} & \cdots \\ \cdots & 0 & 0 & 0 & g_{13}^a N_a & g_{23}^a N_a & \cdots \end{bmatrix} \begin{Bmatrix} \vdots \\ u_1^a \\ u_2^a \\ u_3^a \\ \Delta\theta_1^a \\ \Delta\theta_2^a \\ \vdots \end{Bmatrix}.$$

The above equation gives the derivatives with respect to the parent coordinates of the displacements that are initially obtained in the global coordinate system. In order to obtain the displacement derivatives with respect to the Cartesian global components of the position vector in the current configuration $(\text{i.e.}\ \ y_1, y_2, y_3)$, the inverse of the Jacobian transformation must be employed.

Note:

The Jacobian transformation is given as follows:

Equation 2.66

$$\begin{Bmatrix} \frac{\partial \emptyset}{\partial r} \\ \frac{\partial \emptyset}{\partial s} \\ \frac{\partial \emptyset}{\partial t} \end{Bmatrix} = \begin{bmatrix} \frac{\partial y_1}{\partial r} & \frac{\partial y_2}{\partial r} & \frac{\partial y_3}{\partial r} \\ \frac{\partial y_1}{\partial s} & \frac{\partial y_2}{\partial s} & \frac{\partial y_3}{\partial s} \\ \frac{\partial y_1}{\partial t} & \frac{\partial y_2}{\partial t} & \frac{\partial y_3}{\partial t} \end{bmatrix} \begin{Bmatrix} \frac{\partial \emptyset}{\partial y_1} \\ \frac{\partial \emptyset}{\partial y_2} \\ \frac{\partial \emptyset}{\partial y_3} \end{Bmatrix},$$

where, $\emptyset$ is the variable of interest to be transformed and the square matrix is the Jacobian $[J]$ transformation matrix for the current configuration. Here, the variables of interest are the components of displacements in the global coordinate system $(\mathrm{i.e.}\ u_1, u_2, u_3)$. Thus, the inverse of the Jacobian transformation is written as follows:

Equation 2.67

$$\begin{Bmatrix} \frac{\partial \emptyset}{\partial y_1} \\ \frac{\partial \emptyset}{\partial y_2} \\ \frac{\partial \emptyset}{\partial y_3} \end{Bmatrix} = \begin{bmatrix} \frac{\partial y_1}{\partial r} & \frac{\partial y_2}{\partial r} & \frac{\partial y_3}{\partial r} \\ \frac{\partial y_1}{\partial s} & \frac{\partial y_2}{\partial s} & \frac{\partial y_3}{\partial s} \\ \frac{\partial y_1}{\partial t} & \frac{\partial y_2}{\partial t} & \frac{\partial y_3}{\partial t} \end{bmatrix}^{-1} \begin{Bmatrix} \frac{\partial \emptyset}{\partial r} \\ \frac{\partial \emptyset}{\partial s} \\ \frac{\partial \emptyset}{\partial t} \end{Bmatrix}.$$

As mentioned earlier, the Jacobian matrix $[J]$ at the current configuration contains derivatives of the global coordinates of the position vector in the current configuration with respect to the parent coordinates (r, s, t). For simplicity, let us define J_{ij}^{-1}, the components of the inverse Jacobian $([J]^{-1})$:

Equation 2.68

$$\begin{bmatrix} \frac{\partial y_1}{\partial r} & \frac{\partial y_2}{\partial r} & \frac{\partial y_3}{\partial r} \\ \frac{\partial y_1}{\partial s} & \frac{\partial y_2}{\partial s} & \frac{\partial y_3}{\partial s} \\ \frac{\partial y_1}{\partial t} & \frac{\partial y_2}{\partial t} & \frac{\partial y_3}{\partial t} \end{bmatrix}^{-1} =: \begin{bmatrix} J_{11}^{-1} & J_{12}^{-1} & J_{13}^{-1} \\ J_{21}^{-1} & J_{22}^{-1} & J_{23}^{-1} \\ J_{31}^{-1} & J_{32}^{-1} & J_{33}^{-1} \end{bmatrix}.$$

Regrouping Equation 2.65 and applying Equation 2.67 to it gives:

$$
\begin{Bmatrix} \dfrac{\partial u_1}{\partial y_1} \\ \dfrac{\partial u_1}{\partial y_2} \\ \dfrac{\partial u_1}{\partial y_3} \end{Bmatrix} = \begin{bmatrix} J_{11}^{-1} & J_{12}^{-1} & J_{13}^{-1} \\ J_{21}^{-1} & J_{22}^{-1} & J_{23}^{-1} \\ J_{31}^{-1} & J_{32}^{-1} & J_{33}^{-1} \end{bmatrix} \begin{Bmatrix} \dfrac{\partial u_1}{\partial r} \\ \dfrac{\partial u_1}{\partial s} \\ \dfrac{\partial u_1}{\partial t} \end{Bmatrix}
$$

$$
\begin{Bmatrix} \dfrac{\partial u_2}{\partial y_1} \\ \dfrac{\partial u_2}{\partial y_2} \\ \dfrac{\partial u_2}{\partial y_3} \end{Bmatrix} = \begin{bmatrix} J_{11}^{-1} & J_{12}^{-1} & J_{13}^{-1} \\ J_{21}^{-1} & J_{22}^{-1} & J_{23}^{-1} \\ J_{31}^{-1} & J_{32}^{-1} & J_{33}^{-1} \end{bmatrix} \begin{Bmatrix} \dfrac{\partial u_2}{\partial r} \\ \dfrac{\partial u_2}{\partial s} \\ \dfrac{\partial u_2}{\partial t} \end{Bmatrix}.
$$

$$
\begin{Bmatrix} \dfrac{\partial u_3}{\partial y_1} \\ \dfrac{\partial u_3}{\partial y_2} \\ \dfrac{\partial u_3}{\partial y_3} \end{Bmatrix} = \begin{bmatrix} J_{11}^{-1} & J_{12}^{-1} & J_{13}^{-1} \\ J_{21}^{-1} & J_{22}^{-1} & J_{23}^{-1} \\ J_{31}^{-1} & J_{32}^{-1} & J_{33}^{-1} \end{bmatrix} \begin{Bmatrix} \dfrac{\partial u_3}{\partial r} \\ \dfrac{\partial u_3}{\partial s} \\ \dfrac{\partial u_3}{\partial t} \end{Bmatrix}
$$

Substituting Equation 2.65 in the above gives:

Equation 2.69

$$
\begin{Bmatrix} \dfrac{\partial u_1}{\partial y_1} \\ \dfrac{\partial u_1}{\partial y_2} \\ \dfrac{\partial u_1}{\partial y_3} \end{Bmatrix} = \begin{bmatrix} J_{11}^{-1} & J_{12}^{-1} & J_{13}^{-1} \\ J_{21}^{-1} & J_{22}^{-1} & J_{23}^{-1} \\ J_{31}^{-1} & J_{32}^{-1} & J_{33}^{-1} \end{bmatrix} \begin{bmatrix} \cdots & \dfrac{\partial N_a}{\partial r} & 0 & 0 & \tilde{t}g_{11}^a \dfrac{\partial N_a}{\partial r} & \tilde{t}g_{21}^a \dfrac{\partial N_a}{\partial r} & \cdots \\ \cdots & \dfrac{\partial N_a}{\partial s} & 0 & 0 & \tilde{t}g_{11}^a \dfrac{\partial N_a}{\partial s} & \tilde{t}g_{21}^a \dfrac{\partial N_a}{\partial s} & \cdots \\ \cdots & 0 & 0 & 0 & g_{11}^a N_a & g_{21}^a N_a & \cdots \end{bmatrix} \begin{Bmatrix} \vdots \\ u_1^a \\ u_2^a \\ u_3^a \\ \Delta\theta_1^a \\ \Delta\theta_2^a \\ \vdots \end{Bmatrix}
$$

$$
\begin{Bmatrix} \dfrac{\partial u_2}{\partial y_1} \\ \dfrac{\partial u_2}{\partial y_2} \\ \dfrac{\partial u_2}{\partial y_3} \end{Bmatrix} = \begin{bmatrix} J_{11}^{-1} & J_{12}^{-1} & J_{13}^{-1} \\ J_{21}^{-1} & J_{22}^{-1} & J_{23}^{-1} \\ J_{31}^{-1} & J_{32}^{-1} & J_{33}^{-1} \end{bmatrix} \begin{bmatrix} \cdots & 0 & \dfrac{\partial N_a}{\partial r} & 0 & \tilde{t}g_{12}^a \dfrac{\partial N_a}{\partial r} & \tilde{t}g_{22}^a \dfrac{\partial N_a}{\partial r} & \cdots \\ \cdots & 0 & \dfrac{\partial N_a}{\partial s} & 0 & \tilde{t}g_{12}^a \dfrac{\partial N_a}{\partial s} & \tilde{t}g_{22}^a \dfrac{\partial N_a}{\partial s} & \cdots \\ \cdots & 0 & 0 & 0 & g_{12}^a N_a & g_{22}^a N_a & \cdots \end{bmatrix} \begin{Bmatrix} \vdots \\ u_1^a \\ u_2^a \\ u_3^a \\ \Delta\theta_1^a \\ \Delta\theta_2^a \\ \vdots \end{Bmatrix}.
$$

$$
\begin{Bmatrix} \dfrac{\partial u_3}{\partial y_1} \\ \dfrac{\partial u_3}{\partial y_2} \\ \dfrac{\partial u_3}{\partial y_3} \end{Bmatrix} = \begin{bmatrix} J_{11}^{-1} & J_{12}^{-1} & J_{13}^{-1} \\ J_{21}^{-1} & J_{22}^{-1} & J_{23}^{-1} \\ J_{31}^{-1} & J_{32}^{-1} & J_{33}^{-1} \end{bmatrix} \begin{bmatrix} \cdots & 0 & 0 & \dfrac{\partial N_a}{\partial r} & \tilde{t}g_{13}^a \dfrac{\partial N_a}{\partial r} & \tilde{t}g_{23}^a \dfrac{\partial N_a}{\partial r} & \cdots \\ \cdots & 0 & 0 & \dfrac{\partial N_a}{\partial s} & \tilde{t}g_{13}^a \dfrac{\partial N_a}{\partial s} & \tilde{t}g_{23}^a \dfrac{\partial N_a}{\partial s} & \cdots \\ \cdots & 0 & 0 & 0 & g_{13}^a N_a & g_{23}^a N_a & \cdots \end{bmatrix} \begin{Bmatrix} \vdots \\ u_1^a \\ u_2^a \\ u_3^a \\ \Delta\theta_1^a \\ \Delta\theta_2^a \\ \vdots \end{Bmatrix}
$$

Doing the sub-matrix multiplications and letting:

$$J_{i1}^{-1}\tilde{t}\frac{\partial N_a}{\partial r}+J_{i2}^{-1}\tilde{t}\frac{\partial N_a}{\partial s}+J_{i3}^{-1}N_a=G_i^a \qquad \text{for} \quad i=1,2,3,$$

$$J_{i1}^{-1}\frac{\partial N_a}{\partial r}+J_{i2}^{-1}\frac{\partial N_a}{\partial s}=\frac{\partial N_a}{\partial y_i} \qquad \text{for} \quad i=1,2,3,$$

Equation 2.69 simplifies into:

Equation 2.70

$$\begin{Bmatrix} \frac{\partial u_1}{\partial y_1} \\ \frac{\partial u_1}{\partial y_2} \\ \frac{\partial u_1}{\partial y_3} \\ \frac{\partial u_2}{\partial y_1} \\ \frac{\partial u_2}{\partial y_2} \\ \frac{\partial u_2}{\partial y_3} \\ \frac{\partial u_3}{\partial y_1} \\ \frac{\partial u_3}{\partial y_2} \\ \frac{\partial u_3}{\partial y_3} \end{Bmatrix} = \begin{bmatrix} \cdots & \frac{\partial N_a}{\partial y_1} & 0 & 0 & g_{11}^a G_1^a & g_{21}^a G_1^a & \cdots \\ \cdots & \frac{\partial N_a}{\partial y_2} & 0 & 0 & g_{11}^a G_2^a & g_{21}^a G_2^a & \cdots \\ \cdots & \frac{\partial N_a}{\partial y_3} & 0 & 0 & g_{11}^a G_3^a & g_{21}^a G_3^a & \cdots \\ \cdots & 0 & \frac{\partial N_a}{\partial y_1} & 0 & g_{12}^a G_1^a & g_{22}^a G_1^a & \cdots \\ \cdots & 0 & \frac{\partial N_a}{\partial y_2} & 0 & g_{12}^a G_2^a & g_{22}^a G_2^a & \cdots \\ \cdots & 0 & \frac{\partial N_a}{\partial y_3} & 0 & g_{12}^a G_3^a & g_{22}^a G_3^a & \cdots \\ \cdots & 0 & 0 & \frac{\partial N_a}{\partial y_1} & g_{13}^a G_1^a & g_{23}^a G_1^a & \cdots \\ \cdots & 0 & 0 & \frac{\partial N_a}{\partial y_2} & g_{13}^a G_2^a & g_{23}^a G_2^a & \cdots \\ \cdots & 0 & 0 & \frac{\partial N_a}{\partial y_3} & g_{13}^a G_3^a & g_{23}^a G_3^a & \cdots \end{bmatrix} \begin{Bmatrix} \vdots \\ u_1^a \\ u_2^a \\ u_3^a \\ \Delta\theta_1^a \\ \Delta\theta_2^a \\ \vdots \end{Bmatrix}.$$

The linearized strains are as follows:

$$\varepsilon_{11}=\frac{\partial u_1}{\partial y_1}, \qquad \varepsilon_{22}=\frac{\partial u_2}{\partial y_2}, \qquad \varepsilon_{33}=\frac{\partial u_3}{\partial y_3},$$

$$2\varepsilon_{12}=\left(\frac{\partial u_1}{\partial y_2}+\frac{\partial u_2}{\partial y_1}\right), \qquad 2\varepsilon_{13}=\left(\frac{\partial u_3}{\partial y_1}+\frac{\partial u_1}{\partial y_3}\right), \qquad 2\varepsilon_{23}=\left(\frac{\partial u_2}{\partial y_3}+\frac{\partial u_3}{\partial y_2}\right).$$

The row ordering of $[B_L]$ is consistent with the following Voigt form of the strain vectors:

Linear strains: $\{\varepsilon\} = [\varepsilon_{11} \quad \varepsilon_{22} \quad \varepsilon_{33} \quad 2\varepsilon_{12} \quad 2\varepsilon_{13} \quad 2\varepsilon_{23}]^T.$

The column ordering of $[B_L]$ corresponds to the nodal degrees of freedom, which are:

$$[u_1^1 \quad u_2^1 \quad u_3^1 \quad \Delta\theta_1^1 \quad \Delta\theta_2^1 \quad \cdots \quad u_1^N \quad u_2^N \quad u_3^N \quad \Delta\theta_1^N \quad \Delta\theta_2^N],$$

where, the superscripts denote the node numbers.

Thus, using the displacement derivatives (Equation 2.70) and the strain vector obtained earlier, and considering the above mentioned descriptions regarding the row and column ordering of $[B_L]$, the linear strain-displacement transformation matrix is assembled to give:

$$[B_L] = \begin{array}{c} \begin{array}{ccccccc} \cdots & u_1^a & u_2^a & u_3^a & \Delta\theta_1^a & \Delta\theta_2^a & \cdots \end{array} \\ \begin{bmatrix} \cdots & \dfrac{\partial N_a}{\partial y_1} & 0 & 0 & g_{11}^a G_1^a & g_{21}^a G_1^a & \cdots \\ \cdots & 0 & \dfrac{\partial N_a}{\partial y_2} & 0 & g_{12}^a G_2^a & g_{22}^a G_2^a & \cdots \\ \cdots & 0 & 0 & \dfrac{\partial N_a}{\partial y_3} & g_{13}^a G_3^a & g_{23}^a G_3^a & \cdots \\ \cdots & \dfrac{\partial N_a}{\partial y_2} & \dfrac{\partial N_a}{\partial y_1} & 0 & g_{11}^a G_2^a + g_{12}^a G_1^a & g_{21}^a G_2^a + g_{22}^a G_1^a & \cdots \\ \cdots & \dfrac{\partial N_a}{\partial y_3} & 0 & \dfrac{\partial N_a}{\partial y_1} & g_{11}^a G_3^a + g_{13}^a G_1^a & g_{21}^a G_3^a + g_{23}^a G_1^a & \cdots \\ \cdots & 0 & \dfrac{\partial N_a}{\partial y_3} & \dfrac{\partial N_a}{\partial y_2} & g_{12}^a G_3^a + g_{13}^a G_2^a & g_{22}^a G_3^a + g_{23}^a G_2^a & \cdots \end{bmatrix} \end{array} \begin{array}{c} \\ \varepsilon_{11} \\[2ex] \varepsilon_{22} \\[2ex] \varepsilon_{33} \\[2ex] 2\varepsilon_{12} \\[2ex] 2\varepsilon_{13} \\[2ex] 2\varepsilon_{23} \end{array}$$

where,

$$\left.\begin{aligned} g_{1i}^a &= -\frac{1}{2} h_a \left(\vec{e}_1^{\,f}\right)_i^a \\ g_{2i}^a &= -\frac{1}{2} h_a \left(\vec{e}_2^{\,f}\right)_i^a \end{aligned}\right\} \qquad \text{for} \quad i = 1, 2, 3,$$

$$G_i^a = J_{i1}^{-1}\tilde{t}\frac{\partial N_a}{\partial r} + J_{i2}^{-1}\tilde{t}\frac{\partial N_a}{\partial s} + J_{i3}^{-1} N_a \qquad \text{for} \quad i = 1, 2, 3.$$

Note that in Bathe and Bolourchi's formulations:

1. the strain-displacement transformation matrices obtained are based on the co-rotational coordinate system assumption, resulting in small rotational strains;

2. the column ordering of $[B_L]$ corresponds to the nodal displacements and nodal fiber rotations in the global coordinate system (i.e. $[\cdots \quad u_1^a \quad u_2^a \quad u_3^a \quad \Delta\theta_1^a \quad \Delta\theta_2^a \quad \cdots]$).

2.5.3 Summary of the pros and cons of the existing CB shell elements

The preceding discussion makes it possible to pinpoint the pros and cons of the CB shell elements that are most closely pertinent to the present work:

<u>Huges and Liu shell theory (Section 2.5.1):</u>

- Pros:
  - allows large rotational strain, because the lamina coordinate system is not co-rotational to the fiber coordinate system,
- Cons:
  - uses rate-form constitutive equations, which is beneficial for elastic-plastic deformations, but not for hyperelastic materials,
  - the material matrices are obtained for the rate constitutive equations,
  - the material matrices are not compatible with the finite element formulation presented in Section 2.2.4.

<u>Bathe and Bolourchi shell theory (Section 2.5.2):</u>

- Pros:
  - the material matrices are compatible with the finite element formulation presented in Section 2.2.4.
- Cons:
  - assumes fibers remain straight and normal thus assumes the lamina coordinate system to be co-rotational with the fiber one. Therefore does not admit any transverse shears (Belytschko et al., 2000).

Finally, as can be seen, there is no point in using open source software because the shell theory that we most need (or anything somewhat resembling) has not been developed or implemented yet.

2.6 Measures of deformation in the global coordinate system

2.6.1 Deformation gradient

The deformation gradient of the current configuration with respect to the reference configuration in the global coordinate system is basically the derivatives of the current position vector with respect to the reference position vector: ${}^{\tau}_{\beta}\bar{\bar{F}} = \partial\, {}^{\tau}\vec{y}(r,s,t)/\partial\, {}^{\beta}\vec{y}(r,s,t)$, which, in the indicial notations is written as:

Equation 2.71

$$ {}^{\tau}_{\beta}F_{ij} = \frac{\partial\, {}^{\tau}y_i(r,s,t)}{\partial\, {}^{\beta}y_j(r,s,t)}. $$

Considering that the position vector is a function of the parent coordinate system (Equation 2.33), the above partial derivative must be performed through the chain rule. Recalling from Equation 2.66 that the Jacobian contains the partial derivatives of the position vector (at any time configuration) with respect to the parent coordinate system:

$$ [J] = \begin{bmatrix} \frac{\partial y_1}{\partial r} & \frac{\partial y_2}{\partial r} & \frac{\partial y_3}{\partial r} \\ \frac{\partial y_1}{\partial s} & \frac{\partial y_2}{\partial s} & \frac{\partial y_3}{\partial s} \\ \frac{\partial y_1}{\partial t} & \frac{\partial y_2}{\partial t} & \frac{\partial y_3}{\partial t} \end{bmatrix}, $$

the partial derivatives in Equation 2.71 are evaluated from:

Equation 2.72

$$ \left[{}^{\tau}_{\beta}F\right] = [\,{}^{\tau}J]^{T}\left[{}^{\beta}J\right]^{-T}. $$

In the above equation, $\left[{}^{\beta}J\right]$ and $[\,{}^{\tau}J]$ denote the Jacobian in the reference and the current configurations, respectively.

2.6.2 Right and left Cauchy-Green tensor

The right Cauchy-Green tensor in the global coordinate system is obtained from:

Equation 2.73

$$\left[{}_{\beta}^{\tau}C\right] = \left[{}_{\beta}^{\tau}F\right]^{T}\left[{}_{\beta}^{\tau}F\right].$$

Similarly, the left Cauchy-Green tensor in the global coordinate system is obtained from:

Equation 2.74

$$\left[{}_{\beta}^{\tau}B\right] = \left[{}_{\beta}^{\tau}F\right]\left[{}_{\beta}^{\tau}F\right]^{T}.$$

In the above equations, the left superscript τ denotes the current configuration, and the left subscript β denoting the reference configuration, is replaced by 0 in the total UL formulation (Equation 3.1), and by $\tau - \Delta\tau$ in the incremental UL formulation (Equation 3.2).

2.6.3 Green-Lagrange and Almansi strain tensors

The global Green-Lagrange strain tensor defined in the current configuration τ with respect to the reference configuration β is evaluated from:

Equation 2.75

$$\left[{}_{\beta}^{\tau}E\right] = \frac{1}{2}\left(\left[{}_{\beta}^{\tau}C\right] - [I]\right).$$

The global Almansi strain tensor in the current configuration is evaluated from:

Equation 2.76

$$\left[{}_{\tau}\varepsilon\right] = \frac{1}{2}\left([I] - \left[{}_{\beta}^{\tau}B\right]^{-1}\right).$$

2.7 Anisotropic nonlinear hyperplastic constitutive relations, incompressibility, and application of zero normal stress condition

An elastic material is determined both by physical and mathematical definitions. Physically, a material is called elastic if:

1) under applied loads, the material stores energy but does not dissipate it,
2) the material returns to its original shape once the load is removed,
3) its constitutive behavior depends only on the current state of deformation.

A material is called hyperelastic if (Belytschko et al., 2000; Holzapfel G., 2000):

1) the work done, by stresses, during a deformation is dependent only on the initial (β_0) and final configurations (β_t),
2) the behavior of the material (as a result of the above statement) is path-independent.

Therefore, the work done by the stresses from the initial to the final (current) configuration can be represented by means of a stored strain energy function (per unit undeformed volume). Note that from a mathematical point of view, a hyperelastic material is such that a strain energy function W can be defined; then differentiating the strain energy function with respect to strains yields the stresses in the material, and thus, completely describes the material behavior.

For constant temperature transformations, the Helmholtz potential and strain energy function are related by (Holzapfel G., 2000):

Equation 2.77

$$\rho_0 \psi(\bar{\bar{F}}) = W(\bar{\bar{F}}),$$

where ψ is defined per unit mass and W is defined per unit initial volume as the strain energy function. However, Equation 2.77 is based on the deformation gradient $\bar{\bar{F}}$ and hence may contain rigid body rotations. Therefore, it is more convenient to exclude the rigid body rotations by employing $\bar{\bar{C}}$ instead of $\bar{\bar{F}}$, such that:

$$\psi = \psi(\bar{\bar{C}}) \qquad \text{and} \qquad W = W(\bar{\bar{C}}).$$

If incompressibility is assumed, then the incompressibility condition $\left(\det \bar{\bar{F}} = J = 1\right)$ must be added as a constraint on the strain energy function. There are different ways of enforcing incompressibility depending on the type of the element (3D solid, membrane, or shell). For example, if a 3D element is considered, the nodal displacements and pressures may be separately interpolated, and the effect of interpolated pressure may be added as an extra term in the strain energy function. This approach, called mixed pressure-displacement (u/p) formulation, is adopted in many references (Sussman and Bathe, 1987; Bathe, 1996; Weinberg and Kaasempur-Mofrad, 2006). On the other hand, in case of membrane or shell elements, if the strain energy function is dependent on the deformation gradient, then the general strain energy function can be modified for incompressibility as in (Belytschko et al., 2000; Holzapfel G., 2000; Guccione et al., 1990; Kiendl et al., 2015; and many more):

Equation 2.78

$$\widetilde{W} = W(\bar{\bar{F}}) - p(\det\bar{\bar{F}} - 1),$$

where p is a Lagrange multiplier enforcing $\det\bar{\bar{F}} = 1$, and the deformation gradient is obtained due to the distortional effects only.

A general constitutive equation for the ***first Piola-Kirchhoff*** **(**or nominal**)** ***stress tensor*** $\bar{\bar{P}}$ (that is force measured per unit area in the undeformed configuration) is obtained by differentiating the strain energy function with respect to the deformation gradient. Thus, differentiating Equation 2.78 with respect to $\bar{\bar{F}}$ gives:

$$\bar{\bar{P}} = \frac{\partial\widetilde{W}}{\partial\bar{\bar{F}}^{\,T}} = \left(\frac{\partial W(\bar{\bar{F}})}{\partial\bar{\bar{F}}^{\,T}} - p\frac{\partial(\det\bar{\bar{F}} - 1)}{\partial\bar{\bar{F}}^{\,T}}\right) = \left(\frac{\partial W}{\partial\bar{\bar{F}}^{T}} - p(\det\bar{\bar{F}})\bar{\bar{F}}^{-1}\right).$$

Knowing that $\det\bar{\bar{F}} = J = 1$, the above simplifies to:

Equation 2.79

$$\bar{\bar{P}} = \left(\frac{\partial W}{\partial\bar{\bar{F}}^{T}} - p\bar{\bar{F}}^{-1}\right).$$

Noting that (Belytschko et al., 2000),

Equation 2.80

$$\frac{\partial W}{\partial\bar{\bar{F}}^{T}} = 2\frac{\partial W}{\partial\bar{\bar{C}}}\cdot\bar{\bar{F}}^{T},$$

Equation 2.81

$$\bar{\bar{P}} = \left(2\frac{\partial W}{\partial\bar{\bar{C}}}\cdot\bar{\bar{F}}^{T} - p\bar{\bar{F}}^{-1}\right).$$

Furthermore, the ***Cauchy*** *(or true)* ***stress tensor*** $\bar{\bar{t}}$ (force measured per unit area in the current configuration) can be determined by:

Equation 2.82

$$\bar{\bar{t}} = \frac{1}{J}\,\bar{\bar{F}}.\bar{\bar{P}}\ .$$

Substituting Equation 2.81 into Equation 2.82, the Cauchy stress tensor in terms of strain energy function is obtained as:

Equation 2.83

$$\bar{\bar{t}} = -p\bar{\bar{I}} + 2\bar{\bar{F}} \cdot \frac{\partial W}{\partial \bar{\bar{C}}} \cdot \bar{\bar{F}}^T.$$

Likewise, the ***second Piola-Kirchhoff stress tensor*** can be obtained by:

Equation 2.84

$$\bar{\bar{S}} = J\ \bar{\bar{F}}^{-1} \cdot \bar{\bar{t}} \cdot \bar{\bar{F}}^{-T}.$$

Substituting Equation 2.83 into Equation 2.84, the second Piola-Kirchhoff stress tensor in terms of the strain energy becomes:

Equation 2.85

$$\bar{\bar{S}} = -p\bar{\bar{C}}^{-1} + 2\,\frac{\partial W}{\partial \bar{\bar{C}}},$$

in which, the first and second terms on the RHS represents the volumetric and distortional components of $\bar{\bar{S}}$ respectively.

In the above formulations, the Lagrange multiplier p is an additional unknown that is associated with the incompressibility constraint (i.e. $\det\bar{\bar{F}} = J = 1$) and represents a contribution to the hydrostatic stress (Equation 2.85). Kiendl et al. (2015) solve for the Lagrange multiplier within the context of thin shells by analytically enforcing the necessary plane stress condition for incompressibility. In this formulation, although they claim to use general 3D constitutive models, consistent with any thin shells (i.e. Kirchhoff-Love based shell formulations), the transverse shear strains are neglected, and the transverse normal strain E_{33}, which cannot be neglected in the case of large strains, is statically condensed using the plane stress condition. According to Holzapfel and Ogden (2009), the thin sheet or “membrane” approximation allows to set the transverse normal stress to zero ($S_{33} = S_{13} = S_{23} = 0$), which enable solving for the Lagrange multiplier p. Hence p can be eliminated from the other stress terms (Equation 2.85). It is important to emphasize that these equations are 2D specializations within the framework of a 3D theory and should be distinguished from equations based on a fundamentally 2D theory. In a 2D theory a significant part of the 3D constitutive law is missing. It is important to note that a 2D form of W does not distinguish between compressible and incompressible materials. In a 2D material model, W does not depend on E_{33} and thus $\partial W/\partial E_{33} = 0$ but it does not determine the three-dimensional properties of the material since the dependence of W on E_{33} is not provided.

From a different point of view, the additive decomposition of the strain-energy function into volumetric and deviatoric (distortional) parts (Equation 2.78, and consequently Equation 2.85) is essentially an isotropic condition, and is appropriate for pure hydrostatic tension only (Ni Annaidh et al., 2013). Thus, its generalization to anisotropic materials is not adequate, considering the corresponding physics. The arguments above suggest that, despite its intuitive appeal, it should not be employed when modeling nonlinear, anisotropic materials which are characterized by infinitesimal volume changes when deformed. Certainly, its equivalent formulation in terms of stresses (application of the zero normal stress condition) does not seem a natural or appropriate constitutive assumption to make when modeling the slight compressibility of anisotropic materials. Thus, a formulation of the theory that accounts for infinitesimal volume changes in a physically realistic way is badly needed. We will solve this issue in Section 3.10.1.

2.8 Shear and membrane locking

According to the literature (Ahmad et al., 1970; Hughes and Liu, 1980; Belytschko et al., 2000), shear and membrane lockings are two of the most troublesome characteristics of shell elements.

2.8.1 Shear locking

Shear locking occurs when significant bending is present. It is owed to the use of linear shape functions that cannot accurately model the curvature that is present in the actual material under bending. Instead, a shear stress is introduced which causes the element to reach equilibrium conditions for smaller displacements than the real ones. Therefore, the element appears stiffer than it should be.

In more technical terms, shear locking is a result of the false appearance of transverse shear strains. Indeed, shear locking arises from the inability of many elements to represent deformations in which transverse shear strain should vanish. According to Belytschko et al., (2000): "*Since the shear stiffness is often significantly greater than the bending stiffness, the fake* *shear absorbs a larger part of energy imparted by the external forces and the predicted deflections and strains are much too small*." This is where the name shear locking is originated from.

As described in Section 2.4.1, normals to the midsurface of thin beams and shells remain straight and normal, and as a result, transverse shear strains vanish. This behavior can be thought of as a constraint on the motion of the continuum. In shear-beam or Mindlin-Reissner shell theories (Section 2.4.2), normals remain straight but are allowed to rotate (i.e. the angle between the fiber and midsurface changes) and transverse shear strains do not vanish. Therefore, enforcing the normality constraint in the aforementioned elements results in a penalty term in the energy which appears as a shear energy. As the shell thickness decreases, the penalty factor increases and thus shear locking becomes more prominent (Belytschko et al., 2000). Then, CB shell elements used in thin shell applications exhibit shear locking and special numerical treatments are needed to prevent this phenomenon.

2.8.2 Membrane locking

Membrane locking is due to the inability of shell finite elements to represent inextentional modes of deformation. Shells, just like a piece of paper, should be able to bend without necessarily stretching. This is called inextentional bending. However, stretching a piece of paper by hand is almost impossible. Shells behave similarly: their bending stiffness is small but their membrane stiffness is large. When the finite element cannot bend without stretching, the energy is incorrectly shifted to membrane energy, resulting in underprediction of displacements and strains, otherwise known as membrane locking. This phenomenon is particularly important in simulation of buckling (Belytschko et al., 2000), because many buckling modes are completely or nearly inextensional.

2.8.3 Summary of shear and membrane locking

Table 2.3 provides a sumary of the locking type expected once a finite element is unable to represent deformations satisfying the assumed constraint.

Table 2.3: Analogy of locking phenomena (Belytschko et al., 2000).

Constraint	Shortcoming of finite element motion	Locking type
Kirchhoff-Love constraint (Zero transverse shear strains)	Transverse shear strain appears in pure bending	Shear locking
Inextensibility constraint	Membran strain appears in inextensional bending mode	Membrane locking

2.9 Summary

As a quick summary to Chapter 2, it appears there is no commercial or open source finite element code that can entirely fulfill our requirements (Section 2.3.3). Therefore, it is easier to program something from scratch. Although none of the existing CB shell elements have all the kinematic and kinetic capabilities we are looking for, there are some CB shell elements that we can get inspiration from (Section 2.5.3) to develop a new CB shell FE. To allow for modeling incompressible anisotropic hyperelastic material properties and enforcing the zero normal stress condition, a new approach is needed such that the 3D nature of the constitutive relations can be preserved (Section 2.7).

CHAPTER 3: DEVELOPMENT OF A NEW THICK CONTINUUM-BASED SHELL FINITE ELEMENT WITH SPECIAL MANAGEMENT OF CONSTITUTIVE RELATIONS

As mentioned earlier, our goal is to develop a shell element for anisotropic nearly incompressible hyperelastic soft tissue dynamics. Through the process of shell element development, the following assumptions must be satisfied:

- nonlinear, 3D, large strain and large rotation effects,
- zero normal stress condition in the lamina coordinate system,
- fiber inextensibility in the fiber coordinate system.

To combine the advantages of the two methods detailed previously, and mitigate their shortcomings, the development follows the procedure below:

- implement Hughes and Liu's kinematic description so that large rotational strains are included,
- modify Bathe and Bolourchi's kinetic description to obtain the "standard" material matrices used in finite element formulations,
- implement the shell using the nonlinear UL formulation as described in Section 2.2.4.

Such a procedure requires the following important questions to be addressed:

1. The strain-displacement transformation matrix obtained by Bathe and Bolourchi relates the strains to the displacements with respect to the global and fiber coordinate systems. This relation needs to be established for the displacements of the nodes with respect to the lamina coordinate system, because the constitutive equations must be applied in the lamina coordinate system. Therefore one questions arises: How to obtain $[B_L]$ for the lamina coordinate system?
2. How to develop the hyperelastic nonlinear anisotropic constitutive relations in the lamina coordinate system?
3. How to develop hyperelastic nonlinear anisotropic constitutive relations for UL formulation as opposed to the existing TL formulations?
4. How to apply the plane stress condition in the lamina coordinate system?
5. How to enforce incompressibility?
6. How to apply the fiber inextensibility in the fiber coordinate system?
7. How to account for the change in shell thickness due to large membrane strains?
8. How to prevent the shear and membrane locking effects?

Solutions to the abovementioned questions are presented in the following sections.

3.1 Total and incremental updated Lagrangian formulation using explicit time integration

The advantages inherent to the updated Lagrangian formulation using the central difference (explicit) time integration have been discussed in Sections 2.2.5 and 2.2.6. In the following, more insights on the specific forms of the updated Lagrangian formulation, and the corresponding adjustments to the central difference operator, are provided.

As mentioned earlier, the necessary requirement for the UL formulation is to have the derivatives taken with respect to the current configuration. In some of the published works, (Bathe et al., 1975; Bathe and Bolourchi, 1979; Bathe et al., 1983; Dvorkin and Bathe, 1984; Bucalem and Bathe, 1993; Dvorkin, 1995; Bathe, 1996), although the stresses and material property matrix are derived with respect to the current configuration (as needed for the calculation of the internal forces) and the volume integrations are performed over the current geometry, the reference configuration used for the applied forces and displacements is the initial (undeformed) configuration. The rationale behind this formulation (which we refer to as the total UL formulation) is to have a convenient way of transforming the stresses and strains from the total UL to the TL formulation, and vice-versa, for verification purposes. In a different approach, which we refer to as the incremental UL formulation, the stresses, the material property matrix, and the volume integrations are all determined in the current configuration, and the external forces and the displacements are measured from the previous configuration in time (Belytschko, 2000).

The equilibrium of the finite element system in the central difference explicit operator is considered at time τ and the displacement increments from the reference configuration to time $\tau + \Delta\tau$ are computed using the incremental displacements obtained in the previous two time steps. We write this for the total and the incremental UL formulations, by substituting the proper time configuration for the left subscripts in Equation 2.32, respectively as:

Equation 3.1

$$\left\{{}^{\tau+\Delta\tau}_{0}u\right\} = \frac{\Delta\tau^2}{\left[\,{}^{\tau}M_{ii}\right]}\left(\left\{{}^{\tau}_{0}R\right\} - \left\{{}^{\tau}_{\tau}F\right\}\right) + 2\left\{{}^{\tau}_{0}u\right\} - \left\{{}^{\tau-\Delta\tau}_{0}u\right\},$$

Equation 3.2

$$\left\{{}^{\tau+\Delta\tau}_{\tau}u\right\} = \frac{\Delta\tau^2}{\left[\,{}^{\tau}M_{ii}\right]}\left(\left\{{}^{\tau}_{\tau-\Delta\tau}R\right\} - \left\{{}^{\tau}_{\tau}F\right\}\right) + 2\left\{{}^{\tau}_{\tau-\Delta\tau}u\right\} - \left\{{}^{\tau-\Delta\tau}_{\tau-2\Delta\tau}u\right\},$$

where

- the total and incremental displacement vectors, $\left\{{}^{\tau+\Delta\tau}_{0}u\right\}$ and $\left\{{}^{\tau+\Delta\tau}_{\tau}u\right\}$, can be solved for directly (explicitly),
- a lumped mass matrix $[\,{}^{\tau}M_{ii}]$ is required for simple solution,
- $\{{}^{\tau}_{0}R\}$ and $\{{}^{\tau}_{\tau-\Delta\tau}R\}$ are the total and the incremental external force vectors, respectively,
- $\{{}^{\tau}_{\tau}F\}$ is the internal force vector at the current configuration,
- time steps $(\Delta\tau)$ smaller than the critical time step are required to maintain stability.

3.2 Geometric and kinematic descriptions

As mentioned previously, fibers are required to remain straight but not normal to the surface of the shell. Thus, we employ Hughes and Liu's approach for the definition of the geometry and kinematics of the element (Section 2.5.1.1). In this section, the adjustment necessary for modeling large in-plane strains is discussed.

The continuum representation of the geometry in any configuration is defined as:

Equation 3.3

$${}^{\beta}y(r,s,t) = \sum_{a=1}^{n_{en}} N_a(r,s)\,{}^{\beta}\bar{y}_a + \frac{(t-\bar{t})}{2}\sum_{a=1}^{n_{en}} N_a(r,s)\ {}^{\beta}h_a\ {}^{\beta}\hat{Y}_a\,,$$

where

the initial and the current configurations are represented by $\beta = 0$ and $\beta = \tau$ respectively,

${}^{\beta}\bar{y}_a$: is the position vector of a nodal point *a* on the reference surface in configuration β,

$N_a(r,s)$: is the 2D shape function associated with node a,

n_{en}: is the number of element nodes,

${}^{\beta}\hat{Y}_a$: is director emanating from node a in configuration β,

${}^{\beta}h_a$: is the nodal fiber length in configuration β.

The kinematic expressions can be easily obtained by replacing the displacement variables with the coordinate variables of Equation 3.3. This gives:

Equation 3.4

$$ {}^{\tau+\Delta\tau}_{\beta}u(r,s,t) = \sum_{a=1}^{n_{en}} N_a(r,s)\,{}^{\tau+\Delta\tau}_{\beta}\bar{u}_a + \frac{(t-\bar{t})}{2}\sum_{a=1}^{n_{en}} N_a(r,s)\,{}^{\tau+\Delta\tau}h_a\,{}^{\tau+\Delta\tau}_{\beta}\hat{U}_a, $$

where the left subscript β denoting the reference configuration, is replaced by 0 in the total UL formulation (Equation 3.1), and τ in the incremental UL formulation (Equation 3.2), respectively. In addition,

${}^{\tau+\Delta\tau}_{\beta}\bar{u}_a$: is the displacement of a node in the reference surface from the reference configuration (β) to the configuration at time $\tau+\Delta\tau$,

${}^{\tau+\Delta\tau}_{\beta}\hat{U}_a$: is the displacement of a director (in terms of rotations) at a specific node from configurations β to $\tau+\Delta\tau$,

${}^{\tau+\Delta\tau}h_a$: is the nodal fiber length in the configuration at time $\tau+\Delta\tau$.

The derivation of the displacement of a director at a specific node is detailed in Section 2.5.1.3. Having the notations adjusted to the present formulation, ${}^{\tau+\Delta\tau}_{\beta}\hat{U}_a$ is obtained from ${}^{\tau+\Delta\tau}_{\beta}\hat{U}_a = {}^{\tau+\Delta\tau}\hat{Y}_a - {}^{\beta}\hat{Y}_a$, where

$$ {}^{\tau+\Delta\tau}\hat{Y}_a = \frac{\left({}^{\beta}\hat{Y}_a + {}^{\tau+\Delta\tau}_{\beta}\hat{U}_a^{trial}\right)}{\left\|{}^{\beta}\hat{Y}_a + {}^{\tau+\Delta\tau}_{\beta}\hat{U}_a^{trial}\right\|}, $$

and the trial value of the displacement of a director at a specific node (${}^{\tau+\Delta\tau}_{\beta}\hat{U}_a^{trial}$) is obtained from:

$$\begin{Bmatrix} \left({}^{\tau+\Delta\tau}_{\beta}\widehat{U}_1^{trial} \right)_a \\ \left({}^{\tau+\Delta\tau}_{\beta}\widehat{U}_2^{trial} \right)_a \\ \left({}^{\tau+\Delta\tau}_{\beta}\widehat{U}_3^{trial} \right)_a \end{Bmatrix} = \left[{}^{\beta}s^a \right] \begin{bmatrix} -1 & 0 \\ 0 & -1 \\ 0 & 0 \end{bmatrix} \begin{Bmatrix} {}^{\tau+\Delta\tau}_{\beta}\theta_1 \\ {}^{\tau+\Delta\tau}_{\beta}\theta_2 \end{Bmatrix} = \begin{bmatrix} -\left({}^{\beta}\vec{e}_1^{\,f} \right)_1^a & -\left({}^{\beta}\vec{e}_2^{\,f} \right)_1^a \\ -\left({}^{\beta}\vec{e}_1^{\,f} \right)_2^a & -\left({}^{\beta}\vec{e}_2^{\,f} \right)_2^a \\ -\left({}^{\beta}\vec{e}_1^{\,f} \right)_3^a & -\left({}^{\beta}\vec{e}_2^{\,f} \right)_3^a \end{bmatrix} \begin{Bmatrix} {}^{\tau+\Delta\tau}_{\beta}\theta_1^a \\ {}^{\tau+\Delta\tau}_{\beta}\theta_2^a \end{Bmatrix}.$$

Ultimately, the position vector of a generic point of the shell at time $\tau + \Delta\tau$ is obtained by adding the position vector (Equation 3.3) to the displacement vector (Equation 3.4), as ${}^{\tau+\Delta\tau}y(r,s,t) = {}^{\tau}y(r,s,t) + {}^{\tau+\Delta\tau}_{\beta}u(r,s,t)$. This can equivalently be written as:

Equation 3.5

$${}^{\tau+\Delta\tau}y(r,s,t) = \sum_{a=1}^{n_{en}} N_a(r,s)\,{}^{\tau+\Delta\tau}\bar{y}_a + \frac{(t-\bar{t})}{2} \sum_{a=1}^{n_{en}} N_a(r,s)\;{}^{\tau+\Delta\tau}h_a\;{}^{\tau+\Delta\tau}\widehat{Y}_a\,.$$

A quick comparison between Equation 3.3 and Equation 3.5 suggests that:

$${}^{\tau+\Delta\tau}h_a\;{}^{\tau+\Delta\tau}\widehat{Y}_a = {}^{\beta}h_a\;{}^{\beta}\widehat{Y}_a + {}^{\tau+\Delta\tau}h_a\,{}^{\tau+\Delta\tau}_{\beta}\widehat{U}_a.$$

However, according to Figure 3.1, this relation is off by ${}^{\tau+\Delta\tau}_{\beta}h_a\;{}^{\beta}\widehat{Y}_a$, in which ${}^{\tau+\Delta\tau}_{\beta}h_a$ refers to the change in fiber length from the reference configuration β to the configuration at time $\tau + \Delta\tau$. This effect is understated in small membrane strain applications, and thus has been neglected in the literature. However, if large membrane strains are to be considered, the nodal point fiber lengths at time $\tau + \Delta\tau$ need to be calculated, and Equation 3.3 re-evaluated using (${}^{\beta}h_a = {}^{\beta}h_a + {}^{\tau+\Delta\tau}_{\beta}h_a$). The algorithm for calculating the fiber lengths at $\tau + \Delta\tau$ will be presented in Section 3.11.

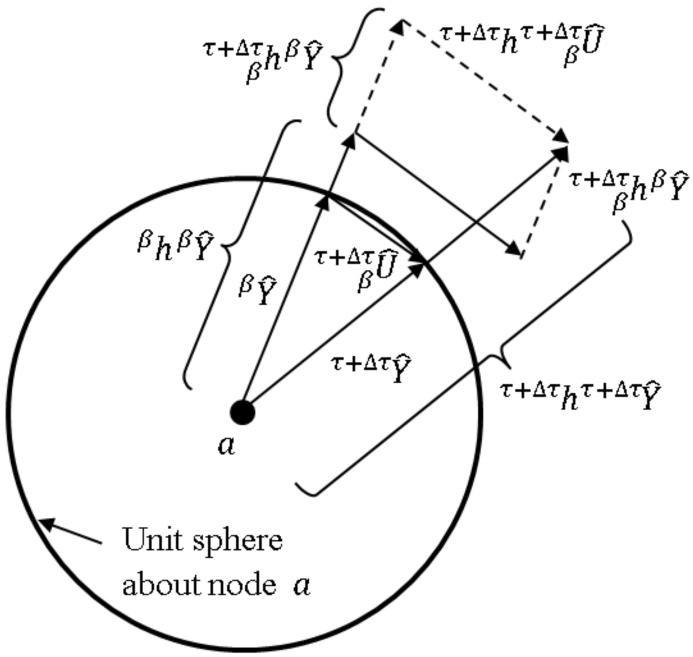

Figure 3.1: Kinematics. Right subscripts a denoting the node number are dropped for convenience.

3.3 Coordinate systems

Although the corotational system (as employed by Bathe and Bolourchi) is computationally more efficient than using multiple coordinate systems (employed by Hughes and Liu), we use multiple coordinate systems to be able to address the following requirements:

- large strains and large rotational strains,
- zero normal stress condition (to be applied in the lamina coordinate system),
- fiber inextensibility (to be applied in the fiber coordinate system).

The derivation of the lamina coordinate system presented in Section 2.5.1.2.2 is general and efficient for any type of analysis. However, we discovered that the algorithm to obtain the fiber coordinate system presented in Section 2.5.1.2.3 is limited to deflections (bending deformations) that are smaller than 90°. This limitation is discussed, and a new robust algorithm is presented in the following sections.

3.3.1 Limitation of the fiber coordinate system presented in Section 2.5.1.2.3

We now demonstrate that the algorithm to obtain the fiber coordinate system presented in Section 2.5.1.2.3 is limited to deflections (bending deformations) that are smaller than 90°. Namely, if the bending deformation exceeds 90°, the algorithm of Section 2.5.1.2.2 results in a flip in the orientation of $\vec{e}_1^{\,f}$ and $\vec{e}_2^{\,f}$ (Figure 3.2). This limitation ruins the application of the boundary conditions as well as the evaluation of the force and displacement vectors. As an example, let us assume a pure bending moment about the $\vec{e}_2^{\,f}$ axis at the right edge in the initial configuration (Figure 3.2, left). The direction of this bending moment is expected to be preserved throughout the analysis. However, once the deflection becomes 90°, the flip in the orientation of $\vec{e}_1^{\,f}$ and $\vec{e}_2^{\,f}$ results in a twisting moment, as opposed to the intended bending moment.

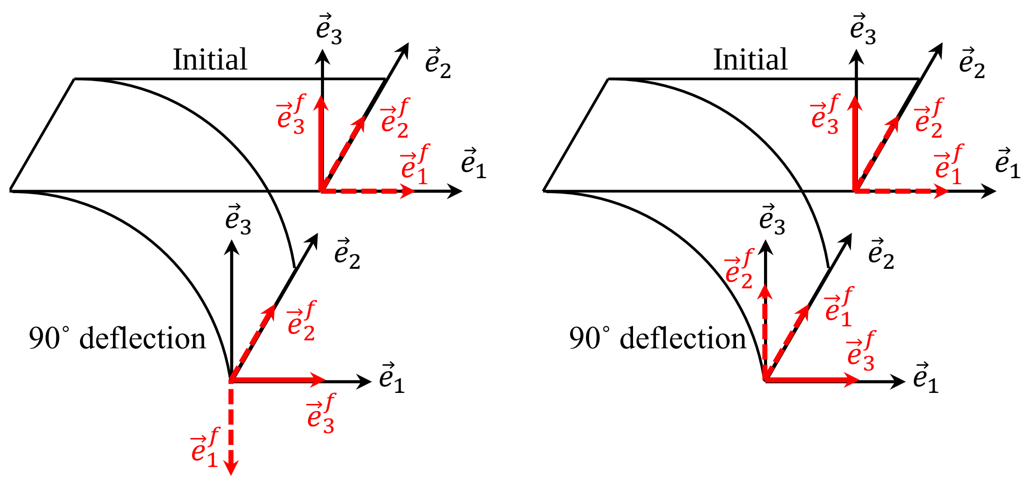

Figure 3.2: Left: physically expected rotation of the fiber coordinate system as the element deflects. Right: Fiber coordinate system at the 90° deflection of the element obtained from the algorithm presented in Section 2.5.1.2.3, changes orientation from that of the initial configuration.

3.3.2 A new algorithm for fiber coordinate system

Considering that we are interested in large bending deformations and large rotations, modifications are needed such that even with the possibility of rotations larger than 90 degrees, the fiber coordinate system preserves its physically expected orientation (Figure 3.2, right). Such consideration disqualifies the employment of the global Cartesian coordinate system, stationary by definition, in the cross product of *Step 6* of the algorithm presented in Section 2.5.1.2.2. Instead, a coordinate system whose rotational displacement, due to deformation, is similar to that of the fiber is required. To avoid adding up to the number of coordinate systems in questions, we suggest two approaches:

1) use the current lamina coordinate system as a reference to obtain the other two bases of the fiber coordinate system when $\hat{Y} = \vec{e}_3^{\,f}$ is known,
2) use the fiber coordinate system of the previous time step as the reference.

In the first approach, the fiber $\hat{Y}$ must be transformed to the lamina coordinate system such that:

$\hat{Y}^l = \left|\hat{Y}_1^l\right|\vec{e}_1^{\,l} + \left|\hat{Y}_2^l\right|\vec{e}_2^{\,l} + \left|\hat{Y}_3^l\right|\vec{e}_3^{\,l}.$

This needs to be followed by Steps 1 to 7 presented in Section 2.5.1.2.3. The only modification takes place in Step 6, in which, the appropriate base of the lamina coordinate system must be considered in the cross product. This approach adds up to the numerical complexity.

In the second approach, knowing that in the UL formulation, the increments in rotations (${}_{\tau-\Delta\tau}^{\tau}\theta_1^a$ and ${}_{\tau-\Delta\tau}^{\tau}\theta_2^a$) are small; j is always equal to 1, and Steps 1, 3 and 4 can be abandoned. In addition, Step 6 is modified such that $\vec{e}_1^{\,f}$ of the previous time step is used in the cross product instead of $\vec{e}_j$. This approach results in simplifications in the algorithm of Section 2.5.1.2.2. To initialize the solution scheme (i.e. for the first time step), the fiber coordinate system can be set to be equal to the already calculated lamina coordinate system.

We employed the second approach due to its numerical efficiency.

3.4 Nodal degrees of freedom

As discussed in Section 2.5.1.4, to avoid the need for inclusion of artificial in-plane torsional stiffness, the rotation about the fiber is eliminated. Thus, 5 degrees of freedom per node are considered.

3.5 Transformation matrices

As illustrated in Figure 2.13, the following relationship holds between the three coordinate systems: $[r] = [q][s]$, where $[q] = [\vec{e}_1^{\,l} \quad \vec{e}_2^{\,l} \quad \vec{e}_3^{\,l}]^T$, and $[s] = \left[\vec{e}_1^{\,f} \quad \vec{e}_2^{\,f} \quad \vec{e}_3^{\,f}\right]$. Thus, $[r] = \left[r_{ij}\right]$; $r_{ij} = \vec{e}_i^{\,l} \cdot \vec{e}_j^{\,f}$.

Note that these transformation matrices must be updated at each new configuration (i.e. time steps).

3.6 Jacobians

The mapping between the isoparametric element (defined by the natural or parent coordinate system) and the physical shell element (in the Cartesian coordinate system) is represented by Jacobian. The Jacobian at any configuration contains the partial derivatives of the position vector in that configuration with respect to the parent coordinate system (for the current configuration see Equation 3.6). Thus, to have the Jacobian in the lamina coordinate system, basically the position vector must be transformed to the lamina coordinate system (Hughes and Liu, 1980; Shabana, 2011) by $\{y^l\} = [q]\{y\}$. Based on this principle, the reference and the current Jacobians are transformed to the lamina coordinate system by Equation 3.7 and Equation 3.8, respectively:

Equation 3.6

$$[\,{}^{\tau}J] = \begin{bmatrix} \dfrac{\partial\,{}^{\tau}y_1}{\partial r} & \dfrac{\partial\,{}^{\tau}y_2}{\partial r} & \dfrac{\partial\,{}^{\tau}y_3}{\partial r} \\ \dfrac{\partial\,{}^{\tau}y_1}{\partial s} & \dfrac{\partial\,{}^{\tau}y_2}{\partial s} & \dfrac{\partial\,{}^{\tau}y_3}{\partial s} \\ \dfrac{\partial\,{}^{\tau}y_1}{\partial t} & \dfrac{\partial\,{}^{\tau}y_2}{\partial t} & \dfrac{\partial\,{}^{\tau}y_3}{\partial t} \end{bmatrix},$$

Equation 3.7

$$\left[{}^{\beta}J^l\right] = \left[{}^{\beta}J\right]\left[{}^{\beta}q\right]^T,$$

Equation 3.8

$$[\,{}^{\tau}J^l] = [\,{}^{\tau}J][\,{}^{\tau}q]^T.$$

Note that in (Sosa and Gil, 2009), the Jacobian is mistakenly considered as a second order tensor and for the transformation, is pre and post-multiplied by rotation matrices. Given that in (Sosa and Gil, 2009), only flat geometries are modeled and only small rotations and small deformations are studied, $[q]$ is numerically an identity matrix and thus this inaccuracy in the theory did not lead to numerical errors.

3.7 Measures of deformation in the lamina coordinate system

Measures of deformation in the global coordinate system are evaluated in Section 2.6. Evaluation of these measures in the lamina coordinate system are illustrated in the following subsections.

3.7.1 Deformation gradient

We obtain the deformation gradient of the current configuration with respect to the reference configuration in the lamina coordinate system from

Equation 3.9

$$\left[{}_{\beta}^{\tau}F^{l}\right] = \left[\,{}^{\tau}J^{l}\right]^{T}\left[{}^{\beta}J^{l}\right]^{-T},$$

where $\left[{}^{\beta}J^{l}\right]$ and $\left[\,{}^{\tau}J^{l}\right]$ are the reference (Equation 3.7) and the current (Equation 3.8) Jacobians, both defined for the lamina coordinate system.

3.7.2 Right and left Cauchy-Green tensor

The right and left Cauchy-Green tensors in the global coordinate system are given in Equation 2.73 and Equation 2.74, respectively. To evaluate these tensors in the lamina coordinate systems, we employ the lamina deformations gradients (Equation 3.9), thus:

Equation 3.10

$$\left[{}_{\beta}^{\tau}C^{l}\right] = \left[{}_{\beta}^{\tau}F^{l}\right]^{T}\left[{}_{\beta}^{\tau}F^{l}\right],$$

and

Equation 3.11

$$\left[{}^{\tau}_{\beta}B^{l}\right] = \left[{}^{\tau}_{\beta}F^{l}\right]\left[{}^{\tau}_{\beta}F^{l}\right]^{T}.$$

In the above equations, the left superscript τ denotes the current configuration, and the left subscript β denoting the reference configuration, is replaced by 0 in the total UL formulation (Equation 3.1), and by $\tau - \Delta\tau$ in the incremental UL formulation (Equation 3.2).

3.7.3 Green-Lagrange and Almansi strain tensors

We evaluate the lamina Green-Lagrange strain tensor defined in the current configuration (τ) with respect to the reference configuration (β) from:

Equation 3.12

$$\left[{}^{\tau}_{\beta}E^{l}\right] = \frac{1}{2}\left(\left[{}^{\tau}_{\beta}C^{l}\right] - [I]\right),$$

where, the lamina right Cauchy-Green tensor of the current configuration with respect to the reference configuration $\left[{}^{\tau}_{\beta}C^{l}\right]$ is obtained from Equation 3.10.

In addition, we obtain the lamina Almansi strain tensor in the current configuration from:

Equation 3.13

$$\left[{}_{\tau}\varepsilon^{l}\right] = \frac{1}{2}\left([I] - \left[{}^{\tau}_{\beta}B^{l}\right]^{-1}\right).$$

where, the lamina left Cauchy-Green tensor of the current configuration with respect to the reference configuration $\left[{}^{\tau}_{\beta}B^{l}\right]$ is obtained from Equation 3.11.

The above formulations were inspired from the formulations of the global Green-Lagrange and global Almansi strain tensors (Equation 2.75 and Equation 2.76, respectively), except that we measured the deformations in the lamina coordinate system.

3.8 Linear strain-displacement transformation matrix in the lamina coordinate system

The column ordering of $[B_L]$, obtained by Bathe and Bolourchi in Section 2.5.2.2, corresponds to the nodal displacements and nodal fiber rotations in the global coordinate system (i.e. $[\cdots \quad u_1^a \quad u_2^a \quad u_3^a \quad \Delta\theta_1^a \quad \Delta\theta_2^a \quad \cdots]$). In addition, the partial derivatives are taken with respect to the current position vector in the global coordinate system. Considering that we are adopting multiple coordinate systems (that is, independent fiber and lamina coordinate systems) and considering that the constitutive relations are applied in the lamina coordinate system, the following two modifications are required:

1. the aforementioned nodal and nodal fiber displacements must be referred to the lamina at the point in question;
2. the partial derivatives with respect to the current position vector in the lamina coordinate system are desired as opposed to the global ones.

As a starting point, the displacements equation in the global coordinate system (Equation 3.4) is written in matrix form as $\{{}^{\tau}_{\beta}\vec{u}\} = [\ {}^{\tau}N]\{{}^{\tau}_{\beta}u^a\}$. Dropping the left scripts and expanding gives:

Equation 3.14

$$\begin{Bmatrix} u_1 \\ u_2 \\ u_3 \end{Bmatrix} = \begin{bmatrix} \cdots & N_a & 0 & 0 & -\frac{(t-\bar{t})}{2} h_a N_a \left(\vec{e}_1^{\,f}\right)_1^a & -\frac{(t-\bar{t})}{2} h_a N_a \left(\vec{e}_2^{\,f}\right)_1^a & \cdots \\ \cdots & 0 & N_a & 0 & -\frac{(t-\bar{t})}{2} h_a N_a \left(\vec{e}_1^{\,f}\right)_2^a & -\frac{(t-\bar{t})}{2} h_a N_a \left(\vec{e}_2^{\,f}\right)_2^a & \cdots \\ \cdots & 0 & 0 & N_a & -\frac{(t-\bar{t})}{2} h_a N_a \left(\vec{e}_1^{\,f}\right)_3^a & -\frac{(t-\bar{t})}{2} h_a N_a \left(\vec{e}_2^{\,f}\right)_3^a & \cdots \end{bmatrix} \begin{Bmatrix} \vdots \\ u_1^a \\ u_2^a \\ u_3^a \\ \theta_1^a \\ \theta_2^a \\ \vdots \end{Bmatrix}.$$

Similarly to Equations 2.64 and 2.65, we take the partial derivatives of Equation 3.14 with respect to the parent coordinates (r, s, t). Noting that:

1. the left super and subscripts (τ and β) are dropped for convenience,
2. h_a is the nodal thickness (i.e. constant) thus its derivatives are zero,
3. the shape functions are 2D (i.e. independent of t), thus $\frac{\partial N_a}{\partial t} = 0$,
4. $\bar{t}$ is a constant and its derivatives are zero,
5. $\frac{\partial t}{\partial t} = 1$ and $\frac{\partial t}{\partial r} = \frac{\partial t}{\partial s} = 0$,

and letting:

6. $\left.\begin{aligned} g_{1i}^a &= -\tfrac{1}{2} h_a \left(\vec{e}_1^{\,f}\right)_i^a \\ g_{2i}^a &= -\tfrac{1}{2} h_a \left(\vec{e}_2^{\,f}\right)_i^a \end{aligned}\right\},\ i = 1,2,3$

7. $(t - \bar{t}) = \tilde{t}$,

the simplified results of the partial derivations gives Equation 3.15.

To transform the nodal and nodal fiber displacements to the lamina coordinate system, we reordered the rows in Equation 3.15 to get Equation 3.16 and then pre-multiplied them by the current $[\,{}^{\tau}q_a]$ transformation matrix to get Equation 3.17.

Equation 3.15

$$\left\{\begin{matrix} \frac{\partial u_1}{\partial r} \\ \frac{\partial u_1}{\partial s} \\ \frac{\partial u_1}{\partial t} \\ \frac{\partial u_2}{\partial r} \\ \frac{\partial u_2}{\partial s} \\ \frac{\partial u_2}{\partial t} \\ \frac{\partial u_3}{\partial r} \\ \frac{\partial u_3}{\partial s} \\ \frac{\partial u_3}{\partial t} \end{matrix}\right\} = \begin{bmatrix} \dots & \frac{\partial N_a}{\partial r} & 0 & 0 & \tilde{t} g_{11}^a \frac{\partial N_a}{\partial r} & \tilde{t} g_{21}^a \frac{\partial N_a}{\partial r} & \dots \\ \dots & \frac{\partial N_a}{\partial s} & 0 & 0 & \tilde{t} g_{11}^a \frac{\partial N_a}{\partial s} & \tilde{t} g_{21}^a \frac{\partial N_a}{\partial s} & \dots \\ \dots & 0 & 0 & 0 & g_{11}^a N_a & g_{21}^a N_a & \dots \\ \dots & 0 & \frac{\partial N_a}{\partial r} & 0 & \tilde{t} g_{12}^a \frac{\partial N_a}{\partial r} & \tilde{t} g_{22}^a \frac{\partial N_a}{\partial r} & \dots \\ \dots & 0 & \frac{\partial N_a}{\partial s} & 0 & \tilde{t} g_{12}^a \frac{\partial N_a}{\partial s} & \tilde{t} g_{22}^a \frac{\partial N_a}{\partial s} & \dots \\ \dots & 0 & 0 & 0 & g_{12}^a N_a & g_{22}^a N_a & \dots \\ \dots & 0 & 0 & \frac{\partial N_a}{\partial r} & \tilde{t} g_{13}^a \frac{\partial N_a}{\partial r} & \tilde{t} g_{23}^a \frac{\partial N_a}{\partial r} & \dots \\ \dots & 0 & 0 & \frac{\partial N_a}{\partial s} & \tilde{t} g_{13}^a \frac{\partial N_a}{\partial s} & \tilde{t} g_{23}^a \frac{\partial N_a}{\partial s} & \dots \\ \dots & 0 & 0 & 0 & g_{13}^a N_a & g_{23}^a N_a & \dots \end{bmatrix} \left\{\begin{matrix} \vdots \\ u_1^a \\ u_2^a \\ u_3^a \\ \theta_1^a \\ \theta_2^a \\ \vdots \end{matrix}\right\}.$$

Equation 3.16

$$\begin{Bmatrix} \frac{\partial u_1}{\partial r} \\ \frac{\partial u_2}{\partial r} \\ \frac{\partial u_3}{\partial r} \\ \frac{\partial u_1}{\partial s} \\ \frac{\partial u_2}{\partial s} \\ \frac{\partial u_3}{\partial s} \\ \frac{\partial u_1}{\partial t} \\ \frac{\partial u_2}{\partial t} \\ \frac{\partial u_3}{\partial t} \end{Bmatrix} = \begin{bmatrix} \cdots & \frac{\partial N_a}{\partial r} & 0 & 0 & \tilde{t}g_{11}^a \frac{\partial N_a}{\partial r} & \tilde{t}g_{21}^a \frac{\partial N_a}{\partial r} & \cdots \\ \cdots & 0 & \frac{\partial N_a}{\partial r} & 0 & \tilde{t}g_{12}^a \frac{\partial N_a}{\partial r} & \tilde{t}g_{22}^a \frac{\partial N_a}{\partial r} & \cdots \\ \cdots & 0 & 0 & \frac{\partial N_a}{\partial r} & \tilde{t}g_{13}^a \frac{\partial N_a}{\partial r} & \tilde{t}g_{23}^a \frac{\partial N_a}{\partial r} & \cdots \\ \cdots & \frac{\partial N_a}{\partial s} & 0 & 0 & \tilde{t}g_{11}^a \frac{\partial N_a}{\partial s} & \tilde{t}g_{21}^a \frac{\partial N_a}{\partial s} & \cdots \\ \cdots & 0 & \frac{\partial N_a}{\partial s} & 0 & \tilde{t}g_{12}^a \frac{\partial N_a}{\partial s} & \tilde{t}g_{22}^a \frac{\partial N_a}{\partial s} & \cdots \\ \cdots & 0 & 0 & \frac{\partial N_a}{\partial s} & \tilde{t}g_{13}^a \frac{\partial N_a}{\partial s} & \tilde{t}g_{23}^a \frac{\partial N_a}{\partial s} & \cdots \\ \cdots & 0 & 0 & 0 & g_{11}^a N_a & g_{21}^a N_a & \cdots \\ \cdots & 0 & 0 & 0 & g_{12}^a N_a & g_{22}^a N_a & \cdots \\ \cdots & 0 & 0 & 0 & g_{13}^a N_a & g_{23}^a N_a & \cdots \end{bmatrix} \begin{Bmatrix} \vdots \\ u_1^a \\ u_2^a \\ u_3^a \\ \theta_1^a \\ \theta_2^a \\ \vdots \end{Bmatrix},$$

Equation 3.17

$$\begin{Bmatrix} \frac{\partial u_1^l}{\partial r} \\ \frac{\partial u_2^l}{\partial r} \\ \frac{\partial u_3^l}{\partial r} \end{Bmatrix} = \begin{bmatrix} \left(\vec{e}_1^{\,l}\right)_1^a & \left(\vec{e}_1^{\,l}\right)_2^a & \left(\vec{e}_1^{\,l}\right)_3^a \\ \left(\vec{e}_2^{\,l}\right)_1^a & \left(\vec{e}_2^{\,l}\right)_2^a & \left(\vec{e}_2^{\,l}\right)_3^a \\ \left(\vec{e}_3^{\,l}\right)_1^a & \left(\vec{e}_3^{\,l}\right)_2^a & \left(\vec{e}_3^{\,l}\right)_3^a \end{bmatrix} \begin{bmatrix} \cdots & \frac{\partial N_a}{\partial r} & 0 & 0 & \tilde{t}g_{11}^a \frac{\partial N_a}{\partial r} & \tilde{t}g_{21}^a \frac{\partial N_a}{\partial r} & \cdots \\ \cdots & 0 & \frac{\partial N_a}{\partial r} & 0 & \tilde{t}g_{12}^a \frac{\partial N_a}{\partial r} & \tilde{t}g_{22}^a \frac{\partial N_a}{\partial r} & \cdots \\ \cdots & 0 & 0 & \frac{\partial N_a}{\partial r} & \tilde{t}g_{13}^a \frac{\partial N_a}{\partial r} & \tilde{t}g_{23}^a \frac{\partial N_a}{\partial r} & \cdots \end{bmatrix} \begin{Bmatrix} \vdots \\ u_1^a \\ u_2^a \\ u_3^a \\ \theta_1^a \\ \theta_2^a \\ \vdots \end{Bmatrix}$$

$$\begin{Bmatrix} \frac{\partial u_1^l}{\partial s} \\ \frac{\partial u_2^l}{\partial s} \\ \frac{\partial u_3^l}{\partial s} \end{Bmatrix} = \begin{bmatrix} \left(\vec{e}_1^{\,l}\right)_1^a & \left(\vec{e}_1^{\,l}\right)_2^a & \left(\vec{e}_1^{\,l}\right)_3^a \\ \left(\vec{e}_2^{\,l}\right)_1^a & \left(\vec{e}_2^{\,l}\right)_2^a & \left(\vec{e}_2^{\,l}\right)_3^a \\ \left(\vec{e}_3^{\,l}\right)_1^a & \left(\vec{e}_3^{\,l}\right)_2^a & \left(\vec{e}_3^{\,l}\right)_3^a \end{bmatrix} \begin{bmatrix} \cdots & \frac{\partial N_a}{\partial s} & 0 & 0 & \tilde{t}g_{11}^a \frac{\partial N_a}{\partial s} & \tilde{t}g_{21}^a \frac{\partial N_a}{\partial s} & \cdots \\ \cdots & 0 & \frac{\partial N_a}{\partial s} & 0 & \tilde{t}g_{12}^a \frac{\partial N_a}{\partial s} & \tilde{t}g_{22}^a \frac{\partial N_a}{\partial s} & \cdots \\ \cdots & 0 & 0 & \frac{\partial N_a}{\partial s} & \tilde{t}g_{13}^a \frac{\partial N_a}{\partial s} & \tilde{t}g_{23}^a \frac{\partial N_a}{\partial s} & \cdots \end{bmatrix} \begin{Bmatrix} \vdots \\ u_1^a \\ u_2^a \\ u_3^a \\ \theta_1^a \\ \theta_2^a \\ \vdots \end{Bmatrix},$$

$$\begin{Bmatrix} \frac{\partial u_1^l}{\partial t} \\ \frac{\partial u_2^l}{\partial t} \\ \frac{\partial u_3^l}{\partial t} \end{Bmatrix} = \begin{bmatrix} \left(\vec{e}_1^{\,l}\right)_1^a & \left(\vec{e}_1^{\,l}\right)_2^a & \left(\vec{e}_1^{\,l}\right)_3^a \\ \left(\vec{e}_2^{\,l}\right)_1^a & \left(\vec{e}_2^{\,l}\right)_2^a & \left(\vec{e}_2^{\,l}\right)_3^a \\ \left(\vec{e}_3^{\,l}\right)_1^a & \left(\vec{e}_3^{\,l}\right)_2^a & \left(\vec{e}_3^{\,l}\right)_3^a \end{bmatrix} \begin{bmatrix} \cdots & 0 & 0 & 0 & g_{11}^a N_a & g_{21}^a N_a & \cdots \\ \cdots & 0 & 0 & 0 & g_{12}^a N_a & g_{22}^a N_a & \cdots \\ \cdots & 0 & 0 & 0 & g_{13}^a N_a & g_{23}^a N_a & \cdots \end{bmatrix} \begin{Bmatrix} \vdots \\ u_1^a \\ u_2^a \\ u_3^a \\ \theta_1^a \\ \theta_2^a \\ \vdots \end{Bmatrix}$$

where the superscript l is used to emphasize that the components are in lamina coordinate system.

Note that $\left(\vec{e}_i^{\,l}\right)_1^a\left(\vec{e}_j^{\,f}\right)_1^a+\left(\vec{e}_i^{\,l}\right)_2^a\left(\vec{e}_j^{\,f}\right)_2^a+\left(\vec{e}_i^{\,l}\right)_3^a\left(\vec{e}_j^{\,f}\right)_3^a$ for $i=1,2,3$ and $j=1,2$ (no summation) is the expanded form of the dot product between vectors $\left(\vec{e}_i^{\,l}\right)^a$ and $\left(\vec{e}_j^{\,f}\right)^a$, that is:

$$\left(\vec{e}_i^{\,l}\right)^a\cdot\left(\vec{e}_j^{\,f}\right)^a=\left(\vec{e}_i^{\,l}\right)_1^a\left(\vec{e}_j^{\,f}\right)_1^a+\left(\vec{e}_i^{\,l}\right)_2^a\left(\vec{e}_j^{\,f}\right)_2^a+\left(\vec{e}_i^{\,l}\right)_3^a\left(\vec{e}_j^{\,f}\right)_3^a,$$

and carrying out the submatrix multiplications in Equation 3.17, and substituting the above expressions gives:

Equation 3.18

$$\begin{Bmatrix}\dfrac{\partial u_1^l}{\partial r}\\ \dfrac{\partial u_2^l}{\partial r}\\ \dfrac{\partial u_3^l}{\partial r}\end{Bmatrix}=\begin{bmatrix}\cdots & \dfrac{\partial N_a}{\partial r}\left(\vec{e}_1^{\,l}\right)_1^a & \dfrac{\partial N_a}{\partial r}\left(\vec{e}_1^{\,l}\right)_2^a & \dfrac{\partial N_a}{\partial r}\left(\vec{e}_1^{\,l}\right)_3^a & \tilde{t}\left(\dfrac{-h_a}{2}\right)\dfrac{\partial N_a}{\partial r}\left(\left(\vec{e}_1^{\,l}\right)^a\cdot\left(\vec{e}_2^{\,f}\right)^a\right) & \tilde{t}\left(\dfrac{-h_a}{2}\right)\dfrac{\partial N_a}{\partial r}\left(\left(\vec{e}_1^{\,l}\right)^a\cdot\left(\vec{e}_1^{\,f}\right)^a\right) & \cdots\\ \cdots & \dfrac{\partial N_a}{\partial r}\left(\vec{e}_2^{\,l}\right)_1^a & \dfrac{\partial N_a}{\partial r}\left(\vec{e}_2^{\,l}\right)_2^a & \dfrac{\partial N_a}{\partial r}\left(\vec{e}_2^{\,l}\right)_3^a & \tilde{t}\left(\dfrac{-h_a}{2}\right)\dfrac{\partial N_a}{\partial r}\left(\left(\vec{e}_2^{\,l}\right)^a\cdot\left(\vec{e}_2^{\,f}\right)^a\right) & \tilde{t}\left(\dfrac{-h_a}{2}\right)\dfrac{\partial N_a}{\partial r}\left(\left(\vec{e}_2^{\,l}\right)^a\cdot\left(\vec{e}_1^{\,f}\right)^a\right) & \cdots\\ \cdots & \dfrac{\partial N_a}{\partial r}\left(\vec{e}_3^{\,l}\right)_1^a & \dfrac{\partial N_a}{\partial r}\left(\vec{e}_3^{\,l}\right)_2^a & \dfrac{\partial N_a}{\partial r}\left(\vec{e}_3^{\,l}\right)_3^a & \tilde{t}\left(\dfrac{-h_a}{2}\right)\dfrac{\partial N_a}{\partial r}\left(\left(\vec{e}_3^{\,l}\right)^a\cdot\left(\vec{e}_2^{\,f}\right)^a\right) & \tilde{t}\left(\dfrac{-h_a}{2}\right)\dfrac{\partial N_a}{\partial r}\left(\left(\vec{e}_3^{\,l}\right)^a\cdot\left(\vec{e}_1^{\,f}\right)^a\right) & \cdots\end{bmatrix}\begin{Bmatrix}\vdots\\ u_1^a\\ u_2^a\\ u_3^a\\ \theta_1^a\\ \theta_2^a\\ \vdots\end{Bmatrix}$$

$$\begin{Bmatrix}\dfrac{\partial u_1^l}{\partial s}\\ \dfrac{\partial u_2^l}{\partial s}\\ \dfrac{\partial u_3^l}{\partial s}\end{Bmatrix}=\begin{bmatrix}\cdots & \dfrac{\partial N_a}{\partial s}\left(\vec{e}_1^{\,l}\right)_1^a & \dfrac{\partial N_a}{\partial s}\left(\vec{e}_1^{\,l}\right)_2^a & \dfrac{\partial N_a}{\partial s}\left(\vec{e}_1^{\,l}\right)_3^a & \tilde{t}\left(\dfrac{-h_a}{2}\right)\dfrac{\partial N_a}{\partial s}\left(\left(\vec{e}_1^{\,l}\right)^a\cdot\left(\vec{e}_2^{\,f}\right)^a\right) & \tilde{t}\left(\dfrac{-h_a}{2}\right)\dfrac{\partial N_a}{\partial s}\left(\left(\vec{e}_1^{\,l}\right)^a\cdot\left(\vec{e}_1^{\,f}\right)^a\right) & \cdots\\ \cdots & \dfrac{\partial N_a}{\partial s}\left(\vec{e}_2^{\,l}\right)_1^a & \dfrac{\partial N_a}{\partial s}\left(\vec{e}_2^{\,l}\right)_2^a & \dfrac{\partial N_a}{\partial s}\left(\vec{e}_2^{\,l}\right)_3^a & \tilde{t}\left(\dfrac{-h_a}{2}\right)\dfrac{\partial N_a}{\partial s}\left(\left(\vec{e}_2^{\,l}\right)^a\cdot\left(\vec{e}_2^{\,f}\right)^a\right) & \tilde{t}\left(\dfrac{-h_a}{2}\right)\dfrac{\partial N_a}{\partial s}\left(\left(\vec{e}_2^{\,l}\right)^a\cdot\left(\vec{e}_1^{\,f}\right)^a\right) & \cdots\\ \cdots & \dfrac{\partial N_a}{\partial s}\left(\vec{e}_3^{\,l}\right)_1^a & \dfrac{\partial N_a}{\partial s}\left(\vec{e}_3^{\,l}\right)_2^a & \dfrac{\partial N_a}{\partial s}\left(\vec{e}_3^{\,l}\right)_3^a & \tilde{t}\left(\dfrac{-h_a}{2}\right)\dfrac{\partial N_a}{\partial s}\left(\left(\vec{e}_3^{\,l}\right)^a\cdot\left(\vec{e}_2^{\,f}\right)^a\right) & \tilde{t}\left(\dfrac{-h_a}{2}\right)\dfrac{\partial N_a}{\partial s}\left(\left(\vec{e}_3^{\,l}\right)^a\cdot\left(\vec{e}_1^{\,f}\right)^a\right) & \cdots\end{bmatrix}\begin{Bmatrix}\vdots\\ u_1^a\\ u_2^a\\ u_3^a\\ \theta_1^a\\ \theta_2^a\\ \vdots\end{Bmatrix}.$$

$$\begin{Bmatrix}\dfrac{\partial u_1^l}{\partial t}\\ \dfrac{\partial u_2^l}{\partial t}\\ \dfrac{\partial u_3^l}{\partial t}\end{Bmatrix}=\begin{bmatrix}\cdots & 0 & 0 & 0 & \left(\dfrac{-h_a}{2}\right)N_a\left(\left(\vec{e}_1^{\,l}\right)^a\cdot\left(\vec{e}_2^{\,f}\right)^a\right) & \left(\dfrac{-h_a}{2}\right)N_a\left(\left(\vec{e}_1^{\,l}\right)^a\cdot\left(\vec{e}_1^{\,f}\right)^a\right) & \cdots\\ \cdots & 0 & 0 & 0 & \left(\dfrac{-h_a}{2}\right)N_a\left(\left(\vec{e}_2^{\,l}\right)^a\cdot\left(\vec{e}_2^{\,f}\right)^a\right) & \left(\dfrac{-h_a}{2}\right)N_a\left(\left(\vec{e}_2^{\,l}\right)^a\cdot\left(\vec{e}_1^{\,f}\right)^a\right) & \cdots\\ \cdots & 0 & 0 & 0 & \left(\dfrac{-h_a}{2}\right)N_a\left(\left(\vec{e}_3^{\,l}\right)^a\cdot\left(\vec{e}_2^{\,f}\right)^a\right) & \left(\dfrac{-h_a}{2}\right)N_a\left(\left(\vec{e}_3^{\,l}\right)^a\cdot\left(\vec{e}_1^{\,f}\right)^a\right) & \cdots\end{bmatrix}\begin{Bmatrix}\vdots\\ u_1^a\\ u_2^a\\ u_3^a\\ \theta_1^a\\ \theta_2^a\\ \vdots\end{Bmatrix}$$

Note that the unit vectors of the lamina coordinate system are functions of the parent coordinate system and that they can be obtained for any specified r,s,t value. The nodal fiber coordinate systems, on the other hand, are obtained at each node from the algorithm presented in Section 3.3.

As done in Equation 2.69, to obtain the partial derivatives of the lamina displacements with respect to the current position vector in the global coordinate system, rows in Equation 3.18

need to be reordered and then be premultiplied by the inverse Jacobian (inverse of Equation 3.6). However, consistent with the assumption of the multiple coordinate systems (i.e. independent fiber and lamina coordinate systems), and considering that the constitutive relations must be applied in the lamina coordinate system, we are interested in obtaining the aforementioned partial derivatives with respect to the current position vector in the lamina coordinate system as opposed to the global one that is obtained above. Thus, to obtain these partial derivatives with respect to the current position vector in the lamina coordinate system, we reorder the rows in Equation 3.18 such that they are consistent with $\begin{bmatrix} \frac{\partial u_1^l}{\partial r} & \frac{\partial u_1^l}{\partial s} & \frac{\partial u_1^l}{\partial t} & \frac{\partial u_2^l}{\partial r} & \frac{\partial u_2^l}{\partial s} & \frac{\partial u_2^l}{\partial t} & \frac{\partial u_3^l}{\partial r} & \frac{\partial u_3^l}{\partial s} & \frac{\partial u_3^l}{\partial t} \end{bmatrix}^T$; by premultiplication by the inverse of the current Jacobian in the lamina coordinate system, we get:

Equation 3.19

$$\begin{Bmatrix} \frac{\partial u_1^l}{\partial y_1^l} \\ \frac{\partial u_1^l}{\partial y_2^l} \\ \frac{\partial u_1^l}{\partial y_3^l} \end{Bmatrix} = \begin{bmatrix} \cdots & [J_a^l]^{-1} \begin{bmatrix} \frac{\partial N_a}{\partial r}(\vec{e}_1^l)_1^a & \frac{\partial N_a}{\partial r}(\vec{e}_1^l)_2^a & \frac{\partial N_a}{\partial r}(\vec{e}_1^l)_3^a & \tilde{t}\left(\frac{-h_a}{2}\right)\frac{\partial N_a}{\partial r}\left((\vec{e}_1^l)^a \cdot (\vec{e}_1^f)^a\right) & \tilde{t}\left(\frac{-h_a}{2}\right)\frac{\partial N_a}{\partial r}\left((\vec{e}_1^l)^a \cdot (\vec{e}_2^f)^a\right) \\ \frac{\partial N_a}{\partial s}(\vec{e}_1^l)_1^a & \frac{\partial N_a}{\partial s}(\vec{e}_1^l)_2^a & \frac{\partial N_a}{\partial s}(\vec{e}_1^l)_3^a & \tilde{t}\left(\frac{-h_a}{2}\right)\frac{\partial N_a}{\partial s}\left((\vec{e}_1^l)^a \cdot (\vec{e}_1^f)^a\right) & \tilde{t}\left(\frac{-h_a}{2}\right)\frac{\partial N_a}{\partial s}\left((\vec{e}_1^l)^a \cdot (\vec{e}_2^f)^a\right) \\ 0 & 0 & 0 & \left(\frac{-h_a}{2}\right)N_a\left((\vec{e}_1^l)^a \cdot (\vec{e}_1^f)^a\right) & \left(\frac{-h_a}{2}\right)N_a\left((\vec{e}_1^l)^a \cdot (\vec{e}_2^f)^a\right) \end{bmatrix} & \cdots \end{bmatrix} \begin{Bmatrix} \vdots \\ u_1^a \\ u_2^a \\ u_3^a \\ \theta_1^a \\ \theta_2^a \\ \vdots \end{Bmatrix}$$

$$\begin{Bmatrix} \frac{\partial u_2^l}{\partial y_1^l} \\ \frac{\partial u_2^l}{\partial y_2^l} \\ \frac{\partial u_2^l}{\partial y_3^l} \end{Bmatrix} = \begin{bmatrix} \cdots & [J_a^l]^{-1} \begin{bmatrix} \frac{\partial N_a}{\partial r}(\vec{e}_2^l)_1^a & \frac{\partial N_a}{\partial r}(\vec{e}_2^l)_2^a & \frac{\partial N_a}{\partial r}(\vec{e}_2^l)_3^a & \tilde{t}\left(\frac{-h_a}{2}\right)\frac{\partial N_a}{\partial r}\left((\vec{e}_2^l)^a \cdot (\vec{e}_1^f)^a\right) & \tilde{t}\left(\frac{-h_a}{2}\right)\frac{\partial N_a}{\partial r}\left((\vec{e}_2^l)^a \cdot (\vec{e}_2^f)^a\right) \\ \frac{\partial N_a}{\partial s}(\vec{e}_2^l)_1^a & \frac{\partial N_a}{\partial s}(\vec{e}_2^l)_2^a & \frac{\partial N_a}{\partial s}(\vec{e}_2^l)_3^a & \tilde{t}\left(\frac{-h_a}{2}\right)\frac{\partial N_a}{\partial s}\left((\vec{e}_2^l)^a \cdot (\vec{e}_1^f)^a\right) & \tilde{t}\left(\frac{-h_a}{2}\right)\frac{\partial N_a}{\partial s}\left((\vec{e}_2^l)^a \cdot (\vec{e}_2^f)^a\right) \\ 0 & 0 & 0 & \left(\frac{-h_a}{2}\right)N_a\left((\vec{e}_2^l)^a \cdot (\vec{e}_1^f)^a\right) & \left(\frac{-h_a}{2}\right)N_a\left((\vec{e}_2^l)^a \cdot (\vec{e}_2^f)^a\right) \end{bmatrix} & \cdots \end{bmatrix} \begin{Bmatrix} \vdots \\ u_1^a \\ u_2^a \\ u_3^a \\ \theta_1^a \\ \theta_2^a \\ \vdots \end{Bmatrix},$$

$$\begin{Bmatrix} \frac{\partial u_3^l}{\partial y_1^l} \\ \frac{\partial u_3^l}{\partial y_2^l} \\ \frac{\partial u_3^l}{\partial y_3^l} \end{Bmatrix} = \begin{bmatrix} \cdots & [J_a^l]^{-1} \begin{bmatrix} \frac{\partial N_a}{\partial r}(\vec{e}_3^l)_1^a & \frac{\partial N_a}{\partial r}(\vec{e}_3^l)_2^a & \frac{\partial N_a}{\partial r}(\vec{e}_3^l)_3^a & \tilde{t}\left(\frac{-h_a}{2}\right)\frac{\partial N_a}{\partial r}\left((\vec{e}_3^l)^a \cdot (\vec{e}_1^f)^a\right) & \tilde{t}\left(\frac{-h_a}{2}\right)\frac{\partial N_a}{\partial r}\left((\vec{e}_3^l)^a \cdot (\vec{e}_2^f)^a\right) \\ \frac{\partial N_a}{\partial s}(\vec{e}_3^l)_1^a & \frac{\partial N_a}{\partial s}(\vec{e}_3^l)_2^a & \frac{\partial N_a}{\partial s}(\vec{e}_3^l)_3^a & \tilde{t}\left(\frac{-h_a}{2}\right)\frac{\partial N_a}{\partial s}\left((\vec{e}_3^l)^a \cdot (\vec{e}_1^f)^a\right) & \tilde{t}\left(\frac{-h_a}{2}\right)\frac{\partial N_a}{\partial s}\left((\vec{e}_3^l)^a \cdot (\vec{e}_2^f)^a\right) \\ 0 & 0 & 0 & \left(\frac{-h_a}{2}\right)N_a\left((\vec{e}_3^l)^a \cdot (\vec{e}_1^f)^a\right) & \left(\frac{-h_a}{2}\right)N_a\left((\vec{e}_3^l)^a \cdot (\vec{e}_2^f)^a\right) \end{bmatrix} & \cdots \end{bmatrix} \begin{Bmatrix} \vdots \\ u_1^a \\ u_2^a \\ u_3^a \\ \theta_1^a \\ \theta_2^a \\ \vdots \end{Bmatrix}$$

where $[J_a^l]^{-1} = [\,^{\tau}q_a][\,^{\tau}J_a]^{-1}$ is obtained from inverting Equation 3.8.

Overall, the linear strain-displacement transformation matrices in the lamina coordinate system can be obtained by rearranging and adding the rows of the large matrix in Equation 3.19 such that the row ordering of $[B_L^l]$ is consistent with the following Voigt form of the linear strain vectors:

Equation 3.20

Linearized strains: $\{e^l\} = [e^l_{11} \quad e^l_{22} \quad e^l_{33} \quad 2e^l_{12} \quad 2e^l_{13} \quad 2e^l_{23}]^T$

$$e^l_{11} = \frac{\partial u^l_1}{\partial y^l_1}\ , \qquad e^l_{22} = \frac{\partial u^l_2}{\partial y^l_2}\ , \qquad e^l_{33} = \frac{\partial u^l_3}{\partial y^l_3}\ ,$$

$$2e^l_{12} = \left(\frac{\partial u^l_1}{\partial y^l_2} + \frac{\partial u^l_2}{\partial y^l_1}\right)\ , \qquad 2e^l_{13} = \left(\frac{\partial u^l_1}{\partial y^l_3} + \frac{\partial u^l_3}{\partial y^l_1}\right)\ , \qquad 2e^l_{23} = \left(\frac{\partial u^l_2}{\partial y^l_3} + \frac{\partial u^l_3}{\partial y^l_2}\right)\ ,$$

where superscript l is used to emphasize that the components are in the lamina coordinate system, as is required by the constitutive equations. Note that the strains obtained above are functions of the parent coordinate system. Thus, the strains at any point within the shell can be obtained by substituting the corresponding r, s, t values in Equation 3.20 through Equation 3.19.

3.9 Plane stress constitutive relations for small strain analysis

As mentioned previously, the constitutive relations must be enforced in the lamina coordinate system (Hughes, 2000). Considering an isotropic linear elastic material, the usual Young's modulus and Poisson's ratio are employed to define the material tangent matrix (also called the constitutive tensor) in the lamina coordinate system:

Equation 3.21

$$[C^l] = \frac{E}{(1+\nu)(1-2\nu)} \begin{bmatrix} 1-\nu & \nu & \nu & 0 & 0 & 0 \\ \nu & 1-\nu & \nu & 0 & 0 & 0 \\ \nu & \nu & 1-\nu & 0 & 0 & 0 \\ 0 & 0 & 0 & 2(1+\nu) & 0 & 0 \\ 0 & 0 & 0 & 0 & 2(1+\nu) & 0 \\ 0 & 0 & 0 & 0 & 0 & 2(1+\nu) \end{bmatrix}.$$

In the UL formulation, and considering small strains, the constitutive tensor relates the Cauchy stresses and Almansi strains in the lamina coordinate system by (Bathe et al., 1975; Bathe, 1996):

Equation 3.22

$$\{\,^{\tau}\sigma^l\} = [\,^{\tau}_{\tau}C^l]\{\,_{\tau}\varepsilon^l\},$$

where the Almansi strains (Equation 3.13) and the Cauchy stresses have the same arrangement:

$$\{\,_{\tau}\varepsilon^{l}\} = [\,_{\tau}\varepsilon^{l}_{11} \quad _{\tau}\varepsilon^{l}_{22} \quad _{\tau}\varepsilon^{l}_{33} \quad _{\tau}\varepsilon^{l}_{12} \quad _{\tau}\varepsilon^{l}_{13} \quad _{\tau}\varepsilon^{l}_{23}]^{T},$$

$$\{\,^{\tau}\sigma^{l}\} = [\,^{\tau}\sigma^{l}_{11} \quad ^{\tau}\sigma^{l}_{22} \quad ^{\tau}\sigma^{l}_{33} \quad ^{\tau}\sigma^{l}_{12} \quad ^{\tau}\sigma^{l}_{13} \quad ^{\tau}\sigma^{l}_{23}]^{T}.$$

In isotropic linear elasticity, the material elasticity tensor (Equation 3.21), also called the 3D Hooke's law, is given in the lamina coordinate system. According to Bathe et al. (1975), the linear material elasticity tensor can be used directly for large displacements, large rotations, but small strains without any transformation.

3.9.1 Application of zero normal stress condition

Dropping the left scripts for convenience, Equation 3.22 is written using the Voigt notations as: $\sigma^{l}_{i} = C^{l}_{ij}\varepsilon^{l}_{j}$. Note that in this formulation, Index 3 corresponds to the direction normal to the surface of the shell. To apply the zero normal stress condition (i.e. $\sigma^{l}_{3} = 0$) in a linear elastic material, the third row of $\left[{}^{\tau}_{\tau}B^{l}_{L}\right]$ (corresponding to the normal strain component ε^{l}_{3}) and the third row and column of $[C^{l}]$ (corresponding to σ^{l}_{3} and ε^{l}_{3}, respectively) must be removed. Consequently, ε^{l}_{3} needs to be reevaluated in terms of the remaining strain and stress components, such that (Hughes, 2000):

Equation 3.23

$$\varepsilon^{l}_{3} = \frac{-\left(\sum_{j=1,2,4,5,6} C^{l}_{3j}\varepsilon^{l}_{j}\right)}{C^{l}_{33}}.$$

The arrays with the third row and/or column removed are referred to as the "reduced" arrays, and are noted with a tilde over bar (e.g. $\{\tilde{\sigma}^{l}\}$). Substituting Equation 3.23 in Equation 3.22 and simplifying gives the other components of the reduced Cauchy stress vector as:

$$\tilde{\sigma}^{l}_{i} = \sum_{j=1,2,4,5,6}\left(C^{l}_{ij} - \frac{C^{l}_{i3}C^{l}_{3j}}{C^{l}_{33}}\right)\varepsilon^{l}_{j}\,.$$

Thus, to have the reduced stress-strain relation $\left(\text{i.e. } \{\tilde{\sigma}^{l}\} = [\tilde{C}^{l}]\{\tilde{\varepsilon}^{l}\}\right)$ satisfying the zero normal stress condition, the reduced material tangent modulus must be reevaluated as (Kiendl at al., 2015):

$$\tilde{C}_{ij}^{l} = C_{ij}^{l} - \frac{C_{i3}^{l} C_{3j}^{l}}{C_{33}^{l}} \quad \text{for} \quad i = 1,2,4,5,6$$

For linear material properties, large rotations, large deformations, and small strains, the material tangent modulus in the incremental and total UL formulations is equal to that of the TL formulation and no additional transformation is needed (Bathe et al., 1975) (Tests 1 to 7 in Section 4.1).

3.10 Constitutive relations for large strain analysis

In case of large strains, an important aspect is the implementation of the constitutive relations. In what follows, we present three techniques for the solution of the large strain problems in the UL formulations.

3.10.1 Technique 1

In *Technique 1*, we consider the total UL formulation (Equation 3.1), where loads and displacements are measured from the undeformed configuration (Bathe and Bolourchi, 1979; Bathe et al., 1975; Bathe, 1996), and we implement large strains using hyperelastic material models.

The constitutive relations, namely the material tangent modulus and the second Piola-Kirchhoff stress tensor, are normally obtained by taking the derivatives of the strain energy function with respect to the Green-Lagrange strains. However, to have the constitutive relations in the lamina coordinate system, we employ the lamina Green-Lagrange strains as opposed to the global ones. Thus, the lamina material tangent modulus and the lamina second Piola-Kirchhoff stress tensor are obtained from Equation 3.24 and Equation 3.25, respectively:

Equation 3.24

$${}_{0}C_{ijrs}^{l} = \frac{\partial^{2}\, {}_{0}^{\tau}W}{\partial\, {}_{0}^{\tau}E_{ij}^{l}\; \partial\, {}_{0}^{\tau}E_{rs}^{l}},$$

Equation 3.25

$$ {}_{0}^{\tau}S_{ij}^{l} = \frac{\partial\, {}_{0}^{\tau}W}{\partial\, {}_{0}^{\tau}E_{ij}^{l}}. $$

The components of the lamina Green-Lagrange strain tensor ${}_{0}^{\tau}E_{ij}^{l}$ are obtained by replacing β with 0 in Equation 3.12.

As needed for the UL formulation, we transform the lamina material tangent modulus (Equation 3.24) to the current configuration using the lamina deformation gradients (modified from Bathe et al. (1975)), such that:

Equation 3.26

$$ {}_{\tau}C_{mnpq}^{l} = \frac{{}^{\tau}\rho}{{}^{0}\rho}\; {}_{0}^{\tau}F_{mi}^{l}\; {}_{0}^{\tau}F_{nj}^{l}\; {}_{0}C_{ijrs}^{l}\; {}_{0}^{\tau}F_{pr}^{l}\; {}_{0}^{\tau}F_{qs}^{l}\,. $$

In addition, we obtain the lamina Cauchy stress tensor by transforming the lamina second Piola-Kirchhoff stress tensor (Equation 3.25):

Equation 3.27

$$ {}^{\tau}\sigma_{sr}^{l} = \frac{{}^{\tau}\rho}{{}^{0}\rho}\; {}_{0}^{\tau}F_{si}^{l}\; {}_{0}^{\tau}S_{ij}^{l}\; {}_{0}^{\tau}F_{rj}^{l}\,. $$

In these relations, left scripts τ and 0 denote the current and the initial configurations, and $[{}_{0}^{\tau}F^{l}]$ is obtained by replacing β with 0 in Equation 3.9. Note that this technique is effective only when the total UL formulation is used with hyperelasticity, in which the constitutive relations are not linear. Therefore, if this transformation is applied to a material with constant constitutive tensor undergoing large strains (Test 8 in Section 4.2), totally different results are obtained (Bathe et al., 1975; Bathe, 1996).

So far, no application of zero normal stress condition and/or incompressibility has been considered in this technique. This is addressed in what follows.

Considering hyperelastic materials, Kiendl et al. (2015) suggests that the zero normal stress condition can be applied either into the strain energy function via a Lagrange multiplier enforcing incompressibility, or iteratively for compressible materials. However, the limitations and concerns associated with the use of Lagrange multipliers have been discussed in Section 2.7. As a remedy, we propose a direct approach for enforcing the zero normal stress condition which works equally well for both incompressible and compressible materials. Considering that the presented approach is direct (i.e. no iterations), it is also expected to be computationally less expensive than that of Kiendl et al. (2015).

Considering the total UL formulation, Equation 3.12 can be re-written as:

$$[{}_0^\tau C^l] = 2[{}_0^\tau E^l] + [I],$$

where $[{}_0^\tau C^l] = [{}_0^\tau F^l]^T [{}_0^\tau F^l]$ (Equation 3.10). Thus, using the properties of the determinant:

Equation 3.28

$$(\det[{}_0^\tau F^l])^2 = \det(2[{}_0^\tau E^l] + [I]).$$

Then, we solve Equation 3.28 for the lamina Green-Lagrange strain in the normal direction. That is, we solve $\det(2[{}_0^\tau E^l] + [I]) - (\det[{}_0^\tau F^l])^2 = 0$ for ${}_0^\tau E_{33}^l$.

Note that:

1) $\det([{}_0^\tau E^l])$ and consequently $\det(2[{}_0^\tau E^l] + [I]) - (\det[{}_0^\tau F^l])^2$ are linear in ${}_0^\tau E_{33}^l$, thus there is only one solution for ${}_0^\tau E_{33}^l$.
2) ${}_0^\tau E_{33}^l$ obtained from the above approach is a function of the remaining eight components of the Green-Lagrange strain tensor only. Thus, if ${}_0^\tau E_{33}^l$ is substituted in the strain energy function, its derivatives with respect to ${}_0^\tau E_{33}^l$ (Equation 3.24 and Equation 3.25) vanish (i.e. ${}_0^\tau S_{33}^l = {}_0 C_{33pq}^l = {}_0 C_{mn33}^l = 0$). Thus, lamina constitutive relations satisfying the zero normal stress condition are developed.
3) This method is valid for both the incompressible and the compressible materials. The only difference is that we set $\det[{}_0^\tau F^l] = 1$ to enforce incompressibility, or we simply use the calculated value of $\det[{}_0^\tau F^l]$ for compressible materials.

This Technique will be verified by Tests 8 to 10 in Sections 4.2 and 4.3.

3.10.2 Technique 2

Technique 2 is designed to enable the use of a constant constitutive tensor (e.g. from linear elasticity) to model large strains in the total UL formulation using explicit time integration. Adjusting Equation 2.4 to the UL formulation, the incremental decomposition of the stress components in the lamina coordinate system becomes (Bathe et al., 1975; Bathe, 1996):

Equation 3.29

$$ {}^{\tau+\Delta\tau}_{\tau}S^{l}_{ij} = {}^{\tau}\sigma^{l}_{ij} + {}_{\tau}S^{l}_{ij} \, . $$

In this relation, the components of the second Piola-Kirchhoff stress increment tensor in the lamina coordinate system referred to the configuration at time τ are calculated from:

Equation 3.30

$$ {}_{\tau}S^{l}_{ij} = {}^{\tau}_{\tau}C^{l}_{ijrs} \, {}^{\tau+\Delta\tau}_{\tau}E^{l}_{rs}, $$

where, ${}^{\tau}_{\tau}C^{l}_{ijrs}$ is the constant constitutive tensor, and the components of the Green-Lagrange strain increment in the lamina coordinate system (${}^{\tau+\Delta\tau}_{\tau}E^{l}_{ij}$) are obtained by, respectively, replacing the left super- and subscripts of Equation 3.12 with $\tau + \Delta\tau$ and τ. Finally, similar to Equation 3.27, the lamina Cauchy stress at time $\tau + \Delta\tau$ are obtained by the following transformation:

$$ {}^{\tau+\Delta\tau}\sigma^{l}_{sr} = \frac{{}^{\tau+\Delta\tau}\rho}{{}^{\tau}\rho} \, {}^{\tau+\Delta\tau}_{\tau}F^{l}_{si} \, {}^{\tau+\Delta\tau}_{\tau}S^{l}_{ij} \, {}^{\tau+\Delta\tau}_{\tau}F^{l}_{rj} \, . $$

The main advantage of this technique is its relatively simple use compared to Technique 1. For instance, assuming that Young's modulus and Poisson's ratio are known for small strain analysis, and that a subroutine to calculate the constitutive relations in small strain analysis has been written, the same may be used for large strain analysis, simply by using the accumulation of the stresses (Equation 3.29) and the current incremental Green-Lagrange strains and the incremental second Piola-Kirchhoff stresses (Equation 3.30). Therefore, the need to evaluate the appropriate material constants for the hyperelastic strain energy function (used in Technique 1), as well as the transformation of the fourth-order constitutive tensor (Equation 3.26) are avoided. Note that since the constant constitutive tensor (from linear elasticity) is employed in this technique, the zero normal stress condition needs to be applied as per Section 3.9.1.

A similar idea for the accumulation of the stresses and the evaluation of incremental stresses and strains from the small strains material law was used in (Bathe et al., 1975) for hypoelasticity including elastoplasticity, in which ${}^{\tau}_{\tau}C^{l}_{ijrs}$ is defined by the history of Cauchy stresses and the accumulation of the instantaneous plastic strain increments.

We will verify this Technique through Test 8 in Section 4.2.

3.10.3 Technique 3

In ***Technique 3***, we propose the incremental linearization of the constitutive relations to model large strains in a material with a constant constitutive tensor (from linear elasticity). Specifically, we consider the incremental UL formulation, in which displacements and loads are measured from the previous configuration (Equation 3.2). Thus, only the increment in the stresses (as opposed to the accumulation of the stresses used in Technique 2) are considered. In this technique, we multiply the constant material tensor (without any transformation) with the linearized strain increments in the lamina coordinate system (Equation 3.20) to obtain the lamina Cauchy stresses in the current configuration:

$$\{\,{}^{\tau}\sigma^{l}\} = [{}^{\tau}_{\tau}C^{l}]\{\,{}_{\tau}e^{l}\}.$$

Note that, as with Technique 2, the procedure of Section 3.9.1 is used to apply the zero normal stress condition.

In addition to the advantages mentioned in Technique 2, complete exclusion of any transformations makes the computation the most efficient compared to the previous two techniques. This Technique is verified in Test 8.

3.11 Fiber length update algorithm for large membrane strains

In the shell theories introduced in Section 2.4, the fiber inextensibility (constant thickness) condition is invoked to avoid numerical ill-conditioning problems. Consequently, the thickness parameters have not been included among the global nodal unknowns. However, this disqualifies the application of these theories to cases where large membrane strains may develop. To remove this limitation and update the thickness parameters, Hughes and Carnoy (1983) proposed the following procedure. This procedure is also used across all shell element types in LS-Dyna (LS-DYNA, 2011).

First, considering that the plane stress assumption is enforced, the strain tensor $\left[\,{}_{\tau}\varepsilon^{l}\right]$ must be computed from the constitutive equations over a typical time/load and at the point under study. This procedure is explained in details in Sections 3.9 and 3.10. Then, the lamina strain tensor must be transformed to the global coordinate system using $\left[\,{}_{\tau}\varepsilon\right] = [\,{}^{\tau}q]^{T}\left[\,{}_{\tau}\varepsilon^{l}\right][\,{}^{\tau}q]$. Then, the mean value of $\left[\,{}_{\tau}\varepsilon\right]$ over the fiber is computed from:

Equation 3.31

$$\left[\,{}_{\tau}\bar{\varepsilon}\right] = \frac{1}{2}\left(\int_{-1}^{+1}\left[\,{}_{\tau}\varepsilon\right]dt\right).$$

Next, the mean component of strain (Equation 3.31) must be projected to produce the straining in the fiber direction. Recalling that $\hat{Y}$ denotes the unit vector in the fiber direction at the point in question, the transformation is done by:

Equation 3.32

$${}_{\tau}\bar{\varepsilon}^{f} = {}^{\tau}\hat{Y}^{T}\left[\,{}_{\tau}\bar{\varepsilon}\right]\,{}^{\tau}\hat{Y}.$$

Finally, the nodal thickness parameters are updated by:

Equation 3.33

$${}^{\tau}h_{a} \leftarrow {}^{\beta}h_{a}\left(1 + {}^{\tau}\bar{\varepsilon}_{a}^{f}\right).$$

Note that the thickness update is performed at the end of each iteration, which is after the element residual force and tangent array are computed. Therefore, the update of h_a lags one step behind the other kinematical quantities (Hughes and Carnoy, 1983).

In essence, by implementing this fiber length update algorithm we obtain the thickness from the conservation of matter and thus incompressibility (volume preservation) is satisfied (Belytschko et al., 2000).

3.12 Force vectors

The force vectors obtained in the following sections are similar to those evaluated in Section 2.2.4. However, considering that all the matrices involved are functions of the parent coordinate system, the integrals must be transformed to the natural coordinates.

3.12.1 External forces

Two of the most common external force vectors, namely the body and surface forces, were introduced in Section 2.2.4. In what follows, the left subscript β denoting the reference configuration, is replaced by 0 in the total UL formulation (1.1), and $\tau - \Delta\tau$ in the incremental UL formulation (1.2). In addition, considering that all the matrices obtained are expressed in the parent coordinate system, the integrals are evaluated in the parent coordinates.

Equation 3.34

$$\{{}^{\tau}_{\beta}R^B\} = \int_s \int_r \int_{-1}^{+1} [\,{}^{\tau}N]^T \{{}^{\tau}_{\beta}f^B\}\, \rho\, J\, dt\, dr\, ds,$$

where $\{{}^{\tau}_{\beta}f^B\}$ is the body force vector (per unit mass), ρ is mass density, J is the determinant of the Jacobian in the current configuration obtained from Equation 3.6, $[\,{}^{\tau}N]$ is the interpolation matrix presented in Equation 3.14, and

$\int_{-1}^{+1} \cdots\, dt =$ integration in the fiber direction,

$\int_s \int_r \cdots\, dr\, ds =$ integration in the lamina surface.

Considering that in both the total and the incremental UL formulations, equilibrium is expressed in the current configuration, J and $[N]$ must be updated for each new configuration for better accuracy. Although the computational efficiency of not updating J and $[N]$ (i.e. using those obtained in the initial or undeformed configuration) may outweigh the numerical errors when deformations and rotations are small (linear elasticity), this is a source of error when large deformations and large rotations are considered. This fact is neglected in many references.

The surface force vector is:

Equation 3.35

$$\left\{{}^{\tau}_{\beta}R^{S_f}\right\} = \int_s \int_r \left[\ {}^{\tau}N\right]^T \left\{{}^{\tau}_{\beta}f^{S_f}\right\} J_s \, dr \, ds \,, \quad t = \begin{cases} +1 & \text{top} \\ -1 & \text{bottom} \end{cases},$$

where $\left\{{}^{\tau}_{\beta}f^{S_f}\right\}$ is the surface force vector (per unit surface area). In the case of pressure, this force vector is obtained from $\left\{{}^{\tau}_{\beta}f^{S_f}\right\} = -tp\vec{n}$, where p is the pressure measured from the reference configuration β to the current configuration τ. Also,

t: $+1$ or -1, corresponding to the surface on which pressure is applied,

$J_s = \left\| \begin{pmatrix} \frac{\partial y_1}{\partial r} & \frac{\partial y_2}{\partial r} & \frac{\partial y_3}{\partial r} \end{pmatrix} \times \begin{pmatrix} \frac{\partial y_1}{\partial s} & \frac{\partial y_2}{\partial s} & \frac{\partial y_3}{\partial s} \end{pmatrix} \right\|$: the current surface Jacobian.

$\vec{n}$: unit normal vector to the surface is obtained from:

Equation 3.36

$$\vec{n} = \frac{\vec{e}_r \times \vec{e}_s}{\|\vec{e}_r \times \vec{e}_s\|}.$$

From the definition of $\vec{n}$ and from the equivalency of Equation 2.57 and Equation 3.36, it is known that $\vec{n} = \vec{e}_3^{\,l}$.

Edge forces, whereby distributed loads are applied along edges of the element (e.g. $s = +1$ or -1) are another common form of external loads (Hughes, 2000). Let $\left\{{}^{\tau}_{\beta}f_e\right\}$ denote the incremental distributed edge load vector; then, the nodal forces are:

$$\left\{{}^{\tau}_{\beta}f_a^{Edge}\right\} = \int_{-1}^{+1} \int_{-1}^{+1} \left(\left[\ {}^{\tau}N_a\right]^T \left\{{}^{\tau}_{\beta}f_e\right\} \ j_e \right)\Big|_{s=+1 \text{ or } -1} dt \, dr,$$

where, j_e is the edge surface Jacobian and is obtained from:

$$j_e = \left\| \begin{pmatrix} \frac{\partial y_1}{\partial r} & \frac{\partial y_2}{\partial r} & \frac{\partial y_3}{\partial r} \end{pmatrix} \times \begin{pmatrix} \frac{\partial y_1}{\partial t} & \frac{\partial y_2}{\partial t} & \frac{\partial y_3}{\partial t} \end{pmatrix} \right\|.$$

In the case of loading along an $r = +1$ or -1 edge, the computation is handled by interchanging r and s. When the reference surface is not taken to be the mid surface, nodal moments are produced even when the distributed edge load is constant. If edge forces or moments are specified per unit edge length, then Hughes (2000) computed the nodal forces as follows: Consider an $r = +1$ or -1 edge. Let $f_i^{line} = f_i^{line}(s)$ denote the edge force and let $m_i^{line} = m_i^{line}(s)$ denote the edge moment. The nodal forces are then given by:

$$\left\{{}_{\beta}^{\tau}f_a^{Edge}\right\} = \int_{-1}^{+1} N_a \,|_{r=+1\ \mathrm{or}-1} \begin{Bmatrix} {}_{\beta}^{\tau}f_1^{line} \\ {}_{\beta}^{\tau}f_2^{line} \\ {}_{\beta}^{\tau}f_3^{line} \\ {}_{\beta}^{\tau}m_1^{line} \\ {}_{\beta}^{\tau}m_2^{line} \end{Bmatrix} j_e \, ds,$$

where, $j_e = \left\| \begin{pmatrix} \frac{\partial y_1}{\partial s} & \frac{\partial y_2}{\partial s} & \frac{\partial y_3}{\partial s} \end{pmatrix} \right\|$ in the current configuration.

Finally, the inclusive external force vector from the reference configuration β to the current configuration τ is evaluated from:

$$\left\{{}_{\beta}^{\tau}R\right\} = \left\{{}_{\beta}^{\tau}R^B\right\} + \left\{{}_{\beta}^{\tau}R^{S_f}\right\} + \left\{{}_{\beta}^{\tau}f^{Edge}\right\}.$$

3.12.2 Internal forces

The internal force vector is obtained from:

$$\left\{{}_{\tau}^{\tau}f^{Internal}\right\} = \int_s \int_r \int_{-1}^{+1} \left[{}_{\tau}^{\tau}\tilde{B}_L^l\right]^T \left\{ {}^{\tau}\tilde{\sigma}^l \right\} J \, dt \, dr \, ds.$$

3.13 Stiffness matrix

If needed in the solution scheme, or for the evaluation of the critical time step (Section 3.16), the stiffness matrix is obtained from the usual updated Lagrangian (UL) finite element formulation (Section 2.2.4):

Equation 3.37

$$\left[{}_{\tau}^{\tau}K_L\right] = \int_s \int_r \int_{-1}^{+1} \left[{}_{\tau}^{\tau}\tilde{B}_L^l\right]^T \left[{}_{\tau}\tilde{C}^l \right] \left[{}_{\tau}^{\tau}\tilde{B}_L^l\right] J \, dt \, dr \, ds.$$

3.14 Mass matrices

Considering that the dimension of the square mass matrix $[M]$ is equal to the total number of the degrees of freedom of the system (that is number of elements $\times$ number of nodes per element (9) $\times$ number of degrees of freedom per node (5)), to avoid the numerical difficulty associated with its inversion, the diagonalized mass matrix is more appealing. In this section, we present 2 lumping methods to diagonalize the mass matrix, namely:

1) the lumped mass matrix that is directly obtained from the procedure explained by Hughes et al. (1981),
2) the lumped mass matrix that is obtained by row summing the consistent mass matrix (Hughes, 2000, and Bathe, 1996).

It is worth noting that diagonalization using these two methods is not performed using the usual eigenvalues and eigenvectors. In addition, the lumped mass matrices obtained from the first (Hughes et al., 1981) and the second approach result in equal mass matrix components for nodal translational DOFs, whereas the mass matrix components corresponding to nodal rotational DOFs are not equal, when large rotations of fibers are considered (e.g. Tests 9, 10). The reason is that Hughes et al. (1981), finds the components of mass matrix that corresponds to nodal rotational DOFs by adjusting the rotational inertia, such that it depends on the thickness but not the fiber direction. Details follow.

3.14.1 M1: Hughes' lumped mass matrix

The following lumped mass matrix is obtained from the procedure proposed by Hughes et al. (1981), where the Jacobian in the current configuration is considered (as opposed to the initial one):

$$\bar{J} = \int_{-1}^{+1} J \, dt,$$

The components of the mass matrix corresponding to the rotational degrees of freedom are evaluated from:

$$m_a^{rotational} = \int_s \int_r N_a^2 \, \rho \, \bar{J} \, dr \, ds,$$

Normalization gives:

$$\widetilde{M}^{rotational} = \sum_{a=1}^{n_{en}} m_a^{rotational},$$

$$\left(m_{normalized}^{rotational}\right)_a \leftarrow \left(\frac{M}{\widetilde{M}^{rotational}}\right) m_a^{rotational},$$

where

$$M = \int_s \int_r \rho \, \bar{J} \, dr \, ds.$$

If a normal Gauss rule (Section 3.18) is employed for numerical integration of the 9-noded CB element, components of the mass matrix representing the translational degrees of freedom are equal to those of the rotational one. That is:

$$\left(m_{lumped}^{translational}\right)_a = \left(m_{normalized}^{rotational}\right)_a$$

Rotational inertia is adjusted as follows:

$$\langle z_a \rangle = \frac{(z_a^+ + z_a^-)}{2},$$

$$[z_a] = z_a^+ - z_a^-,$$

$$\alpha_a = \frac{1}{2}\int_{-1}^{+1} z_a^2 \, dt = \langle z_a \rangle^2 + \frac{1}{12}[z_a]^2.$$

Average thickness is obtained from:

$$h_{avg} = \frac{\sum_{a=1}^{n_{en}} [z_a]}{n_{en}}.$$

Area and volume are respectively given by $A = V/h_{avg}$, and $V = \int_s \int_r \bar{J} \, dr \, ds$.

Finally,

$$(\alpha_a)_{max} = \max\left\{\alpha_a \text{ and } \frac{A}{8}\right\}$$

and

$$\left(m^{rotational}_{lumped}\right)_a = \left(m^{rotational}_{normalized}\right)_a \ (\alpha_a)_{max} \qquad \text{(no sum)},$$

where a is the node number. Note that there are 3 translational and 2 rotational degrees of freedom per node. Thus, repeating the $\left(m^{translational}_{lumped}\right)_a$ and $\left(m^{rotational}_{lumped}\right)_a$ values, respectively, 3 and 2 times, for each node, on the diagonal of the lumped mass matrix, gives:

$$[\ {}^{\tau}M_{ii}]_a = \begin{bmatrix} \left(m^{trans}_{lump}\right)_a & 0 & \cdots & & 0 \\ 0 & \left(m^{trans}_{lump}\right)_a & & & \\ \vdots & & \left(m^{trans}_{lump}\right)_a & & \vdots \\ & & & \left(m^{rot}_{lump}\right)_a & \\ 0 & & \cdots & & \left(m^{rot}_{lump}\right)_a \end{bmatrix}.$$

3.14.2 M2: Lumping the consistent mass matrix through row summing technique

We obtained the consisten mass matrix in the UL formulation from:

Equation 3.38

$$\left[\ {}^{\tau}M^{consistent}\right]_a = \int_s \int_r \int_{-1}^{+1} [\ {}^{\tau}N]_a^T\, [\ {}^{\tau}N]_a\, \rho\, J\, dt\, dr\, ds$$

where, for accuracy in large deformations (nonlinear analysis), the Jacobian determinant J and the interpolation matrix $[\ {}^{\tau}N]_a$ are updated for each configuration.

The consistent 5×5 mass matrix obtained from Equation 3.38 may be lumped using the row sum technique (Hughes, 2000, and Bathe, 1996):

$$\left[{}^{\tau}M^{consistent} \right]_a = \begin{bmatrix} (m_{11})_a & (m_{12})_a & \cdots & (m_{15})_a \\ (m_{21})_a & (m_{22})_a & & (m_{25})_a \\ \vdots & & \ddots & \vdots \\ (m_{51})_a & (m_{52})_a & \cdots & (m_{55})_a \end{bmatrix}$$

$$\xrightarrow{diagonalize} \quad [M_{ii}]_a = \begin{bmatrix} \left(\sum_{i=1}^{5} m_{1i}\right)_a & 0 & \cdots & 0 \\ 0 & \left(\sum_{i=1}^{5} m_{2i}\right)_a & & \vdots \\ \vdots & & \ddots & \\ 0 & \cdots & & \left(\sum_{i=1}^{5} m_{5i}\right)_a \end{bmatrix}.$$

3.15 Numerical integration for shell elements

In order to solve the integrals for the stiffness matrices and the force vectors, it is necessary to employ numerical integration (Bathe and Bolourchi, 1979). In this work, the Gaussian quadrature integration method is used for the isoparametric finite element analysis of the quadrilateral elements. In numerical analysis, a quadrature rule is an approximation of the definite integral of a function. It is usually stated as a weighted sum of function values at specified points within the domain of integration. Similar to parent coordinates, the domain of the integration for such a rule is conventionally taken as $[-1\,,\ 1]$.

The lamina shape functions and quadrature rules for the Lagrange elements (i.e. elements with internal nodes) are shown in Table 3.1. As shown in Table 3.1, a normal and a reduced Gaussian rule respectively refer to the cases, in which, the number of integration points are equal and less than that of the element nodes.

As formulated by Hughes and Liu (1980), if either the normal rule or the reduced rule is used solely, then the element is called a uniform integration element and if the normal and reduced rules are combined, the element is called a selective integration element.

Table 3.1: Normal and reduced Gaussian rules for Lagrange elements (Hughes and Liu, 1980).

	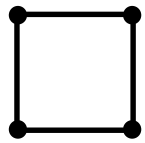	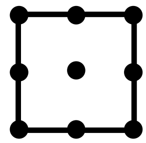	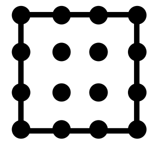
Lamina shape functions	Bilinear	Biquadratic	Bicubic
Normal Gaussian rule	2×2	3×3	4×4
Reduced Gaussian rule	1×1	2×2	3×3

In general, selective integration is used when both shear and membrane locking need to be avoided (i.e. in thin shell applications). However, a shortcoming of the classical selective integration method is that an explicit segregation of transverse shear terms from the other effects is required. In the general anisotropic nonlinear and nearly incompressible continuum applications, the segregation of effects is not possible. The reason is that full coupling between the effects may exist (Hughes and Liu, 1980). The same authors described a procedure which enables the attributes of selective and reduced integration to be attained in the formulation of a general anisotropic nonlinear and nearly incompressible shell element of heterosis type (i.e. a correct-rank and high accuracy general shell element with no numerical instabilities). However the cost of the complexity of the precedure did not add accuracy to the uniform normal integration procedure in case of the general shell elements. The interested reader is referred to (Hughes and Liu, 1988).

The above statements are in agreement with the arguments on the numerical integration scheme presented in Bathe and Bolourchi (1979) according to which: *"With higher order elements, no reduced integration is necessary to obtain accurate solutions. In general, shell analysis reduced integration in the evaluation of an element stiffness matrix must be employed with care and, in practice, is still best avoided. Furthermore, considering materially nonlinear* *analysis, a higher-order integration may be desirable anyway, in order to capture the variation in the constitutive relations."*

Considering that using reduced integration in general large displacement shell analysis adds complexity for no additional accuracy or advantage, uniform normal integration has been adopted in the present work.

In the general nonlinear case, fiber integrals must be evaluated by a numerical integration technique. Hughes and Liu (1980) suggested the following three methods for the fiber numerical integration and discussed the advantages inherent to each method.

1. If the shell consists of one homogenous elastic layer, then the integrand is a smooth function of t and thus the Gaussian quadrature is most efficient. If the reference surface is taken to be the midsurface $(\text{i.e. } \bar{t} = 0)$, then the 1-point Gauss rule (i.e. the midpoint rule) only senses the membrane effects. Therefore at least two points are required to resolve the bending behaviour.
2. If it is required to include the fiber points on the top and bottom surfaces of the shell $(\text{i.e. } t = \pm 1)$ in the evaluation, then the Lobatto rules are most accurate for smooth integrands. The first two members of the Lobatto family are namely the 2-point trapezoidal rule and the 3-point Simpson's rule.
3. For nonhomogeneous shell elements (example: biological soft tissues) that are built up from a series of layers of different materials in which the material properties and stresses may be discontinuous functions of t, the Gaussian rules may be effectively used over each layer. If there are a large number of approximately equal-sized layers, the midpoint rule on each layer is sufficient. However, if there are few layers or if the layers vary considerably in thickness, then different Gaussian rules should be assigned to individual layers.

Considering that only one homogeneous layer for the soft tissue under study is assumed herein, and considering that both membrane and bending behaviours are of interest, two integration points will be employed for the fiber integrations.

3.16 Critical time step

In an explicit scheme, convergence is ensured by respecting a maximum time step criterion, i.e. this method is numerically stable as long as $\Delta\tau < \Delta\tau_{critical}$. This critical time step is equal to:

$$\Delta\tau_{critical} = \frac{T_n}{\pi} = \frac{2}{\omega_n},$$

in which T_n is the smallest period of vibration in the finite element assemblage. Note that $T_n = \frac{2\pi}{\omega_n}$.

According to Bathe (1996), this time step restriction applies to both linear and nonlinear systems. The reason is that for each time step, the nonlinear response calculation can be approximated with linear analysis. However, whereas in the linear analysis the stiffness properties remain constant, in a nonlinear analysis these properties change with time. Since the value of T_n is not constant during the response calculation, the time step $\Delta\tau$ needs to be decreased if the system stiffens and increased if the system softens. Note that this time step adjustment must be performed such that the time step criterion is satisfied, that is:

$$\Delta\tau < \frac{2}{\omega_n}.$$

Natural frequencies occur when the forcing function is zero and damping is neglected, that is:

Equation 3.39

$$[\,{}^{\tau}M_{ii}]\{\,{}^{\tau}\ddot{u}\} + [{}^{\tau}_{\tau}K_L]\{\,{}^{\tau}u\} = \{0\}.$$

Let $\{u\} = \{\bar{u}\}e^{j\omega\tau}$ where, $j^2 = -1$ and $\{\bar{u}\}$ is the eigenvector corresponding to natural frequency ω. Then $\{\ddot{u}\} = (j\omega)^2\{\bar{u}\}e^{j\omega\tau} = -\omega^2\{\bar{u}\}e^{j\omega\tau}$. Substituting the aforementioned into Equation 3.39 gives:

$$(-\omega^2[\,{}^{\tau}M_{ii}] + [{}^{\tau}_{\tau}K_L])\{\bar{u}\}e^{j\omega\tau} = \{0\}.$$

For non-trivial solutions for $\{\bar{u}\}$,

Equation 3.40

$$\det(-\omega^2[\,{}^{\tau}M_{ii}] + [{}^{\tau}_{\tau}K_L]) = 0\,.$$

Therefore, Equation 3.40 must be solved to find the natural frequencies of the structure. However, solving for the determinant of a large square matrix and finding the roots of it can result in numerical overflow. The natural frequencies can easily be obtained by reducing Equation 3.40 to the standard eigen problem of the following form:

$$[{}_{\tau}^{\tau}K_L][\Phi] = [\,{}^{\tau}M_{ii}][\Phi][\Omega^2],$$

where, the columns of $[\Phi]$ are the eigenvectors $\{\phi_i\}$, and the entries of the diagonal matrix $[\Omega^2]$ are the eigenvalues ω_i^2 :

$$[\Phi] = [\{\phi_1\} \quad \{\phi_2\} \quad \cdots \quad \{\phi_n\}]$$

$$[\Omega^2] = \begin{bmatrix} \omega_1^2 & 0 & \dots & 0 \\ 0 & \omega_2^2 & 0 & \vdots \\ \vdots & & \ddots & 0 \\ 0 & 0 & 0 & \omega_n^2 \end{bmatrix}.$$

Considering individual eigenvectors and eigenvalues:

Equation 3.41

$$[{}_{\tau}^{\tau}K_L]\{\phi\} = \omega^2[\,{}^{\tau}M_{ii}]\{\phi\}.$$

Considering that $[{}_{\tau}^{\tau}K_L]$ is symmetric, and $[\,{}^{\tau}M_{ii}]$ is non-singular (i.e is invertible and its determinant is not zero), Equation 3.41 can be reduced to the standard eigenproblem form ($[A]\{x\} = b\{x\}$, where $[A]$ is symmetric) using the following steps:

Step 1: premultiply both sides by $[\,{}^{\tau}M_{ii}]^{-1}$. Knowing that $[\,{}^{\tau}M_{ii}]^{-1}[\,{}^{\tau}M_{ii}] = [I]$, the above reduces to (Felippa, 2014): $[\,{}^{\tau}M_{ii}]^{-1}[{}_{\tau}^{\tau}K_L]\{\phi\} = \omega^2\{\phi\}$,

Step 2: premultiply both sides by $[\,{}^{\tau}M_{ii}]^{1/2}$ to get: $[\,{}^{\tau}M_{ii}]^{-1/2}[{}_{\tau}^{\tau}K_L]\{\phi\} = \omega^2[\,{}^{\tau}M_{ii}]^{1/2}\{\phi\}$,

Step 3: knowing that $[\,{}^{\tau}M_{ii}]^{-1/2}[\,{}^{\tau}M_{ii}]^{1/2} = [I]$, rewrite the above as:
$[\,{}^{\tau}M_{ii}]^{-1/2}[{}_{\tau}^{\tau}K_L][\,{}^{\tau}M_{ii}]^{-1/2}[\,{}^{\tau}M_{ii}]^{1/2}\{\phi\} = \omega^2[\,{}^{\tau}M_{ii}]^{1/2}\{\phi\}$,

Step 4: letting $[\,{}^{\tau}M_{ii}]^{1/2}\{\phi\} = \{\phi'\}$ the above becomes:

$$[\,{}^{\tau}M_{ii}]^{-1/2}[{}_{\tau}^{\tau}K_L][\,{}^{\tau}M_{ii}]^{-1/2}\{\phi'\} = \omega^2\{\phi'\},$$

Since $[\,^{\tau}M_{ii}]$ is a diagonal matrix and since $[^{\tau}_{\tau}K_L]$ is symmetric, the product of $[\,^{\tau}M_{ii}]^{-1/2}[^{\tau}_{\tau}K_L][\,^{\tau}M_{ii}]^{-1/2}$ is symmetric and thus the eigenvalues $(\omega^2)_i$ are real.

Therefore, using Equation 3.42, Matlab generates a column vector λ whose entries are $(\omega^2)_i$:

Equation 3.42

$$\lambda = \mathrm{eig}\big([\,^{\tau}M_{ii}]^{-1/2}[^{\tau}_{\tau}K_L][\,^{\tau}M_{ii}]^{-1/2}\big).$$

In general, $\Delta\tau_{critical}$ is related to the stiffness of the elements, through $(\omega_i)_{max}$, which varies with the load in nonlinear systems, therefore $\Delta\tau_{critical}$ needs updating during the calculations, as already mentioned. To avoid stability problems, the time step employed in the analysis must be smaller than the calculated critical time step. That is:

Equation 3.43

$$\Delta\tau = \frac{\Delta\tau_{critical}}{n}$$

where, the safety factor n is larger than 1.

3.17 Operation count

As mentioned at the outset, the purpose of this work is to develop a CB shell FE that provides a good combination of accuracy and efficiency compared to existing CB shell FEs. Considering that existing CB shell FEs were formulated in different programing languages and run on machines with dissimilar capabilities, the CPU times reported in the literature is not a neutral measure for efficiency comparisons. We believe the operation count (i.e. counting the total number of loops/iterations) to be a more equitable means of comparison. The FE formulations normally follow the main routine presented in Figure 3.3, from which the number of operations can be evaluated (ABAQUS, 2005, LS-DYNA, 2011, Segal, 2010, Bathe, 1996, Miller et. al., 2007, ANSYS, 2008, FEAP, 2012). Note that with the explicit method, the outer loop over load increments does not exist.

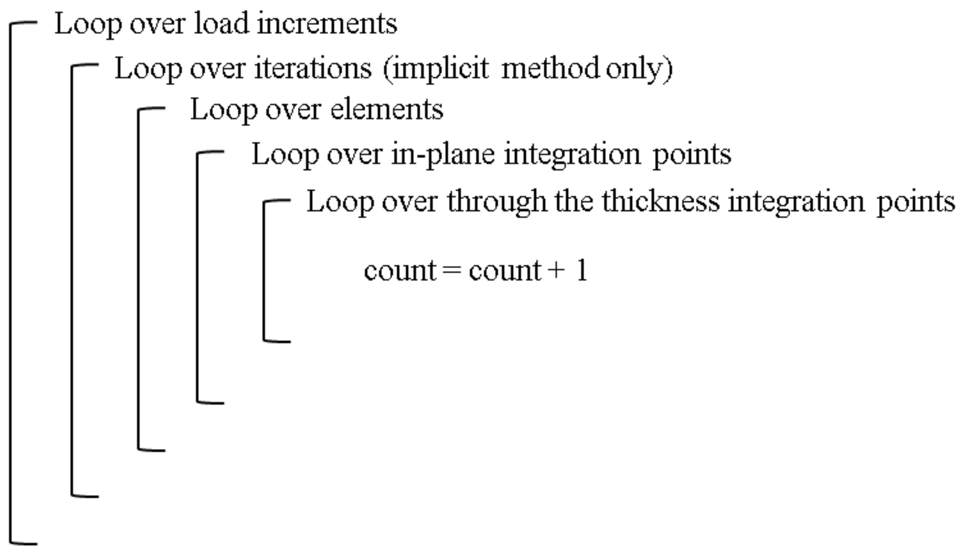

Figure 3.3: Main routine and operation count.

3.18 Numerical implementation of the present CB shell FE

It was concluded from Sections 2.3, 2.4, and 2.5.3 that a nonlinear anisotropic incompressible hyperelastic CB shell finite element for the formulation of soft tissue dynamics using explicit time integration did not exist in the literature or in any of the available software packages. Given the novelty of the proposed shell theory, serious theoretical and programming modifications to the existing software packages was required. Therefore, it was deemed more efficient to bypass this obstacle and program the shell theory from scratch.

As detailed out in Chapter 3, it was required to compute multiplications, derivatives and integrals of large matrices at each time step. Some well-known numerical computing environments that have built-in functions with the aforementioned capabilities are Matlab, Mathematica, and Maple. Due to its convenience and availability, Matlab was employed for the implementation of the proposed shell theory.

The present 9-noded CB shell FE was implemented in Matlab (Version R2016a, MathWorks Inc., USA), and all the FE analyses were carried out on a workstation with two Intel Xeon E5640 2.67 GHz 8-core processor and 32 GB of RAM. The workflow of the numerical implementation, presented in Figure 3.4, resulted in about 2600 lines of code. We paired our

Matlab code with the preprocessor module of GiD (Version 12.0.6, CIMNE, Spain) for its convenience to create the geometry, mesh, and connectivity table. In addition, using GiD, generation of the nodal point coordinates, as well as the prescription of the loading and boundary conditions was made much more efficient. Due to GiD's limitation in illustrating curved edges in its postprocessor module, we postprocessed our results entirely in Matlab.

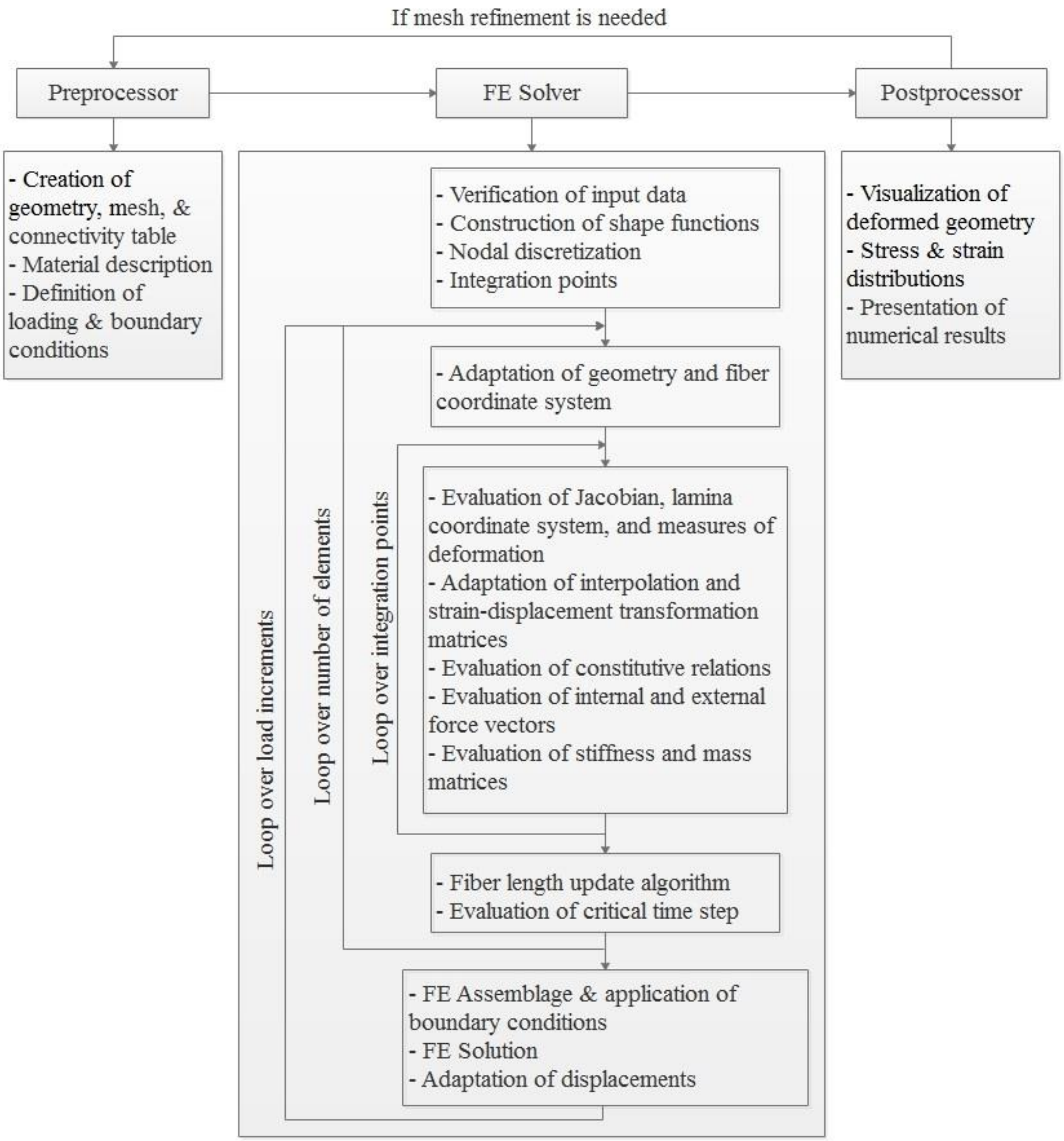

Figure 3.4: Flowchart of the numerical implementation of the present CB shell FE.

CHAPTER 4: RESULTS AND DISCUSSION OF NUMERICAL TESTS

To establish the accuracy and efficiency of the present CB shell FE, it was submitted to a range of de facto standard test problems presented in many references. In particular, the element was tested for: combined small membrane (in-plane) and small bending deformations in two planes (Test 1), medium bending deformation (Test 2), medium pure bending deformation of initially irregular elements (Test 3), large pure bending deformation (Test 4), combined membrane and bending deformations of an initially curved structure (Test 5), pre-twist and bending deformations in two planes (Test 6), stress convergence and the effect of incompressibility on a thick-walled cylinder (Test 7), insensitivity to large in-plane distortions and large membrane strains of initially irregular elements (Test 8), as well as the combined large 3D deformations (combined bending, shear, and membrane deformations) of thick and thin cylinders (Tests 9 and 10). In addition, the accuracy of the three Techniques, implementation of material incompressibility, and the application of the plane stress condition (all presented in Section 3.10), as well as the fiber length update algorithm (Section 3.11) were verified in the context of nonlinear hyperelastic material properties (Tests 8 to 10). Furthermore, the accuracy and efficiency of the mass matrices presented in Section 3.14 are studied in Tests 4, 9, and 10. For each test, analytical solutions are provided as references.

4.1 Small strain analysis of linear elastic materials: insensitivity to initially irregular elements and/or geometries, large deformations and rotations, shear and membrane locking

4.1.1 Test 1: Linear elastic, small bending deformation and rotations, small strains

A dynamic analysis of a simply supported aluminium square plate subjected to a step normal uniform pressure (Figure 4.1) was carried out and the results were compared with the analytical linear static solution (Kanoknukulchai, 1979) and other finite elements introduced in Bathe and Bolourchi, 1979; Liu and Lin, 1979; Belytschko et. al., 1983 (Table 4.1). The maximum deflection in the center of the plate versus time (i.e. the dynamic response due to a step pressure) obtained from the present 1 shell and 4 shells per quarter meshes are presented in Figure 4.2. In addition, vertical displacements at the maximum deflection obtained from the 4 shells per quarter mesh is illustrated in Figure 4.3.

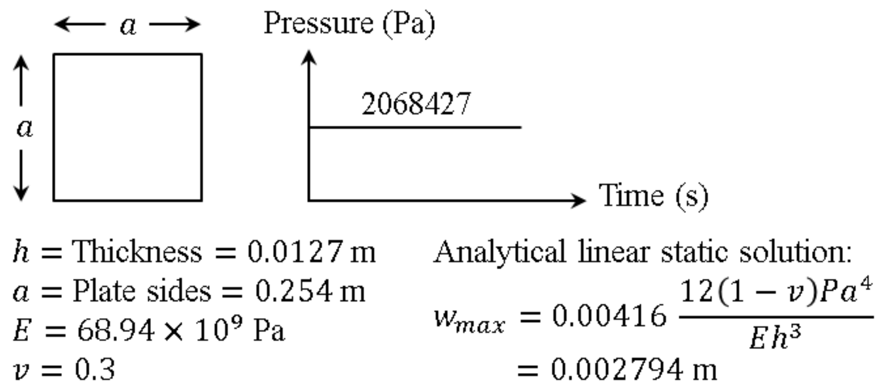

Figure 4.1: Geometry, loading condition, and analytical linear static solution.

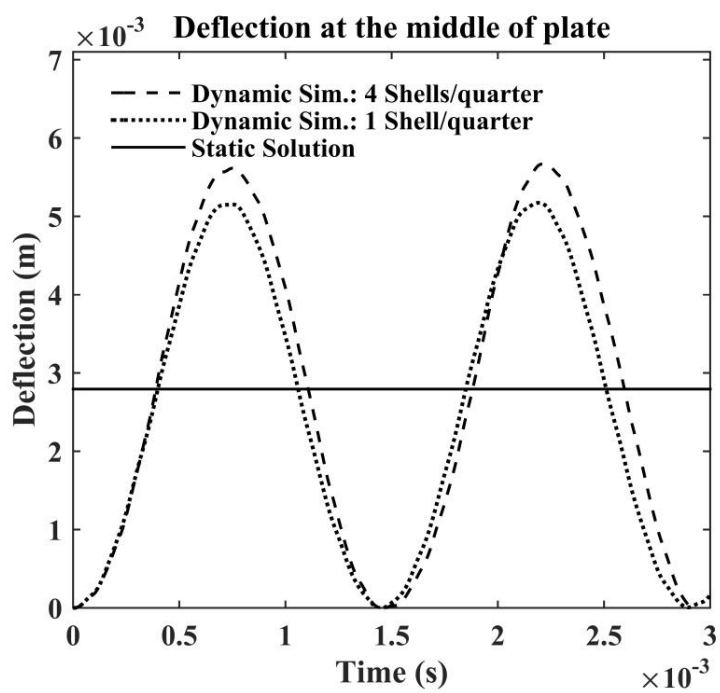

Figure 4.2: Dynamic response of the simply supported plate due to step pressure.

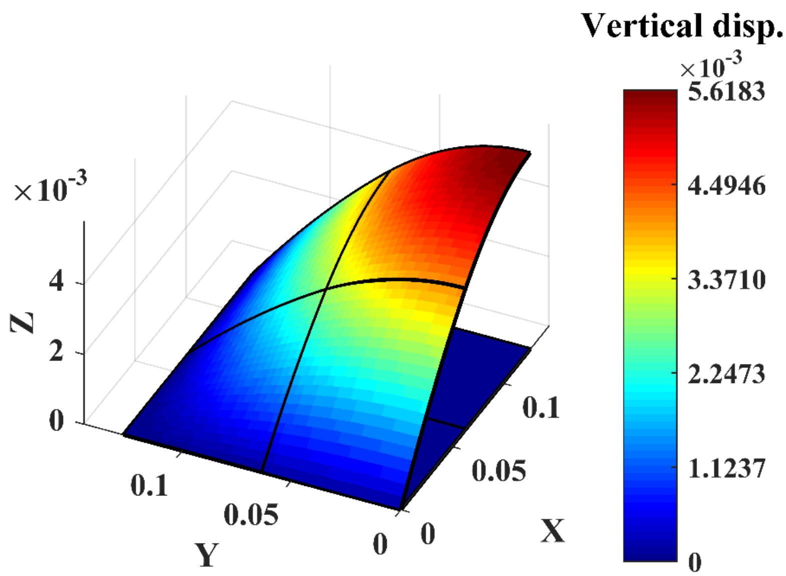

Figure 4.3: Vertical displacements at the maximum deflection obtained from the 4 shells per quarter mesh. Units are in meters.

As expected from the step loading condition and absence of damping in the analysis, the dynamic response oscillates at constant amplitude with a magnitude almost equal to the analytical linear static solution (Figure 4.2). The difference between the amplitude of the dynamic simulation and the analytical static solution translates into the error calculated by:

Equation 4.1

$$error = \frac{amplitude - w_{max}^{analytical}}{w_{max}^{analytical}} \times 100\% \,.$$

As presented in Table 4.1, use of only one of our 9-noded CB shell FE to model one quarter of the simply support plate under uniform normal pressure, required only 1,404 loops to reach the maximum deflection with an error of −7.2%. This error was 1.8% less than that of (Belytschko et al., 1983), while the operation count was 1.1 times smaller. Comparing the present 1-shell-per-quarter mesh with those in (Bathe and Bolourchi, 1979) and (Liu and Lin, 1979), it was only 4.9% less accurate, but ran 6.4 times faster than that in (Bathe and Bolourchi, 1979). Although no information in regards to the numerical integration was provided in (Liu and Lin, 1979), considering the load increments, element numbers, and assuming the fewest integration points (1×1×1), our computations was still 1.4 times faster. Knowing that increasing the number of elements (mesh refinement) decreases the error in the convergence of the solution, we repeated this test using four of the present 9-noded CB shell FE per quarter and achieved an error of −1.2%. This was 1.1% more accurate, and about as efficient as (Bathe and Bolourchi, 1979). The four-element mesh was also 7.8% more accurate than (Belytschko et al., 1983) but the operation count was about 5 times larger. The authors of (Belytschko et al., 1983) considered 2D analysis (i.e. in-plane stresses and in-plane deformations only) and used one-point quadrature rule for the numerical integration of their element. To avoid the resulting numerical ill-conditioning, they implemented hourglassing control. However, no information on the expense of this control on the computation time was provided. Overall, the best combination of accuracy and efficiency was achieved by employing four of the present CB shell FE per quarter of the plate.

Table 4.1: Results of Test 1.

	(Bathe & Bolourchi, 1979):	**(Liu & Lin, 1979):**	**(Belytschko et al., 1983):**	**Present:**	**Present:**
Mesh per quarter	9 plates	16 plates	16 plates	1 shell	4 shells
Element type	8-noded	4-noded	4-noded	9-noded	9-noded
Integration points	2×2×2	NA	1×1×1	3×3×2	3×3×2
Error (Equation 4.1)	+ 2.3 %	− 2.3 %	− 9.0 %	− 7.2 %	− 1.2 %
Time integration	Implicit	Implicit	Explicit	Explicit	Explicit
Average Δt (s)	2.2×10^{-5}	2.2×10^{-5}	6.0×10^{-6}	8.4×10^{-6}	4.2×10^{-6}
Increments to max. deflection	125	125	100	78	121
Total loops to max. deflection (Figure 3.3)	9,000	2,000×NA	1,600	1,404	8,712

4.1.2 Test 2: Elastic, moderate bending deformations and rotations, small strains

Although the results obtained from Test 1 were promising, the analysis was limited to small bending deformations (linear analysis). To verify the accuracy and efficiency of our CB shell FE in large bending deformations (nonlinear analysis), we conducted Test 2. In this test, a dynamic analysis of a cantilevered beam subjected to a large step normal uniform pressure (Figure 4.4) was carried out. The large magnitude of the uniform pressure resulted in moderate bending deformations (nonlinear response), but small strains. Distribution of vertical displacements at the maximum deflection obtained from 3-element mesh is illustrated in Figure 4.5. Results obtained in this study were compared with the analytical nonlinear static solution obtained from page 17 of (Sathyamoorthy, 1997) and another finite element introduced in (Shantaram et al., 1976) (Table 4.2).

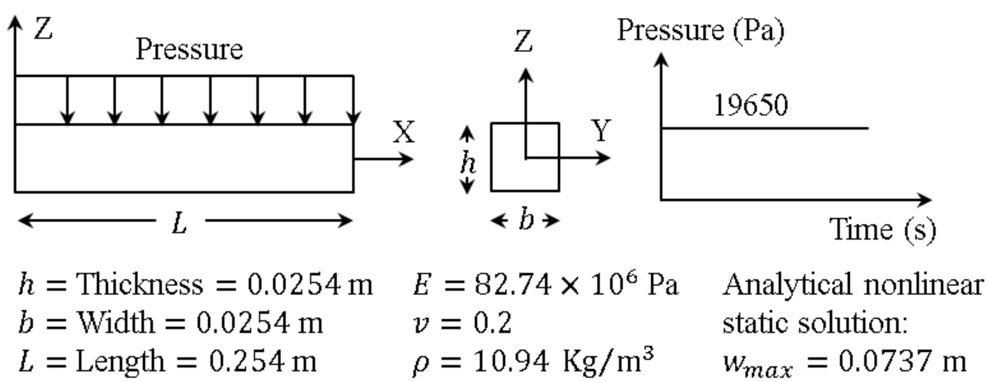

Figure 4.4: Geometry, loading condition, and analytical nonlinear static solution.

According to Table 4.2, using two of the present CB shell FE resulted in an error 0.9% larger than that achieved in (Shantaram et al., 1976), but the number of operations was about 1.3 times smaller. In the process of mesh refinement, we employed three of our CB shell finite elements. This, in comparison with (Shantaram et al., 1976), resulted in an error 0.6% lower and a computation count 1.1 times larger. Considering a good efficiency and accuracy combination, either the two-element or the three-element mesh of the present 9-noded CB shell FE did a good job of analysing the large deflection of this cantilever beam.

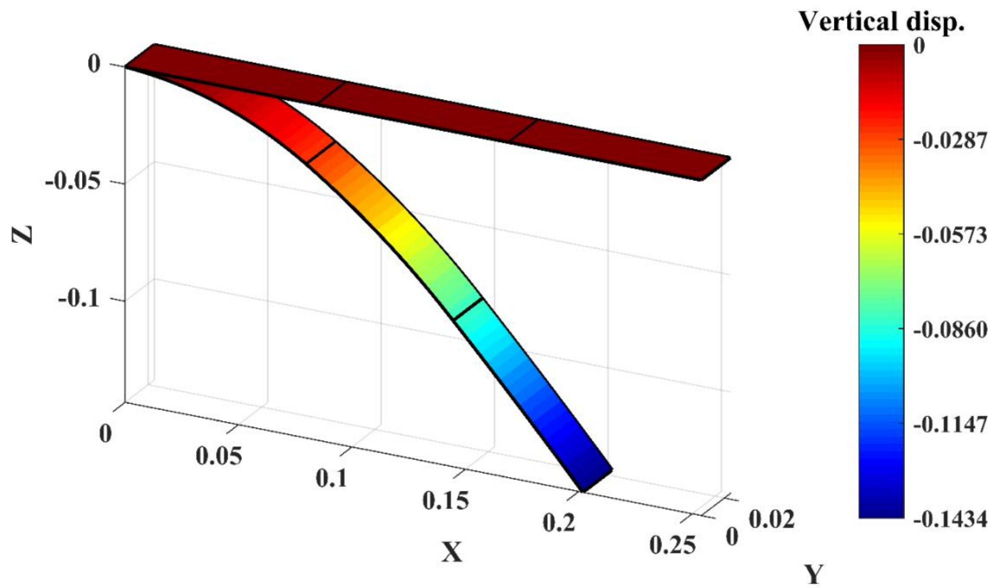

Figure 4.5: Vertical displacements at the maximum deflection obtained from 3-element mesh. Units are in meters.

Table 4.2: Results of Test 2.

	(Shantaram et al., 1976):	Present:	Present:
Mesh	5 plates	2 shells	3 shells
Element type	8-noded	9-noded	9-noded
Integration point	2×2×1	3×3×2	3×3×2
Error (Equation 4.1)	+ 3.4 %	− 4.3 %	− 2.8 %
Time integration	Explicit	Explicit	Explicit
Average Δt (s)	2.0×10^{-6}	3.7×10^{-6}	3.6×10^{-6}
Total loops to max. deflection (Figure 3.3)	33,000	25,056	37,638

The high accuracy achieved in Tests 1 and 2, even with few elements, was allowed by the fact that the limitation on the bending deformations/rotations (shear locking) was eliminated by the application of two independent coordinate systems. Thus, our CB shell FE has truly large bending deformation capabilities. Also, considering Tests 1 and 2, our calculated Δt (Section 3.16) was much larger than the Δt calculated in (Shantaram et al., 1976; Belytschko et al., 1983; Bathe and Bolourchi, 1979; Liu and Lin, 1979), obtained from dividing the thickness of the element by the sound speed (obtained from the material properties of the element). Although this approach is also used in (LS-DYNA, 2011) for solid (3D) shell elements, the present time step control is more efficient.

4.1.3 Test 3: Elastic, moderate pure bending deformations and rotations, small strains

Through Test 2, we verified the accuracy and efficiency of the geometric nonlinear behaviour (i.e. large bending deformation) of the present CB shell FE when used as initially regular geometry. However, as reported in (Bathe et al., 1983), higher order shell elements (i.e. quadrilateral elements that include more than four nodes) are generally sensitive to using elements that have irregular geometries in the undeformed configuration, and lock in large (nonlinear) bending deformations. Hence, in Test 3, we studied the effect of using initially irregular element mesh in the large deflections of a cantilever beam. Basically, the cantilevered beam shown in Figure 4.6 was analyzed for its small strain, moderate displacement and moderate rotation (up to 90 degrees) response due to a concentrated end moment (i.e. moderate pure bending deformation), and the results were verified against the static analytical solution derived from page 54 of (Sathyamoorthy, 1997). The idealization was done using regular and irregular 3-element, as well as regular and irregular 4-element (of the present 9-noded CB shell) meshes (Figure 4.7). Deformation of the cantilever beam at the maximum load configuration, using the irregular 4-element mesh is illustrated in Figure 4.8. The tip displacement ratios (numerical over analytical) of the irregular 3-element mesh evaluated from this study and those tabulated in (Dvorkin, 1995) are presented in Table 4.3. Figure 4.9 shows axial, transverse and rotational displacement ratios vs. moment parameters due to the applied tip moment for the 3- and 4-element meshes.

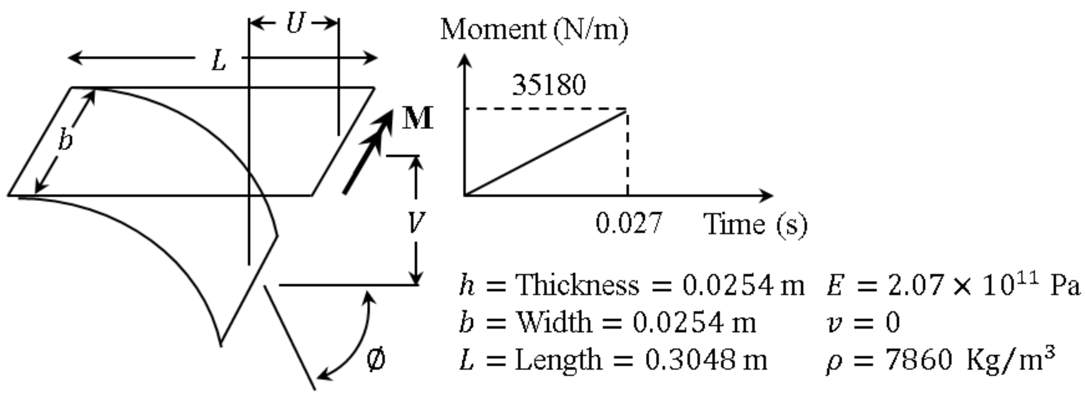

Figure 4.6: Geometry, loading condition, and material properties.

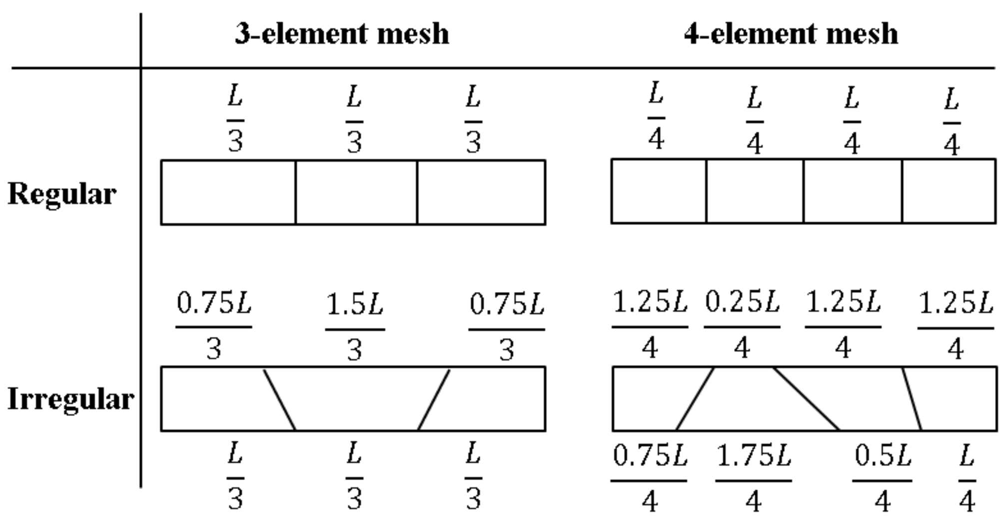

Figure 4.7: Schematic of the four meshes considered.

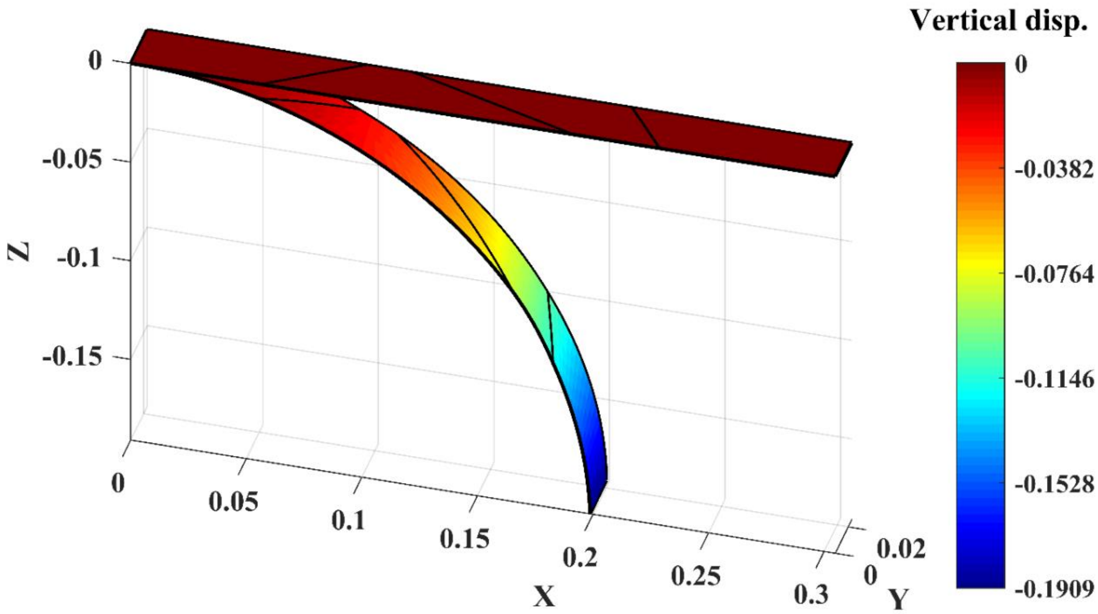

Figure 4.8: Deformation of the cantilever beam at the maximum load configuration, using the irregular 4-element mesh. Units are in meters.

Table 4.3: Results of Test 3.

	(Dvorkin, 1995): Irregular 3-element (4-noded) mesh			**Present: Irregular 3-element (9-noded) mesh**		
ϕ^{Analyt}	18°	45°	72°	18°	45°	72°
Moment parameter	0.05	0.125	0.2	0.05	0.125	0.2
ϕ^{Num}/ϕ^{Analyt}	0.95	0.84	0.76	1.05	1.02	0.93
U^{Num}/U^{Analyt}	0.89	0.68	0.56	1.06	1.03	0.85
V^{Num}/V^{Analyt}	0.95	0.86	0.81	1.02	1.01	0.94

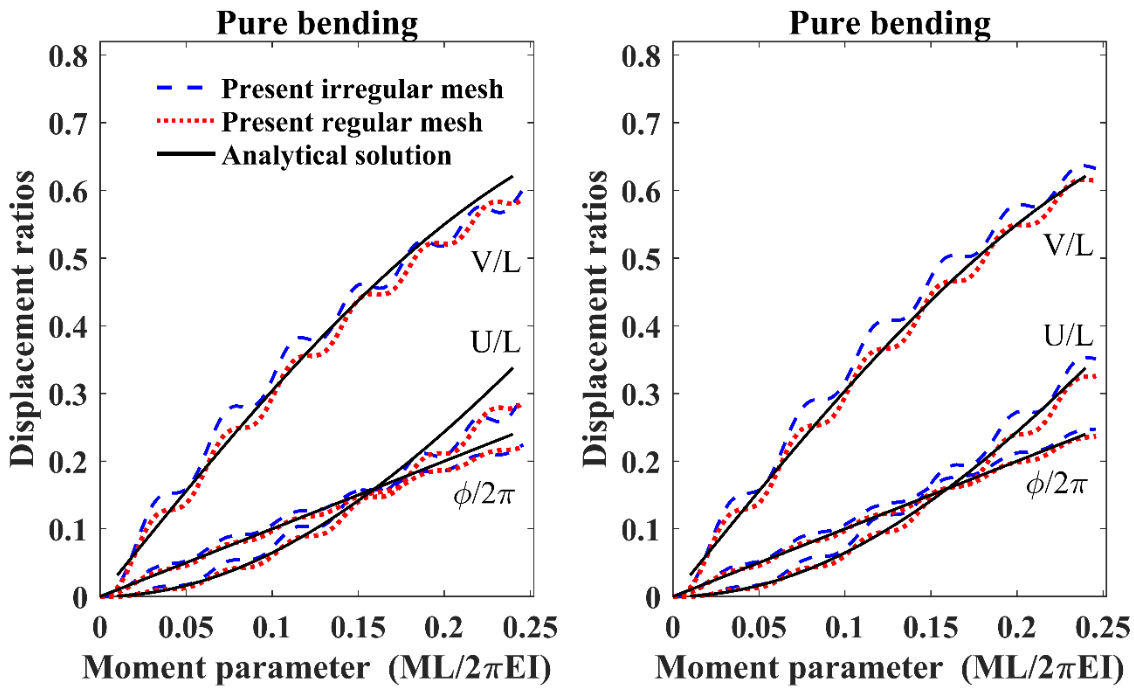

Figure 4.9: Pure bending of a cantilever beam. Left: 3-element mesh; Right: 4-element mesh.

Considering that we performed dynamic analysis using the explicit method (i.e. no equilibrium iteration per load increment is performed), the accurate comparison with the static analytical solution requires the dynamic amplification factor (causing the response oscillation amplitudes) to be minimized. Thus, we applied the moment as a ramp with a low loading rate (Figure 4.6). As presented in Figure 4.9, left, the regular 3-element mesh yielded a very accurate response solution up to 45 degrees (approximated to the moment parameter of 0.125), but the accuracy in the response degraded slightly for larger bending deformations up to 90 degrees (approximated to the moment parameter of 0.25). As expected, we achieved a more accurate large deflection response by refining the mesh to four regular elements (Figure 4.9, right). Still, regardless of the number of elements used, the predictive capabilities of the present 9-noded CB shell FE were insensitive to the irregularity of the mesh. That is, both the irregular (3- and 4-element) meshes closely resembled the response of the corresponding regular mesh, and were accurate (Figure 4.9, left and right, respectively). This claim is backed up by Table 4.3, in which, the normalized (numerical/analytical) tip (axial, transverse and rotational) deflection ratios obtained at different bending rotations and/or moment parameters from the present irregular 3-element mesh are very close to unity. In addition, the present ratios are much closer to unity in comparison with those tabulated in (Dvorkin, 1995). Specifically, at a small bending deformation of 18°, the tip rotational and transverse normalized displacements obtained from the present study and (Dvorkin, 1995) are very close to unity (the numerical solutions were at most 5% off from the analytical ones). At the same deformation, the axial tip deflection obtained in the present study was off by 6% only, whereas that of (Dvorkin, 1995) was off by 11% from the analytical one. Although the present irregular 3-element mesh responded accurately as the bending deformation increased to 45° (rotational, axial and transverse solutions were only off by 2%, 3% and 1% from the corresponding analytical solutions), the discrepancies of these solutions obtained in (Dvorkin, 1995) jumped to 16%, 32% and 14%, respectively. The accuracy of the response of the irregular mesh containing three of the present 9-noded CB shell FE was best validated against the theoretical solution at the bending deformation of 72°, where the rotational, axial and transverse deflections were, respectively, off by 7%, 15% and 6% only, whereas, those in (Dvorkin, 1995) were off by 24%, 44%, and 19%, in that order. Thus, not only was the formulation of the present 9-noded CB shell FE more straightforward than the mixed interpolation tensorial components used in (Dvorkin and Bathe, 1984), (Bucalem and Bathe, 1993), and (Dvorkin, 1995), but it was also more accurate and more insensitive to initially irregular elements in large bending deformations. One asset in this regard is the derivation of the lamina coordinate system, discussed in Section 2.5.1.2.2.

4.1.4 Test 4: Elastic, large pure bending deformations and rotations, small strains

So far, the bending deformations were limited to 90°, thus either Hughes' fiber coordinate system algorithm (Section 2.5.1.2.3) or the present fiber coordinate system algorithm (Section 3.3.2) does an accurate job. To demonstrate the limitation of the Hughes' fiber coordinate system algorithm discussed in Section 3.3.1, and to evaluate accuracy of the present fiber coordinate system algorithm (Section 3.3.2) we performed Test 4. In this test, the cantilever beam shown in Figure 4.10 was modeled using 15 of the present 9-noded CB shell FEs, to analyse for its small strain, large displacement and large rotation (0° − 360° degrees) due to a concentrated end moment (i.e. large pure bending deformation). Failure in large bending deformations due to the limitation of the Hughes' fiber coordinate system is illustrated in Figure 4.11. To validate the robustness of the present fiber coordinate system, and the effect of the mass matrices of Section

3.14 on the response, the FE results are plotted (Figure 4.12: moment versus tip axial and transverse displacements) against those of the static analytical solution (Sathyamoorthy (1997), page 54). Finally, the deformed shape of the cantilever beam at the maximum load configuration obtained from the present fiber coordinate system (Section 3.3.2) and M1 (mass matrix of Section 3.14.1) is illustrated in Figure 4.13.

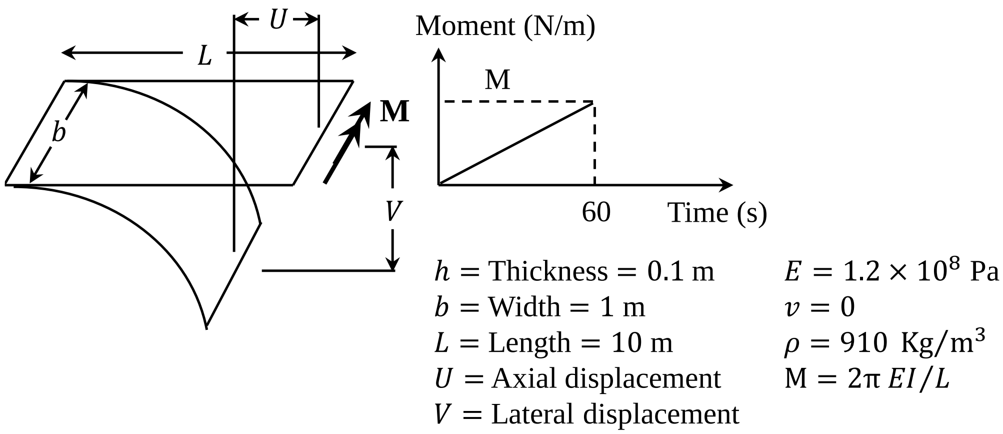

Figure 4.10: Geometry, loading condition, and material properties.

In this test, 15 of the present 9-noded CB shell FE elements were used to model pure bending deformation of an initially flat cantilevered element. As expected, the employment of Hughes' fiber coordinate system induced twisting in the cantilevered beam, where pure tip bending moment was modeled (Figure 4.11). The good accuracy between the present FE model and the analytical solution for all range of bending deformations ($0° - 360°$), as illustrated in Figure 4.12, is an indication of the reliability of the present algorithm for updating the fiber coordinate system, as well as the insensitivity of the present CB shell FE to shear and membrane locking even though very large bending deformations (360°) are considered. As far as the effect of mass matrices on the accuracy of the results is considered, the axial end displacements obtained from both mass matrices are almost identical, with an error of 1.34% at the max load configuration. The transverse load displacements are also identical up to 90% of the maximum load, but the error obtained from M2 at the max load configuration is about 7% larger than that of M1, thus, proving M1 more reliable in extreme deformation configurations. Ultimately, the deformed shape resulted from the present fiber coordinate system (in combination with M1) matches the expected circular shape (Figure 4.13).

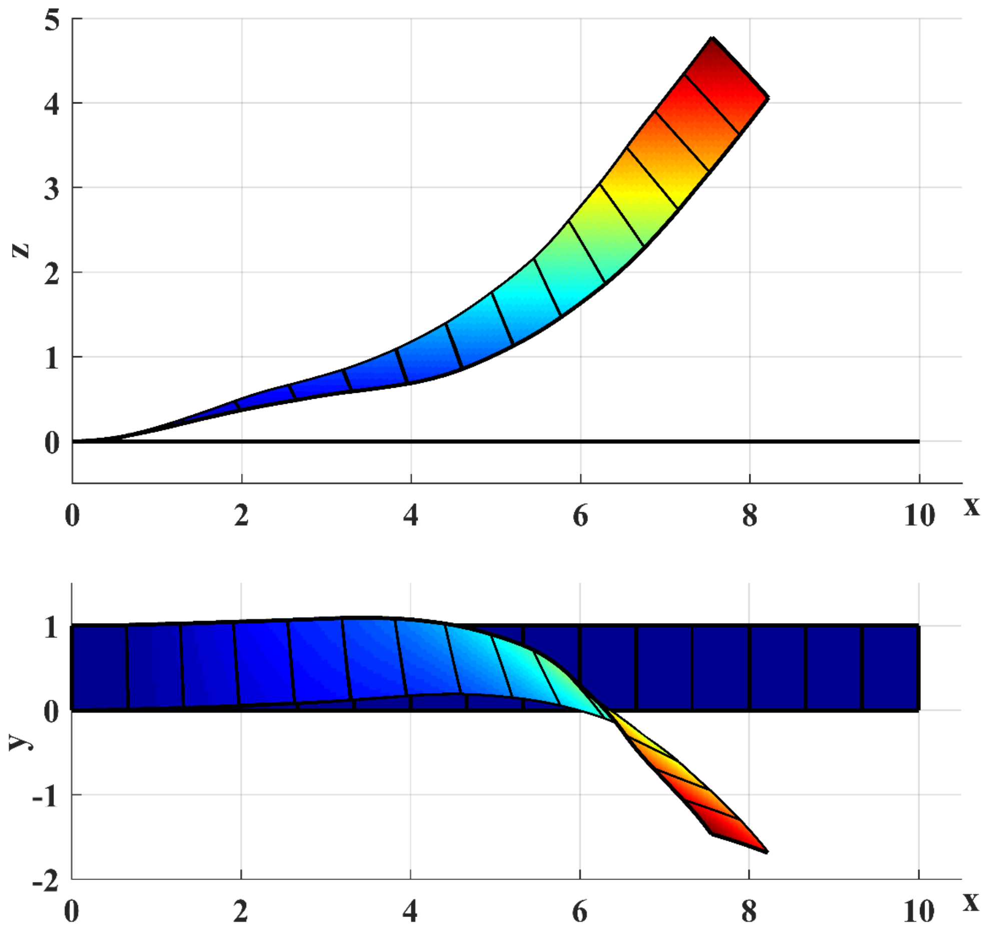

Figure 4.11: Failure in the deformation of the cantilever beam subjected to a pure tip bending moment due the limitation of the former fiber coordinate system, as discussed in Section 3.3.1 . Units are in meters.

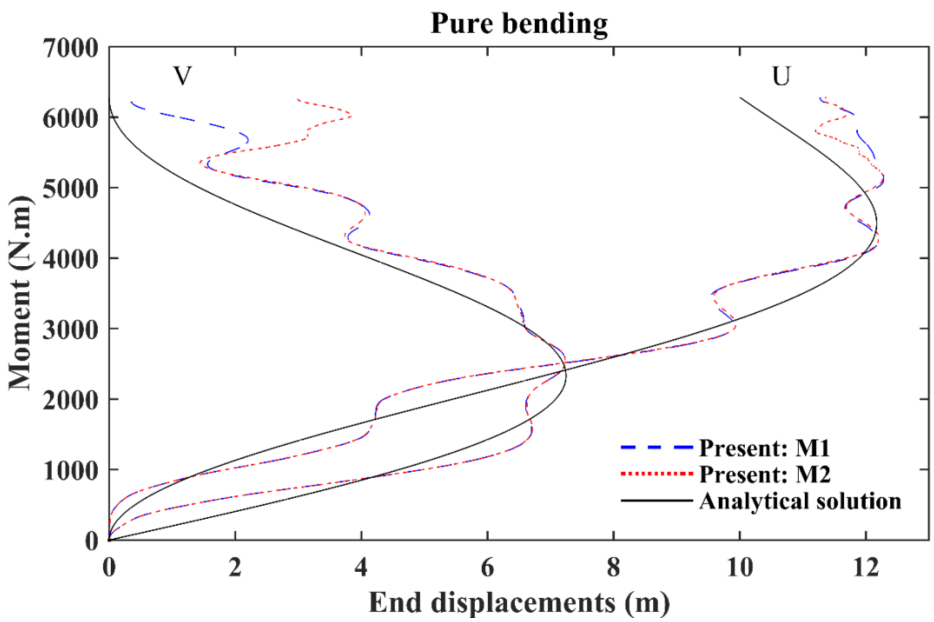

Figure 4.12: Comparison between the end displacements, in large pure bending of a cantilever beam, obtained from M1 (mass matrix presented in Section 3.14.1) and M2 (mass matrix presented in Section 3.14.2). In both cases, the new fiber coordinate system (Section 3.3.2) is employed.

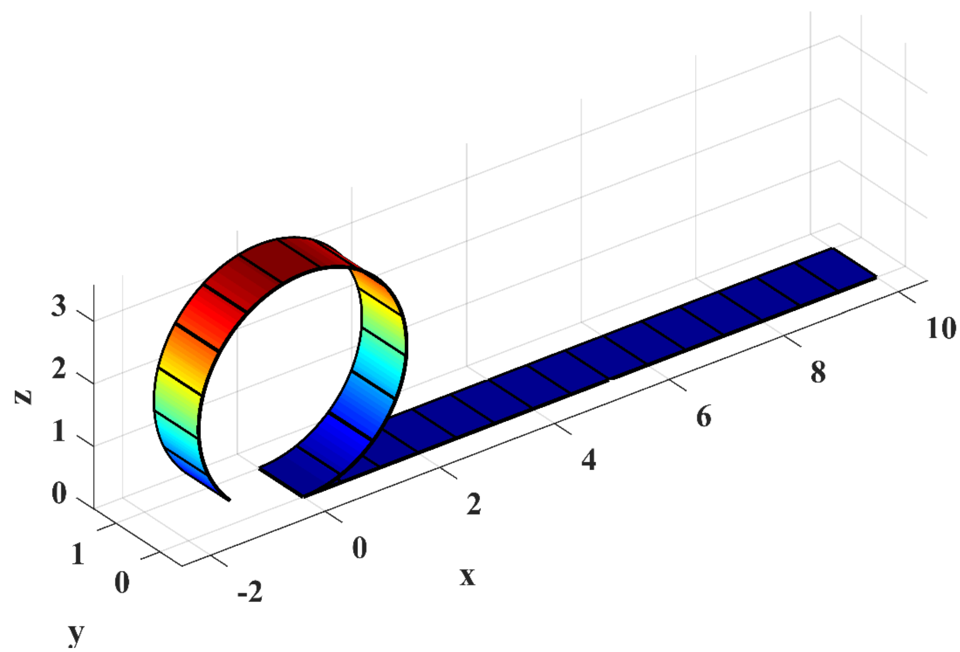

Figure 4.13: Deformation of the cantilever beam at the maximum load configuration obtained from the new fiber coordinate system (Section 3.3.2) and M1 (mass matrix of Section 3.14.1). Units are in meters.

4.1.5 Test 5: Scordelis-Lo roof, initially singly-curved, membrane and bending deformation

It is worth noting that because the present CB shell FE has proven accurate and efficient in large bending deformations (Tests 1 to 4), it properly handles curvatures, whether initial or acquired. However, to further verify this claim, we conducted Test 5. Figure 4.14 illustrates the geometry, material properties, boundary conditions, and loading condition of a Scordelis-Lo roof (singly-curved shell structure) subjected to a uniform pressure in the vertical Z-direction. The test result most frequently displayed is the vertical displacement at the midpoint of the free edge. The theoretical value for this result is 0.3086 (MacNeal and Harder,1985; Zienkiewicz, 1977), but most elements converge to a slightly lower value (e.g. 0.302 as reported in Comsol, 2006). Convergence due to mesh refinement in this study is presented in Figure 4.15. Figure 4.16 illustrates the vertical displacements in region 1 with a 6×6 mesh.

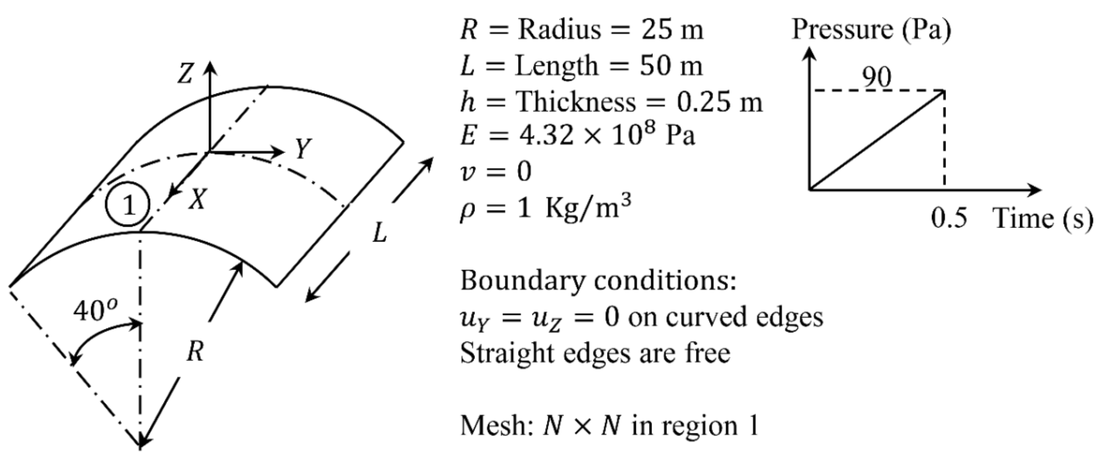

Figure 4.14: Geometry, material properties, boundary conditions, and loading condition for a Scordelis-Lo roof.

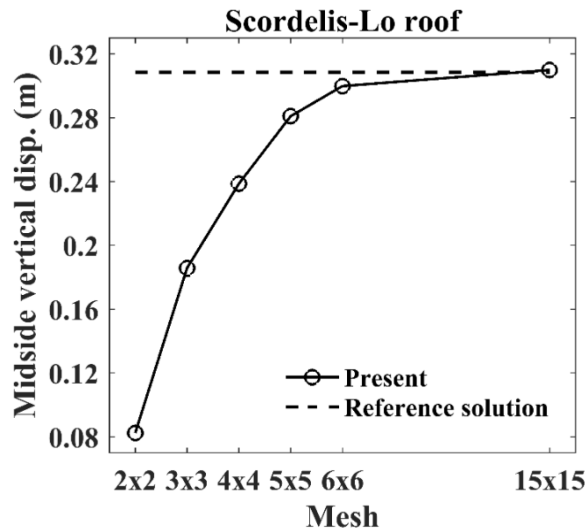

Figure 4.15: Convergence of Test 5 to the analytical solution.

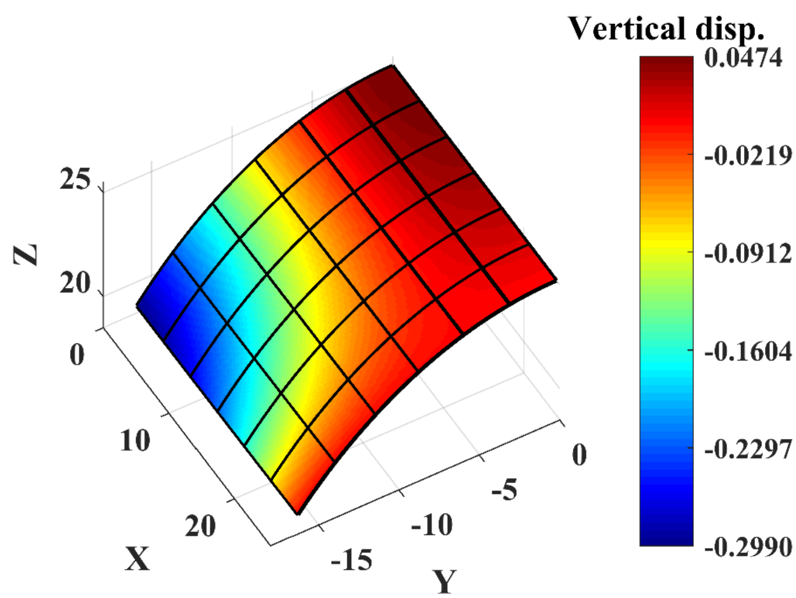

Figure 4.16: Vertical displacement in region 1 of the Scordelis-Lo roof with a 6×6 mesh. Units are in meters.

In this test, both in-plane (membrane) and bending deformations contribute significantly to this singly-curved structure. Using a 6×6 mesh of the present 9-noded CB shell FE the displacement convergence with an error of 2.8% was achieved (Figure 4.15 and Figure 4.16).

This proves the present CB shell FE more accurate and more efficient than the COMSOL's 4-noded quadrilateral element (Comsol, 2006), and less accurate and less efficient than the 8-noded quadrilateral element in (MacNeal and Harder, 1985), where a mesh of 24×24 and a mesh of 2×2 are respectively needed to obtain the same percent error.

4.1.6 Test 6: Large pre-twist, bending deformation in both planes

This test is considered as a common benchmark problem to determine the effects of warping in shell and solid finite elements (MacNeal, 1976; MacNeal and Harder, 1985). The geometry, material properties, and loading condition of a cantilevered beam with an overall pre-twist of 90° are illustrated in Figure 4.17. The theoretical solutions of tip deflections in the direction of loading are 0.005424 (in) and 0.001754 (in) for independent tip loading of one unit in the X- and Y-directions, respectively (MacNeal, 1976; MacNeal and Harder, 1985; Pakravan and Krysl, 2016). Convergence due to mesh refinement of the normalized (numerical/theoretical) displacements is presented in Figure 4.18. Displacement in X-direction using 8 elements along the pre-twisted cantilevered beam are illustrated in Figure 4.20

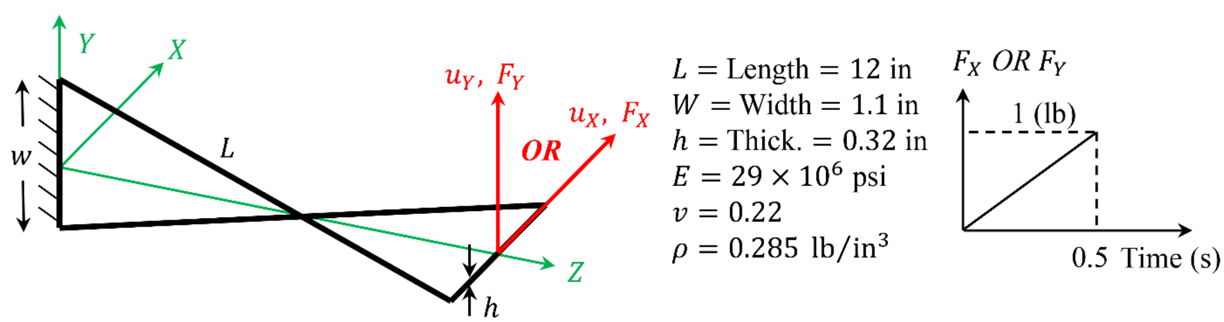

Figure 4.17: Geometry, material properties, and loading condition of a cantilevered beam with an overall pre-twist of 90°.

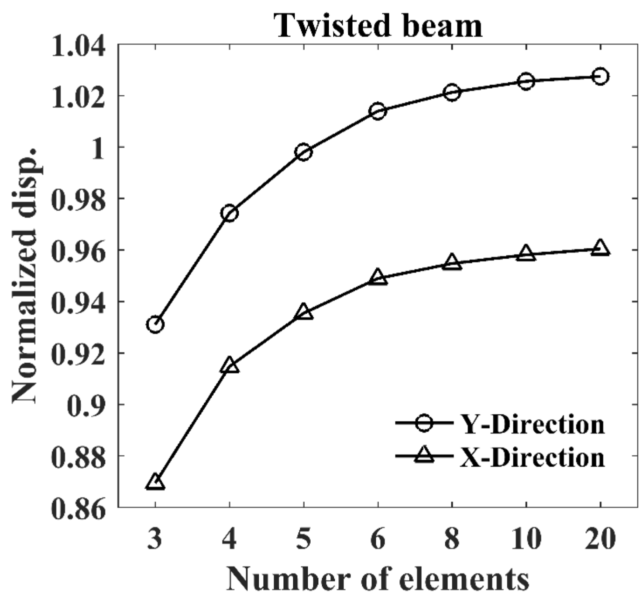

Figure 4.18: Convergence of the normalized (numerical/theoretical) displacements in the X- and Y-directions due to mesh refinement.

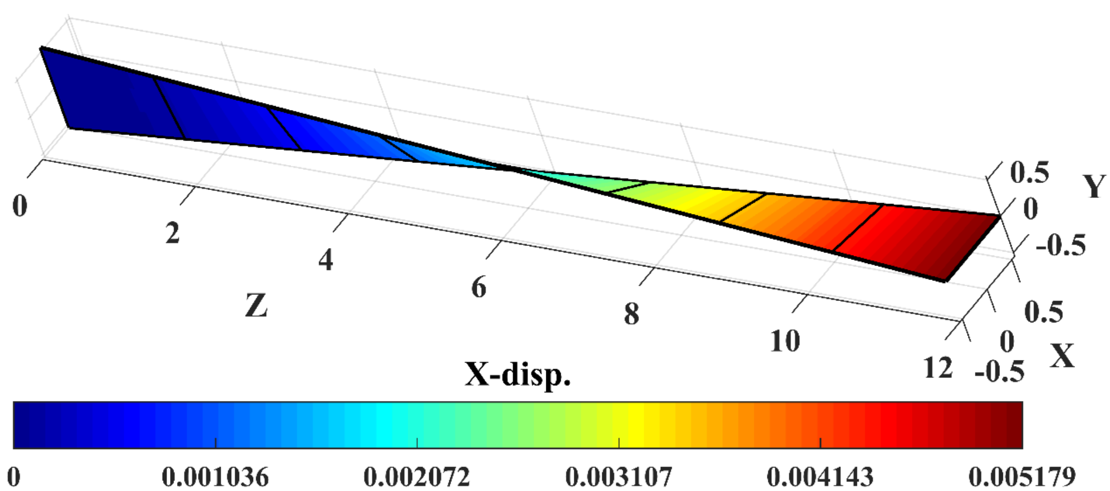

Figure 4.19: displacement in X-direction using 8 elements along the pre-twisted cantilevered beam. Units are in inches.

In the pre-twisted element, the lamina coordinate system (the principal axes of the cross section) rotates along the element's length, and the pre-twist leads to a coupling of bending in both planes. Also, like in asymmetric bending, deflections of a pre-twisted cantilevered beam exhibit components both parallel and normal to the direction of loading. Comparison of the present FE results showed excellent convergence to the theoretical solution, indicating the accurate development of the stiffness matrix (Equation 3.37), bending ability in both planes, and insensitivity of the present CB shell FE to pre-twist. As the number of the present CB shell FEs along the pre-twisted cantilevered beam increased from 3 to 20, the warping of each element decreased from 30° to 4.5°, which decreased the errors in the normalized displacements from -6.9% to 2.1% and from -13% to -4.5% in the Y- and X- direction, respectively. As illustrated in Figure 4.18, displacement convergence, with the above mentioned errors, was already achieved using 8 elements along the beam, where the warping of each element was 11.25°. Considering the 8-noded quadrilateral element presented in (MacNeal and Harder, 1985), convergence with an error of 2% in both directions was accomplished using 12 elements (7.5° warping per element) along the beam.

4.1.7 Test 7: Thick-walled cylinder, linear elastic, small in-plane strains

A wedge of an infinitely long thick-walled cylindrical pipe (Figure 4.20, left) subjected to an internal pressure (Figure 4.20, right) is considered for finite element analysis using an $m \times n$ mesh. The material properties are taken as isotropic linear elastic, and two values of Poisson's ratios, 0.49 and 0.4999, are separately considered to test the effect of nearly incompressibility. This problem was proposed in (MacNeal and Harder, 1985). The plane-strain condition is assumed in the axial direction of the pipe which together with the radial symmetry confines the material in all but the radial direction.

Table 4.4 details out the effect of mesh refinement and Poison's ratio on the percent errors evaluated for the radial displacement, as well as the circumferential and radial stresses on the inner and outer surfaces of the pipe wall. In addition, the analytical and finite element stress results, when $\nu = 0.49$, across the pipe wall in the circumferential and radial directions, under 1 MPa pressure for various mesh refinements are presented in Figure 4.21. Finally, the absence of stress jumps (in both circumferential and radial directions) across the elements for the 2×3 mesh is illustrated in Figure 4.22.

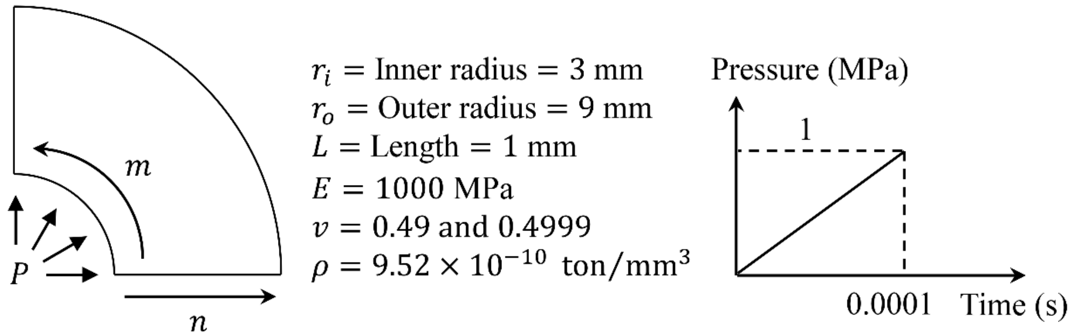

Figure 4.20: Geometry, material properties, and loading condition. m and n represent the number of elements in the circumferential and radial directions, respectively.

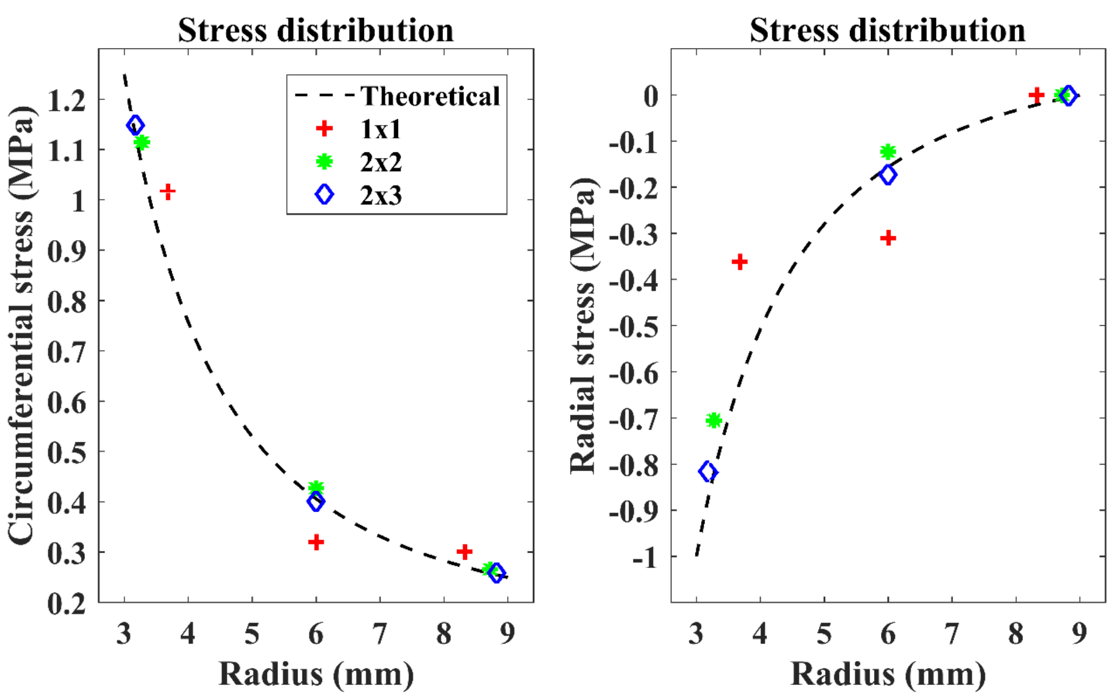

Figure 4.21: Comparison between the analytical and finite element stress results in the circumferential (left) and radial (right) directions. Readings are taken at the integration points closest to the inner, middle, and outer radii, under an internal pressure of 1 MPa, with v=0.49.

Table 4.4: present errors obtained from Equation 4.1, and computation costs for different mesh sizes and Poison's ratios. r_i and r_o , respectively, represent the radii of the innermost and the outermost integration points across the pipe wall for each mesh.

	Present: 1×1		**Present: 2×2**		**Present: 2×3**	
$\boldsymbol{\nu}$	**0.49**	**0.4999**	**0.49**	**0.4999**	**0.49**	**0.4999**
Radial disp. error $(\boldsymbol{r_i})$	0.01%	0.01%	0.0%	0.0%	0.0%	0.0%
Circ. stress error $(\boldsymbol{r_i})$	16.5%	16.9%	4.4%	4.6%	1.5%	1.5%
Circ. stress error $(\boldsymbol{r_o})$	10.9%	11.5%	3.1%	3.3%	1.8%	1.9%
Rad. Stress error $(\boldsymbol{r_i})$	−41.9%	−42.8%	−13.8%	−14.1%	−7.2%	−7.3%
Average Δt (s)	4.3×10^{-7}	4.3×10^{-8}	1.8×10^{-7}	1.9×10^{-8}	1.4×10^{-7}	1.4×10^{-8}
Total loops to max. load (Figure 6)	4.2×10^{3}	4×10^{4}	3.9×10^{4}	3.9×10^{5}	7.8×10^{4}	7.7×10^{5}

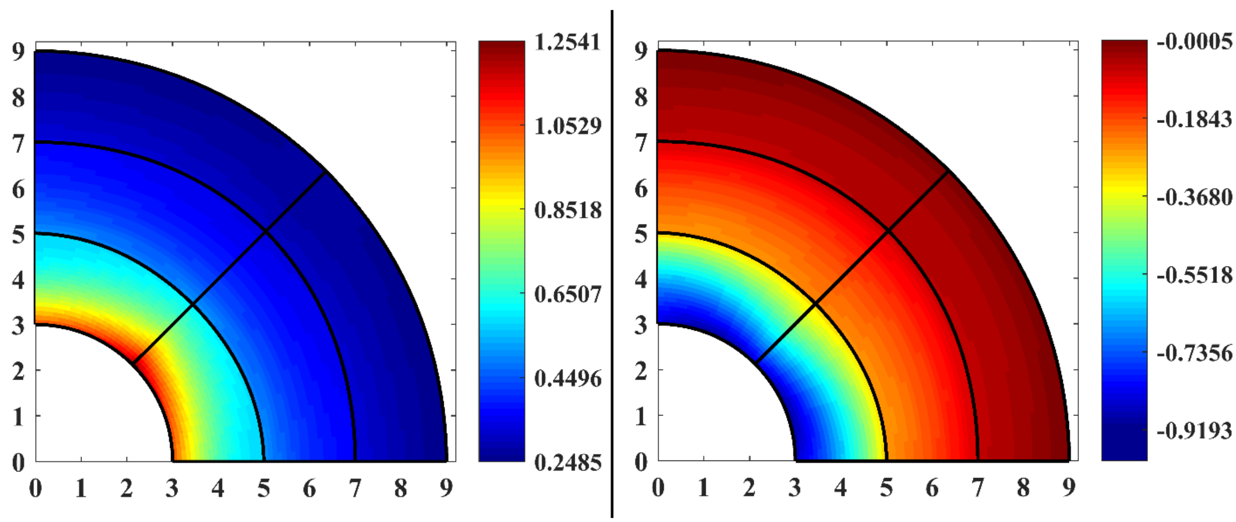

Figure 4.22: Circumferential (left) and radial (right) stress distribution across the pipe wall for the 2×3 mesh. Units for stress and radius are MPa and mm, respectively.

According to Table 4.4, radial displacement convergence was achieved with a 1×1 mesh, proving the present CB shell FE more accurate than the 8-noded quadrilateral element employed in (MacNeal and Harder, 1985), where a minimum of 1×5 mesh for a 10° section is needed to achieve the same result. Despite the displacement convergence in a 1×1 mesh of the present CB shell FE, the errors on stresses in the circumferential and radial directions were still large. Thus, to achieve convergence in stresses as well, mesh refinement was performed. In reference (MacNeal and Harder, 1985), any error less than, or equal to, 10% is ranked as "very good" for this experiment. As listed in Table 4.4, the largest errors corresponded to the radial stresses at r_i (the innermost integration point across the pipe wall) for each mesh. Refining the mesh from 2×2 elements to 2×3 elements reduced this error from −13.8% to −7.2%, while, making the computation 2 times more expensive. Thus, the best accuracy and efficiency combination was attained using a 2×3 mesh. The influence of Poison's ratio on the errors presented was negligible (a maximum of 0.2% on average), thus proving the present CB shell FE volumetric locking insensitive. Increasing the Poison's ratio from 0.49 to 0.4999 decreased the critical time increment by one-tenth, making the computation 10 times more expensive. Thus, it is best avoided. Finally, the absence of stress jumps across the elements within the mesh (another measure of convergence) was verified by illustrating the circumferential and radial stress distributions across the pipe wall (Figure 4.22).

Tests 1 to 8 were performed with the constitutive relation for small strain analysis (based on the appropriate Almansi strain tensors presented Section 3.9) using both the total UL (Equation 3.1) and the incremental UL (Equation 3.2) formulations, with a safety factor of 1.1 for the time step evaluation (Equation 3.43). The results obtained from both formulations were identical.

4.2 Large strain analysis of linear elastic materials: insensitivity to initially irregular elements and/or geometries, large distortion, verifications of Techniques 1, 2, 3 and the fiber length update algorithm

To verify the correctness of the three techniques presented in Section 3.10 for large strain analysis, together with the accuracy and efficiency of our 9-noded CB shell finite element when subjected to large in-plane distortions, as well as the use of an initially irregular mesh and geometry, we performed Test 8.

4.2.1 Test 8: Nonlinear isotropic elastic, large distortions, large strains

A plane stress large strain analysis of one quarter of a simply supported rubber sheet with a central hole subjected to in-plane edge pressure (Figure 4.23, left) was carried out for each of the three techniques presented in Section 3.10. In Technique 1 (Section 3.10.1), we used the hyperelastic incompressible Mooney-Rivlin material model $W = C_1(I_1 - 3) + C_2(I_2 - 3)$, where the material constants C_1 and C_2 are given in (Bathe et al., 1975) and were derived from an analytical and experimental investigation done in (Iding et al., 1974). For consistency with linear elasticity, relationships can be established between material constants C_1 and C_2 and Young's modulus and Poisson's ratio. Namely, $E = 2\mu(1 + \nu)$, where $\mu = 2(C_1 + C_2)$, and ν satisfies the incompressibility assumption. These material constants and properties are provided in Figure 4.23, left. Knowing Young's modulus and Poisson's ratio for the material allows for the determination of a constant material elasticity tensor which was used in combination with Technique 2 (Section 3.10.2) and Technique 3 (Section 3.10.3). In these analyses, we employed only 2 of the present CB shell FE to model one quarter of the rubber sheet (Figure 4.23, top-right) and compared the results with those presented in (Bathe et al., 1975) using thirty 4-noded elements per quarter (Figure 4.23, top-middle). To have a common ground with the static response analysis presented in (Bathe et al., 1975), we ramp-loaded the plate at two different loading rates, to study the effect of the loading rate on the response (Figure 4.23, bottom-right: 60 and 400 increments to final load). These load-deformation responses are presented in Figure 4.24 to Figure 4.26. In addition, the deformation of the quarter of the rubber sheet at the maximum load configuration obtained from Technique 3 is illustrated in Figure 4.27. In this test, a safety factor of 1.01 for the time step evaluation (Equation 3.43) is considered.

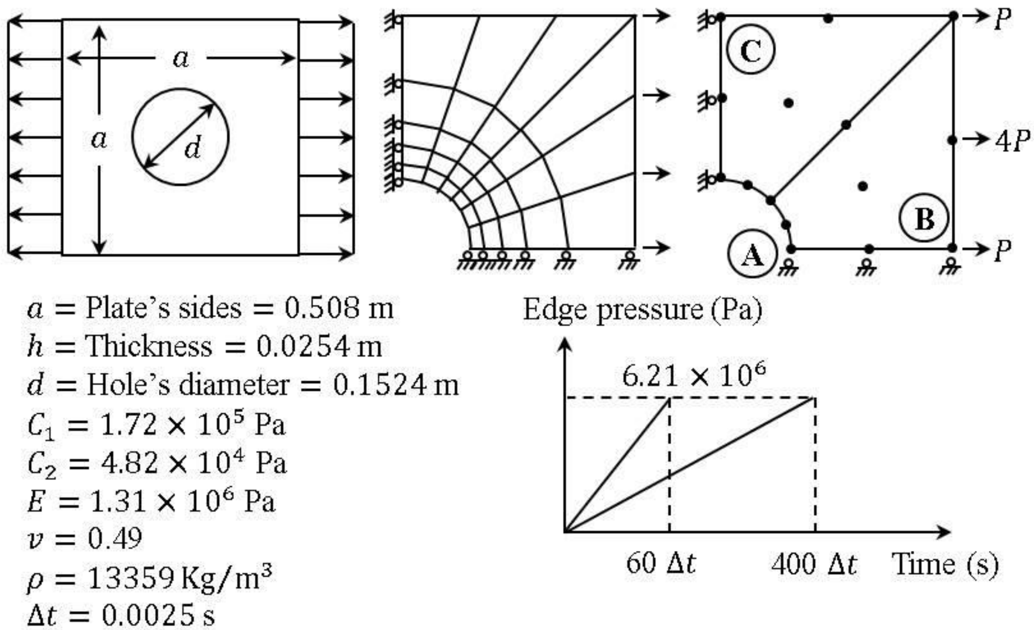

Figure 4.23: Left: Geometry and material properties; Middle: Mesh employed in (Bathe et al., 1975); Right: Mesh employed herein; Bottom: Loading rates. Δt is the average time step for Techniques 1, 2 and 3.

Table 4.5: Results of Test 8.

	(Bathe et al., 1975):	**Present:**	**Present:**
Mesh	30 plates/ quarter	2 shells/ quarter	2 shells/ quarter
Element type	4-noded	9-noded	9-noded
Integration points	2×2×1	3×3×2	3×3×2
Iterations to final load	20	60	400
Total loops to max. deflection (Figure 3.3)	2,400	2,160	14,400

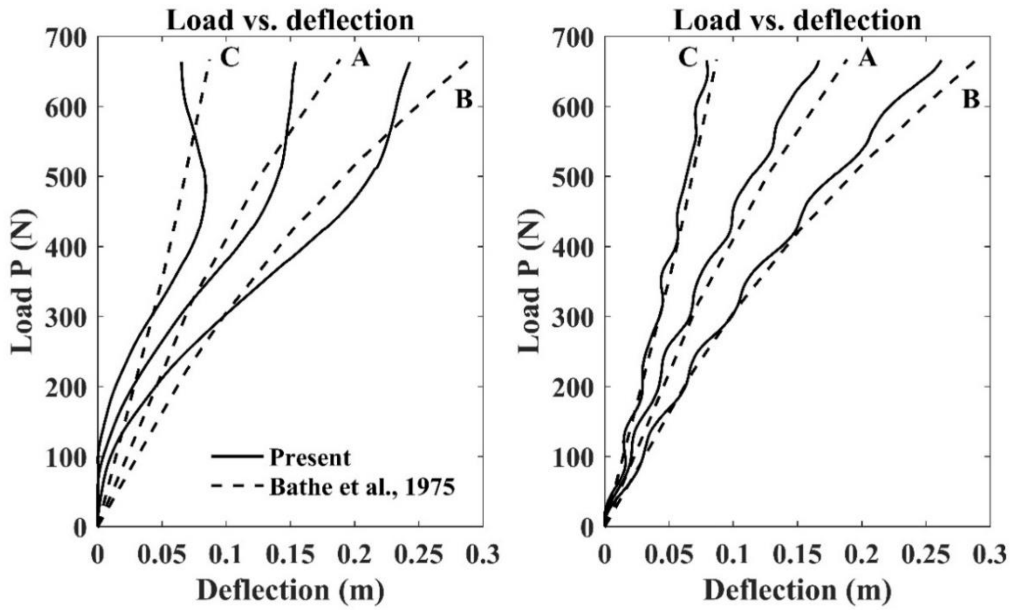

Figure 4.24: Load vs. displacement curves obtained from Technique 1 at locations A, B and C. Left: 60 increments to final load. Right: 400 increments to final load.

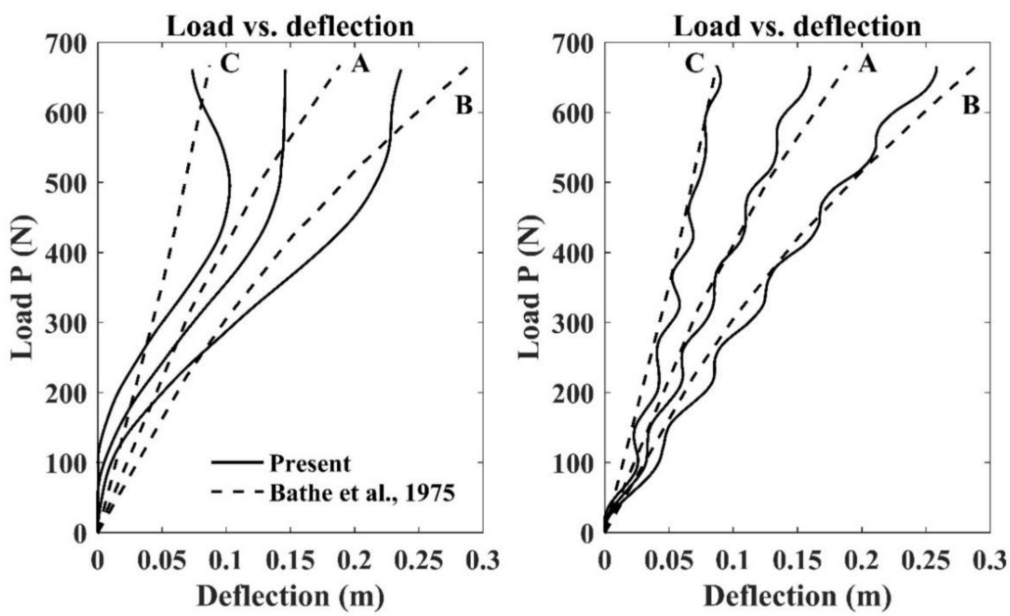

Figure 4.25: Load vs. displacement curves obtained from Technique 2 at locations A, B and C. Left: 60 increments to final load. Right: 400 increments to final load.

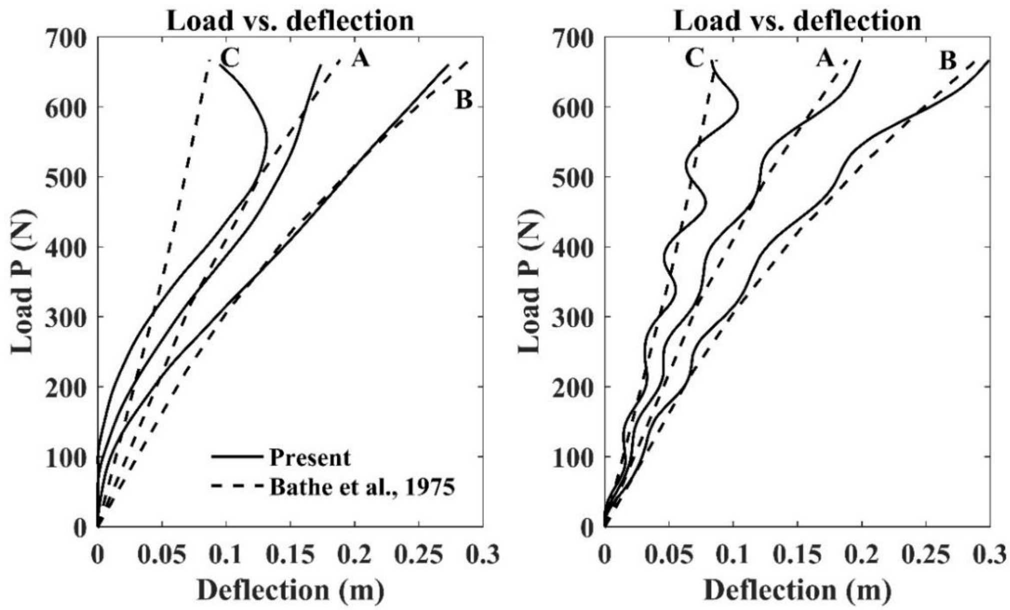

Figure 4.26: Load vs. displacement curves obtained from Technique 3 at locations A, B and C. Left: 60 increments to final load. Right: 400 increments to final load.

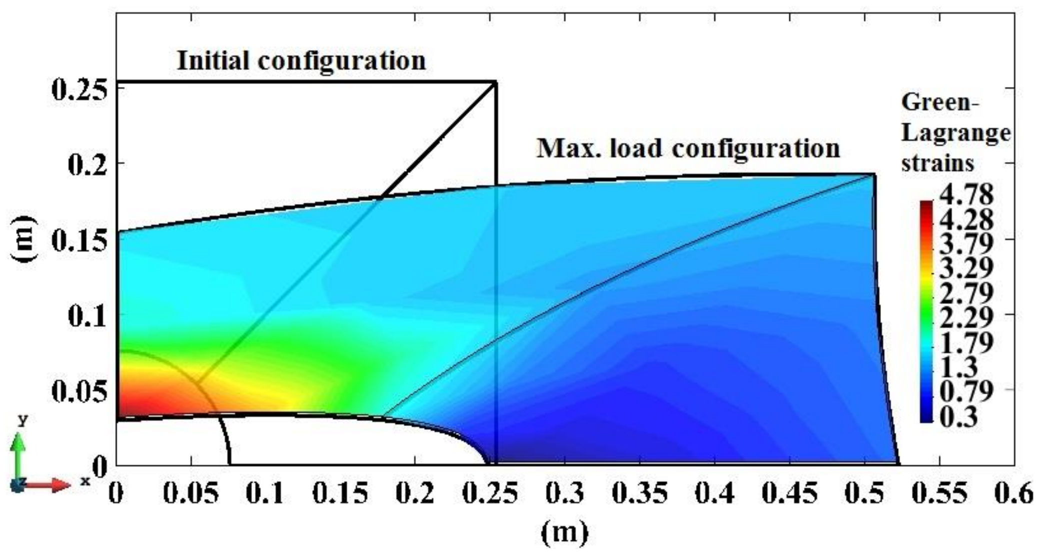

Figure 4.27: Illustration of the initial configuration, maximum load (deformed) configuration and the distribution of the Green-Lagrange strains at the max load configuration, obtained from Technique 3 with 60 increments to final load.

We used the Mooney-Rivlin (nonlinear, hyperelastic, invariant based) material model for Technique 1 (Section 3.10.1), and a constant isotropic constitutive tensor for Technique 2 (Section 3.10.2) and Technique 3 (Section 3.10.3). Basically, Techniques 2 and 3 are designed to work with materials that can be described by Young's modulus and Poisson's ratio (i.e. a constant constitutive tensor). To enable comparison between the present explicit dynamic analysis and the static analysis of (Bathe at al., 1975), we ramp-loaded the rubber sheet. To investigate the effect of the loading rate on the deformation response, the analysis was performed using two different loading rates (Figure 4.23, bottom-right). In the first attempt, an arbitrary 60 increments to the final load (equivalent to 4.14×10^7 Pa/s) was considered. The total UL (Equation 3.1) load deformation responses at points A, B, and C obtained from Technique 1 using the Mooney-Rivlin model (Figure 4.24, left), is in good agreement with those obtained from Technique 2 using the constant isotropic constitutive tensor (Figure 4.25, left). In addition, the results obtained from both techniques follow the deformation responses at the specified static load increments described in (Bathe at al., 1975). Due to the fast loading rate, the responses of the present dynamic analyses exhibit large amplitudes and small frequencies. Carrying out the incremental UL formulation (Equation 3.2) via Technique 3 (using the same constant isotropic constitutive tensor as in Technique 2), the load vs. displacement curves obtained for points A and B were in excellent agreement with those of (Bathe at al., 1975) (Figure 4.26, left). The oscillatory response of the present dynamic analysis at point C, although manifest in amplitude (due to the fast loading rate), evenly follows the deformation response at the specified static load increments described in (Bathe at al., 1975). In the second attempt, to mitigate the dynamic amplification effect, we decreased the loading rate to an arbitrary 400 increments to the final load (equivalent to 6.21×10^6 Pa/s). As expected, the amplitudes of the oscillations decreased, and the accuracy of Techniques 1, 2 and 3 is made evident by the excellent agreements of the load vs. displacement curves (for all the three points) with those of (Bathe at al., 1975) (Figure 4.24 to Figure 4.26, all right).

Performance-wise, due to the bypass of the transformation of the fourth-order constitutive tensor (done through eight nested for-loops), Techniques 2 and 3 are computationally less expensive than Technique 1. In addition, if an accurate response of point C is not the goal of the analysis, Technique 3 with 60 load increments is slightly (1.1 times) more efficient than (Bathe at al., 1975), and the responses at points A and B are more accurate than those obtained from the remaining two techniques. Although the 400 load increments may not be the most efficient, the accuracy of the responses obtained proves all the three techniques valid and accurate in modelling large strains.

At the maximum load configuration (illustrated in Figure 4.27), Green-Lagrange strains of up to 4.8 are measured, which also numerically proves that the strains analysed are indeed very large (using constant linear constitutive tensor). This accuracy in response was achieved using only two of the present CB shell FE (as opposed to thirty plates (Bathe at al., 1975)), proving the present element to be insensitive to the adoption of initially irregular elements and large distortions (Figure 4.27). The insensitivity of our CB shell element to initially irregular elements and large distortions, validates the correctness of the algorithm to update and transform the two independent coordinate systems. Furthermore, the volume of the rubber sheet changed by 0.5% only with such a large in-plane stretching, thereby validating the nodal fiber length adaptation algorithm presented in Section 3.11.

4.3 Large strain analysis of anisotropic nonlinear hyperelastic incompressible materials: insensitivity to initially curved geometry and large 3D deformations; verification of Technique 1 and of the fiber length update algorithm

The accuracy of Techniques 1-3 in a flat and irregular geometry undergoing large in-plane strain and large in-plane distortions was verified by Test 8. We performed two additional tests (Tests 9 and 10), to further verify the accuracy of Technique 1 (Section 3.10.1), the procedure of direct application of incompressibility and plane stress conditions, as well as to verify the accuracy of the fiber length update algorithm for large 3D strains (Section 3.11) in thin and thick shell structures, when initially curved geometries (uncoincident lamina and global coordinate system) are considered, and the structure undergoes large 3D (in-plane and transverse) deformations (large discrepancies between lamina and fiber coordinate systems). In these tests, we modeled the pressurization of axisymmetric, closed-end cylinders, using the mass matrices presented in Section 3.14. We considered Guccione's 3D homogeneous hyperelastic anisotropic material model (Equation 4.2) for both tests. The reason for considering thin and thick structures under similar loading and boundary conditions is to verify that inclusion of transverse shears in the formulation of thin structures, where transverse shears are physically not present, does not cause artificial stiffening.

Due to symmetry, we modeled only one-quarter of the structures in which we used 2 of the present CB shell FE in the circumferential direction and eight elements in the longitudinal direction. In addition, we considered a practical but perhaps not optimal safety factor of 2 for the time step evaluation (Equation 3.43).

4.3.1 Test 9: Nonlinear anisotropic incompressible hyperelastic: human thoracic aorta

In Labrosse et al. (2009), segments of fresh human thoracic aortas from eight male sexagenarians were pressurized under closed-end and free extension conditions. Then, material constants for different three-dimensional hyperelastic anisotropic constitutive models were determined from the experimental data. In this study, we modeled the pressurization of an axisymmetric, thin-walled, closed-end cylinder (Figure 4.28, left) with Guccione's homogeneous hyperelastic anisotropic material model of the form:

Equation 4.2

$$W = \frac{C_1}{2}\left[\exp\left(C_2 {E^l_{\theta\theta}}^2 + C_3\left({E^l_{zz}}^2 + {E^l_{rr}}^2 + {E^l_{rz}}^2 + {E^l_{zr}}^2\right) + C_4\left({E^l_{\theta z}}^2 + {E^l_{z\theta}}^2 + {E^l_{\theta r}}^2 + {E^l_{r\theta}}^2\right)\right) - 1\right],$$

where the material constants (Figure 4.28, left) were taken from Labrosse et al. (2009). We used Technique 1 (Section 3.10.1) to develop the constitutive relations, and enforce the material incompressibility and the plane stress condition (in the radial direction presented by index rr).

The structure was pressurized from 0 to 18.66 kPa (physiological range) at two different loading rates (Figure 4.28, right). In the faster loading rate, the pressure was ramped up to 18.66 kPa in 0.07 seconds, which corresponds to the physiological pressurization rate in early systole (that is 80 mmHg in 0.04 seconds (Labrosse et al., 2010). The slower loading rate (18.66 kPa in 0.14 seconds) was chosen to study the effect of loading rate on the amplitude of the oscillations in the solution. The FE modeling was performed using the two mass matrices presented in Section 3.14 (M1 and M2) to study their effect on the simulations. Comparison between the experimental, analytical and finite element data (obtained from the two loading rates and two mass matrices) is presented in Figure 4.29. To verify that the stress discontinuities (stress jumps) were small everywhere in the structure, we plotted pressure bands over the deformed geometry at the maximum load configuration using the faster loading rate in combination with M1 (Figure 4.30) and M2 (Figure 4.31). According to Bathe (1996), pressure band (obtained from Equation 4.3) is a more conclusive way of presenting stress discontinuities when 3D stresses and 3D deformations are present.

Equation 4.3

$$\text{Pressure band} = \frac{-(\sigma_{xx} + \sigma_{yy} + \sigma_{zz})}{3}$$

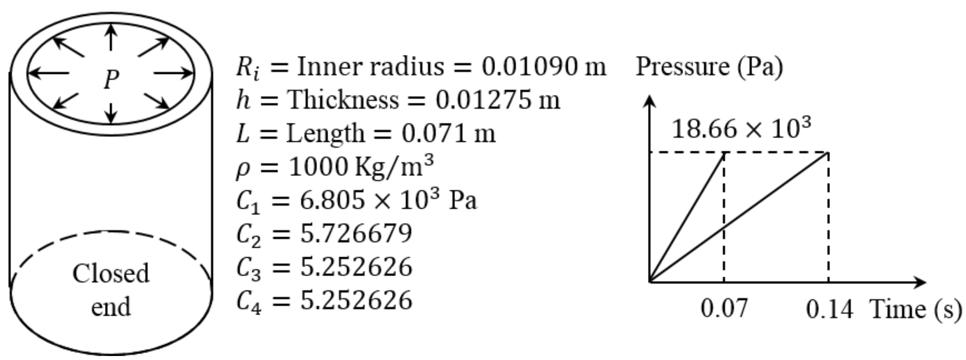

Figure 4.28: Left: Human thoracic aorta geometry and material properties; Right: Loading rates.

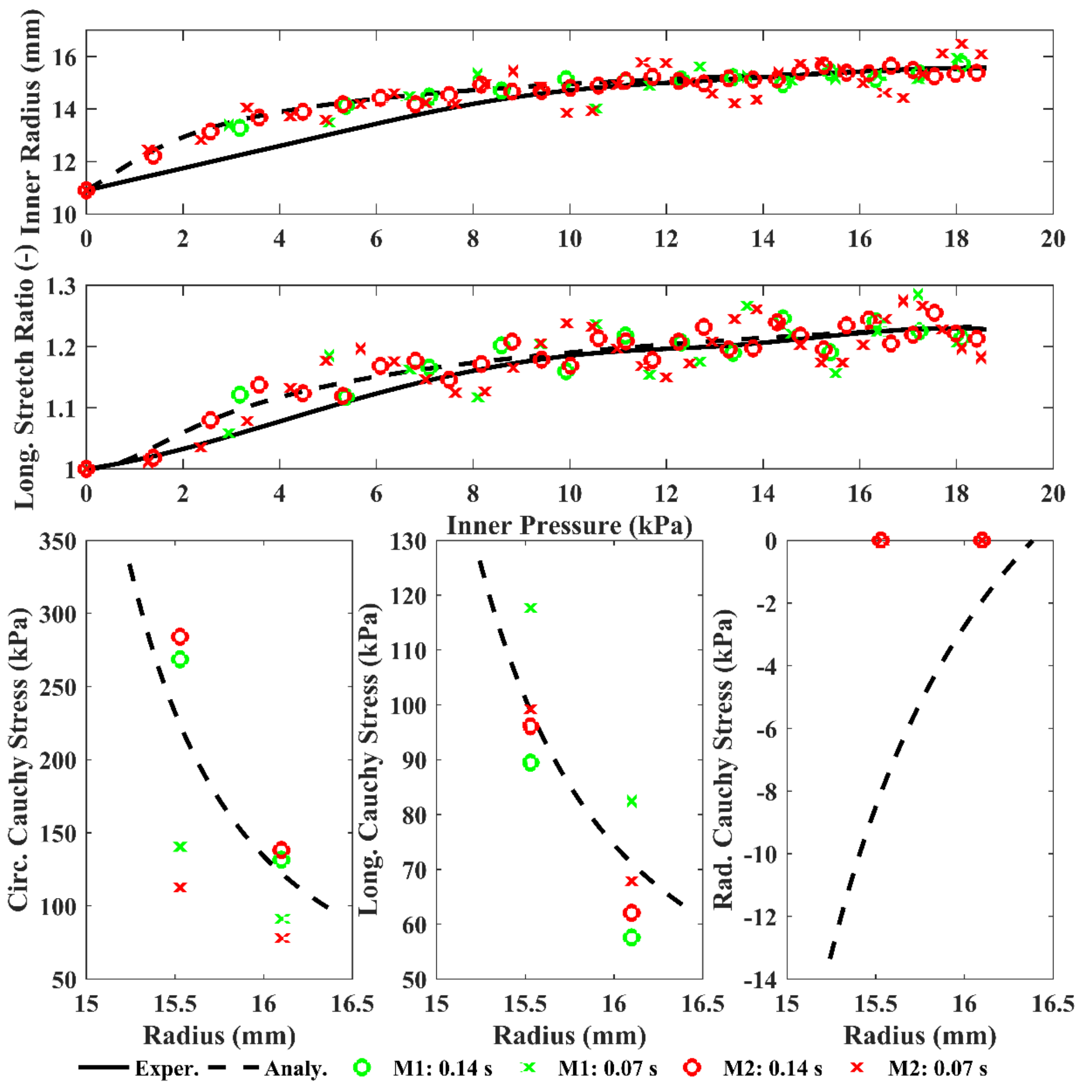

Figure 4.29: Comparison between the experimental, analytical and finite element data for human thoracic aorta under pressurization with closed-end and free extension conditions: inner radius vs. pressure (top) and longitudinal stretch ratio vs. pressure (middle). Comparison between the analytical and finite element stress results across the aorta wall in the circumferential (bottom-left), longitudinal (bottom-middle), and radial (bottom-right) directions, measured at 13.33 kPa and close to the open end of the aorta. In the legend, M1 and M2 refer to the mass matrices of Sections 3.14.1 and 3.14.2, respectively. Measurements are taken in the middle to prevent influence of the boundary conditions.

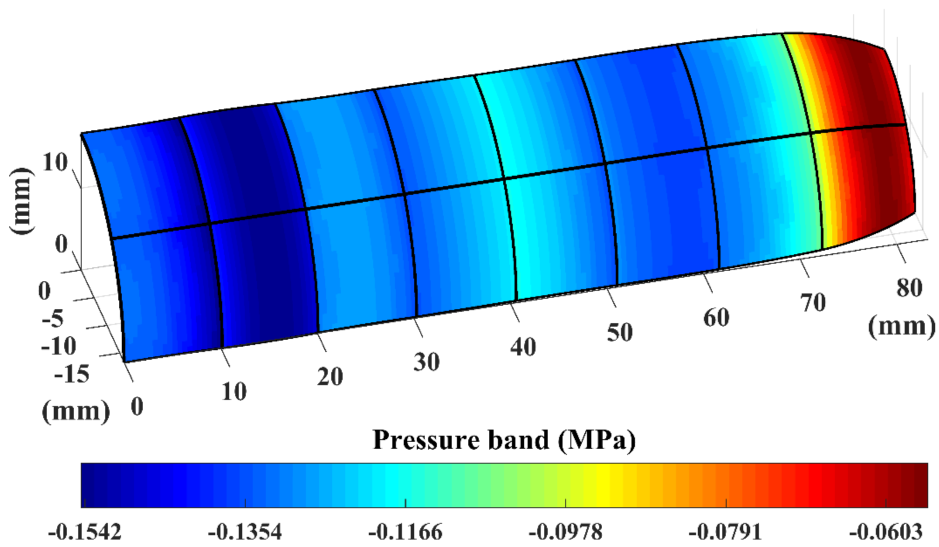

Figure 4.30: Deformation and distribution of pressure band (Equation 4.3) due to pressurization under closed-end and free extension conditions at the maximum load configuration obtained with M1 (mass matrix of Section 3.14.1) and the faster loading rate.

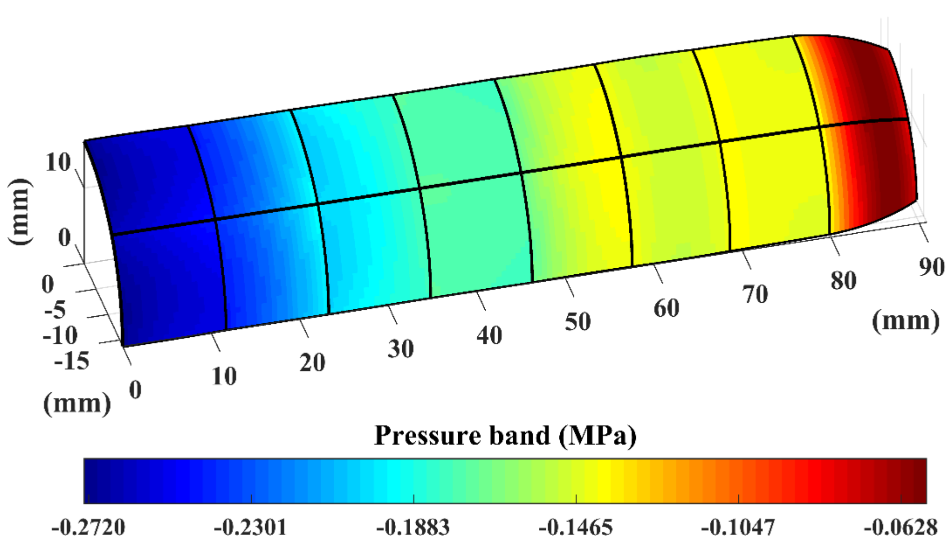

Figure 4.31: Deformation and distribution of pressure band (Equation 4.3) due to pressurization under closed-end and free extension conditions at the maximum load configuration obtained with M2 (mass matrix of Section 3.14.2) and the faster loading rate.

4.3.2 Test 10: Nonlinear anisotropic incompressible hyperelastic: dog carotid artery

In this test, we studied the pressurization of a segment of a closed-end dog carotid artery. The model consisted of an axisymmetric, thick-walled, closed-end cylinder (Figure 4.32, left) with homogeneous hyperelastic anisotropic Guccione's material model presented by Equation 4.2, where we obtained the material constants from the experimental data published in (Takamizawa and Hayashi, 1987) using an approach similar to that presented in Labrosse et al. (2009). The structure was pressurized from $0 - 26.66$ kPa at two different loading rates (Figure 4.32, right). The slower loading rate (26.66 kPa in 0.1 second) was consistent with the physiological pressurization rate before the cardiac cycle starts in early systole, and the faster loading rate (26.66 kPa in 0.01 second) was chosen to study the effect of loading rate on the amplitude of the oscillations in the solution. Comparison between the experimental, analytical and finite element data (obtained from the two loading rates and mass matrices of Section 3.14 (M1 and M2)) is presented in Figure 4.33. To verify that the stress discontinuities were small everywhere in the structure, we plotted pressure bands over the deformed geometry at the maximum load configuration using M2 in combination with the faster (Figure 4.34) and the slower (Figure 4.35) loading rates.

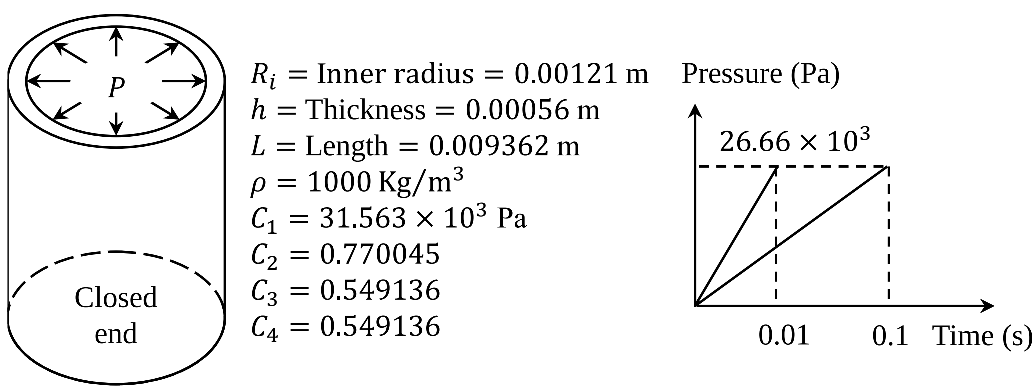

Figure 4.32: Left: Dog carotid artery geometry and material properties; Right: Loading rates.

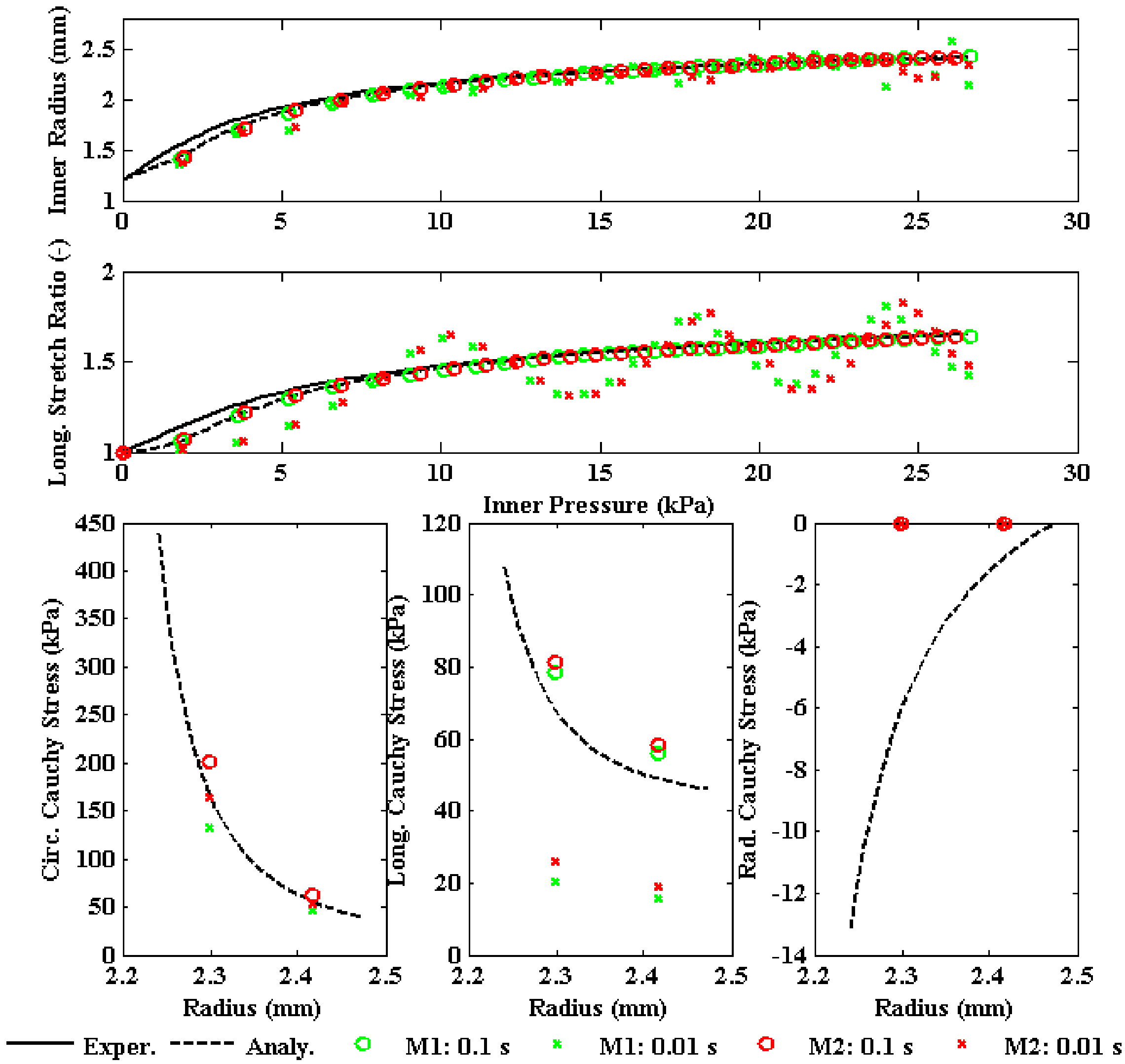

Figure 4.33: Comparison between the experimental, analytical and finite element data for dog carotid artery under pressurization with closed-end and free extension conditions: inner radius vs. pressure (top) and longitudinal stretch ratio vs. pressure (middle). Comparison between the analytical and finite element stress results across the aortic wall in the circumferential (bottom-left), longitudinal (bottom-middle), and radial (bottom-right) directions, measured at 13.33 kPa and close to the open end of the artery. In the legends, M1 and M2 refer to the mass matrices of Sections 3.14.1 and 3.14.2, respectively. Measurements are taken in the middle to prevent influence of the boundary conditions.

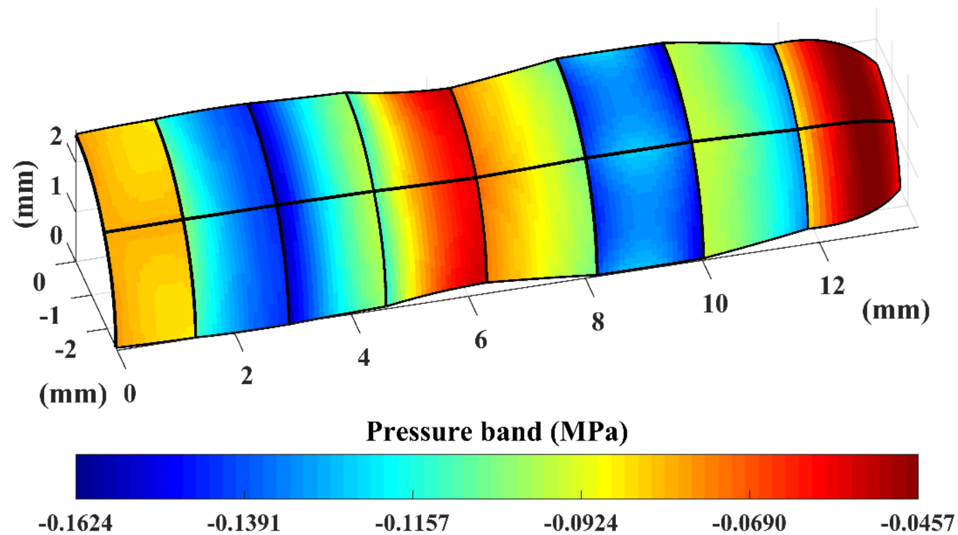

Figure 4.34: Deformation and distribution of pressure band due to pressurization under closed-end and free extension conditions at the maximum load configuration obtained with M2 (mass matrix of Section 3.14.2) and the faster loading rate.

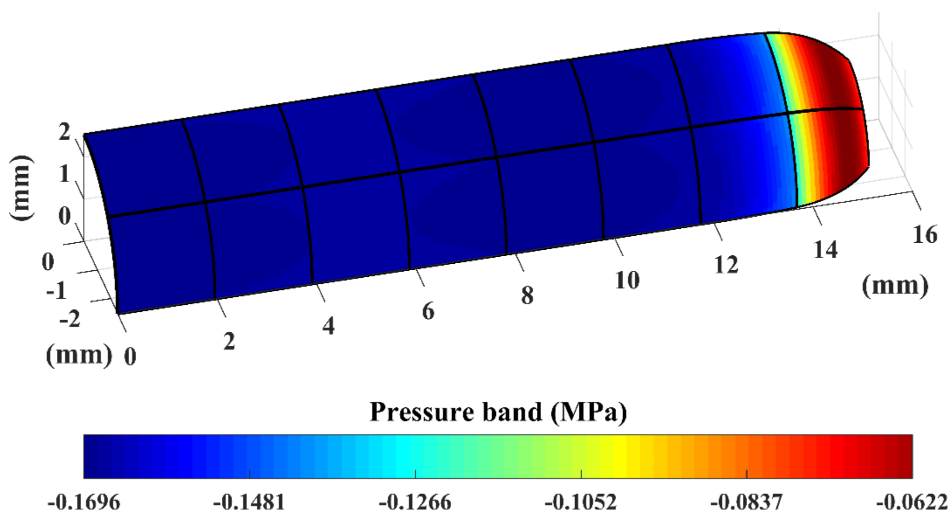

Figure 4.35: Deformation and distribution of pressure band due to pressurization under closed-end and free extension conditions at the maximum load configuration obtained with M2 (mass matrix of Section 3.14.2) and the slower loading rate.

In Test 9, a thin-walled cylindrical structure was loaded within the physiological pressure range ($0 - 18.66$ kPa) in two different loading periods (fast: 0.07 seconds, slow: 0.14 seconds), whereas in Test 10, a thick-walled cylinder was loaded to beyond the physiological pressure range ($0 - 26.66$ kPa) in 0.01 and 0.1 seconds. Therefore, a total of four loading rate and mass matrix combinations were considered in each test. We took the material constants for Test 9 from Labrosse et al. (2010), and evaluated the constants for Test 10, from the experimental data published in (Takamizawa and Hayashi, 1987), using a similar approach presented by Labrosse et al. (2009). Note that the material model was selected because it is able to handle full 3D strains, and because we could evaluate the corresponding material constants. It is worth emphasizing the very important point that 2D or membrane type material models include in-plane strains only, and cannot describe 3D material properties. In particular, features such as residual stresses, through-thickness stress distributions, and torsional deformations cannot be captured with a 2D material model. Provided that the present CB shell FE performs well for a 3D material model, it will perform equally well for any other 3D models.

Due to the prescribed geometry, boundary conditions, loading conditions, and material properties, both structures undergo large 3D (in-plane and out of plane) distortions next to the closed end, and large in-plane and normal strains elsewhere in the structure.

Comparisons between the experimental, analytical and finite element results conducted for Tests 9 and 10 are, shown in Figures 4.29 and 4.33 respectively for the inner radius (top) and the longitudinal stretch ratio (middle) upon pressurization. For practical purposes, the curves do not exhibit significant differences between each other, over the specified pressure ranges. As expected, the faster loading rate in both tests resulted in an oscillatory response, which happened to be more pronounced in the longitudinal direction. Considering that, in this document, the reference surface of the shell is taken to be the mid-surface, the analysis is done on the mid-surface (middle radius) of the structure and the values of the internal radius are obtained from subtracting half of the thickness (nodal fiber lengths) from the middle radius. Thus, the accuracy of the present FE inner radius vs. pressure curves, as well as the negligible change in the volume of the structure (-0.8% and -0.3% for Tests 9 and 10, respectively) confirmed the accuracy of the fiber length update algorithm (Section 3.11) for large 3D strains and large 3D distortions of curved geometries. Furthermore, the FE results obtained from both mass matrices are in excellent agreement for the same loading conditions (Figures 4.29 and 4.33, top and middle). The average critical time step calculated from M2 (Section 3.14.2) was only about 1.034 times larger than that of M1 (Section 3.14.1), so both formulations resulted in the same number of operations. Comparison between the analytical and the present FE stress distributions across the wall (pressurized to 13.33 kPa) in the three circumferential, longitudinal, and radial directions is shown in Figures 4.29 and 4.33 (Tests 9 and 10, respectively), bottom- left to right, in that order. The analytical curves illustrate that the stresses were the highest towards the inside of the aortic wall for the circumferential and longitudinal directions, as expected in the absence of residual stresses in the model. As illustrated in Figure 4.29, bottom-left (circumferential direction), there is a favorable comparison between the analytical and the present FE stress distributions obtained from both mass matrices with the slower loading rate. As for the longitudinal direction (Figure 4.29 bottom-middle), convergence was best achieved by M2 (Section 3.14.2) at both loading rates, followed by M1 with the slower loading rate. As illustrated in Figure 4.33 (Test 10), there was a great similarity in the FE results obtained from both mass matrices under the same loading conditions, while the slower loading rate decreased the amplitude of the oscillations.

Finally, the analytical radial stresses were the highest towards the inside of the wall (Figures 4.29 and 4.33 bottom-right), where the stress magnitude was equal to that of the applied pressure (13.33 kPa), and equal to zero on the outside surface, where no external pressure was applied. However, consistent with the plane stresses assumption associated with the CB shell elements, the radial stresses (normal to the shell surface) obtained from the present CB shell FE remained zero across the element thickness.

Consistent with the large discrepancies between the stress results obtained from M1 and M2 at the faster loading rate in Test 9, there was a noticeable difference between the ranges of the pressure band over the deformed aorta in those scenarios (Figures 4.30 and 4.31, respectively). Considering that the stress results obtained from M1 and M2 were in good agreement for each of the loading rates, we were interested in the influence of the loading rate on the pressure band for the same mass matrix. Comparison between Figures 4.34 and 4.35 suggested that not only decreasing the loading rate decreased the amplitudes of the response oscillations, but also did produce a smoother deformed shape (i.e. removed the inklings along the artery), and reduced stress jumps between the elements. Overall, the stress jumps, although small across each element, appear to be the most pronounced in the elements closest to the closed end. This is because those elements undergo the largest 3D deformations and distortions. Should it be required, a smoother pressure band could be achieved either through mesh refinement (as verified through Test 7), or by decreasing the loading rate (as verified trough Tests 9 and 10).

In conclusion, the results obtained from Tests 9 and 10 validate Technique 1, the procedure of direct application of incompressibility and plane stress condition (Section 3.10.1), as well as the fiber length update algorithm for large membrane strains in thin and thick shell structures (Section 3.11). In addition, the present CB shell FE is proven insensitive to initially non-coincident lamina and global coordinate system, large divergence between lamina and fiber coordinate systems (due to large in-plane and transverse deformations), and membrane and shear locking. There was a good match in the FE results obtained from both mass matrices under the same loading conditions. The discrepancies between the analytical and the present FE stresses in the longitudinal direction were larger than those of the circumferential direction. This was because the amplitudes of oscillations caused by the faster loading rate were larger in the longitudinal direction than the circumferential one. To maintain the best overall convergence to the analytical solution, the slower loading rate was favorable. Comparison between the analytical circumferential and longitudinal (in-plane) stresses, and the analytical radial (normal) stresses validated the statement of Section 2.4.2, according to which: "***normal stresses can be neglected in structural theories because they are much smaller than the in-plane stresses***."

CHAPTER 5: CONCLUSION

5.1 Summary of findings

Geometrically and materially nonlinear FE analysis requires a CB shell FE that is accurate, reliable and versatile. It was concluded from Sections 2.3, 2.4, and 2.5.3 that a nonlinear anisotropic incompressible hyperelastic CB shell finite element for the formulation of soft tissue dynamics using explicit time integration did not exist in theoretical literature or in any of the studied software packages. Thus, considering the novelty of the proposed shell element, serious theoretical and programming modifications to the existing software packages were required. Therefore, we found it more efficient to bypass this obstacle and program the desired shell element from scratch. As mentioned throughout this document, it is required to carry out derivations, multiplications, and integrals of large matrices at each time step. Due to its built-in functions with the aforementioned capabilities, convenience, and availability, we employed Matlab for the implementation and development of the present thick 9-noded CB shell FE. To achieve the best accuracy and for the reasons mentioned in Section 3.4, we assumed 5 DOFs per node. Consistent with the Mindlin-Reissner shell theory (Section 2.4.2), to take the transverse shears into consideration, and to enable modelling large in-plane and large out of plane deformations, we employed two independent (lamina and fiber) coordinate systems (Section 3.3). The nonlinearity of the shape functions (for the 9-noded shell element) enabled accurate modelling of curvatures under bending conditions, and shear locking was prevented. In addition, considering that the normals were allowed to rotate due to deformation (i.e. there was no normality constraint) shear locking did not happen regardless of the thickness of the structure (Section 2.8).

Due to the mechanical behaviour of soft tissues, we were interested in developing a thick shell element which can undergo large deformations and large rotational strains (i.e. we were not interested in inextensional modes of bending). Although membrane locking was not an issue in our field of application, we numerically verified that it does not occur in the present 9-noded CB shell FE, as we were able to model inextensional modes of bending. Knowing that the constitutive relations must be applied on the lamina coordinate system, we developed the lamina strain-displacement transformation matrix by evaluating the nodal point and nodal fiber displacements with respect to the lamina coordinate system, and obtained the partial derivatives with respect to the current position vector in the lamina coordinate system, as opposed to the global ones. In other words, we transformed the nodal point displacements, and the position vectors from the global coordinate system to the lamina coordinate system (Section 3.8).

Next, we developed the hyperelastic nonlinear anisotropic constitutive relations by deriving the strain energy function with respect to the lamina Green-Lagrange strains, and used the lamina deformation gradient tensor to evaluate the lamina Cauchy stresses, as opposed to the global ones (Technique 1 in Section 3.10.1). As a new approach, we directly enforced the zero normal stress condition by evaluating the normal strains as a function of the remaining strain components, and substituting it in the strain energy function. This method, which is based on the conservation of matter, is expected to work equally well for compressible and incompressible materials. In addition to Techniques 1, we developed 2 new techniques that enable modelling large strains using linearly elastic material properties, which were tested to be accurate (Sections 3.10.2 and 3.10.3). Considering that in the Mindlin-Reissner shell theory, fibers are assumed to remain straight but not normal after deformation, a constant thickness condition was invoked in the kinematics of the shell to avoid numerical ill-conditioning problems. To update the thickness changes due to large membrane straining, we evaluated the lamina strains from the constitutive equations, and then projected their mean values onto the fiber direction. Finally, we re-evaluated the current thickness using the thickness of the reference configuration and the aforementioned fiber strains (Section 3.11).

To find the mass and stiffness matrices, as well as the force vectors, we employed the normal Gaussian rule (3×3) to integrate over the in-plane (r and s) parent coordinates, and 2 through the thickness integration points because of transverse shears (Section 3.15). We obtained the critical time step, required for explicit analysis, from the stiffness and the mass matrices through the maximum natural frequency, which, consequently varied with the load in nonlinear systems (Section 3.16). As was presented in Tables 4.1 and 4.2, and discussed in Section 4.1.2, the present average time increments were much larger than those classically obtained from dividing the thickness of the element by the sound speed (obtained from the material properties). This also contributed to making the number of operations smaller.

Eventually, the present 9-noded CB shell FE was tested to be accurate and efficient for a broad variety of geometries, loading conditions, and material properties.

5.2 Specific contributions of the present CB shell FE and the UL constitutive relations

The most important contributions of the new proposed CB shell FE lie in its accuracy and efficiency in analyzing large bending deformations (Tests 1 to 4) and its insensitivity to initially irregular elements and geometries as well as large distortions (Tests 3, and 5 to 10), compared to existing CB shell FE elements. Accuracy was achieved by employing a 9-noded quadrilateral element, two independent coordinate systems to implement the kinematic and kinetic assumptions of the modified Mindlin-Reissner shell theory, and proper selection of the number of integration points. Insensitivity of the present CB shell FE to large 3D deformations, and geometric irregularities enabled employment of smaller number of elements (larger elements), which, combined with formulation of Section 3.16, resulted in enlargement of the time step (Δt). In addition, due to selection of explicit time integrations, the need for equilibrium iterations was circumvented. The abovementioned factors, resulted in a reduction in the number of operations, which consequently is expected to reduce the computation time, provided that all the CB shell elements (considered in this document) were implemented using the same programming language and the tests run on the same machine.

In addition, the three techniques presented in Section 3.10, and the fiber length update algorithm presented in Section 3.11 were shown to be accurate in modelling large in-plane and out of plane (3D) distortions, and large 3D strains of initially irregular elements and geometries. Technique 1, which, details the appropriate derivation of the constitutive relations from the hyperelastic strain energy function, and their transformation to the current configuration within the lamina coordinate system, and direct application of zero normal stress condition through volume evolution constrains was further verified through Tests 8 to 10. Techniques 2 and 3, which, allow for the accurate modelling of large strains using a constant linear constitutive tensor in the total and incremental UL formulations, respectively, were verified through Test 8. It was made evident that Techniques 2 and 3 are computationally more efficient than Technique 1 due to exclusion of the transformation of the fourth-order constitutive tensor, and may bypass the need of determining the material constants for hyperelastic strain energy functions.

5.3 Limitations and recommendation for future work

The present CB shell FE was implemented in the Matlab environment due to its availability and convenience, but the element could be made numerically more efficient by using a faster programming language. Considering that 2 through the thickness integration points are necessary for the prevention of shear locking in bending deformations, the efficiency of the element could be doubled by reducing the number of through the thickness integration points from 2 to 1 when only in-plane deformations are modelled (e.g. Tests 7 and 8). Moreover, to further leverage the small number of elements required per model, the loop over the elements (Figure 3.3) could be circumvented by running the elemental calculations in parallel, thereby reducing the number of operations and making the code even more efficient. The present 9-noded CB shell FE was proven efficient and accurate, not only in modeling linearly elastic materials (engineering applications), but also in modeling anisotropic incompressible nonlinear hyperelastic materials (biological soft tissues). To make a full use of this element in the surgical simulation realm, the formulations need to be expanded to integrate contact constraints with the structural variational equations, and to implement the contact constraints in the finite element analysis. Contact problems are categorized as boundary nonlinearities, because both contact boundaries and contact stresses are unknown, and there is an abrupt change in contact forces. Many contact algorithms exist in the literature (Bathe, 1996; Belytschko et al., 2000; Wriggers, 2002).

5.4 Final remarks

Some difficulties we encountered in the process of shell development were partly due to the hidden fundamental details in the formulations of the existing CB shell elements, exaggerations in the capabilities of the elements and/or types of deformations, and theoretical mistakes in the literature, as are discussed in this document. In addition, the hyperelastic constitutive relations in the literature were either limited to brick elements or plate elements (i.e. flat Kirchhoff-Love shell elements), which undergo small deformations and/or distortions. In these cases, the transverse shears were excluded from the analysis, thickness update was done through the kinematics (if any), and the lamina coordinate system remained collinear with the global coordinate system, thus no rotation of the material matrices (between the different coordinate systems) was needed. Furthermore, the constitutive relations were developed for the classical TL formulations and implicit time integration (equilibrium iterations) is employed. So, not only did we have to come up with a way to implement the hyperelastic constitutive relations in the lamina coordinate system, which is non-collinear with the global coordinate system and undergoes large rotations, but we also had to include the transverse shears while correctly enforcing incompressibility and the zero normal stress condition (as discussed in Section 2.7, Lagrange multipliers should not be used for 3D anisotropic hyperelastic material models). Furthermore, we had to come up with an approach to transform the lamina constitutive relations to the UL formulations, where stresses and strains are measured from the previous configuration as opposed to the initial one. Despite numerous dead ends, we managed to address all these issues directly, and without adding any complexities to the formulation of CB shell FE (recall from Section 2.5 that some authors attempted to resolve this issues at the cost of using mixed tensorial interpolations, mixed displacement and pressure formulations, and ending up either with a membrane element or a 3D (solid) shell element as opposed to a CB shell element).

To conclude, geometrically and materially nonlinear FE analysis requires a CB shell finite element that is accurate, reliable and versatile. The tests performed proved our CB shell FE to be capable of handling large bending deformations and large in-plane distortions, being insensitive to shear and membrane locking, and insensitive to initially irregular elements. In addition, the three implementation techniques presented were shown to be accurate in large strain analyses. It appears that the application and robust derivation of two independent coordinate systems, the proper formulation of the incremental and the total UL governing equations and the use of precise matrix transformations, as well as the optimal critical time step calculation method made the present CB shell FE efficient and accurate in comparison with the existing CB shell FEs. This made it possible to use fewer elements to model complex geometries, and achieve excellent efficiency-accuracy combination.

Bibliography

A Finite Element Analysis Program. (2011, April 16). Retrieved April 30, 2012, from Berkeley : http://www.ce.berkeley.edu/projects/feap/

A modular approach to cellular functions . (2012). Retrieved May 2012, from MBI Info: http://www.mechanobio.info/

ABAQUS, I. (2013). *ABAQUS/Explicit.* Retrieved May 21, 2012, from ABAQUS 6.13 Simulia: http://129.97.46.200:2080/v6.13/

Ahmad, S., Irons, B. M., & Zienkiewicz, O. C. (1970). Analysis of thick and thin shell structures by curved elements. *International Journal of Numerical Method Engineering*, 419-451.

ANSYS, I. (2008). *ANSYS LS-DYNA User's Guide.* Canonsburg: ANSYS, Inc.

Auricchio, F., Ferrara, A., & Morganti, S. (2012). Comparision and critical analysis of invariant-based models with respect to their ability in fitting human aortic valve data. *Annual Solid Structural Mechanics*, 1-14.

Bathe, K. (1996). *Finite element procedures.* New Jersey: Pearson Education.

Bathe, K. (2013). Insights and Advances in the Analysis of Structures. *Proceedings Fifth International Conference on Structural Engineering, Mechanics and Computation, SEMC 2013.* University of Cape Town (A. Zingoni, ed.), Taylor & Francis.

Bathe, K., & Bolourchi, S. (1979). A geometric and material nonlinear plate and shell element. *Computers and Structures*, 23-48.

Bathe, K., Dvorkin, E., & Ho, L. (1983). Our Discrete-Kirchhoff and isoparametric shell elements for nonlinear analysis - An assessment. *J. Computers and Structures*, 89-98.

Bathe, K., Ramm, E., & Wilson, E. (1975). Finite element formulation for large deformation dynamic analysis. *International Journal for Numerical Methods in Engineeerign*, 353-386.

Belytschko, T., Lin, J. I., & Chen-Shyh, T. (1983). Explicit algorithms for the nonlinear dynamics of shells. *Computer methods in applied mechanics and engineering*, 225-251.

Belytschko, T., Liu, W., & Moran, B. (2000). *Nonlinear finite elements for continua and structures.* New York: John Wiley & Sons, LTD.

Bucalem, M., & Bathe, K. (1993). Higher-order MITC general shell elements. *Int. J. for Numerical Methods in Engineering*, 3729-3754.

Comsol. (2006). *COMSOL Multiphysics: Version 3.3.* Comsol.

Dvorkin, E. (1995). Nonlinear analysis of shells using MITC formulation. *Archived of Computational Methods in Engineering*, 1-50.

Dvorkin, E., & Bathe, K. (1984). A continuum mechanics based four-node shell element for general non-linear analysis. *Engineering computations*, 77-88.

Einstein, D. R., Reinhallb, P., Nicosiac, M., Cochranc, R., & Kunzelmanc, K. (2003). Dynamic Finite Element Implementation of Nonlinear, Anisotropic Hyperelastic Biological Membranes. *Computer Methods in Biomechanics and Biomechanical Engineering*, 33-44.

Famaey, N., & Sloten, J. (2008). Soft tissue modeling for applications in vitual surgery and surgical robotics. *Computer Methods in Biomechanics and Biomedical Engineering*, 351-366.

FEAP. (2012). Retrieved April 30, 2012, from Bridge Art: http://www.bridgeart.net/software/programs/feap

Felippa, C. (2014, April 20). *Matrix Finite Element Methods in Dynamincs.* Retrieved from Department of Aerospace Engineering Sciences University of Colorado: http://www.colorado.edu/engineering/CAS/courses.d/MFEMD.d/MFEMD.Ch09.d/MFEMD.Ch09.pdf

Fung, Y. (1967). Elasticity of soft tissues in simple elongation. *American Journal of Physiology*, 1532-1544.

Guccione, J., McCulloch, A., & Waldman, L. (1990). Passive material properties of intact ventricular myocardium determined from a cylinderical model. *Journal of Biomedical Engineering*, 42-58.

Holzapfel, G. (2000). *Nonlinear solid mechanics- A continuum approach for engineering.* New York: John Wiley & Sons, LTD.

Holzapfel, G. A., Gasser, T. C., & Ogden, R. W. (2000). A new constitutive frame work for arterial wall mechanics and a comparative study of material models. *Journal of Elasticity*, 1-48.

Holzapfel, G. A., Gasser, T. C., & Ogden, R. W. (2000). A new constitutive framework for arterial wall mechanica and a comparative study of material models. *Journal of Elasticity*, 1-48.

Holzapfel, G., & Ogden, R. (2009). On planar biaxial tests for anisotropic nonlinearly elastic solids. A continuum mechanical frame work. *Mathematics and mechanics of solids*, 474-489.

Hughes, T. (2000). *The Finite Element Method: Linear static and dynamic finite element analysis.* New York: Dover Publications Inc.,.

Hughes, T., & Carnoy, E. (1982). Nonlinear finite element shell formulation accounting for large membrane strains. *Computer methods in applied mechanics and engineering*, 69-82.

Hughes, T., & Liu, W. (1980). Nonlinear finite element analysis of shells: Part I. Three-dimensional shells. *Computer methods in applied mechanics and engineering*, 331-362.

Hughes, T., Liu, W., & Levit, I. (1981). Nonlinear Dynamic Finite Element Analysis of Shells. *Nonlinear finite element analysis in structural mechanics*, 149-168.

Iding, R. H., Pister, K. S., & Taylor, R. L. (1974). Identification of nonlinear elastic solids by a finite element method. *Computer methods in applied mechanics and engineering*, 121-142.

Ingber, D. (2003). Mechanobiology and diseases of mechanotransduction Mechanobiology and diseases of mechanotransduction. *Ann. Med.*, 564–577.

Kanoknukulchai, W. (1979). A simple and efficient finite element for general shell analysis. *Numerical methods engineering*, 179-200.

Kiendl, J., Hsu, M., Wu, M., & Reali, A. (2015). Isogeometric Kirchhoff–Love shell formulations for general hyperelastic materials. *Computer Methods in Applied Mechanics and Engineering*, 280-303.

Kim, D., & Bathe, K. (2008). A 4-node 3D-shell element to model shell surface tractions and incompressible behaviour. *J. Computers and Structures*, 2027–2041.

Krakeland B. (1977). *Large displacement analysis of shells considering elastic-plastic and elasto-viscoplastic materials.* Norway: The Norwegian Institute of Technology.

Labrosse, M., Beller, C., Mesana, T., & Veinot, J. (2009). Mechanical behavior of human aortas: Experiments, material constants and 3-D finite element modeling including residual stress. *Journal of Biomechanics*, 996-1004.

Labrosse, M., Boodhwani, M., Sohmer, B., & Beller, C. (2011). Modeling leaflet correction techniques in aortic valve repair: A finite element study. *Journal of Biomechanics*, 2292-2298.

Labrosse, M., Lobo, K., & Beller, C. (2010). Structural analysis of the natural aortic valve in dynamics: From unpressurized to physiologically loaded. *Journal of Biomechanics*, 1916-1922.

Liu, S., & Lin, T. (1979). Elastic-plastic dynamic analysis of structures using known elastic solutions. *Int. J. Earthquake Eng. & Struct. Dynamics* , 147-159.

LS-DYNA. (2011). Retrieved May 4, 2012, from Livermore Software Technology Corporation: http://www.lstc.com/products/ls-dyna

LSTC Aplications. (2011). Retrieved May 4, 2012, from Livermore Software Technology Corporation: http://www.lstc.com/applications

MacNeal, R. (1976). *The NASTRAN Theoretical Manual*, Section 15.2.

MacNeal, R., & Harder, R. (1985). A proposed set of standard proplems to test finite elemnt accuracy. *Finite Elements in Analysis and Design*, 3-20.

May-Newman, K., & Yin, F. (1998). A constitutive law for mitral valve tissue. *Journal of Bioengineering*, 38-47.

McCulloch, A. (2011, March). *Continuity 6, A Problem Solving Environment for Multi-Scale Biology*. Retrieved May 2, 2012, from UCSD: http://www.continuity.ucsd.edu/Continuity/Documentation/Overview

Miller, K., Joldes, G., Lance, D., & Wittek, A. (2007). Total Lagrangian explicit finite element algorithm for computing soft tissue deformation. *Communications in numerical methods in engineering*, 121-134.

Nastran. (2005). Element Library Reference Manual. In *Nastran.* UGS Corp.

NEI Explicit. (2011, April). *Nastran Finite Element Analysis and Simulation Software.* Retrieved April 30, 2012, from NEi Explicit: http://www.nenastran.com/engineeringsoftware/nei-explicit.php

Ni Annaidh, A., Destrade, M., Gilchrist, M., & Murphy, J. (2013). Deficiencies in numerical models of anisotropic nonlinearly elastic materials. *Biomech Model Mechanobiol*, 781-791.

Pakravan, A., & Krysl, P. (2016). Mean-strain 10-node tetrahedron with energy-sampling stabilization. *International Journal for Numerical Methods in Engineering*.

Ramm, E. (1977). A plate/shell element for large deflections and rotations. In O. J. Bathe K. J., *Formulations and computational algorithms in finte element analysis.* MIT Press.

Samani, A., & Plewes, D. (2004). A method to measure hyoerelastic parameters of ex vivo breast tissue samples. *Physics in Medicine and Biology*, 4395-4405.

Sathyamoorthy, M. (1997). *Nonlinear analysis of structures.* New York: CRC Press.

Segal, G. (2010). Programmers Guide. In *Sepran.* Netherlands: Ingenieursbureau Sepra.

Shabana, A. (2011). *Computational continuum mechanics.* Cambridge: Cambridge University Press.

Shantaram, D., Owen, D., & Zeinkiewicz, O. (1976). Dynamic Transient behaviour of two- and three- dimensional structures including placticity large deformation effects and fluid interaction . *Earthquake engineering and structural dynamics*, 561-578.

SIMULIA. (2011, March). *ABAQUS Analysis User's Manual*. Retrieved April 2012, from ABAQUS Documentation: http://www.kxcad.net/ABAQUS/Documentation/docs/v6.6/books/usb/default.htm?startat=pt06ch23s06abo23.html

Sosa, J., & Gil, A. (2009). Analysis of a continuum-based beam element in the frame work of explicit FEM. *Finite Elements in Analysis and Design*, 583-591.

Speelman, L., Bosboom, E., & et al. (2008). Patient-Specific AAA Wall Analysis: 99-Percentile versus Peak Stress. *ELSEVIER*, 668-676.

Sun, W., & Sacks, M. S. (2005). Finite element implementation of a generalized Fung-elastic constitutive model for planar soft tissues. *Biomechanics and Modeling in Mechanobiology*, 190-199.

Sussman, T., & Bathe, K. (1987). A finite-element formulation for nonlinear incompressible elastic and inelastic analysis. *Computers and Structures*, 357-409.

Sussman, T., & Bathe, K. (2013). 3D-shell elements for structures in large strains. *J. Computers and Structures*, 2-12.

Takamizawa, K., & Hayashi, K. (1987). Strain energy density function and uniform strain hypothesis for arterial mechanics. *Journal of biomechanics*, 7-17.

Weinberg, E., & Kaasempur-Mofrad, M. (2006). A large-strain finite element formulation for biological tissues with application to mitral valve leaflet tissue mechanics. *Journal of Biomechanics*.

Wriggers, P. (2002). *Computational contact mechanics.* Chichester: John Wiley & Sons, LTD.

Zienkiewicz, O. (1977). The Finite Element Method. London: McGraw-Hill.